Spring 2019

Modeling complex oxides: Thermochemical behavior of nepheline-forming Na-Al-Si-B-K-Li-Ca-Mg-Fe-O and hollandite-forming Ba-Cs-Ti-Cr-Al-Fe- Ga-O systems

Stephen A. Utlak

Modeling complex oxides: Thermochemical behavior of nepheline-forming Na-Al-Si-B-K-Li-Ca-Mg-Fe-O and hollandite-forming Ba-Cs-Ti-Cr-Al-Fe-Ga-O systems

by

Stephen A. Utlak

Bachelor of Science
Clemson University, 2011

Master of Engineering
University of South Carolina, 2013

Submitted in Partial Fulfillment of the Requirements

For the Degree of Doctor of Philosophy in

Nuclear Engineering

College of Engineering and Computing

University of South Carolina

2019

Accepted by:

Theodore M. Besmann, Major Professor

Travis W. Knight, Committee Member

Jamil A. Khan, Committee Member

Vijay Jain, Committee Member

Cheryl L. Addy, Vice Provost and Dean of the Graduate School

Dedication

To my loved ones for their unwavering support. Without your encouragement and belief in me, this would not have been possible.

Acknowledgements

I gratefully acknowledge the financial support provided by the U.S. Department of Energy Waste Treatment and Immobilization Plant Project, Albert Kruger, Michael Schweiger, and Chuck Henager for their involvement with this research project, and Ted Besmann for advising me throughout my dissertation work.

Abstract

High concentrations of Na_2O and Al_2O_3 in the liquid high-level radioactive waste (HLW) stored at the Hanford Site can cause nepheline ($NaAlSiO_4$) to precipitate in a vitrified monolithic waste form upon cooling. Nepheline phase formation removes glass-former SiO_2 and -modifier Al_2O_3 from the immobilization matrix in greater proportion to alkalis, which can reduce glass durability and consequently increase the leach rate of radionuclides into the surrounding environment.

Current uncertainty in defining the HLW glass composition region prone to precipitating nepheline necessitates targeting a conservative waste loading, which raises operational costs by extending the liquid radioactive waste disposal mission and increases the required permanent repository storage capacity. An accurate thermochemical representation of HLW glass compositions is necessary to obtain a comprehensive understanding of the composition-temperature space for nepheline formation, which can facilitate the development of a phase field model of the mesoscale microstructural evolution of nepheline crystallization in HLW glass. As such an understanding of nepheline nucleation and grain growth kinetic behavior may lead to significant improvements in the production efficiency of durable HLW glass, generating thermochemical descriptions of the constituent phases is of primary importance.

Thus, a database consisting of the oxides of the nepheline-forming Na_2O-Al_2O_3-SiO_2 system and HLW glass nepheline solutes B_2O_3, K_2O, CaO, Li_2O, MgO, Fe_2O_3, and FeO has been developed to yield a thermochemical model capable of characterizing nepheline precipitation in HLW glass at equilibrium. Due to their high molar concentrations within vitrified glass, Na_2O, Al_2O_3, B_2O_3, and SiO_2 were considered major oxides whereas more dilute B_2O_3, K_2O, CaO, Li_2O, MgO, Fe_2O_3, and FeO were treated as minor constituents. All pseudo-binary systems composed of the major as well as major-minor oxide systems were thermodynamically assessed according to the CALculation of PHAse Diagrams (CALPHAD) methodology. Additionally, all pseudo-ternary systems consisting of the major oxides were assessed due to the increased probability of interactions between these higher concentration oxides. Gibbs energies of solid solution phases and the oxide liquid were modeled using the compound energy formalism (CEF) and two-sublattice partially ionic liquid (TSPIL) model, respectively.

Accuracy of the thermodynamic database was validated by comparing model calculations to HLW glass experimental data. Both annealed and canister centerline cooled (CCC) glass sample data were considered. Additionally, nepheline phase compositional data was included for comparison with database computations. Results of these comparisons indicate that the database-derived calculations agree well with HLW glass experimental data. As phase precipitation in a CCC glass sample is dependent on kinetics, however, a phase field or similar model will need to be utilized to obtain a non-equilibrium description of CCC HLW glass behavior, which in turn often require accurate Gibbs energies of phases.

Hollandite has been studied as a candidate ceramic waste form for the disposal of HLW due to its inherent leach resistance and ability to immobilize alkaline-earth metals such as Cs and Ba at defined lattice sites in the crystallographic structure. The chemical and structural complexity of hollandite-type phases with a large number of potential additives and compositional ranges for high-level waste immobilization would require impractical systematic experimental exploration. Modeling the equilibrium behavior of the complex hollandite-forming oxide waste system would aid in the design and processing of hollandite waste forms by predicting their thermodynamic stability. Thus, a BaO-Cs_2O-TiO_2-Cr_2O_3-Al_2O_3-Fe_2O_3-FeO-Ga_2O_3 thermodynamic database was developed according to the CALPHAD methodology. The CEF was used to model solid solutions such as hollandite while the TSPIL model characterized the oxide melt. The database was validated by experimental hollandite compositional data, and an isothermal BaO-Cs_2O-TiO_2 pseudo-ternary diagram with added hollandite solutes was generated to extrapolate phase equilibrium behavior to regions not experimentally explored.

TABLE OF CONTENTS

List of Tables

List of Figures

Chapter 1

Background

Immobilizing high-level liquid radioactive waste in a borosilicate glass matrix is being used for long-term storage of U.S. defense nuclear waste.[1] Certain types of radioactive waste that contain high concentrations of Na_2O and Al_2O_3, however can cause nepheline, $NaAlSiO_4$, to precipitate,[1] which would act to remove glass-former SiO_2 and glass-modifier Al_2O_3. Nepheline formation can thus cause severe deterioration of the durability of the resulting waste glass.[1]

Sodium aluminoborosilicate glasses with high concentrations of Al_2O_3 and Na_2O are susceptible to nepheline crystallization if the glass compositions are within or near the nepheline primary phase field of the pseudo-ternary Na_2O-Al_2O_3-SiO_2 phase diagram.[1-8] Uncertainty related to the prediction of nepheline phase formation in waste glass necessitates a conservatively dilute waste loading, which results in more filled canisters than is necessary for disposition of the material. An increase in produced canisters results in an increase in operational costs as well as the requirement for more costly temporary and permanent waste storage capacity.

An accurate phase field model that couples waste glass chemistry with the kinetics and morphology evolution of nepheline phase formation would reduce the uncertainty in the prediction of waste glass compositions in which nepheline would form. This in turn

would enable confidence in higher canister waste loadings and thereby reduce the quantity of canisters needed. Development of a phase field model, however, requires an accurate thermodynamic description of the equilibrium behavior of nepheline and associated phases within the multicomponent glass system, which will require a self-consistent thermodynamic database to yield the necessary set of thermochemical values.[9-13]

Towards this goal, the database must include the nepheline-forming oxides Na_2O, Al_2O_3, and SiO_2. Also, according to studies,[1, 4, 5, 8, 14-25] Li_2O, K_2O, Fe_2O_3, B_2O_3, CaO, and MgO are HLW glass oxides that can influence the precipitation of nepheline. Thus, these oxides should also be included to ultimately obtain a database composed of the oxides Na_2O, Al_2O_3, SiO_2, B_2O_3, K_2O, Li_2O, CaO, MgO, Fe_2O_3, and FeO. Further discussion of the basis for the selection of these particular constituents to form the multicomponent glass database is included in Section 2.3. To develop this database, thermodynamic assessments of pseudo-binary and -ternary subsystems composed of the constituent oxides will be conducted according to the CALPHAD methodology.[26]

In addition to the development of a HLW glass database to describe nepheline equilibrium behavior, the CALPHAD assessment approach[26] was also applied to characterize the stability of the hollandite phase in HLW. Ceramic waste forms such as hollandite have been shown to accommodate nearly all the constituents in nuclear waste including radioactive and non-radioactive components and are known to be resistant to hydrothermal leaching ubiquitous with geologic sequestration. Ceramic waste forms offer better durability and higher waste loadings for some species for which existing HLW glass formulations are inappropriate or inefficient.[27-30] Specifically, titanate ceramics, e.g., SYNROC,[31] have been extensively studied for use in immobilizing nuclear wastes due to

their inherent leach resistance.[32-34] Titanate hollandite ceramics can be generally expressed as $A_x(Ti^{+4},M)_8O_{16}$ where A represents alkali and alkaline earth metal cations such as Cs^{+1}, Ba^{+2}, Rb^{+1}, K^{+1}, and Sr^{+2} and M represents +2/+3 cations such as Al^{+3}, Fe^{+3}, Fe^{+2}, Ga^{+3}, Cr^{+3}, Zn^{+2}, and Mg^{+2}.[30, 35] Studies have been conducted to analyze the effect of M-site substitution on the crystallographic structure of hollandite and Cs incorporation.[28, 30, 36-40] To reduce the magnitude of the possible experiential work and target specific hollandite formulations, a thermodynamic database consisting of the oxides BaO, Cs_2O, TiO_2, Cr_2O_3, Al_2O_3, Fe_2O_3, FeO, and Ga_2O_3 has been developed to provide phase relations to guide development of compositions that are likely to form the hollandite phase as well as avoid secondary Cs parasitic phases.

The thermodynamic models that will characterize liquid and solid solution phases are the compound energy formalism[41] (CEF) and two-sublattice partially ionic liquid model[42] (TSPIL), respectively. The specific desire to use the TSPIL model stemmed from the ability of the model to provide a continuous description of a liquid that changes in character with varying composition[26] as well as the ease of scalability of the model to higher-order systems. The capability of both databases to accurately predict the equilibrium behavior of nepheline and hollandite in a HLW system will be validated by comparing calculation results to experimental data.

1.1. FactSage

FactSage is a thermochemical software and database package originally formed in 2001 from the fusion of the FACT-Win and ChemSage computational thermochemistry software suites.[43] A brief history of these latter two software packages is provided by Bale et al.[43] While FactSage is primarily used to calculate and plot binary, ternary, and

multicomponent phase equilibria for various applications in research laboratories and industry,[43] the thermochemical optimization capability and supporting software components are of primary importance in this work. As the general purpose of optimization within the CALPHAD method as well as the mathematics of the optimization technique employed by FactSage are discussed in Section 2.4, this section will rather focus on the software mechanisms involved in conducting an optimization within FactSage.

The functions of FactSage are made available as separate modules within a graphical user interface (GUI) that runs on a Microsoft Windows operating system with the modules labeled as 'Compound,' 'Solution,' 'Equilib,' and 'OptiSage' used in the process of conducting an optimization. The tutorial accompanying the OptiSage module explains the way these four modules interface in sufficient detail that a user can conduct an example assessment. Thus, what follows will be a brief summary of the purpose and use of each module in the context of optimizing a system.

The Compound module consists of a library of databases containing Gibbs energy expressions of chemical compound solid, liquid, and/or gaseous phases in polynomial form as a function of temperature. Values for heat capacities, enthalpies, and entropies of the compounds are also listed in accordance with eq. (2.13). Each database is intended for a particular application, e.g., FTdemoBASE is to be used when following FactSage tutorials while FToxidBASE, FTsaltBASE, and FTfrtzBASE can be used when analyzing oxide systems, salt systems, and nitrate based fertilizers, respectively. Additionally, users can create a new compound database(s) as part of the development of an assessed thermodynamic database. Solution endmember Gibbs energies (Sections 2.5.2 & 2.5.3) as

well as stoichiometric compounds known to form in a binary or ternary system of interest are obtained or derived from compounds in the Compound module.

The Solution module enables the construction of models to characterize the nonstoichiometric behavior of solid or liquid solution phases. As discussed in Sections 2.5.2 & 2.5.3, the CEF and TSPIL models employ a sublattice approach to account for solution phase defects and, thus, sublattice-based models are available for selection. The Gibbs energy functions of the solution endmembers are based on compounds obtained from the Compound module with possible inclusions of stoichiometric multipliers and/or optimized values. Interaction parameters of any order and various form including the Redlich-Kister power series (Sections 2.5.2 & 2.5.3) can also be added to the models with zero typically assigned as the starting value of the parameters. The assessor needs to anticipate the interaction parameters that may be needed to optimize a solution phase as part of the development of the initial solution model as additional interaction parameters cannot be added in the OptiSage module GUI.

Within the context of conducting an assessment, the Equilib module is used to generate a ChemSage file that is imported into OptiSage.

The OptiSage module allows the user to optimize solution phases and stoichiometric compounds to experimental data by adjusting the values of parameters that can include solution endmember or line compound standard enthalpies, standard entropies, or heat capacities as well as interaction parameter such as the A and B coefficients of a Redlich-Kister expanded polynomial (eq. (2.18)). The selection of the parameters to optimize is significantly dependent on the judgment of the assessor who must take into account knowledge of the system thermochemical behavior as well as make use of

assessment experience to anticipate the effect the inclusion of a new parameter into the optimization will have on the ability of the solid solution and/or liquid model(s) to reproduce all experimental data incorporated into the assessment. As described in Section 2.4.2, FactSage implements a sequential Bayesian parameter estimation technique to optimize the selected parameters to experimental data. The iterative process will stop when the errors of the parameters are less than a convergence limit or the maximum number of iterations is reached. The number, type, and order of experimental data sets to incorporate into an optimization is chosen at the discretion of the assessor but it is a good practice to optimize to thermochemical as well as phase equilibria data when available. It was concluded through the conduction of the assessments in this work that activity data was preferred to initiate an assessment if starting with zero values for interaction parameters to obtain good first estimates. Enthalpy of mixing data was then beneficial to include with activity data to further adjust the parameter values. Other thermochemical data such as partial Gibbs energies of system components could also be added at this step of the assessment. Phase equilibria data such as liquidus, solidus, or invariant points were then introduced to refine parameter values such that the calculated values yielded by the models aligned with the concomitant experimental data to a sufficient extent, which is also decided at the discretion of the assessor. As previously alluded, the process of selecting the parameters to optimize, order in which to optimize the parameters, experimental data to include, and order in which to include that experimental data is altogether reliant on the assessor. Upon completion of the optimization routine, a best set of assessed parameters is obtained that ideally enable the model(s) to characterize the equilibrium behavior of the system of interest.

Chapter 2

Literature Review

This section will use information that exists in published literature to discuss the formation of the glass system database, nepheline precipitation in HLW glass, the CALPHAD method including models for thermodynamic assessments, and solutions that are known to form in the Na_2O-Al_2O_3-B_2O_3-SiO_2-Fe_2O_3-Li_2O-K_2O-CaO-MgO system.

2.1. Nepheline precipitation

As nepheline consists of one mole of Na_2O and Al_2O_3 as well as two moles of SiO_2, the precipitation of a mole of nepheline removes three moles of the glass-former SiO_2 and glass-modifier Al_2O_3 from the glass matrix.[7] This results in reduced glass durability and hence the potential for an increased leach rate of radionuclides into the surrounding environment.[7] Analysis of experimental glass composition studies[8, 24, 44] conducted by Li et al.[1] determined that glasses with a ratio of $SiO_2/(SiO_2 + Na_2O + Al_2O_3) > 0.62$ (Fig. 2.1), where the chemical formulas represent mass fractions in glass, do not precipitate nepheline. This empirical mass ratio limit is known as the nepheline discriminator and is used as a process control constraint at the Defense Waste Processing Facility[45] as well as for Hanford site models.[46]. The nepheline discriminator has been proven to be conservative as indicated by a result of a study conducted by Vienna et al.,[47] which compiled and plotted nepheline

crystallization data for 747 HLW glass compositions (Fig. 2.2). This plot indicates that HLW glass compositions exist with SiO_2 mass concentrations greater than 0.62 that do not precipitate nepheline.

Reducing the SiO_2 mass concentration limit would enable high Al_2O_3 concentration glasses to be produced, which would allow for higher waste loadings to be targeted.[23] Effort has been directed towards refining the nepheline discriminator to reduce known conservatism.[18-20, 23, 47] However, as the basis of the discriminator is fundamentally empirical, it is desirable to consider a method of describing nepheline precipitation that is based on a physical understanding of the glass system. Thus, nepheline crystallization can likely be characterized by a thermochemical equilibrium model due to the rapid kinetics of nepheline crystallization in melts.[8, 48] As such, this may represent an alternative method to the discriminator approach to identify glass compositions that will precipitate nepheline. An accurate thermochemical representation of waste glass compositions is necessary to allow a more precise understanding of the composition-temperature space for nepheline formation, which can facilitate the development of a physical model utilizing kinetics and growth descriptions in a phase field approach to predict nepheline precipitation in glass. This would be the most reliable type of model and could be confidently extended to regions where measurements are lacking. The development of such a model requires accurate thermochemical descriptions of the constituent phases, which is the objective of the current effort.

2.2. Nepheline experimental observations

Li et al.[1] applied Raman spectroscopy as well as optical, scanning electron, and transmission electron microscopy to sodium aluminoborosilicate glasses that precipitated

nepheline as the primary phase. The Raman spectroscopic results indicated that nanocrystals formed in certain glass composition melts and were thus present in the quenched glass samples. Transmission optical micrographs (Fig. 2.3) indicated that glass samples with high alumina concentrations resulted in significant nepheline crystallization that showed a regular pattern of a light nepheline phase in the matrix. In addition, nepheline was present in a canister centerline cooled and thus slowly cooled medium-alumina concentrated glass sample (Fig. 2.4) as well as isothermally treated samples in the form of large crystals (Fig. 2.5). Scanning electron microscopy micrographs were obtained of an NP-BL sample was heat treated at 816ºC for 72 hours in a temperature gradient furnace, and nepheline crystals of various morphologies were observed (Fig. 2.6).

McCloy et al.[5] applied multi-nuclear magnetic resonance (NMR), Raman, and Mossbauer spectroscopies to analyze the effect of Si, Al, B, Na, and Fe as nuclear glass network melt structure precursors to nepheline crystallization. The crystallographic structure of nepheline was first considered in order to appreciate its crystallization in the complex melt. Per the study, the nepheline structure is described as a 'stuffed tridymite derivative' meaning that six-membered ring layers are stacked and the channels within these rings are filled with specific cations (Fig. 2.7). The nepheline crystal formation is formed by the stacking of the ring layers along the c-axis in an eclipsed or cis arrangement in which the layers are mirror images. Four types of tetrahedral sites exist in the nepheline structure and are indicated as T(1), T(2), T(3), and T(4) in Fig. 2.7. Aluminum and silicon tetrahedra form six-membered rings that alternate. Additional silicon atoms added to the nepheline structure have been observed (Dollase & Thomas[49]) as well as substitutions with calcium, iron, and other cations (Tait et al.[16]). The general occupation, however, of the

tetrahedral sites is considered to be aluminum on the T(1) site with potential silicon anti-site defects, silicon on the T(2) site with potential aluminum anti-site defects, silicon on the T(3) site with potential aluminum anti-site defects, and aluminum on the T(4) site with potential silicon anti-site defects. The T(1) and T(2) sites are generally considered to be fully ordered whereas the T(3) and T(4) sites are partially disordered in aluminum and silicon. Short-range order of the nepheline tetrahedral sites has also been observed in nuclear magnetic resonance studies.[50] Iron is often observed in natural nepheline crystals (Vulic et al.[51]) in a valence state of Fe^{+3} (Tait et al.[16]) as the smaller Fe^{+2} is not as favored to occupy the channel sites.[52] Pierce et al.[3] has also shown that the +3 valence state of boron can occupy a tetrahedral site in synthetic materials but the specific site is not currently known.

The NMR study conducted by McCloy et al.[5] indicated two sites for aluminum, silicon, and sodium in the samples that crystallized nepheline as well as a change in boron speciation that resulted in an increase of boron (IV) after nepheline crystallization. The Raman spectroscopy results (McCloy et al.[5]) indicated that a significant part of the glass matrix is composed of metaborate chains or rings, which suggests the presence of a large quantity of non-bridging oxygens as well as a separation of the borate from the aluminosilicate network. Mossbauer spectroscopy (McCloy et al.[5]) in combination with iron redox chemical measurements indicated that iron plays a minor role in the sodium aluminosilicate glasses with a predominance of the Fe^{+3} valence state present. It was also observed that iron oxide spinel always forms with the crystallization of nepheline.

2.3. Selection of oxides to construct database and systems to assess

Three high-level nuclear waste glass composition variability studies (CVSs) were conducted to ensure that the Hanford Site glass product would be acceptable.[53] A concise summary of CVS-I,[54] CVS-II,[54] and CVS-III,[55] was documented by Hrma et al.[56] The glass composition regions selected for the CVSs were based on results of previous scoping and solubility studies as well as projections of glass compositions that may be produced at the Hanford Site.[53] The acceptable glass composition region was defined by the major oxide components in the feed, glass additives, and recycle streams of SiO_2, B_2O_3, Al_2O_3, Fe_2O_3, ZrO_2, Na_2O, Li_2O, CaO, MgO, and all 'other' remaining waste components of which K_2O is included.[8, 53] Table 2.1 lists the glass composition range covered by CVS-1[54] and CVS-2,[54] which are the ranges over which glass property models are considered to be useful and valid.[53]

Matlack et al.[57] were tasked with determining a glass composition optimized for waste loading while retaining acceptable durability and processing characteristics. Four glass compositions limited by bismuth, chromium, aluminum, and aluminum + sodium were provided by the DOE Office of River Protection to Matlack et al.[57] for analysis. The study concluded that an aluminum-limited waste had the best combination of high waste loading as well as glass and melt properties[57] displays the oxide composition of the aluminum-limited waste denoted as HLW-E-AL-27.

The main disadvantage of high-aluminum HLW glass is the potential to precipitate nepheline, which reduces glass durability.[7] As the waste at the Hanford Site contains high concentrations of aluminum mostly due to the reprocessing of cladding material used in Site production reactors, nepheline precipitation in glass will be a limiting factor for the

vast majority of the waste processed at the Hanford Site. Li et al.[8] established that, of the oxides listed in Table 2.2, B_2O_3, Fe_2O_3, Li_2O, K_2O, CaO, and MgO can affect nepheline precipitation. Thus, the proposed Na_2O-Al_2O_3-SiO_2-B_2O_3-K_2O-Li_2O-CaO-MgO-Fe_2O_3-FeO database to be assessed consists of the recommended oxides for glass property models that can impact nepheline precipitation.

Per Table 2.2, the oxides at greater than 10% molar concentration are SiO_2, Al_2O_3, B_2O_3, and Na_2O, and are thus considered in this work to be major components of the database. The remaining oxides known to affect nepheline precipitation in HLW glass at less than 10% molar concentration, those being Fe_2O_3, Li_2O, K_2O, CaO, and MgO, are labeled as minor components. FeO will also be considered as Fe commonly exists as an equilibrium mixture of Fe^{+2} and Fe^{+3} in glass.[58, 59] Due to relatively high molar concentrations, the major components exist in the glass in sufficient concentrations that it is likely these components will interact with all other major as well as minor components, whereas it is more unlikely that a minor-minor oxide interaction would occur due to the dilute concentrations of these components. As such, the database will be developed by assessing all pseudo-binary and -ternary systems consisting of the major oxides as well as all pseudo-binary systems of the major-minor oxides.

2.4. CALPHAD methodology overview

Cacciamani[60] developed the flowchart displayed in Fig. 2.8 that outlines the steps involved in performing a CALPHAD assessment. Descriptions of each step will herein be provided.

Thermodynamic modeling of phases involves constructing a model of a phase that exists within a binary or higher order system. Thermodynamic solution models such as the

CEF and TSPIL are most often developed within software packages such as FactSage[43] or Thermo-Calc.[61] These models can be used to calculate thermodynamic properties of ordered and disordered solid solutions as well as liquids.

2.4.1. Evaluation of experimental data

It is necessary to collect and critically evaluate experimental data applicable to the system being assessed as inaccurate data will result in a poor optimization. In analyzing the quality of experimental data, details to be considered include the experimental technique used, phases present within the system, purity of the sample analyzed, experimental conditions, quantities measured, and accuracy of the measurements.[62] Per Saunders & Miodownik,[63] many experimental techniques can be utilized to obtain thermochemical data. Isothermal and isoperibol calorimeters can be used to measure heat contents of pure substances from which heat capacities may be derived whereas adiabatic and heat-flow calorimeters are more effective at directly measuring heat capacities and enthalpies of transformation. Calorimetric techniques such as the drop method and electromagnetic levitation calorimetry can also be utilized to measure enthalpies and heat capacities of pure substances or reactions. Differential scanning calorimetry (DSC) measures the heat absorbed or released during a transformation and thus is often used to quantify thermodynamic properties during phase transformations. Differential thermal analysis (DTA) is more sensitive to temperature changes in a sample than DSC and, consequently, is more often used to determine temperatures of material phase changes. Combustion bomb calorimetry has been successfully used to measure enthalpies of formation of carbides, borides, and nitrides. Gas phase equilibria techniques used to determine thermochemical properties from activities derived from measured vapor

pressures include static methods, dew-point and non-isothermal methods, as well as Knudsen effusion and Langmuir free-evaporation methods. Electromotive force (EMF) experiments can also be conducted to measure partial Gibbs energies.

Experimental techniques also exist to determine phase equilibria and can be categorized as non-isothermal and isothermal techniques. Non-isothermal methods include thermal analysis techniques such as generating cooling curves, DSC, and DTA as well as chemical potential techniques such as EMF, magnetic susceptibility measurements, resistivity methods, and dilatometric methods. Isothermal techniques include metallography that involves the use of optical or electron microscopy, x-ray diffraction, sampling and equilibration methods, and diffusion couples.

Thermodynamic data can also be estimated when experimental data is not available or sufficient for a system. Spencer[64] details methods of thermodynamic data estimation of heat capacities, entropies, and enthalpies of formation for metallurgical applications. Also discussed are the thermophysical property data requirements for single phases as well as two phases that enable the correlation of this data to phase diagrams generated via the CALPHAD method.

Thermochemical data can also be generated from semi-empirical or ab-initio methods such as Density Functional Theory[65] (DFT). Ab-initio calculations, however, are currently limited to relatively small unit cell analyses due to the computational requirements inherent to calculation methods such as DFT. Consequently, first principle methods to calculate thermochemical data remain relatively restricted within the CALPHAD community.

2.4.2. Sequential Bayesian estimation for optimization

The next step in the CALPHAD process is the optimization of the thermodynamic models to thermochemical data. Optimizations are most often conducted within software packages that have a module specifically for optimization procedures such as OptiSage within the FactSage software suite,[43] which uses a sequential Bayesian parameter estimation technique as the main optimization routine.[66]

The goal of sequential Bayesian estimation within the context of the CALPHAD method is to determine values for unknown coefficients of a Gibbs energy function such that the function can output calculated thermodynamic values within the desired accuracy of a corresponding experimentally determined data point. The following mathematical description is based on texts authored by Walton,[67] Konigsberger & Gamsjager,[68] Konigsberger,[69] and Konigsberger & Eriksson.[66]

According to Bayesian estimation theory, an error function can be established consisting of a term accounting for the difference between values calculated by the model and corresponding experimental data as well as a term accounting for the difference between original and final model parameters:

$$E(P) = \sum_{j,k=1}^{n} \left(f_j(P) - y_j\right) C_{yjk}^{-1} \left(f_k(P) - y_k\right) + \sum_{j,k=1}^{m} \left(P_j - P_j^o\right) C_{P^o jk}^{-1} \left(P_k - P_k^o\right) \qquad (2.1)$$

where y_j and $f_j(P)$ are the j^{th} experimental value and corresponding model calculated value as a function o2f the model parameters $P_1,\ldots,P_m$, respectively. The variables $P_1^o,\ldots, P_m^o$ represent *a priori* model parameters to use as initial values for the minimization process. C_{yjk} and $C_{p^o jk}$ are covariance matrices of experimental function values y and *a priori* parameters p^o, respectively. The inverse of the C variables are weighting matrices, which

enable different weightings for the two parts of the error function to represent the confidence of the assessor in the accuracy of the experimental data as compared to the original model properties.

Eq. (2.1) can be rewritten in matrix form as:

$$E(P) = (f(P) - y)^{\mathrm{T}} C_{\mathrm{y}}^{-1} (f(P) - y) + (P - P^{\mathrm{o}})^{\mathrm{T}} C_{\mathrm{p^o}}^{-1} (P - P^{\mathrm{o}}) \quad (2.2)$$

where f(p) and P are the model calculation vector function and model parameter vector, respectively.

Minimizing eq. (2.2) according to a Newton-Raphson method[67] algorithm yields the recursive formula:

$$P^{\mathrm{i+1}} - P^{i} = \left((S^{\mathrm{T}}) C_{\mathrm{y}}^{-1} S + C_{\mathrm{p^o}}^{-1} \right)^{-1} \cdot \left(C_{\mathrm{p^o}}^{-1} \left(P^{\mathrm{o}} - P^{\mathrm{i}} \right) \right) + S^{\mathrm{T}} C_{\mathrm{y}}^{-1} \left(y - f\left(p^{\mathrm{i}} \right) \right) \quad (2.3)$$

where S is the sensitivity matrix of derivatives of the model calculations, $f(P)$, with respect to the model parameters, P. For an element jk of the sensitivity matrix:

$$S_{\mathrm{jk}} = \partial f_{\mathrm{j}}(P) / \partial P_{\mathrm{k}} \quad (2.4)$$

$P^{\mathrm{i+1}}$ values are iteratively determined until the $P^{\mathrm{i+1}} - P^{\mathrm{i}}$ delta is less than a prescribed convergence limit at which point a final best set of model parameters is obtained.

2.4.3. Lagrange multiplier method for Gibbs energy minimization

As previously stated, the Lagrange multiplier method is used to minimize the Gibbs energy of thermodynamic models.

The following characterization of the Lagrange multiplier method is based on the texts of Hillert[70] as well as Lukas et al.[26] The total Gibbs energy of a system is defined by summing the number of moles of the phase α, n^{α}, multiplied by the integral molar Gibbs energy of each phase α, G_{m}^{α}, with the constraint that $n^{\alpha} \geq 0$:

$$G = \sum_{\alpha} n^{\alpha} \cdot G_{\mathrm{m}}^{\alpha} \tag{2.6}$$

The equilibrium condition of the system may then be expressed as:

$$\min[G(n^{\alpha}, T, p, y_{\mathrm{k}}^{\alpha s})] = \min\left[\sum_{\alpha} n^{\alpha} \cdot G_{\mathrm{m}}^{\alpha}(T, p, y_{\mathrm{k}}^{\alpha s})\right] \tag{2.5}$$

where T and p are the temperature and pressure of the system, respectively, while $y_{\mathrm{k}}^{\alpha s}$ represents the site fraction of the k species on sublattice s of the phase α.

The minimum of the total Gibbs energy as described by eq. (2.5) can be obtained through the application of the Lagrange-multiplier method with the system subjected to the following three constraints:

$$n_{\mathrm{i}} - \sum_{\alpha} n^{\alpha} \sum_{\mathrm{s}} a^{\mathrm{s}} \sum_{\mathrm{k}} b_{\mathrm{i}}^{\mathrm{k}} \cdot y_{\mathrm{k}}^{\alpha s} = 0 \tag{2.7}$$

$$\sum_{\mathrm{k}} y_{\mathrm{k}}^{\alpha s} - 1 = 0 \tag{2.8}$$

$$\sum_{\mathrm{s}} a^{\alpha s} \sum_{\mathrm{k}} \nu_{\mathrm{k}} \cdot y_{\mathrm{k}}^{\alpha s} = 0 \tag{2.9}$$

where n_{i} is the total content of each element in the i system, $a^{\alpha s}$ is the number of sites on the sublattice s in one mole of phase α, $b_{\mathrm{i}}^{\mathrm{k}}$ is the number of i atoms per unit of k species, and ν_{k} is the valency of k species. Eqs. (2.7) - (2.9) establish that the total amount of each i component in phase α remains constant, the site fractions in each sublattice of phase α sum to unity, and the charge of each ionic species in phase α sums to zero, respectively.

Each constraint can be multiplied by a Lagrange multiplier and then added to the total Gibbs energy of the system to form a target function to be minimized:

$$\min[L(T,p,n_i,y_k^{\alpha s},n^{\alpha},\beta,\gamma,\delta)] \tag{2.10}$$
$$= \sum_{\alpha} n^{\alpha}\cdot G_m^{\alpha}(T,p,y_k^{\alpha s}) + \beta\left[n_i - \sum_{\alpha} n^{\alpha}\sum_{s} a^{s}\sum_{k} b_i^{k}\cdot y_k^{\alpha s}\right]$$
$$+\gamma\left[\sum_{k} y_k^{\alpha s} - 1\right] + \delta\left[\sum_{s} a^{\alpha s}\sum_{k} \nu_k\cdot y_k^{\alpha s}\right]$$

where β, γ, and δ are the Lagrange multipliers.

A set of nonlinear equations is then obtained by setting the first derivatives of L with respect to each of the unknowns to zero. The partial derivatives with respect to the Lagrange multipliers β, γ, and δ will yield Eqs. (2.7) - (2.9) while the partial derivatives with respect to n^{α} and $y_k^{\alpha s}$ result in Eqs. (2.11) & (2.12), respectively:

$$\frac{\partial L}{\partial n^{\alpha}} = G_m^{\alpha} - \beta\sum_{s} a^{\alpha s}\sum_{k} b_i^{k}\cdot y_k^{\alpha s} = 0 \tag{2.11}$$

$$\frac{\partial L}{\partial y_k^{\alpha s}} = n^{\alpha}\frac{\partial G_m^{\alpha}}{\partial y_k^{\alpha s}} - \beta\sum_{\alpha} n^{\alpha}\sum_{s} a^{\alpha s}\sum_{k} b_i^{k} + \gamma + \delta\sum_{s} a^{\alpha s}\sum_{k} \nu_k = 0 \tag{2.12}$$

As the set of equations defined by Eqs. (2.7) - (2.9), (2.11), & (2.12) yield equilibrium conditions for the unknowns $y_k^{\alpha s}$, n^{α}, β, γ, and δ, the variables T, p, and n_i must be given initial values and held constant during the minimization routine. Values for these unknown variables for the system at equilibrium can be determined through the use of a root-finding algorithm such as the Newton-Raphson method.

2.4.4. Model validation and database formation

Once the thermodynamic models are optimized, phase diagrams can be generated and compared with phase equilibria experimental and/or derived data. As indicated in Fig. 2.9, intensive and extensive thermochemical data can be deduced from the Gibbs energies of the optimized models and thus can also be compared to corresponding input data. The accuracy of the model to predict empirical data, assuming the data is of a quality

nature, indicates the reliability of the model to predict phase equilibria or thermochemical data for which no experimental measurements exist.

Thermodynamic models that have been successfully optimized can then be added to databases from which other users can conduct thermochemical equilibrium analyses of systems that include the components of the optimized system. The caveat to this ability being that the subsystems of higher order system databases must be self-consistent. Consequently, higher-order systems are developed by first modeling and optimizing pseudo-binary and then -ternary systems that are then combined to form a complex database of quaternary or greater components.

2.5. Thermodynamic modeling

Sections 2.5.1 – 2.5.3 will review the thermodynamic approach to modeling stoichiometric compounds as well as solid and liquid solutions.

2.5.1. Stoichiometric compounds

The Gibbs energy of a stoichiometric compound is defined as:

$$G_{\text{compound}} = \Delta H^{\text{o}}_{298.15\text{K}} + \int_{298.15\text{K}}^{\text{T}} C_{\text{p}}\,\text{d}T - T\left(S^{\text{o}}_{298.15\text{K}} + \int_{298.15\text{K}}^{\text{T}} \frac{C_{\text{p}}}{T}\,\text{d}T\right) \tag{2.13}$$

where $\Delta H^{\text{o}}_{298.15\text{K}}$ is the change in the compound enthalpy at a standard state of 298.15 K and 1 bar, T is the temperature of the compound in K, C_{p} is the heat capacity, and $S^{\text{o}}_{298.15\text{K}}$ is the compound entropy at the defined standard state conditions.

Supported by the theory presented by Berman & Brown,[71] the heat capacity in eq. (2.13) can be expressed as the polynomial:

$$C_{\text{p}} = a + b\cdot 10^{-3}T + c\cdot 10^{5}T^{-2} + d\cdot 10^{-9}T^{2} + eT^{-0.5} + f\cdot 10^{8}T^{-3} + gT^{-1} + h\cdot 10^{-8}T^{3} \tag{2.14}$$

2.5.2. Compound energy formalism

The CEF[41] will be used to characterize the equilibrium behavior of solid solutions that form in HLW glass. Phase nonstoichiometry is modeled through a sublattice formalism, e.g., $(A,B)_2(C,D)_1$, in which each sublattice represents a crystallographic lattice site and point defects such as interstitials, vacancies, and/or anti-site substitutions are accounted for by the inclusion of species in each sublattice. For the example sublattice, *A*, *B*, *C*, and *D* are sublattice species representing chemical elements, compounds, or vacancies that can substitute within each sublattice on a given lattice site. Combinations of species across sublattices, e.g., A_2C_1, A_2D_1, B_2C_1, and B_2D_1, are known as model endmembers that are assigned Gibbs energies that can be equivalent to stoichiometric compounds or derived from an optimization. Mixing of these endmembers according to the CEF theory (eq. (2.15)) yields the stable stoichiometric range of the solid solution within the binary or higher order system of interest.

The molar Gibbs energy of a phase modeled using the CEF can be expressed as:

$$G_{\mathrm{m}} = \Sigma \Delta_{\mathrm{f}}{}^{\mathrm{o}} G_{\mathrm{end}} \Pi y_{\mathrm{J}}^{\mathrm{s}} + RT\Sigma\Sigma n^{\mathrm{s}} y_{\mathrm{J}}^{\mathrm{s}} \ln y_{\mathrm{J}}^{\mathrm{s}} + {}^{\mathrm{E}} G_{\mathrm{m}} + {}^{\mathrm{mag}} G \qquad (2.15)$$

where $\Delta_{\mathrm{f}}{}^{\mathrm{o}} G_{\mathrm{end}}$ is the molar Gibbs energy of formation of an endmember, $y_{\mathrm{J}}^{\mathrm{s}}$ is the site fraction of the J^{th} constituent in the n^{th} sublattice, and n^{s} is the stoichiometric coefficient of the n^{th} sublattice. The first, second, third, and fourth terms of eq. (2.15) are the Gibbs energy surface of reference, ideal entropy of mixing, excess Gibbs energy of mixing, and the magnetic contribution to the Gibbs energy, respectively.

The Gibbs energy surface of reference effectively mixes the endmembers resulting from the sublattice structure using the Gibbs energy of each endmember such that a surface of reference can be plotted above a composition plane. If no excess term was present and

the temperature of a system low enough that the ideal entropic mixing term was negligible, then this surface of reference could be used to predict the equilibrium behavior of the material.

The ideal entropy of mixing accounts for mixing of species on the same sublattice without energetic interaction between the species, i.e., all energy of the mixing species is kinetic energy due to motion.

The excess Gibbs energy, which accounts for the departure from ideal mixing of species on the same sublattice due to attraction or repulsion of the mixing constituents,[72] can be described with a generalized regular solution expression:

$$^{\mathrm{E}}G_{\mathrm{m}} = \Pi y_{\mathrm{J}}^{\mathrm{s}} \Sigma y_{\mathrm{B}}^{\mathrm{t}} L_{\mathrm{A,B:D:G}} \ldots + \Pi y_{\mathrm{J}}^{\mathrm{s}} \Sigma\Sigma y_{\mathrm{B}}^{\mathrm{t}} y_{\mathrm{D}}^{\mathrm{u}} L_{\mathrm{A,B:D,E:G}} \ldots + \ \ldots \tag{2.16}$$

where the subscripts A, B, D, E, and G as well as superscripts t and u refer to the constituents in a sublattice and the sublattice designations, respectively, in a generalized CEF formulation for a three sublattice phase $(A,B)_{\mathrm{k}}^{\mathrm{t}}(D,E,F)_{\mathrm{l}}^{\mathrm{u}}(G)_{\mathrm{m}}^{\mathrm{v}}$. The subscripts *k*, *l*, and *m* in the generalized formula represent the sublattice stoichiometric coefficients. The commas separating constituents in the interaction parameter designations of eq. (2.16) indicate the interactions between constituents on the same sublattice whereas the colons separate sublattices. eq. (2.16) can be expanded to describe binary, ternary, and higher-order interactions between sublattice constituents as needed.

The interaction parameters of eq. (2.16) can be expressed as Redlich-Kister power series in terms of site fractions. As an example, for a binary interaction between the A and B species of eq. (2.17):

$$L_{\mathrm{A,B:D:G}} = \sum_{k=0}^{n} {}^{\mathrm{k}}L_{\mathrm{A,B:D:G}}(y_{\mathrm{A}}^{\mathrm{t}} - y_{\mathrm{B}}^{\mathrm{t}})^{\mathrm{k}} \tag{2.17}$$

The L term on the right-hand side of eq. (2.17) can be expanded as a polynomial of the form:

$$^{k}L_{A,B:D:G} = A + B \cdot T + C \cdot T \cdot \ln(T) + D \cdot T^{2} + E \cdot T^{3} + F \cdot T^{-1} \quad (2.18)$$

where the variables A, B, C, D, E, and F are coefficients that can be empirically determined through the optimization technique discussed in Section 2.4.2. In practice, only the A and B coefficients of eq. (2.18) are included in an assessment unless experimental data can justify the assignment of an empirically-derived value to an additional coefficient. For instance, the C coefficient that can be incorporated into an optimization if experimental heat capacity data exists for the system being assessed.[26]

The magnetic Gibbs energy term of eq. (2.15) is defined by:

$$^{mag}G = RT \cdot f(\tau) \cdot \ln(\beta(x) + 1) \quad (2.19)$$

where $\beta(x)$ is the average magnetic moment per mole of atoms in Bohr magnetons as a function of sublattice site fractions, τ is the ratio T / $T_C(x)$ where $T_C(x)$ is the magnetic ordering critical temperature, also known as the Curie or Néel temperature for ferromagnetic or antiferromagnetic materials, respectively, as a function of sublattice site fractions, and $f(\tau)$ represents a power series as a function τ that expands Inden's description of the magnetic heat capacity.[73]

To introduce the composition dependence of ^{mag}G, the terms $\beta(x)$ and $T_C(x)$ of eq. (2.19) are expressed as Redlich-Kister power series similar to the excess Gibbs energy term of eq. (2.15). For instance, when considering a binary interaction of species A and B on a sublattice, these magnetic terms can be expanded as:

$$T_C(x) = x_A T_C(A) + x_B T_C(B) + x_A x_B \sum_{k=0}^{n} {}^{k}T_C \, (x_A - x_B)^k \quad (2.20)$$

$$\beta(x) = x_A\beta(A) + x_B\beta(B) + x_A x_B \sum_{k=0}^{n} {}^{k}\beta\,(x_A - x_B)^k \tag{2.21}$$

where ${}^{k}T_C$ and ${}^{k}\beta$ are empirical parameters evaluated by optimizing to experimental data.

2.5.3. Two-sublattice partially ionic liquid model

Hillert et al.[42] discuss the development of a TSPIL model for liquid solutions with different tendencies for ionization. The TSPIL model is based on the concept that the strength of ionization of ionic substances results in each atom being surrounded by unlike atoms in a form of chemical ordering. This ordering can be treated as two sublattices, one containing only cations and the other anions. Charged vacancies may be introduced on either cationic or anionic sublattices with the valency of the vacancy on either sublattice corresponding to the average for the ions on the other sublattice. Negatively charged vacancies on the anionic sublattice can be considered vacant sites with an excess of electrons. Positively charged vacancies on the cationic sublattice, however, would require the development of an additional rule to account for the valencies of the two kinds of vacancies. Rather than implementing this approach, however, it is possible instead to introduce a neutral species on the anionic sublattice to account for deviations from stoichiometry towards the nonmetallic side of the system. Thus, the cation sublattice will contain only positively charged ions whereas the anion sublattice can contain negatively charged ions and vacancies as well as neutral species. As described by Lukas et al.,[26] the general TSPIL sublattice formula can be written as:

$$\left(C_i^{+\nu_i}\right)_P\left(A_j^{-\nu_j}, Va, B_k^0\right)_Q$$

where *C*, *A*, *Va*, and *B* denote cations, anions, hypothetical vacancies, and neutral species, respectively, while the indices i, j, and k represent specific sublattice constituents. The

superscripts $+\nu_i$ and $-\nu_j$ represent the charge of the i^{th} or j^{th} cation or anion, respectively, while 0 indicates a neutral species. Electroneutrality is maintained by allowing the stoichiometry (P and Q) to vary as a function of site fractions:

$$P = \Sigma \nu_j y_{A_j} + Q y_{Va} \tag{2.22}$$

$$Q = \Sigma \nu_i y_{C_i} \tag{2.23}$$

The Gibbs energy of an ionic liquid can then be expressed as:

$$G_m = \Sigma\Sigma y_{C_i} y_{A_j} {}^{o}G_{C_i:A_j} + Q\left(y_{Va}\Sigma y_{C_i} {}^{o}G_{C_i} + \Sigma y_{B_k} {}^{o}G_{B_k}\right) + RT\left[P\Sigma y_{C_i} \ln y_{C_i} + Q\left(\Sigma y_{A_j} \ln y_{A_j} + y_{Va} \ln y_{Va} + \Sigma y_{B_k} \ln y_{B_k}\right)\right] + {}^{E}G_m \tag{2.24}$$

where ${}^{o}G_{C_i:A_j}$ is the Gibbs energy of formation for $\nu_i + \nu_j$ moles of atoms of the endmember C_iA_j while ${}^{o}G_{C_i}$, and ${}^{o}G_{B_k}$ are the values for C_i and B_k, respectively. The first, second, and third terms of eq. (2.24) are the Gibbs energy surface of reference for all possible types of constituents, the configurational entropy on each sublattice, and the excess Gibbs mixing energy, which can be expressed as:

$${}^{E}G_m = \Sigma\Sigma\Sigma y_{i_1} y_{i_2} y_j L_{i_1,i_2:j} + \Sigma\Sigma\Sigma y_i y_{j_1} y_{j_2} L_{i:j_1,j_2} + \Sigma\Sigma y_i y_{j_1} y_{Va} L_{i:j_1,Va} + \ldots \tag{2.25}$$

As discussed in relation to the CEF model, the interaction parameters of eq. (2.25) can be expressed using the Redlich-Kister power series described by eq. (2.17) with the L terms defined by the eq. (2.18) polynomial.

2.6. Tables

Table 2.1. Glass composition range covered by CVS-1 & CVS-2 studies[53]

Oxide component	Lower bound (wt%)	Upper bound (wt%)
SiO_2	42	57
B_2O_3	5	20
Al_2O_3	0	17
Fe_2O_3	0.5	15
Na_2O	5	20
Li_2O	1	7
CaO	0	10
MgO	0	8
Other oxides (K_2O)	1	10

Table 2.2. Oxide composition of HLW-E-AL-27 glass[57]

Oxide	Glass Composition HLW-E-AL-27 (wt%)	Glass Composition HLW-E-AL-27 (mol%)
SiO_2	30.50	35.06
Al_2O_3	23.97	16.24
B_2O_3	15.19	15.07
Na_2O	9.58	10.68
Li_2O	3.57	8.25
CaO	6.08	7.49
Fe_2O_3	5.90	2.55
F	0.67	2.44
P_2O_5	1.05	0.51
NiO	0.40	0.37
Cr_2O_3	0.52	0.24
ZrO_2	0.39	0.22
MgO	0.12	0.21
SO_3	0.20	0.17
Bi_2O_3	1.14	0.17
PbO	0.41	0.13
K_2O	0.14	0.10
ZnO	0.08	0.07
BaO	0.05	0.02
CdO	0.02	0.01
TiO_2	0.01	0.01

2.7. Figures

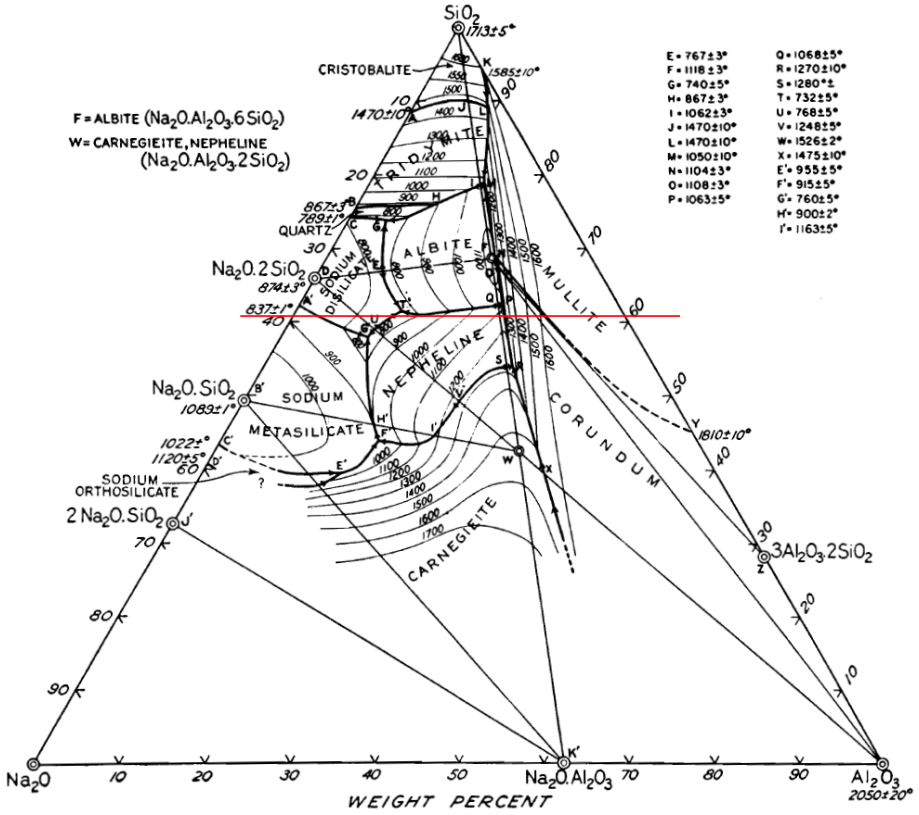

Fig. 2.1. Na_2O-Al_2O_3-SiO_2 liquidus projections[74] with nepheline discriminator

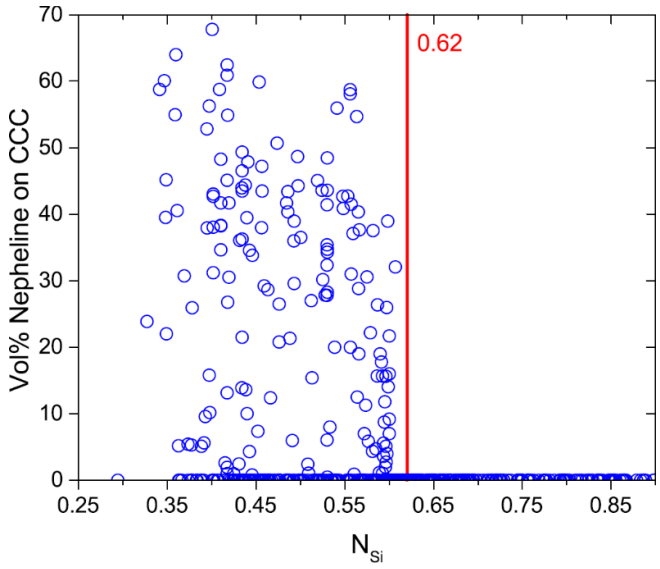

Fig. 2.2. Nepheline volume percent in CCC glass samples versus normalized SiO_2 concentration for 747 HLW glass compositions[47]

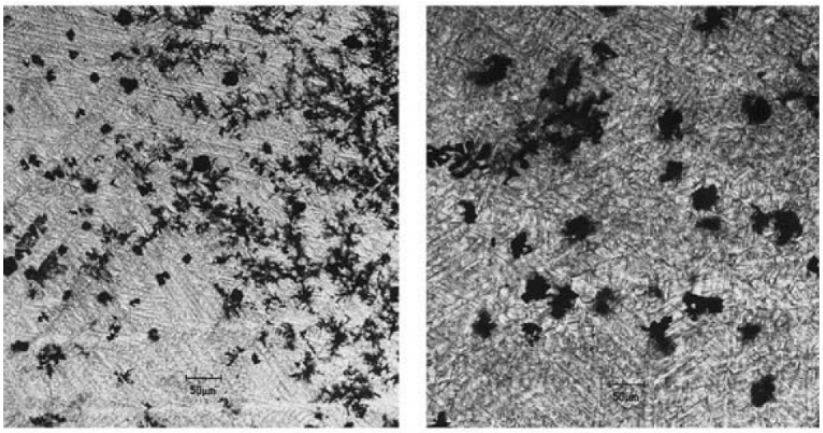

Fig. 2.3. Transmission optical micrographs of slowly cooled glass samples showing nepheline phase in matrix[1]

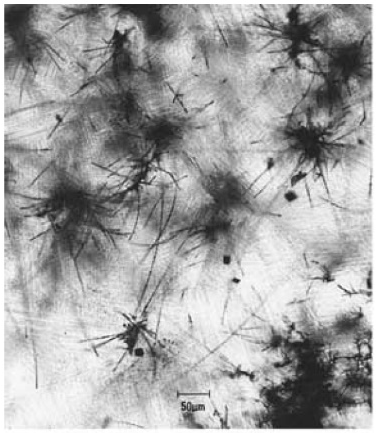

Fig. 2.4. Nepheline present in slowly cooled medium-alumina glass sample[1]

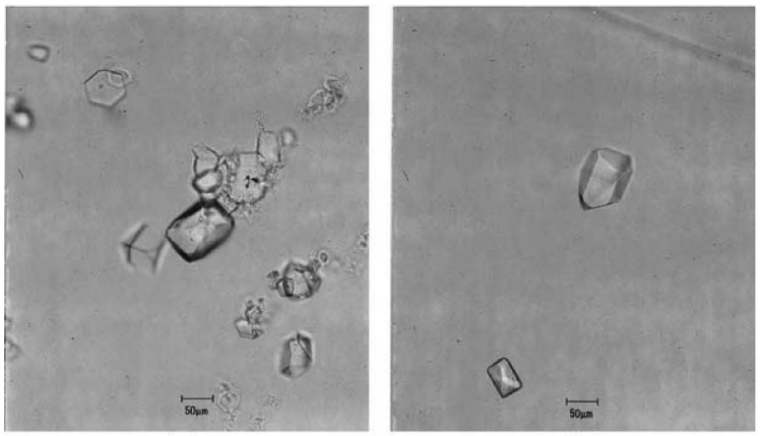

Fig. 2.5. Transmission optical micrographs of isothermally heat treated glass simples with nepheline crystals[1]

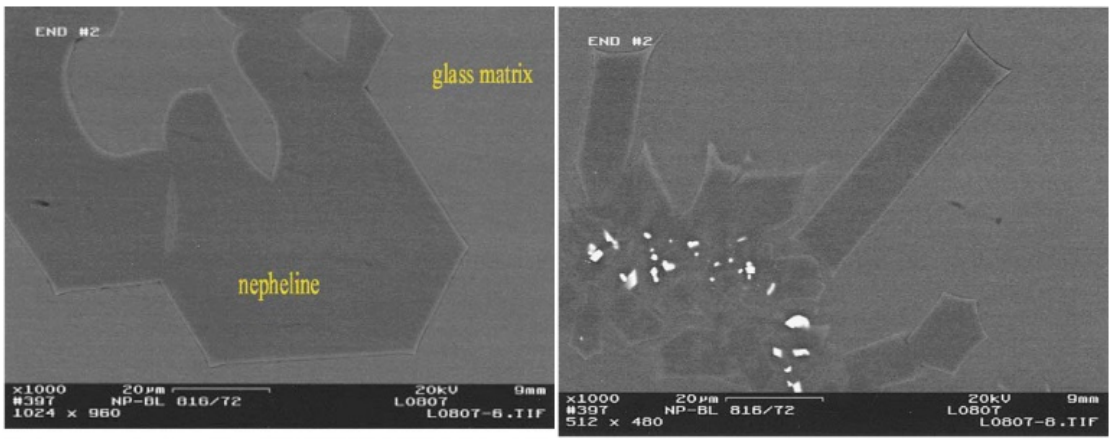

Fig. 2.6. SEM micrographs of nepheline crystals with various morphologies[1]

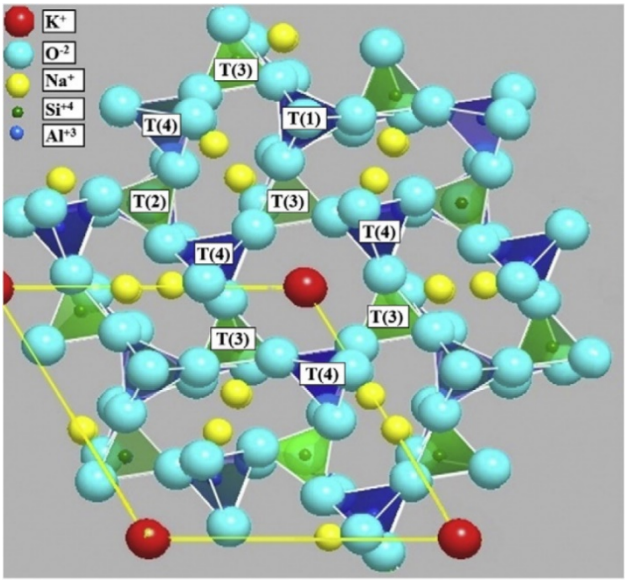

Fig. 2.7. Crystal structure of nepheline[5]

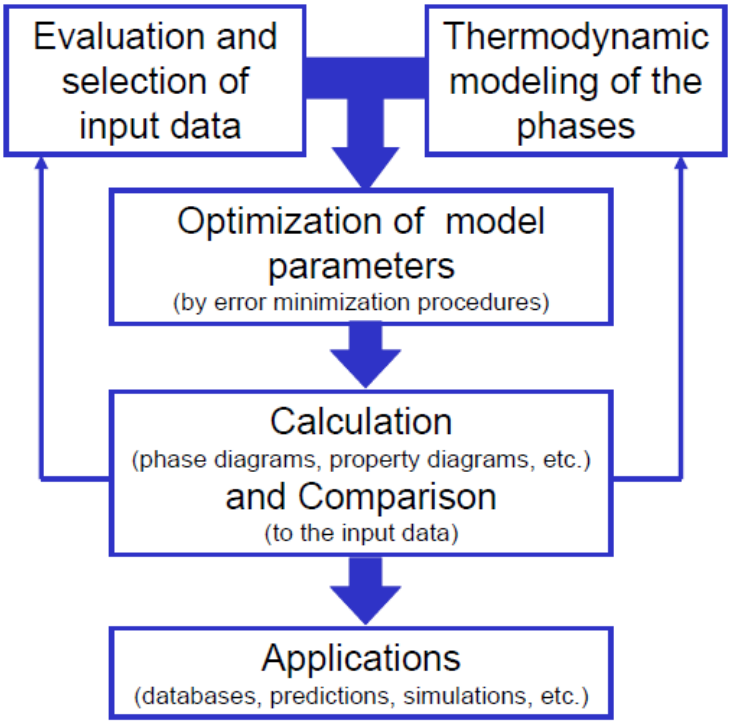

Fig. 2.8. CALPHD assessment flowchart[60]

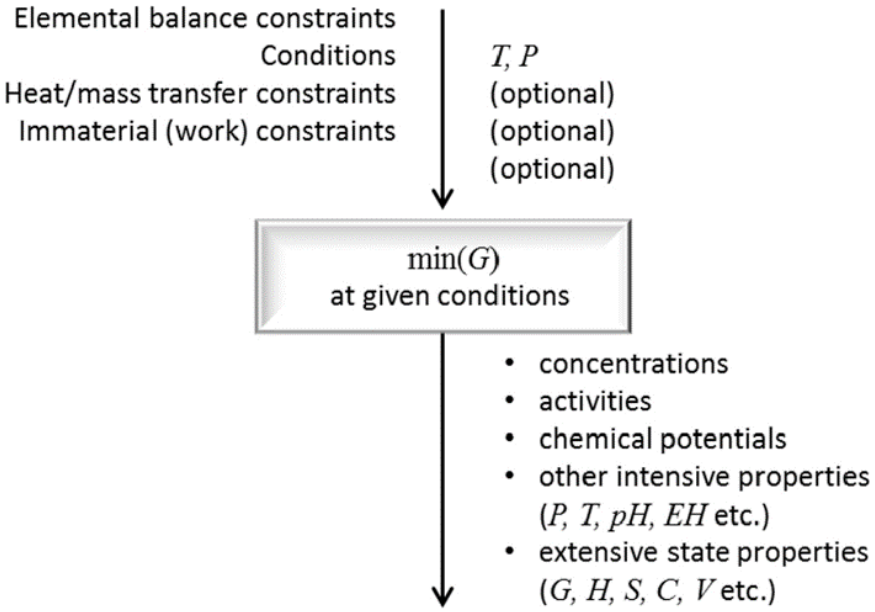

Fig. 2.9. Block diagram of Gibbs'ian thermochemical method[75]

Chapter 3

Thermodynamic Assessment of the Pseudoternary Na_2O-Al_2O_3-SiO_2 System[1]

[1] Utlak S. A., Besmann T. M., Thermodynamic Assessment of the Pseudoternary Na_2O-Al_2O_3-SiO_2 System. *J. Am. Ceram. Soc.* 2018;101:928-948. Reprinted here with permission of publisher.

3.1. Abstract

Vitrified high-level radioactive waste that contains high concentrations of Na_2O and Al_2O_3, such as the waste stored at the Hanford site, can cause nepheline to precipitate in the glass upon cooling in the canisters. Nepheline formation removes oxides such as Al_2O_3 and SiO_2 from the host glass, which can reduce its chemical durability. Uncertainty in the extent of precipitated nepheline necessitates operating at an enhanced waste loading margin, which increases operational costs by extending the vitrification mission as well as increasing waste storage requirements. A thermodynamic evaluation of the Na_2O-Al_2O_3-SiO_2 system that forms nepheline was conducted by utilizing the compound energy formalism and ionic liquid model to represent the solid solution and liquid phases, respectively. These were optimized with experimental data and used to extrapolate phase boundaries into regions of temperature and composition where measurements are unavailable. The intent is to import the determined Gibbs energies into a phase field model to more accurately predict nepheline phase formation and morphology evolution in waste glasses to allow for the design of formulations with maximum loading.

3.2. Introduction

Immobilizing high-level liquid radioactive waste in a borosilicate glass matrix is being used for long-term storage of U.S. defense nuclear waste.[1] Certain types of radioactive waste that contain high concentrations of Na_2O and Al_2O_3, however can cause nepheline, $NaAlSiO_4$, to precipitate,[1] which would act to remove glass-former SiO_2 and glass-modifier Al_2O_3. Nepheline formation can thus cause severe deterioration of the durability of the resulting waste glass.[1]

Sodium aluminoborosilicate glasses with high concentrations of Al_2O_3 and Na_2O are susceptible to nepheline crystallization if the glass compositions are within or near the nepheline primary phase field of the pseudoternary Na_2O-Al_2O_3-SiO_2 phase diagram.[1-8] Uncertainty related to the prediction of nepheline phase formation in waste glass necessitates a conservatively dilute waste loading, which results in more filled canisters than is necessary for disposition of the material. An increase in produced canisters results in an increase in operational costs as well as the requirement for more costly temporary and permanent waste storage capacity.

An accurate phase field model that couples waste glass chemistry with nepheline phase formation would reduce the uncertainty in the prediction of waste glass compositions in which nepheline would form. This in turn would enable confidence in higher canister waste loadings and thereby reduce the quantity of canisters needed. Development of phase field models, however, require an accurate thermodynamic model of nepheline and associated phases within the multi-component glass system. That will require a consistent thermodynamic assessment yielding a set of thermochemical values and models in the nepheline-forming system as it relates to the complex multicomponent nature of waste glass systems.[9-13] The goal of this work was to develop and optimize a thermodynamic database for the Na_2O-Al_2O_3-SiO_2 system using the compound energy formalism[41] (CEF) and two-sublattice partially ionic liquid[42] (TSPIL) models to represent solid solution and liquid phases, respectively.

Previous assessments of the Na_2O-Al_2O_3,[76-80] Na_2O-SiO_2,[77, 81-87] and Al_2O_3-SiO_2[79, 80, 83, 88-95] pseudobinary systems as well as the pseudoternary Na_2O-Al_2O_3-SiO_2[76-78, 83] system are reported. However, a critically assessed and self-consistent database for these

pseudobinary and -ternary systems using the CEF and TSPIL solution models does not currently exist. Thus, in order to integrate developed models with other systems optimized using these approaches, such assessments were performed in the current effort. The specific desire to use the TSPIL model is the ability of the model to provide a continuous description of a liquid that changes in character with varying composition[26] as well as the ease of scalability of the model to higher-order systems. This is useful for the current effort, which is to ultimately develop a ten component assessed thermodynamic database representative of glass prepared from high-level radioactive liquid waste at the Hanford site. Documented in this report is the successful development of a self-consistent thermodynamic database for the Na_2O-Al_2O_3-SiO_2 system using the CEF and TSPIL models.

3.3. Nepheline Precipitation

As nepheline consists of 1 mole of Na_2O and Al_2O_3 as well as 2 moles of SiO_2, the precipitation of a mole of nepheline removes 3 moles of the glass-former SiO_2 and glass-modifier Al_2O_3 from the glass matrix.[7] This results in reduced glass durability and hence the potential for an increased leach rate of radionuclides into the surrounding environment.[7] Analysis of experimental glass composition studies[8, 24, 44] conducted by Li et al.[1] determined that glasses with a ratio of SiO_2 /(SiO_2 + Na_2O + Al_2O_3) >0.62, where the chemical formulas represent mass fractions in glass, do not precipitate nepheline as a primary phase. This empirical mass ratio limit is known as the nepheline discriminator. Nepheline precipitation, however, can also likely be characterized by a thermochemical equilibrium model due to the rapid kinetics of nepheline crystallization in melts.[8, 48] As such, this may represent an alternative method to the discriminator approach to identify glass compositions that will precipitate nepheline. An accurate thermochemical

representation of waste glass compositions is necessary to allow a more precise understanding of the composition-temperature space for nepheline formation, which can facilitate the development of a physical model utilizing kinetics and growth descriptions in a phase field approach to predict nepheline precipitation in glass. This would be the most reliable type of model and could be confidently extended to regions where measurements are lacking. The development of such a model requires accurate thermochemical descriptions of the constituent phases, which is the objective of the current effort.

3.4. Thermodynamic Modeling

The pseudoternary Na_2O-Al_2O_3-SiO_2 system was assessed with the CALPHAD technique[26] using the OptiSage module of FactSage.[43] Five solid solutions as well as the liquid phase that form in the Na_2O-Al_2O_3-SiO_2 system have been thermodynamically modeled. The solid solutions considered in this work are mullite, β-Al_2O_3, the high-temperature allotrope of sodium aluminate, nepheline, and carnegieite. All model end-member Gibbs energies other than the liquid end-members for Na_4SiO_4 and $NaAlO_2$ were obtained from previous referenced assessments, whereas the Redlich-Kister interaction parameters of each model other than those for mullite were determined in this work.

3.4.1. Stoichiometric Compounds

Twenty-three stoichiometric compounds were incorporated into the pseudoternary Na_2O-Al_2O_3-SiO_2 thermodynamic database (Table 3.1). The allotropic phases of Na_4SiO_4 have been neglected in favor of a single compound description as the polymorphic transition of Na_4SiO_4 was deemed to not influence the overall pseudoternary assessment.

3.4.2. Compound Energy Formalism

The CEF representations of the oxide solid solutions were used with two or more sublattices. Generating all possible combinations of single constituents on each sublattice yields a set of stoichiometric end-members.

The molar Gibbs energy of a phase modeled using the CEF can be expressed as:

$$G_{\mathrm{m}} = \Sigma \Delta_{\mathrm{f}}{}^{\mathrm{o}} G_{\mathrm{end}} \Pi y_{\mathrm{J}}^{\mathrm{s}} + RT\Sigma\Sigma n^{\mathrm{s}} y_{\mathrm{J}}^{\mathrm{s}} \ln y_{\mathrm{J}}^{\mathrm{s}} + {}^{\mathrm{E}} G_{\mathrm{m}} \quad (3.1)$$

where $\Delta_{\mathrm{f}}{}^{\mathrm{o}} G_{\mathrm{end}}$ is the molar Gibbs energy of formation of an end-member, $y_{\mathrm{J}}^{\mathrm{s}}$ is the site fraction of the J$^{\mathrm{th}}$ constituent in the n$^{\mathrm{th}}$ sublattice, and n^{s} is the stoichiometric coefficient of the n$^{\mathrm{th}}$ sublattice. The first, second, and third terms of Equation (3.1) are the Gibbs energy surface of reference, ideal entropy of mixing, and excess Gibbs energy of mixing, respectively.

The excess Gibbs energy, which accounts for the departure from ideal mixing of species on the same sublattice due to attraction or repulsion of the mixing constituents,[72] can be described with a generalized regular solution expression:

$${}^{\mathrm{E}} G_{\mathrm{m}} = \Pi y_{\mathrm{J}}^{\mathrm{s}} \Sigma y_{\mathrm{B}}^{\mathrm{t}} L_{\mathrm{A,B:D:G}} \ldots + \Pi y_{\mathrm{J}}^{\mathrm{s}} \Sigma\Sigma y_{\mathrm{B}}^{\mathrm{t}} y_{\mathrm{D}}^{\mathrm{u}} L_{\mathrm{A,B:D,E:G}} \ldots + \ldots \quad (3.2)$$

where the subscripts A, B, D, E, and G as well as superscripts t and u refer to the constituents in a sublattice and the sublattice designations, respectively, in a generalized CEF formulation for a three sublattice phase $(A,B)_{\mathrm{k}}^{\mathrm{t}}(D,E,F)_{\mathrm{l}}^{\mathrm{u}}(G)_{\mathrm{m}}^{\mathrm{v}}$. The subscripts k, l, and m in the generalized formula represent the sublattice stoichiometric coefficients. The commas separating constituents in the interaction parameter designations of Equation (3.2) indicate the interactions between constituents on the same sublattice, whereas the colons separate sublattices. Equation (3.2) can be expanded to describe, in principle, constituent interactions of a multicomponent system of any order.

The interaction parameters of Equation (3.2) can be expressed as a Redlich-Kister power series in terms of site fractions. As an example, for a binary interaction between the A and B species of Equation (3.2):

$$L_{\mathrm{A,B:D:G}} = \sum_{k=0}^{n} {}^{\mathrm{k}}L_{\mathrm{A,B:D:G}}(y_{\mathrm{A}}^{\mathrm{t}} - y_{\mathrm{B}}^{\mathrm{t}})^{\mathrm{k}} \tag{3.3}$$

The solution model defined by Equation (3.1) becomes regular or subregular solution when the exponent k in Equation (3.3) equals 0 or 1, respectively.[72] Thus, as indicated by the Equations (3.9) – (3.13) displayed in Sections 3.5.1 – 3.5.5, the mullite, β-Al_2O_3, nepheline, and carnegieite phases were modeled as regular solutions while the sodium aluminate phase was characterized as a subregular solution.

The L term on the right-hand side of Equation (3.3) can be expanded as a polynomial of the form:

$${}^{k}L_{A,B:D:G} = A + B \cdot T + C \cdot T \cdot \ln(T) + D \cdot T^2 + E \cdot T^3 + F \cdot T^{-1} \tag{3.4}$$

where the variables A, B, C, D, E, and F are coefficients that can be empirically determined by optimizing the model Gibbs energy function defined by Equation (3.1) to thermochemical or phase equilibria data. In practice, only the A and B coefficients of Equation (3.4) are included in an assessment unless experimental data can justify the assignment of an empirically derived value to an additional coefficient.[26]

3.4.3. Two-Sublattice Partially Ionic Liquid Model

Hillert et al.[42] discuss the development of a TSPIL model for liquid solutions with different tendencies for ionization. The TSPIL model is based on the concept that the strength of ionization of ionic substances results in each atom being surrounded by unlike atoms in a form of chemical ordering. This ordering can be treated as two sublattices, one

containing only cations and the other anions. Charged vacancies may be introduced on either cationic or anionic sublattices with the valency of the vacancy on either sublattice corresponding to the average for the ions on the other sublattice. Negatively charged vacancies on the anionic sublattice can be considered vacant sites with an excess of electrons. Positively charged vacancies on the cationic sublattice, however, would require the development of an additional rule to account for the valencies of the two kinds of vacancies. Rather than implementing this approach, however, it is possible instead to introduce a neutral species on the anionic sublattice to account for deviations from stoichiometry towards the nonmetallic side of the system. Thus, the cation sublattice will contain only positively charged ions whereas the anion sublattice can contain negatively charged ions and vacancies as well as neutral species. As described by Lukas et al., [26] the general TSPIL sublattice formula can be written as:

$$\left(C_{\mathrm{i}}^{+\nu_{\mathrm{i}}}\right)_{\mathrm{P}}\left(A_{\mathrm{j}}{}^{-\nu_{\mathrm{j}}}, Va, B_{\mathrm{k}}^{0}\right)_{\mathrm{Q}}$$

where *C*, *A*, *Va*, and *B* denote cations, anions, hypothetical vacancies, and neutral species, respectively, while the indices i, j, and k represent specific sublattice constituents. The superscripts $+\nu_{\mathrm{i}}$ and $-\nu_{\mathrm{j}}$ represent the charge of the i^{th} or j^{th} cation or anion, respectively, while 0 indicates a neutral species. Electroneutrality is maintained by allowing the stoichiometry (P and Q) to vary as a function of site fractions:

$$P = \Sigma \nu_{\mathrm{j}} y_{A_{\mathrm{j}}} + Q y_{Va} \tag{3.6}$$

$$Q = \Sigma \nu_{\mathrm{i}} y_{C_{\mathrm{i}}} \tag{3.5}$$

The Gibbs energy of an ionic liquid can then be expressed as:

$$G_{\mathrm{m}} = \Sigma\Sigma y_{C_{\mathrm{i}}} y_{A_{\mathrm{j}}} {}^{\mathrm{o}} G_{C_{\mathrm{i}}:A_{\mathrm{j}}} + Q\left(y_{\mathrm{Va}} \Sigma y_{C_{\mathrm{i}}} {}^{\mathrm{o}} G_{C_{\mathrm{i}}} + \Sigma y_{B_{\mathrm{k}}} {}^{\mathrm{o}} G_{B_{\mathrm{k}}}\right) \tag{3.7}$$

$$+ RT\left[P\Sigma y_{C_{\mathrm{i}}} \ln y_{C_{\mathrm{i}}} + Q\left(\Sigma y_{A_{\mathrm{j}}} \ln y_{A_{\mathrm{j}}} + y_{Va} \ln y_{Va} + \Sigma y_{B_{\mathrm{k}}} \ln y_{B_{\mathrm{k}}}\right)\right] + {}^{\mathrm{E}} G_{\mathrm{m}}$$

where ${}^{o}G_{C_i:A_j}$ is the Gibbs energy of formation for $\nu_i + \nu_j$ moles of atoms of the end-member C_iA_j while ${}^{o}G_{C_i}$, and ${}^{o}G_{B_k}$ are the values for C_i and B_k, respectively. The first, second, and third terms of Equation (3.7) are the Gibbs energy surface of reference for all possible types of constituents, the random configurational entropy on each sublattice, and the excess Gibbs mixing energy, which can be expressed as:

$${}^{E}G_m = \Sigma\Sigma\Sigma y_{i_1} y_{i_2} y_j L_{i_1,i_2:j} + \Sigma\Sigma\Sigma y_i y_{j_1} y_{j_2} L_{i:j_1,j_2} + \Sigma\Sigma y_i y_{j_1} y_{Va} L_{i:j_1,Va} + \ldots \quad (3.8)$$

As discussed in relation to the CEF model, the interaction parameters of Equation (3.8) can be expressed as a Redlich-Kister power series described by Equation (3.3) with the L terms expanded as polynomials of the form defined by Equation (3.4).

3.5. Solution Phase Descriptions

3.5.1. Mullite

Schneider et al.,[96] note that mullite is a member of the compositional series of orthorhombic aluminosilicates with the general composition $Al_2(Al_{2+2x}Si_{2-2x})O_{10-x}$. The stoichiometric end-members are sillimanite, Al_2SiO_5, at x = 0, mullite, $3Al_2O_3 \cdot 2SiO_2$, at x = 0.25, 2/1 mullite, $2Al_2O_3 \cdot SiO_2$, at x = 0.40, and the SiO_2-free phase ι-alumina, Al_2O_3, at x = 1.

Mullite has been modeled by Swamy et al.[88] using a three sublattice CEF model as:

$$(Al^{+3})_2^{\gamma}[Al^{+3}, Si^{+4}]_1^{\alpha}\{O^{-2}, Va\}_5^{\beta}$$

This CEF sublattice structure accounts for the mullite octahedral and tetrahedral sites specific to the first and second sublattices denoted by the γ and α superscripts, respectively, with the possibility of vacancies accommodated on the third, anion sublattice.

The Gibbs energy relation for the mullite phase is expressed in Equation (3.9), with values listed in Table 3.2:

$$G_{\mathrm{m}}^{\mathrm{mullite}} = y_{\mathrm{Al}^{+3}}^{\alpha} y_{\mathrm{O}^{-2}}^{\beta} \, {}^{\mathrm{o}} G_{\mathrm{Al_3O_5^{-1}}} + y_{\mathrm{Al}^{+3}}^{\alpha} y_{\mathrm{Va}}^{\beta} \, {}^{\mathrm{o}} G_{\mathrm{Al_3^{+9}}} + y_{\mathrm{Si}^{+4}}^{\alpha} y_{\mathrm{O}^{-2}}^{\beta} \, {}^{\mathrm{o}} G_{\mathrm{Al_2SiO_5}} \quad (3.9)$$

$$+ y_{\mathrm{Si}^{+4}}^{\alpha} y_{\mathrm{Va}}^{\beta} \, {}^{\mathrm{o}} G_{\mathrm{Al_2Si^{+10}}}$$

$$+ RT\left(y_{\mathrm{Al}^{+3}}^{\alpha} \ln y_{\mathrm{Al}^{+3}}^{\alpha} + y_{\mathrm{Si}^{+4}}^{\alpha} \ln y_{\mathrm{Si}^{+4}}^{\alpha} + 5 y_{\mathrm{O}^{-2}}^{\beta} \ln y_{\mathrm{O}^{-2}}^{\beta} + 5 y_{\mathrm{Va}}^{\beta} \ln y_{\mathrm{Va}}^{\beta}\right)$$

$$+ y_{\mathrm{Al}^{+3}}^{\alpha} y_{\mathrm{Si}^{+4}}^{\alpha} y_{\mathrm{O}^{-2}}^{\beta} \, {}^{0} L_{\mathrm{Al}^{+3}:\mathrm{Al}^{+3},\mathrm{Si}^{+4}:\mathrm{O}^{-2}} + y_{\mathrm{Al}^{+3}}^{\alpha} y_{\mathrm{Si}^{+4}}^{\alpha} y_{\mathrm{Va}}^{\beta} \, {}^{0} L_{\mathrm{Al}^{+3}:\mathrm{Al}^{+3},\mathrm{Si}^{+4}:\mathrm{Va}}$$

3.5.2. β-Al_2O_3

The β-Al_2O_3 phase has been modeled by Lambotte & Chartrand[76] using a three sublattice CEF model:

$$(\mathrm{Na_2O})_1[\mathrm{Al_2O_3}]_{11}\{\mathrm{Na_2O}, \mathrm{Va}\}_1^{\alpha}$$

Bragg[97] and Beevers & Ross[98] determined that β-Al_2O_3 with the general formula $Na_2O{\cdot}11Al_2O_3$ has a hexagonal unit cell composed of $Al_{11}O_{16}$ spinel-like blocks separated by Na_2O layers in which sodium can occupy Beevers-Ross, anti Beevers-Ross, or mid oxygen sites. Rather than explicitly modeling each of these sites, hyperstoichiometry with respect to Na_2O is accommodated by Na_2O on the third sublattice.

The Gibbs energy relation for the β-Al_2O_3 phase is expressed in Equation (3.10) with values listed in Table 3.2:

$$G_{\mathrm{m}}^{\beta-\mathrm{Al_2O_3}} = y_{\mathrm{Na_2O}}^{\alpha} \, {}^{\mathrm{o}} G_{\mathrm{Na_4Al_{22}O_{35}}} + y_{\mathrm{Va}}^{\alpha} \, {}^{\mathrm{o}} G_{\mathrm{Na_2Al_{22}O_{34}}} + RT\left(y_{\mathrm{Na_2O}}^{\alpha} \ln y_{\mathrm{Na_2O}}^{\alpha} + y_{\mathrm{Va}}^{\alpha} \ln y_{\mathrm{Va}}^{\alpha}\right)$$

$$+ y_{\mathrm{Na_2O}}^{\alpha} y_{\mathrm{Va}}^{\alpha} \, {}^{0} L_{\mathrm{Na_2O:Al_2O_3:Na_2O,Va}} \quad (3.10)$$

In the current assessment, it was necessary to decrease by -19.72 kJ/mol, or 0.18%, the β"-Al_2O_3 enthalpy of Lambotte & Chartrand[76] to properly reproduce the peritectoid decomposition of β"-Al_2O_3.

3.5.3. Sodium aluminate

The solubility of SiO_2 in a matrix of the high-temperature form of sodium aluminate, $NaAlO_2$, has been described by a two sublattice CEF model utilized by Jak et al.[77] as well as Lambotte & Chartrand[76]:

$$((\mathrm{Na}-\mathrm{Al})^{+4},(\mathrm{Va}-\mathrm{Si})^{+4})_1^{\alpha}[\mathrm{O}^{-2}]_2$$

In this sublattice formula, a neutral vacancy substitutes for Na^{+1} and Si^{+4} substitutes for Al^{+3} to maintain charge neutrality. The dash notation used in the first sublattice represents a coupled substitution in that a vacancy substitutes for a Na^{+1} cation for every Si^{+4} replacing an Al^{+3}. Consequently, the entire homogeneity range from SiO_2 to stoichiometric $NaAlO_2$ is described by this sublattice structure. As noted by Lambotte & Chartrand,[76] while this sublattice formalism does not describe the physical mechanism of solubility between $NaAlO_2$ and $NaAlSiO_4$, the formalism is capable of reproducing the observed liquidus.

The Gibbs energy relation for the sodium aluminate phase is expressed in Equation (3.11) with values listed in Table 3.2:

$$\begin{aligned} G^{\mathrm{m}}_{\mathrm{NaAlO_2}} = {} & y^{\alpha}_{\mathrm{NaAl^{+4}}}\,{}^{\mathrm{o}}G_{\mathrm{NaAlO_2}} + y^{\alpha}_{\mathrm{VaSi^{+4}}}\,{}^{\mathrm{o}}G_{\mathrm{SiO_2}} \\ & + RT\left(y^{\alpha}_{\mathrm{NaAl^{+4}}}\ln y^{\alpha}_{\mathrm{NaAl^{+4}}} + y^{\alpha}_{\mathrm{VaSi^{+4}}}\ln y^{\alpha}_{\mathrm{VaSi^{+4}}}\right) \\ & + y^{\alpha}_{\mathrm{NaAl^{+4}}}y^{\alpha}_{\mathrm{VaSi^{+4}}}\,{}^{0}L_{\mathrm{NaAl^{+4}},\mathrm{VaSi^{+4}}:\mathrm{O^{-2}}} \\ & + y^{\alpha}_{\mathrm{NaAl^{+4}}}y^{\alpha}_{\mathrm{VaSi^{+4}}}\,{}^{1}L_{\mathrm{NaAl^{+4}},\mathrm{VaSi^{+4}}:\mathrm{O^{-2}}}\,(\mathrm{y}_{\mathrm{NaAl^{+4}}}-\mathrm{y}_{\mathrm{VaSi^{+4}}})^{1} \end{aligned} \tag{3.11}$$

3.5.4. Nepheline

The nepheline solid solution has been modeled by Lambotte & Chartrand[76] using a three sublattice CEF model:

$$((\mathrm{Na}-\mathrm{Al})^{+4},(\mathrm{Va}-\mathrm{Si})^{+4})_8^{\alpha}[\mathrm{Si}^{+4}]_8\{\mathrm{O}^{-2}\}_{32}$$

Mixing of Al and Si on any of the four tetrahedral sites does not need to be considered as the elements are not observed to exchange sites.[16, 50, 99] The first sublattice allows accommodation of excess SiO_2, which results in Al^{+3} being replaced by Si^{+4} with the charge difference compensated by vacancy formation on the larger of the alkali cation sites.

The Gibbs energy relation for the nepheline phase is expressed in Equation (3.12) with values listed in Table 3.2:

$$G_{\mathrm{m}}^{\mathrm{nepheline}} = y_{\mathrm{NaAl}^{+4}}^{\alpha}\ {}^{\mathrm{o}}G_{\mathrm{Na_8Al_8Si_8O_{32}}} + y_{\mathrm{VaSi}^{+4}}^{\alpha}\ {}^{\mathrm{o}}G_{\mathrm{Si_{16}O_{32}}} + 8RT\left(y_{\mathrm{NaAl}^{+4}}^{\alpha}\ln y_{\mathrm{NaAl}^{+4}}^{\alpha} + y_{\mathrm{VaSi}^{+4}}^{\alpha}\ln y_{\mathrm{VaSi}^{+4}}^{\alpha}\right) + y_{\mathrm{NaAl}^{+4}}^{\alpha}y_{\mathrm{VaSi}^{+4}}^{\alpha}\ {}^{0}L_{\mathrm{NaAl}^{+4},\mathrm{VaSi}^{+4}:\mathrm{Si}^{+4}:\mathrm{O}^{-2}} \quad (3.12)$$

3.5.5. Carnegieite

The carnegieite solid solution that forms within the Na_2O-Al_2O_3-SiO_2 system has been modeled by Lambotte & Chartrand[76] using the three sublattice CEF model:

$$((\mathrm{Na}-\mathrm{Al})^{+4}, (\mathrm{Va}-\mathrm{Si})^{+4})_4^{\alpha}[\mathrm{Si}^{+4}]_4\{\mathrm{O}^{-2}\}_{16}$$

Accounting for mixing of Al and Si on the first lattice site is considered unnecessary as Stebbins et al.[50] experimentally determined that Al-Si disordering does not occur in carnegieite.

The Gibbs energy relation for the carnegieite phase is expressed by Equation (3.13) with values listed in Table 3.2:

$$G_{\mathrm{m}}^{\mathrm{carnegieite}} = y_{\mathrm{NaAl}^{+4}}^{\alpha}\ {}^{\mathrm{o}}G_{\mathrm{Na_4Al_4Si_4O_{16}}} + y_{\mathrm{VaSi}^{+4}}^{\alpha}\ {}^{\mathrm{o}}G_{\mathrm{Si_8O_{16}}} + 4RT\left(y_{\mathrm{NaAl}^{+4}}^{\alpha}\ln y_{\mathrm{NaAl}^{+4}}^{\alpha} + y_{\mathrm{VaSi}^{+4}}^{\alpha}\ln y_{\mathrm{VaSi}^{+4}}^{\alpha}\right) + y_{\mathrm{NaAl}^{+4}}^{\alpha}y_{\mathrm{VaSi}^{+4}}^{\alpha}\ {}^{0}L_{\mathrm{NaAl}^{+4},\mathrm{VaSi}^{+4}:\mathrm{Si}^{+4}:\mathrm{O}^{-2}} \quad (3.13)$$

3.5.6. Oxide liquid

The oxide liquid for the Na_2O-Al_2O_3-SiO_2 system has been modeled using the TSPIL as:

$$(Al^{+3}, Na^{+1})_P(AlO_2^{-1}, O^{-2}, SiO_4^{-4}, SiO_2^0)_Q$$

Mao et al.,[100] included SiO_2^0 in the anionic sublattice to account for the silica network in the liquid. Network Si are altered with the addition of oxygen from a basic oxide such as Na_2O to form the anion SiO_4^{-4}; hence the inclusion of SiO_4^{-4} on the anionic sublattice. Benoit & Ispas[101] experimentally determined that the addition of a basic oxide such as CaO to liquid Al_2O_3-SiO_2 acted to increase the predominance of 4 coordinated Al. Also, due to the amphoteric character of Al_2O_3, Mao et al.[100] concluded that the dissociation of Al_2O_3 will result in the partial formation of Al^{+3} with free O atoms associating with other Al atoms until a complete network is formed. Mao et al.[100] modeled this network with an Al^{+3} cation and AlO_2^{-1} anion. As Na_2O is a more basic oxide than CaO, which was the oxide explicitly considered by Mao et al.,[100] this approach has been used in the current work.

The resultant Gibbs energy relation for the oxide liquid is defined by Equation (3.14).

$$G_m^{liquid} = y_{Al^{+3}}y_{AlO_2^{-1}}\,{}^{o}G_{Al_4O_6} + y_{Al^{+3}}y_{O^{-2}}\,{}^{o}G_{Al_2O_3} + y_{Al^{+3}}y_{SiO_4^{-4}}\,{}^{o}G_{Al_4Si_3O_{12}} + \quad (3.14)$$

$$y_{Na^{+1}}y_{AlO_2^{-1}}\,{}^{o}G_{NaAlO_2} + y_{Na^{+1}}y_{O^{-2}}\,{}^{o}G_{Na_2O} + y_{Na^{+1}}y_{SiO_4^{-4}}\,{}^{o}G_{Na_4SiO_4} + (3y_{Al^{+3}} +$$

$$y_{Na^{+1}})(y_{SiO_2^0}\,{}^{o}G_{SiO_2^0}) + (y_{AlO_2^{-1}} + 2y_{O^{-2}} + 4y_{SiO_4^{-4}})RT(y_{Al^{+3}}\ln y_{Al^{+3}} + y_{Na^{+1}}\ln y_{Na^{+1}}) +$$

$$(3y_{Al^{+3}} + y_{Na^{+1}})RT(y_{AlO_2^{-1}}\ln y_{AlO_2^{-1}} + y_{O^{-2}}\ln y_{O^{-2}} + y_{SiO_4^{-4}}\ln y_{SiO_4^{-4}} + y_{SiO_2^0}\ln y_{SiO_2^0}) +$$

$$y_{Al^{+3}}y_{AlO_2^{-1}}y_{SiO_2^0}\left[{}^{0}L_{Al^{+3}:AlO_2^{-1},SiO_2^0} + {}^{1}L_{Al^{+3}:AlO_2^{-1},SiO_2^0}(y_{AlO_2^{-1}} - y_{SiO_2^0})^1 +\right.$$

$$\left.{}^{2}L_{Al^{+3}:AlO_2^{-1},SiO_2^0}(y_{AlO_2^{-1}} - y_{SiO_2^0})^2\right] + y_{Al^{+3}}y_{Na^{+1}}y_{AlO_2^{-1}}\left[{}^{0}L_{Al^{+3},Na^{+1}:AlO_2^{-1}} +\right.$$

$$\left.{}^{1}L_{Al^{+3},Na^{+1}:AlO_2^{-1}}(y_{Al^{+3}} - y_{Na^{+1}})^1\right] + y_{Na^{+1}}y_{O^{-2}}y_{SiO_2^0}\left[{}^{0}L_{Na^{+1}:O^{-2},SiO_2^0} + {}^{1}L_{Na^{+1}:O^{-2},SiO_2^0}(y_{O^{-2}} -\right.$$

$$\left.y_{SiO_2^0})^1 + {}^{2}L_{Na^{+1}:O^{-2},SiO_2^0}(y_{O^{-2}} - y_{SiO_2^0})^2 + {}^{3}L_{Na^{+1}:O^{-2},SiO_2^0}(y_{O^{-2}} - y_{SiO_2^0})^3\right] +$$

$$y_{Na^{+1}}y_{SiO_4^{-4}}y_{SiO_2^0}\left[{}^{0}L_{Na^{+1}:SiO_4^{-4},SiO_2^0} + {}^{1}L_{Na^{+1}:SiO_4^{-4},SiO_2^0}(y_{SiO_4^{-4}} - y_{SiO_2^0})^1 +\right.$$

$$\left.{}^{2}L_{Na^{+1}:SiO_4^{-4},SiO_2^0}(y_{SiO_4^{-4}} - y_{SiO_2^0})^2 + {}^{3}L_{Na^{+1}:SiO_4^{-4},SiO_2^0}(y_{SiO_4^{-4}} - y_{SiO_2^0})^3\right] +$$

$$y_{Na^{+1}}y_{O^{-2}}y_{SiO_4^{-4}}\,{}^{0}L_{Na^{+1}:O^{-2},SiO_4^{-4}} + y_{Na^{+1}}y_{AlO_2^{-1}}y_{SiO_4^{-4}}y_{SiO_2^0}\left[{}^{AlO_2^{-1}}L_{Na^{+1}:AlO_2^{-1},SiO_4^{-4},SiO_2^0}\left(y_{AlO_2^{-1}} +\right.\right.$$

$$\left.\left.\frac{1-y_{AlO_2^{-1}}-y_{SiO_4^{-4}}-y_{SiO_2^0}}{3}\right) + {}^{SiO_2^0}L_{Na^{+1}:AlO_2^{-1},SiO_4^{-4},SiO_2^0}\left(y_{SiO_2^0} + \frac{1-y_{AlO_2^{-1}}-y_{SiO_4^{-4}}-y_{SiO_2^0}}{3}\right)\right] +$$

$$y_{Na^{+1}}y_{AlO_2^{-1}}y_{SiO_2^0}\left[{}^{0}L_{Na^{+1}:AlO_2^{-1},SiO_2^0} + {}^{1}L_{Na^{+1}:AlO_2^{-1},SiO_2^0}(y_{AlO_2^{-1}} - y_{SiO_2^0})^1\right] +$$

$$y_{Na^{+1}}y_{AlO_2^{-1}}y_{O^{-2}}\,{}^{0}L_{Na^{+1}:AlO_2^{-1},O^{-2}} + y_{Al^{+3}}y_{Na^{+1}}y_{AlO_2^{-1}}y_{SiO_2^0}\left[{}^{0}L_{Al^{+3},Na^{+1};AlO_2^{-1},SiO_2^0} +\right.$$

$$\left.{}^{1}L_{Al^{+3},Na^{+1};AlO_2^{-1},SiO_2^0}(y_{AlO_2^{-1}} - y_{SiO_2^0})^1 + {}^{2}L_{Al^{+3},Na^{+1};AlO_2^{-1},SiO_2^0}(y_{Al^{+3}} - y_{Na^{+1}})^1\right] +$$

$$y_{Al^{+3}}y_{Na^{+1}}y_{AlO_2^{-1}}y_{SiO_4^{-4}}\,{}^{0}L_{Al^{+3},Na^{+1};AlO_2^{-1},SiO_4^{-4}}$$

The reciprocal and zeroth order Na^{+1}:AlO_2^{-1},O^{-2} as well as the second order Al^{+3}:AlO_2^{-1},SiO_2^0 interaction parameters were necessary to suppress computed unobserved miscibility gaps. Additionally, the enthalpy and entropy values of the $Na_{10}SiO_7$ and $Na_6Si_2O_7$ compounds were determined from the optimization as these values are not well determined experimentally.[81] The Na_4SiO_4 and $NaAlO_2$ end-member enthalpy values were

also optimized in this work to obtain an overall good fit of the liquidus in the pseudobinary subsystems.

The Na^{+1}:SiO_4^{-4},SiO_2^0 interaction parameters are set equal to those for Na^{+1}:O^{-2},SiO_2^0 per negative charge:

$$^{k}L_{Na^{+1}:SiO4_4^{-4},SiO_2^0} = 2\,{}^{k}L_{Na^{+1}:O^{-2},SiO_2^0} \quad (3.15)$$

with values for the parameters of the oxide liquid model listed in Table 3.3.

3.6. Discussion

A majority of the experimental data for the Na_2O-Al_2O_3-SiO_2 system has been previously critically assessed (see Swamy et al.[88] and Mao et al.[89] for the Al_2O_3-SiO_2 pseudobinary, Lambotte & Chartrand[81] for the Na_2O-SiO_2 pseudobinary, and Lambotte & Chatrand[76] for the Na_2O-Al_2O_3 and Na_2O-Al_2O_3-SiO_2 pseudobinary and -ternary systems, respectively) and thus were not repeated in this work.

3.6.1. Al_2O_3-SiO_2 pseudobinary system

Phase equilibria were used as the primary source of experimental data with generally good agreement between determinations of the liquidus temperatures of the phases. However, as noted by Mao et al.,[89] there exist large uncertainties in the available activity data, which restricts their utility.

Fig. 3.1 indicates the cristobalite liquidus agrees with the one experimental data point available and that there is a good overall fit to the mullite liquidus. Corundum liquidus data is sparse but what is available is reproduced with sufficient accuracy. All invariant points have been well fit by the mullite CEF and oxide liquid TSPIL models including the SiO_2 (high-cristobalite) + mullite eutectic at 1820 K as reported by Howald & Eliezer[91] (Table 3.4).

3.6.2. Na_2O-Al_2O_3 pseudobinary system

The β-Al_2O_3 + $NaAlO_2$ eutectic, β-Al_2O_3 melting point, and β-Al_2O_3 and corundum liquidus data measured by Rolin & Thanh[102] as well as the $NaAlO_2$ melting point reported by Weber & Venero[103] are accurately reproduced by the condensed phase Gibbs energies and the oxide liquid model (Fig. 3.2 & Table 3.4).

3.6.3. Na_2O-SiO_2 pseudobinary system

In considering the invariant points of the Na_2O-SiO_2 phase diagram (Fig. 3.3) a compromise was required with respect to the fits of the observed $Na_{10}SiO_7$ and Na_4SiO_4 melting and eutectic points containing either or both phases, with a greater weight given to the melting temperatures. Hence, the $Na_{10}SiO_7$ and Na_4SiO_4 phase melting points are well fit while the eutectic points show a greater discrepancy (Table 3.4). Regardless, the Na_2O-SiO_2 system when extended to include Al_2O_3 well-reproduced experimental observations.

A better fit of the partial Na_2O(β) Gibbs energy data for the Na_4SiO_4 + Na_2SiO_3 and Na_4SiO_4 + $Na_6Si_2O_7$ equilibrium compositions in Fig. 3.4 could be attained by fitting the enthalpy of Na_4SiO_4 to the partial Gibbs energy data. It was decided, however, to retain the Na_4SiO_4 Gibbs energy formalism derived in the assessment of Wu et al.[84] as the liquidus and melting point of Na_4SiO_4 are well predicted in that assessment, with the oxide liquid model of Na_4SiO_4 behavior considered accurate. A good fit of the oxide liquid model parameters to the enthalpy of mixing and Na_2O activity data was obtained (Fig. 3.5 & Fig. 3.6).

3.6.4. Na_2O-Al_2O_3-SiO_2 pseudoternary system

All pseudoternary Na_2O-Al_2O_3-SiO_2 isoplethal section liquidus and invariant data are well reproduced as indicated in Fig. 3.7 – Fig. 3.16 as well as in the data comparison in

Table 3.5. The difference with respect to activity apparent in Fig. 3.8 does not significantly affect agreement between the computed and observed phase equilibria. All pseudoternary two and three phase equilibria data at 1873 K are accurately reproduced (Fig. 3.9), and all liquidus projection invariant points for the Na_2O-Al_2O_3-SiO_2 system are well-reproduced by the pseudoternary CEF and TSPIL models (Fig. 3.10 & Table 3.6).

3.7. Summary

The composition of potential vitrified high-level defense nuclear waste to be produced at the Hanford site can be prone to nepheline precipitation[1-8], which would have the effect of degrading the durability of the glass matrix.[7] Thus, to avoid the problem, waste loading may be restricted to possibly over-conservative levels. An accurate simulation of time-dependent nepheline precipitation behavior in the vitrification of the waste, however, would allow more closely controlled compositions, and thus possibly provide an opportunity to confidently increase waste loading.

The thermodynamic models and values for the Na_2O-Al_2O_3-SiO_2 system developed in this work is an initial step in obtaining a practical simulation based on a quantitative representation of nepheline formation during vitrification. The Na_2O-Al_2O_3-SiO_2 pseudobinary subsystems and pseudoternary overall system were assessed and successfully optimized to reproduce experimentally determined phase equilibria and thermochemical data. Thus, a consistent set of thermochemical values and models that represent the system was developed and can be used in the simulation of waste glass behavior. To represent the waste glass with important additional constituents found in practical formulations, Fe, Mg, Mn, Ca, B, and K, will be included in the next phase of the current effort. The resulting database, while of value in providing a baseline for nepheline precipitation at equilibrium,

will also be necessary for creating phase field models of nepheline nucleation and grain growth for simulating process dependent behavior. Such an ultimate understanding may lead to significant improvements in the production efficiency for producing durable high-level defense nuclear waste glass at the Hanford site.

3.8. Acknowledgements

The authors gratefully acknowledge the financial support provided by the U.S. Department of Energy Waste Treatment and Immobilization Plant Project. The authors also thank Albert Kruger, Michael Schweiger, and Chuck Henager for their involvement with the commencement of this research project.

3.9. Tables

Table 3.1. Enthalpy, entropy, and heat capacity constant values of specified compounds

Compound	T range (K)	$\Delta H^0_{298.15\,K}$ (J · mol^{-1})	$S^0_{298.15\,K}$ (J · mol^{-1} · K^{-1})	C_p^* constants								Reference
				a	b	c	d	e	f	g	h	
Al_2O_3(corundum)	298.15 < T < 600.00 600.00 < T < 1500.00 1500.00 < T < 2327.00 2327.00 < T < 4000.00	-1676383.29	50.94	67.48039 116.2579 156.0582 192.464	134.9399 14.45137 -14.18213	-18.77562 -42.41404 -247.3334	-85232.68 -1671.19 3776.411					Bale et al.[43]
$Al_2O_3(\ell)$	298.15 < T < 600.00 600.00 < T < 1500.00 1500.00 < T < 2327.00 2327.00 < T < 4000.00	-1565298.09	98.6775	67.48039 116.2579 156.0582 192.464	134.9399 14.45137 -14.18213	-18.77562 -42.41404 -247.3334	-85232.68 -1671.19 3776.411					Bale et al.[43]
Al_2SiO_5(sillimanite)	298.15 < T < 3000.00	-2587770	95.79	183.87	18.15	-123.6			16.024	3205.2		Saxena et al.[104]
$NaAlO_2$(β)	298.15 < T < 2140.00	-1134391.9	70.36	139.1606				-1143.4999	1.40428967			Lambotte & Chartrand[76]
$NaAlO_2$(γ)	298.15 < T < 2140.00	-1133094.9	72.1127	139.1606				-1143.4999	1.40428967			Lambotte & Chartrand[76]
$NaAlO_2$(δ)	298.15 < T < 2140.00	-1131939.9	72.7989	139.1606				-1143.4999	1.40428967			Lambotte & Chartrand[76]
$NaAl_{11}O_{17}$(β'-Al_2O_3)	298.15 < T < 2400.00	-9518595	350.6617	1033.31968		-28.59755		-9556.42804	3.42089133			Lambotte & Chartrand[76]
$Na_2Al_{12}O_{19}$(β"-Al_2O_3)	298.15 < T < 2000.00	-10690701.36	418.6424	1157.35601	19.93868	-34.89447	-6403.41	-10425.19423	3.73188145			$\Delta H^0_{298.15\,K}$ this work, $S^0_{298.15\,K}$ and C_p[76]
$NaAlSiO_4$(α-carnegieite)	298.15 < T < 2000.00	-2083514.4	127.8933	236.01526		-35.34312		-1592.79852	4.2757827			Lambotte & Chartrand[76]
$NaAlSiO_4$(β-nepheline)	298.15 < T < 2000.00	-2093227.3	125.5874	228.26221		-19.39261		-1641.05096	2.248258167			Lambotte & Chartrand[76]
$NaAlSi_3O_8$(low-albite)	298.15 < T < 2000.00	-3935000	207.4	394.18993		-76.68033		-2438.11327	10.17706412			Lambotte & Chartrand[76]
$NaAlSi_3O_8$(high-albite)	298.15 < T < 2000.00	-3923302.7	219.6723	394.18993		-76.68033		-2438.11327	10.17706412			Lambotte & Chartrand[76]
$NaAlSi_3O_8$(monalbite)	298.15 < T < 2000.00	-3915260.6	226.1	394.18993		-76.68033		-2438.11327	10.17706412			Lambotte & Chartrand[76]
Na_2O(γ)	298.00 < T < 1405.00 1405.0 0< T < 1500.00	-417982	75.0610	66.216 104.6	43.8651	-8.1337	-14087.5004					Wu et al.[84]
Na_2O(β)	298.00 < T < 1405.00 1405.0 0< T < 1500.00	-416224.72	76.7788	66.216 104.6	43.8651	-8.1337	-14087.5004					Wu et al.[84]
Na_2O(α)	298.00 < T < 1405.00 1405.0 0< T < 1500.00	-404300.32	86.3720	66.216 104.6	43.8651	-8.1337	-14087.5004					Wu et al.[84]

Table 3.1 cont'd. Enthalpy, entropy, and heat capacity constant values of specified compounds

Compound	T range (K)	$\Delta H^0_{298.15\,K}$ (J · mol^{-1}	$S^0_{298.15\,K}$ (J · mol^{-1} · K^{-1})	C_p* constants a	b	c	d	e	f	g h	Reference
$Na_2O(\ell)$	298.00 < T < 1405.00 1405.0 0< T < 1500.00	-356602.72	120.3205	66.216	43.8651	-8.1337	-14087.5004				Wu et al.[84]
Na_2SiO_3(s)	298.15 < T < 1363.00 1363.00 < T < 1450.00	-1561430	113.847	234.77 177.31792				-2218.9	1.353		Bale et al.[43]
$Na_2Si_2O_5(\alpha)$	298.15 < T < 1148.00 1148.00 < T < 1250.00	-2470070	165.7	250.69 261.20712		-156.51			22.17		Bale et al.[43]
$Na_2Si_2O_5(\beta)$	298.15 < T < 951.00 951.00 < T < 1148.00 1148.00 < T < 1250.00	-2469652	166.1395	250.69 292.88 261.20712		-156.51			22.17		Bale et al.[43]
$Na_2Si_2O_5(\gamma)$	298.15 < T < 951.00 951.00 < T < 1148.00 1148.00 < T < 1250.00	-2469024	166.7804	250.69 292.88 261.20712		-156.51			22.17		Bale et al.[43]
Na_4SiO_4(s)	298.15 < T < 1358.00 1363.00 < T < 1450.00	-2108979	195.811	162.59024 259.408	74.22416						Bale et al.[43]
$Na_6Si_2O_7$(s)	298.15 < T < 1397.00	-3617193.47	349.1774	461.006		-203.6927		-1005.180017	32.28358041		$\Delta H^0_{298.15\,K}$ and $S^0_{298.15\,K}$ this work, C_p[43]
$Na_6Si_8O_{19}$(s)	298.15 < T < 1082.00	-9187800	636.5	987.691985		-355.406298		-4020.72	54.10599850		Bale et al.[43]
$Na_{10}SiO_7$(s)	298.15 < T < 1358.00	-3327528.29	528.3676	361.238242	205.819466	-24.4011	-42262.50116				$\Delta H^0_{298.15\,K}$ and $S^0_{298.15\,K}$ this work, C_p[43]
SiO_2(low-quartz)	298.15 < T < 373.00 373.00 < T < 848.00 848.00 < T < 850.00	-910699.94	41.46	80.0119918 80.0119918 0.04184	8.4400217	-35.46684 -35.46684	-45212.70148	-240.2759989 -240.2759989	4.915683694 4.915683694	6.055044634	Wu et al.[84]
SiO_2(high-quartz)	298.15 < T < 1995.99 1995.99 < T < 3000.00	-908626.77	44.2068	80.011992 85.772		-35.46684		-240.276	4.91568369		Wu et al.[84]
SiO_2(high-tridymite)	298.15 < T < 1991.28 1991.28 < T < 3000.00	-907045.13	45.5237	75.372668 85.772		-59.5809508			9.58246123		Wu et al.[84]
SiO_2(high-cristobalite)	298.15 < T < 1995.99 1995.99 < T < 3000.00	-906377.23	46.0288	83.513598 85.772		-24.5536		-374.693	2.80072194		Wu et al.[84]
$SiO_2(\ell)$	298.15 < T < 1995.99 1995.99 < T < 3000.00	-896795.87	50.8291	83.513598 85.772		-24.5536		-374.693	2.80072194		Wu et al.[84]

* $C_p(\mathrm{J \cdot mol^{-1} \cdot K^{-1}}) = a + b \cdot 10^{-3}T + c \cdot 10^{5}T^{-2} + d \cdot 10^{-9}T^{2} + eT^{-0.5} + f \cdot 10^{8}T^{-3} + gT^{-1} + h \cdot 10^{-8}T^{3}$

Table 3.2. Model parameters for solid solutions

Mullite $(Al^{+3})_2[Al^{+3}, Si^{+4}]\{O^{-2}, Va\}_5$

$^{o}G_{Al_3O_5^{-1}} = {}^{o}G_{Al_3Va^{+9}} = 3/2\,{}^{o}G_{Al_2O_3(corundum)} + 86508.38 - 0.418T$

$^{o}G_{Al_2SiO_5} = {}^{o}G_{Al_2SiVa^{+10}} = {}^{o}G_{Al_2SiO_5(sillimanite)} + 9957.92 - 3.347T$

$^{0}L_{Al^{+3}:Al^{+3},Si^{+4}:O^{-2}} = {}^{0}L_{Al^{+3}:Al^{+3},Si^{+4}:Va} = -92048.0$

β-Al_2O_3 $(Na_2O)_1[Al_2O_3]_{11}\{Na_2O, Va\}_1$

$^{o}G_{Na_4Al_{22}O_{35}} = 2\,{}^{o}G_{NaAl_{11}O_{17}} + {}^{o}G_{Na_2O(\alpha)} - 154808$

$^{o}G_{Na_2Al_{22}O_{34}} = 2\,{}^{o}G_{NaAl_{11}O_{17}}$

$^{0}L_{Na_2O:Al_2O_3:Na_2O,Va} = -271700 - 3T$

Sodium aluminate $((Na - Al)^{+4}, (Va - Si)^{+4})_1[O^{-2}]_2$

$^{o}G_{NaAlO_2} = {}^{o}G_{NaAlO_2(\delta)}$

$^{o}G_{SiO_2} = {}^{o}G_{SiO_2(high-cristobalite)} + 6276.0 + 4.1840T$

$^{0}L_{NaAl^{+4},VaSi^{+4}:O^{-2}} = -50100 - 43.26T$

$^{1}L_{NaAl^{+4},VaSi^{+4}:O^{-2}} = -25100 + 1.13T$

Nepheline $((Na - Al)^{+4}, (Va - Si)^{+4})_8[Si^{+4}]_8\{O^{-2}\}_{32}$

$^{o}G_{Na_8Al_8Si_8O_{32}} = 8\,{}^{o}G_{NaAlSiO_4(\beta-nepheline)}$

$^{o}G_{Si_{16}O_{32}} = 16\left({}^{o}G_{SiO_2(high-tridymite)} + 6276.0\right)$

$^{0}L_{NaAl^{+4},VaSi^{+4}:Si^{+4}:O^{-2}} = 24980 - 75.075T$

Carnegieite $((Na - Al)^{+4}, (Va - Si)^{+4})_4[Si^{+4}]_4\{O^{-2}\}_{16}$

$^{o}G_{Na_4Al_4Si_4O_{16}} = 4\,{}^{o}G_{NaAlSiO_4(\alpha-carnegieite)}$

$^{o}G_{Si_8O_{16}} = 8\left({}^{o}G_{SiO_2(high-cristobalite)} + 4184.0\right)$

$^{0}L_{NaAl^{+4},VaSi^{+4}:Si^{+4}:O^{-2}} = 36000 - 18.1T$

Table 3.3. Model parameters for oxide liquid

Oxide liquid $(Al^{+3}, Na^{+1})_P(AlO_2^{-1}, O^{-2}, SiO_4^{-4}, SiO_2^0)_Q$
${}^{o}G_{Al^{+3}:AlO_2^{-1}} = 2{}^{o}G_{Al_2O_3(\ell)}$
${}^{o}G_{Al^{+3}:O^{-2}} = {}^{o}G_{Al_2O_3(\ell)} + 900000$
${}^{o}G_{Al^{+3}:SiO_4^{-4}} = 2{}^{o}G_{Al_2O_3(\ell)} + 3{}^{o}G_{SiO_2(\ell)} + 300000$
${}^{o}G_{Al^{+3}:SiO_2^0} = 3{}^{o}G_{SiO_2(\ell)}$
${}^{o}G_{Na^{+1}:AlO_2^{-1}} = 1/2{}^{o}G_{Al_2O_3(\ell)} + 1/2{}^{o}G_{Na_2O(\ell)} - 111739.198 + 14.17779T$
${}^{o}G_{Na^{+1}:O^{-2}} = {}^{o}G_{Na_2O(\ell)}$
${}^{o}G_{Na^{+1}:SiO_4^{-4}} = 2{}^{o}G_{Na_2O(\ell)} + {}^{o}G_{SiO_2(\ell)} - 353175.963 + 24.67013T$
${}^{o}G_{Na^{+1}:SiO_2^0} = {}^{o}G_{SiO_2(\ell)}$
${}^{0}L_{Al^{+3}:AlO_2^{-1},SiO_2^0} = 313000 - 132.44T$
${}^{1}L_{Al^{+3}:AlO_2^{-1},SiO_2^0} = 1292.6 - 7.613T$
${}^{2}L_{Al^{+3}:AlO_2^{-1},SiO_2^0} = -10T$
${}^{0}L_{Al^{+3},Na^{+1}:AlO_2^{-1}} = -18000 - 11.64T$
${}^{1}L_{Al^{+3},Na^{+1}:AlO_2^{-1}} = 239000 - 84.08T$
${}^{0}L_{Na^{+1}:AlO_2^{-1},O^{-2}} = -12T$
${}^{0}L_{Na^{+1}:O^{-2},SiO_2^0} = -143800 + 18.318T$
${}^{1}L_{Na^{+1}:O^{-2},SiO_2^0} = -15400 + 3.029T$
${}^{2}L_{Na^{+1}:O^{-2},SiO_2^0} = 810 - 2.6381T$
${}^{3}L_{Na^{+1}:O^{-2},SiO_2^0} = -34800 + 14.38T$
${}^{0}L_{Na^{+1}:SiO_4^{-4},SiO_2^0} = 2^0L_{Na^{+1}:O^{-2},SiO_2^0}$
${}^{1}L_{Na^{+1}:SiO_4^{-4},SiO_2^0} = 2^1L_{Na^{+1}:O^{-2},SiO_2^0}$
${}^{2}L_{Na^{+1}:SiO_4^{-4},SiO_2^0} = 2^2L_{Na^{+1}:O^{-2},SiO_2^0}$
${}^{3}L_{Na^{+1}:SiO_4^{-4},SiO_2^0} = 2^3L_{Na^{+1}:O^{-2},SiO_2^0}$
${}^{0}L_{Na^{+1}:O^{-2},SiO_4^{-4}} = -176800$
${}^{0}L_{Na^{+1}:AlO_2^{-1},SiO_2^0} = -177680 + 27.968T$
${}^{1}L_{Na^{+1}:AlO_2^{-1},SiO_2^0} = -42200$
${}^{AlO_2^{-1}}L_{Na^{+1}:AlO_2^{-1},SiO_4^{-4},SiO_2^0} = -689000 + 334.46T$
${}^{SiO_2^0}L_{Na^{+1}:AlO_2^{-1},SiO_4^{-4},SiO_2^0} = -14.89 - 155.5T$
${}^{0}L_{Al^{+3},Na^{+1}:AlO_2^{-1},SiO_2^0} = -0.2357$
${}^{1}L_{Al^{+3},Na^{+1}:AlO_2^{-1},SiO_2^0} = 305000 - 151.7T$
${}^{2}L_{Al^{+3},Na^{+1}:AlO_2^{-1},SiO_2^0} = -45T$
${}^{0}L_{Al^{+3},Na^{+1}:AlO_2^{-1},SiO_4^{-4}} = -350T$

Table 3.4. Invariant points of Na_2O-Al_2O_3-SiO_2 pseudobinary subsystems

Invariant Point	Calculated		Measured		References
Al_2O_3-SiO_2 System (Fig. 3.1)	$X_{Al_2O_3}$ **	T (K)	$X_{Al_2O_3}$	T (K)	
Mullite T_m*	0.653	2162	0.666	2163	Klug et al.[105]
SiO_2(high-cristobalite) + mullite eutectic	0.038	1820	0.0332	1820	Howald & Eliezer[91]
Na_2O-Al_2O_3 System (Fig. 3.2)	$X_{Al_2O_3}$	T (K)	$X_{Al_2O_3}$	T (K)	
Na_2O(α) T_m		1405.0		1405.2	Wu et al.[84]
$NaAlO_2$(δ) T_m		2141	0.500	2140	Weber & Venero[103]
$NaAlO_2$(δ) + β-Al_2O_3 eutectic	0.650	1859	0.652	1858	Weber & Venero[103]
β-Al_2O_3 T_m	0.893	2272	0.895	2273	Rolin & Than[102]
SiO_2(high-cristobalite) T_m		1995		1996	Weber & Venero[103]
Al_2O_3(corundum) T_m		2327		2327	Eriksson et al.[80]
Na_2O-SiO_2 System (Fig. 3.3)	X_{SiO_2}	T (K)	X_{SiO_2}	T (K)	
Na_2O(β) + $Na_{10}SiO_7$ eutectic	0.128	1209.5	0.14	1123.2	Rys[106]
$Na_{10}SiO_7$ T_m		1244.3		1245.2	Rys[106]
$Na_{10}SiO_7$ + Na_4SiO_4 eutectic	0.235	1046.2	0.21	1139.2	Rys[106]
Na_4SiO_4 T_m		1381		1391	Kracek[107]
				1356	D'Ans & Lottler[108]
				1383	Rys[106]
Na_4SiO_4 + $Na_6Si_2O_7$ eutectic	0.370	1364	0.373	1273	D'Ans & Lottler[108]
			0.365	1302	Rys[106]
$Na_6Si_2O_7$ T_m		1389		1395	D'Ans & Lottler[108]
				1380	Meshalkin[109]
$Na_6Si_2O_7$ + Na_2SiO_3 eutectic	0.452	1303	0.455	1288	D'Ans & Lottler[108]
			0.451	1295	Meshalkin[109]
Na_2SiO_3 T_m		1362		1361	D'Ans & Lottler[108]
				1362	Kracek[107]
				1363	Willgallis[110]
				1361	D'Ans & Lottler[108]
				1366	Meshalkin[109]
				1364	Rys[106]
Na_2SiO_3 + $Na_2Si_2O_5$(γ) eutectic	0.630	1110	0.625	1113	D'Ans & Lottler[108]
			0.628	1119	Kracek[107]
			0.633	1110	Willgallis[110]
$Na_2Si_2O_5$(γ) T_m		1148		1147	Kracek,[107] D'Ans &
$Na_2Si_2O_5$(γ) + $Na_6Si_8O_{19}$ peritectic	0.740	1058		1081	Williams & Glasser[111]
				1071	Schairer[112]
$Na_6Si_8O_{19}$ + SiO_2(high-quartz) eutectic	0.746	1057	0.735	1066	D'Ans & Lottler[108]
			0.745	1066	Kracek[107]
			0.725	1072	Williams & Glasser[111]
			0.746	1061	Schairer[112]

* T_m = melting temperature
** $X_{compound}$ = mole fraction of compound

Table 3.5. Invariant points ofNa_2O-Al_2O_3-SiO_2 isopleths

Invariant Point	Calculated		Measured		Reference
$Na_2Si_2O_5$-$NaAlSi_3O_8$ System (Fig. 3.7)	$X_{NaAlSi_3O_8}$	T (K)	$X_{NaAlSi_3O_8}$	T (K)	
$Na_2Si_2O_5$ + $NaAlSi_3O_8$(high-albite) eutectic	0.290	1040	0.298	1040	Schairer & Bowen[74]
$NaAlSi_3O_8$(monalbite) T_m		1393		1393	Schairer & Bowen[74]
$Na_2Si_2O_5$-$NaAlSiO_4$ System (Fig. 3.11)	$X_{NaAlSiO_4}$	T (K)	$X_{NaAlSiO_4}$	T (K)	
$Na_2Si_2O_5$(γ) + nepheline eutectic	0.353	1019	0.345	1042	Tilley[113]
Carnegieite T_m		1796		1799	Tilley[113]
Na_2SiO_3-$NaAlO_2$ System (Fig. 3.12)	X_{NaAlO_2}	T (K)	X_{NaAlO_2}	T (K)	
Na_2SiO_3 + sodium aluminate eutectic	0.293	1248	0.270	1242	Schairer & Bowen[74]
Sodium aluminate T_m		2141		2141	Schairer & Bowen[74]
Na_2SiO_3-$NaAlSiO_4$ System (Fig. 3.13)	$X_{NaAlSiO_4}$	T (K)	$X_{NaAlSiO_4}$	T (K)	
Na_2SiO_3 + nepheline eutectic	0.458	1182	0.413	1193	Tilley[113]
$NaAlO_2$-SiO_2 System (Fig. 3.14)	X_{SiO_2}	T (K)	X_{SiO_2}	T (K)	
Nepheline + $NaAlSi_3O_8$(monalbite) eutectic	0.695	1349	0.693	1341	Greig[114]
$NaAlSi_3O_8$(monalbite) + SiO_2(high-tridymite)	0.829	1315	0.834	1337	Schairer & Bowen[74]
$NaAlSi_3O_8$-Al_2O_3 System (Fig. 3.15)	$X_{Al_2O_3}$	T (K)	$X_{Al_2O_3}$	T (K)	
$NaAlSi_3O_8$(monalbite) + mullite eutectic	0.040	1382	0.038	1378	Schairer & Bowen[74]
$NaAlSiO_4$-Al_2O_3 System (Fig. 3.16)	$X_{Al_2O_3}$	T (K)	$X_{Al_2O_3}$	T (K)	
Carnegieite + β-Al_2O_3 eutectic	0.076	1759	0.086	1764	Schairer & Bowen[74]

Table 3.6. Invariant points of Na_2O-Al_2O_3-SiO_2 system (Fig. 3.10)

Invariant Point	Calculated				Measured				Reference
	X_{Na_2O}	$X_{Al_2O_3}$	X_{SiO_2}	T (K)	X_{Na_2O}	$X_{Al_2O_3}$	X_{SiO_2}	T (K)	
$NaAlSiO_4 + Na_2SiO_3$	0.386	0.114	0.5	1183	0.393	0.107	0.5	1179	Tilley[113]
					0.392	0.108	0.5	1173	Spivak[115]
$Na_2Si_2O_5 + NaAlSiO_4$	0.311	0.067	0.622	1020	0.312	0.065	0.623	1041	Tilley[113]
$NaAlSi_3O_8 + NaAlSiO_4$	0.153	0.152	0.695	1350	0.153	0.153	0.694	1341	Greig & Barth[114]
$NaAlSi_3O_8 + SiO_2$	0.085	0.085	0.830	1316	0.083	0.083	0.834	1335	Schairer & Bowen[74]
$NaAlSi_3O_8 + Na_2Si_2O_5$	0.260	0.044	0.696	1041	0.258	0.045	0.697	1040	Schairer & Bowen [74]
$NaAlSi_3O_8 + Al_2O_3$	0.124	0.133	0.743	1383	0.12	0.158	0.722	1381	Schairer & Bowen [74]
$NaAlSiO_4 + Al_2O_3$	0.235	0.276	0.489	1758	0.238	0.288	0.475	1748	Schairer & Bowen [74]
$Na_2SiO_3 + Na_2Si_2O_5 + NaAlSiO_4$	0.311	0.067	0.622	1019	0.327	0.063	0.61	1033	Tilley[113]
$NaAlSi_3O_8 + Na_2Si_2O_5 + SiO_2$	0.234	0.026	0.740	1015	0.214	0.028	0.758	1013	Schairer & Bowen [74]
$NaAlSi_3O_8 + Al_6Si_2O_{13} + SiO_2$	0.080	0.091	0.829	1298	0.08	0.084	0.835	1323	Schairer & Bowen [74]
$NaAlSiO4 + Al_6Si_2O_{13} + Al_2O_3$	0.150	0.156	0.695	1346	0.119	0.129	0.752	1377	Schairer & Bowen [74]
$NaAlSi_3O_8 + NaAlSiO_4 + Al_6Si_2O_{13}$	0.150	0.156	0.695	1346	0.149	0.156	0.695	1336	Schairer & Bowen [74]
$NaAlSi_3O_8 + NaAlSiO_4 + Na_2Si_2O_5$	0.311	0.067	0.622	1019	0.268	0.078	0.654	1005	Schairer & Bowen [74]

3.10. Figures

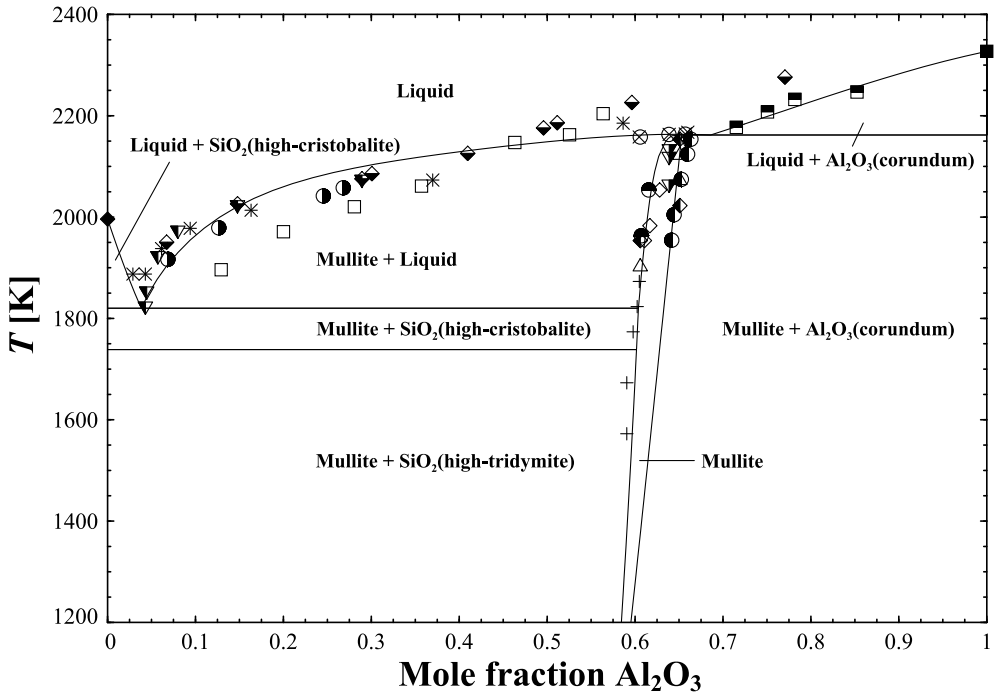

Fig. 3.1. Computed Al_2O_3-SiO_2 pseudobinary phase diagram with experimental measurements shown as points. Data: ▽116 ✳117 ◆118 ◑119 □120 ▬121 ○105 ◆103 ■122 ×105 ▽105 ◐105 ◓123 +124 ◇125 △125 ◧125

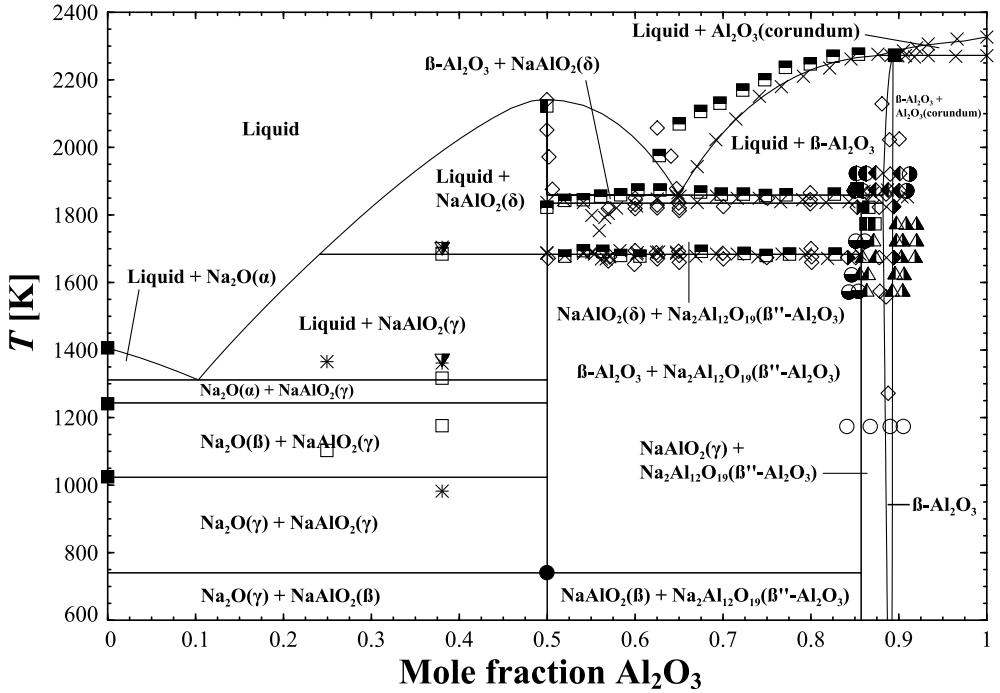

Fig. 3.2. Computed Na_2O-Al_2O_3 pseudobinary phase diagram with experimental measurements shown as points. Data: ▲126 □106 ✳106 ▽106 ●127 ◇103 ◧74 ▬128 ×102 ◐129 ◧129 ◓129 ◭129 ◑129 ◆130 ◭129 ○131 ■102

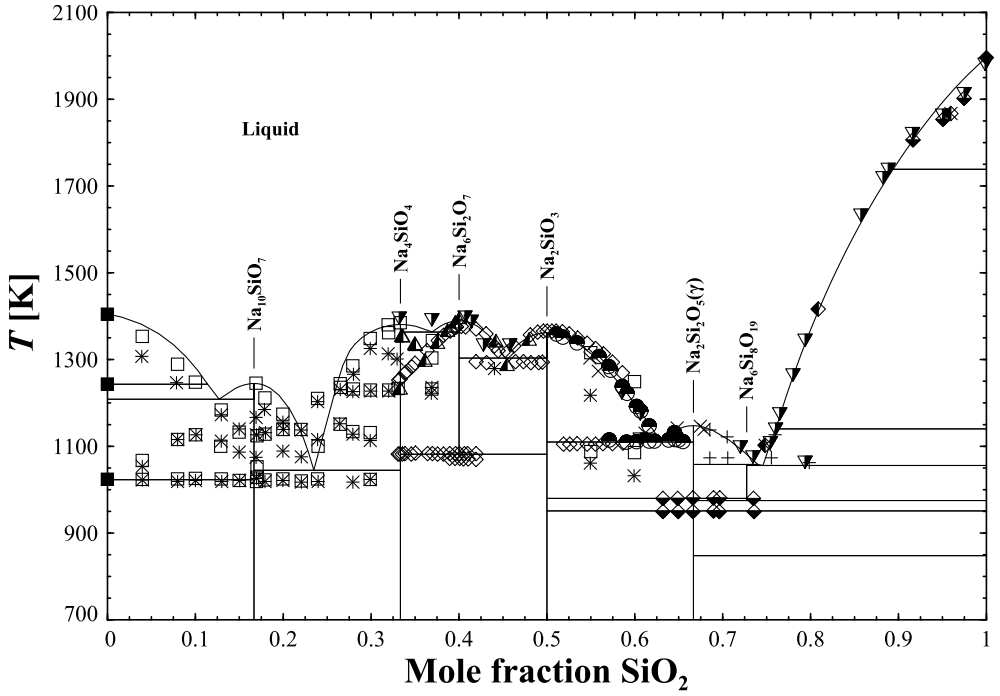

Fig. 3.3. Computed Na_2O-SiO_2 pseudobinary phase diagram with experimental measurements shown as points. Data: ■[84] □[106] ✳[106] ◭[132] ╳[133] ▽[107] ◇[109] ◓[110] ◆[134] ┼[112]

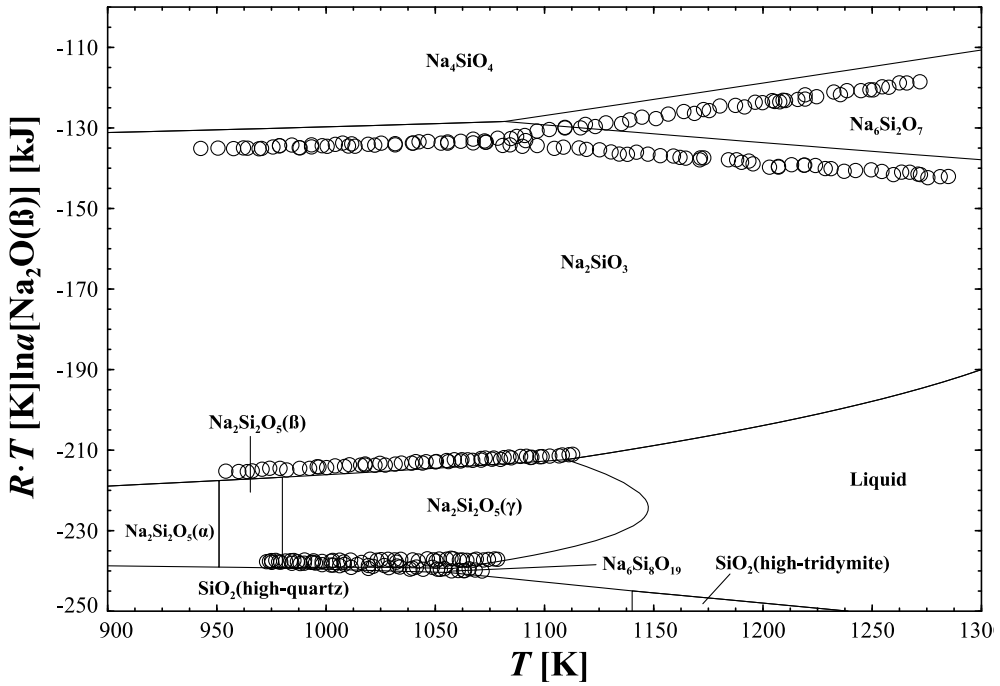

Fig. 3.4. Partial Gibbs energy for $Na_2O(\beta)$ within the Na_2O-SiO_2 system with experimental measurements shown as points. Data: ◯[135, 136]

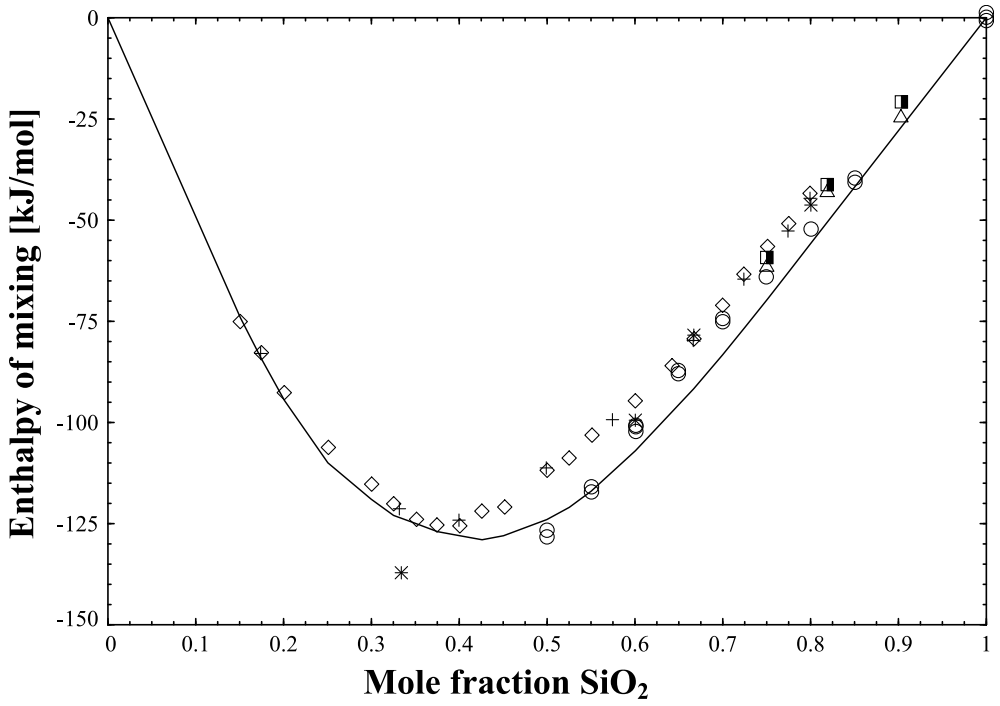

Fig. 3.5. Computed curve of the enthalpy of mixing for Na_2O-SiO_2 at 1450 K with experimental measurements shown as points. Data: ◇[137] +[137] ◯[138] ✳[139] ◨[140] △[140]

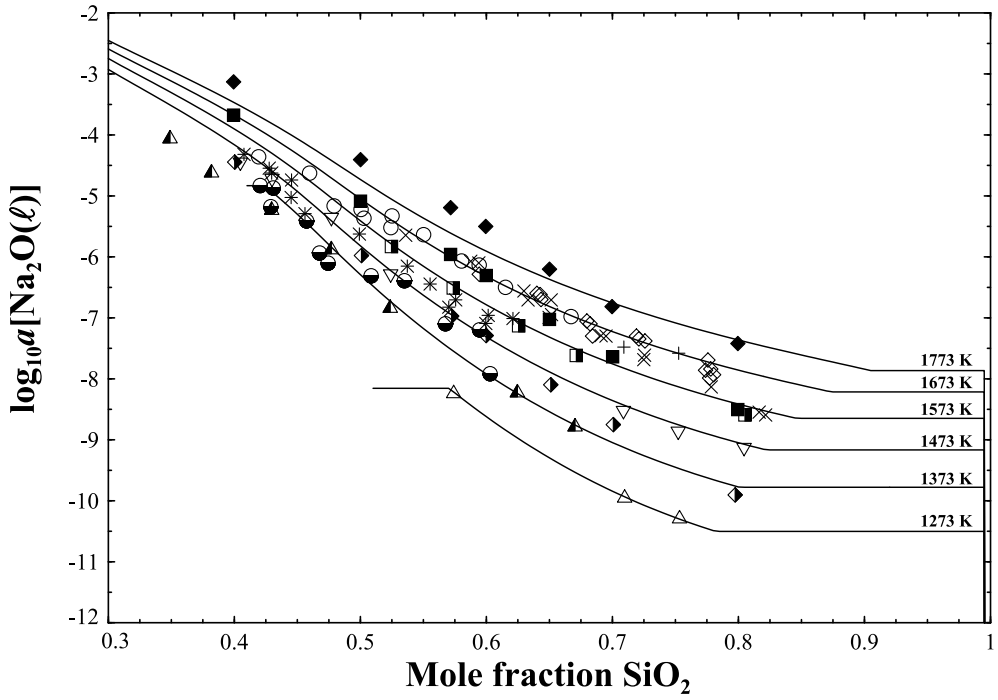

Fig. 3.6. Computed activity curve for Na_2O in Na_2O-SiO_2 liquid with experimental measurements shown as points. Data: ◆1773 K[141, 142] ■1573 K[141, 142] ◑1373 K[141, 142] ○1573 K[143] ✳1473 K[143] ◒1373 K[143] ◇1673 K[144] ×1573 K[144] +1673 K[135, 136] ◨1573 K[135, 136] ▽1473 K[135, 136] ◭1373 K[135, 136] △1273 K[135, 136]

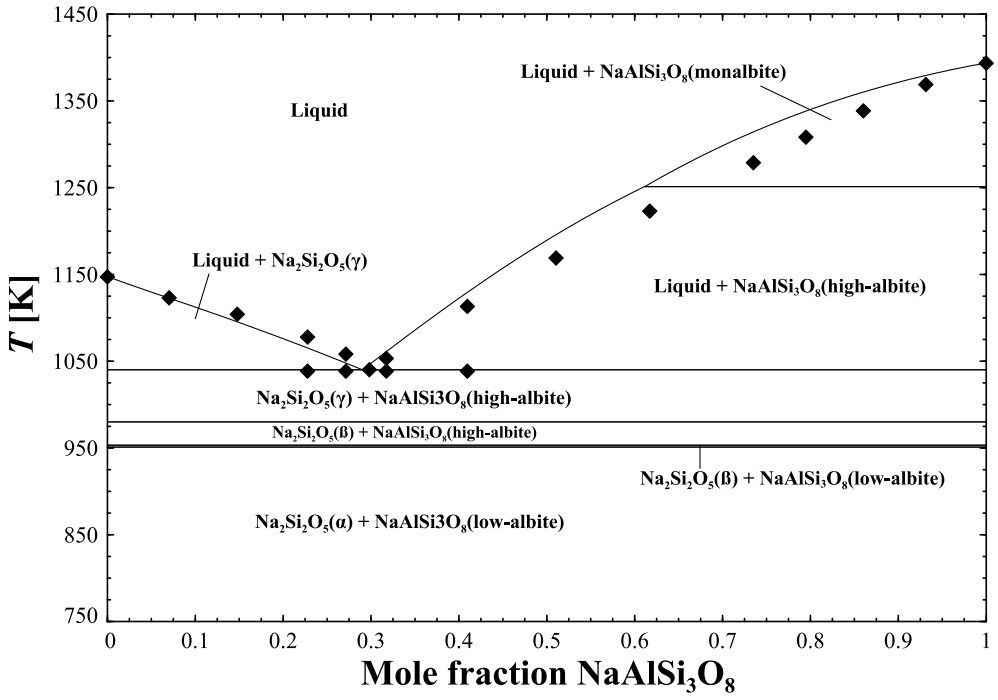

Fig. 3.7. Computed $Na_2Si_2O_5$-$NaAlSi_3O_8$ isoplethal section with experimental measurements shown as points. Data: ◆[74]

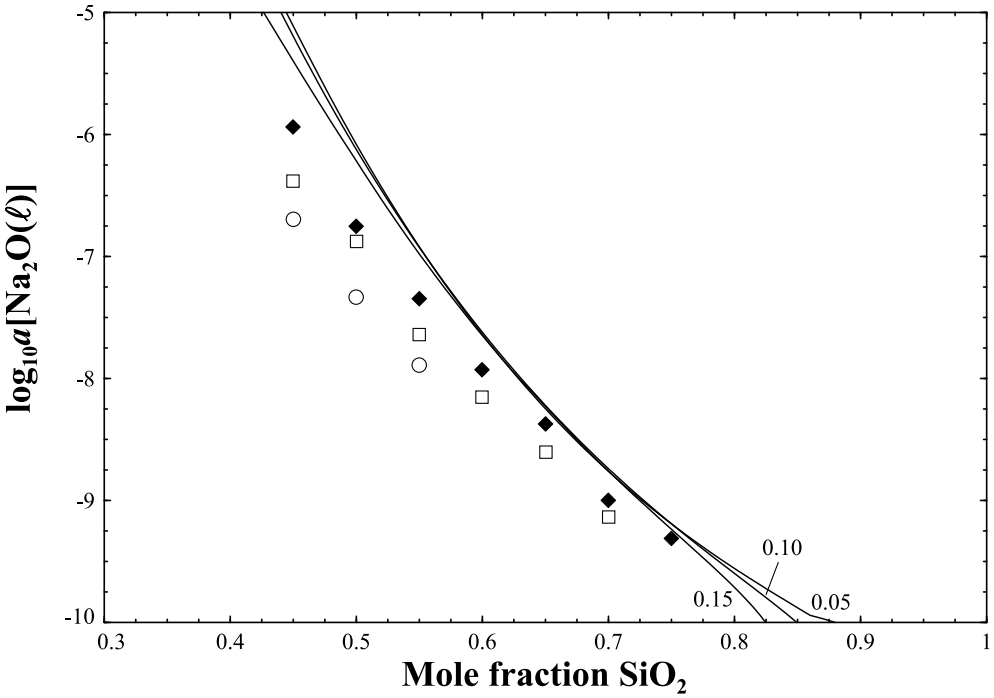

Fig. 3.8. Computed activity of Na_2O in the liquid phase as a function of $Na_2O/(Na_2O+ SiO_2)$ for fixed Al_2O_3 contents. Experimental measurements shown as points. Data: ◆ $X_{Al_2O_3}= 0.05$[145] □ $X_{Al_2O_3}= 0.10$[145] ○ $X_{Al_2O_3}= 0.15$[145]

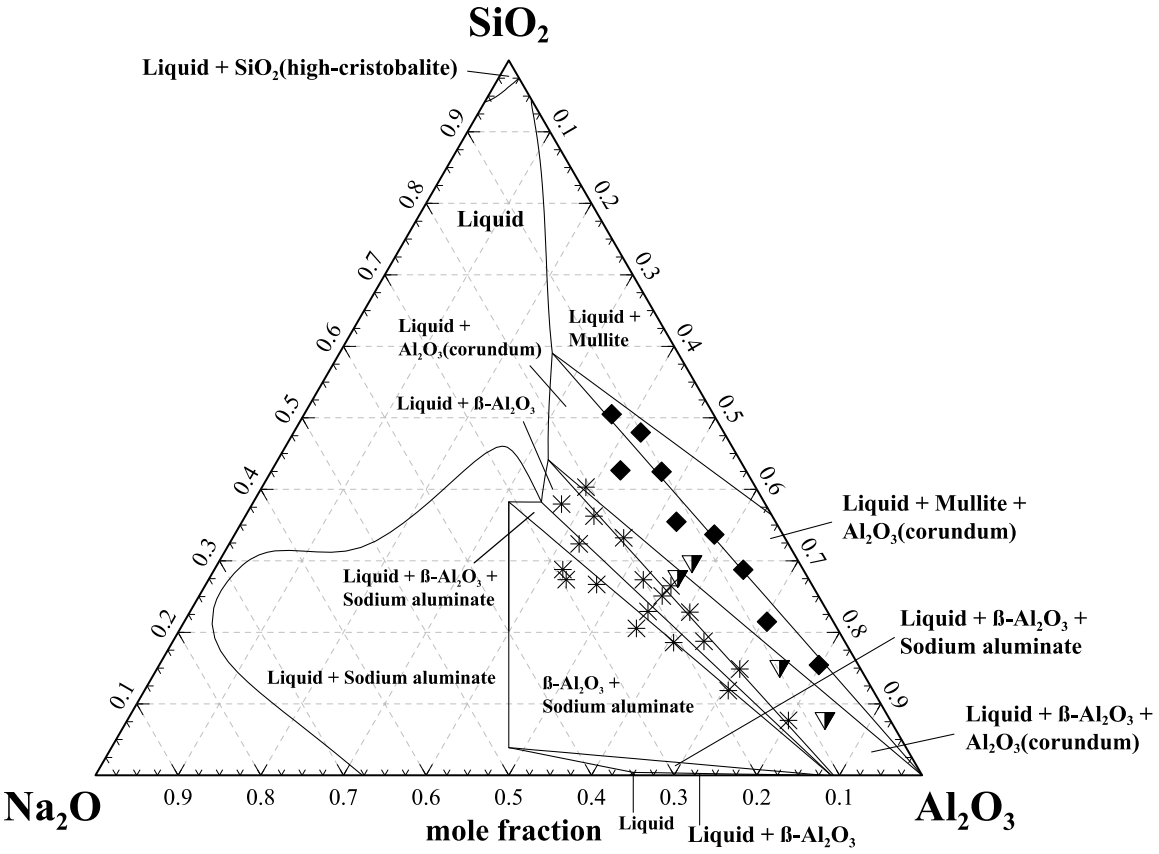

Fig. 3.9. Isothermal section of the Na_2O-Al_2O_3-SiO_2 system at 1873 K with experimental measurements shown as points. Data: ◆[146] ▽[146] ✳[146]

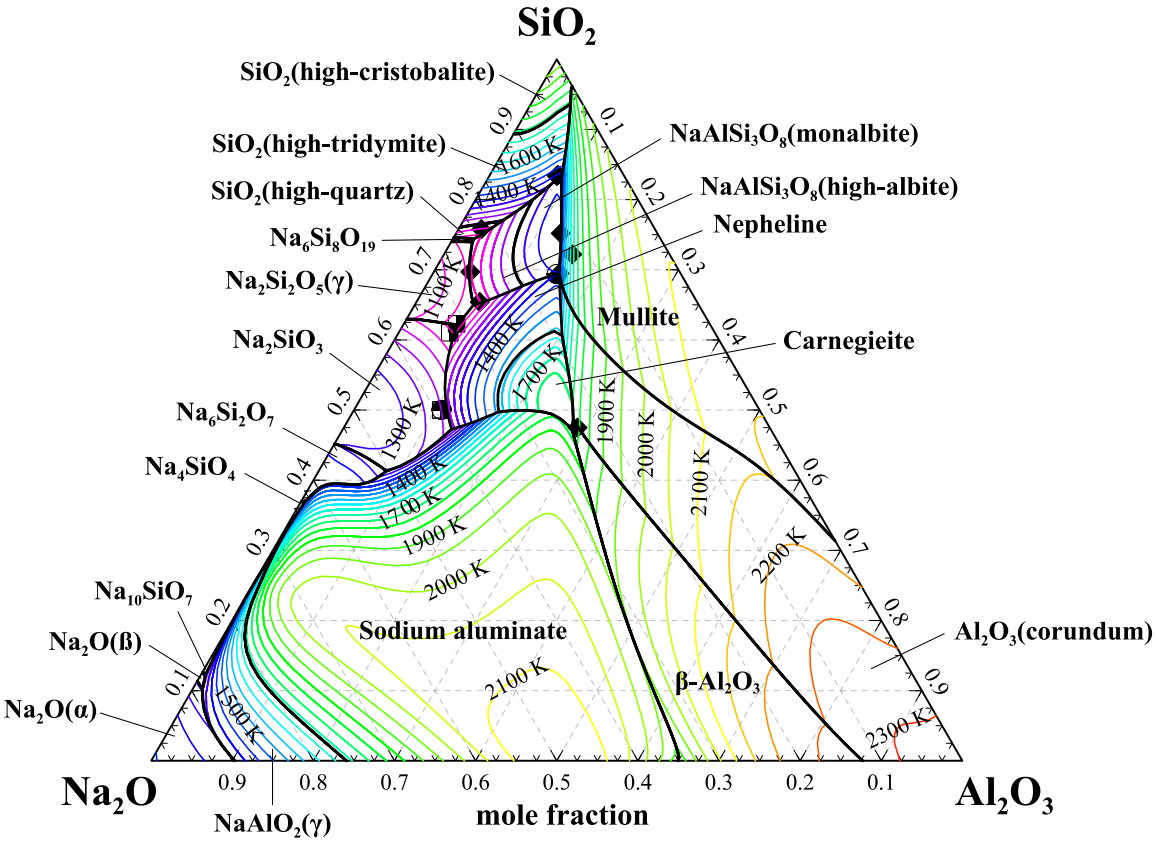

Fig. 3.10. Liquidus projections and invariant points computed for the Na_2O-Al_2O_3-SiO_2 system. Data: ◆[74] ◨[113] ◒[114] ◓[115]

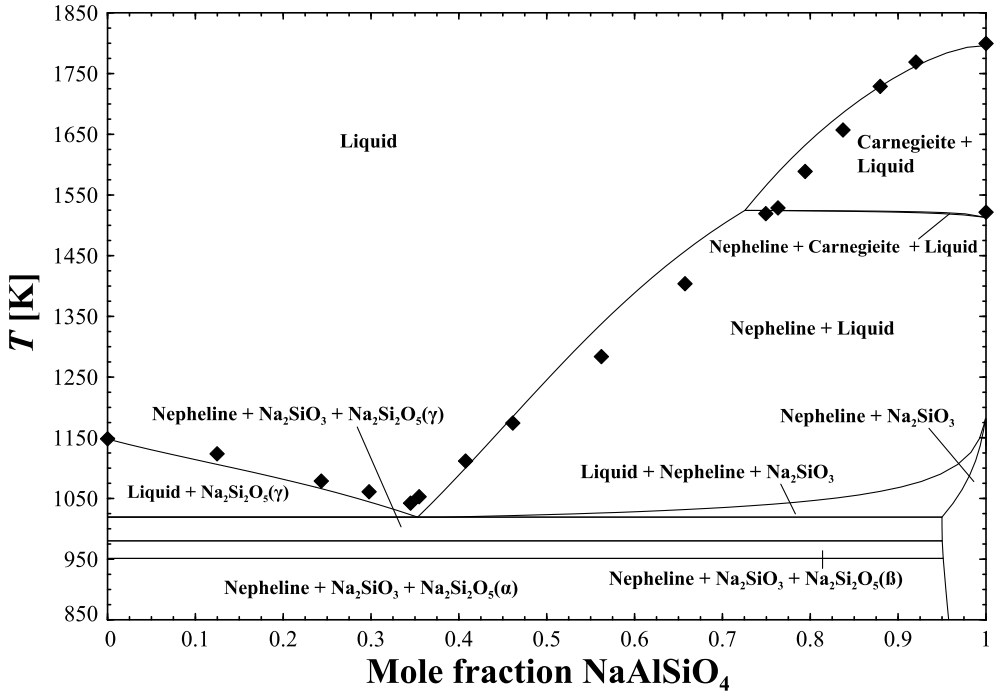

Fig. 3.11. Computed $Na_2Si_2O_5$-$NaAlSiO_4$ isoplethal section with experimental measurements shown as points. Data: ◆[74]

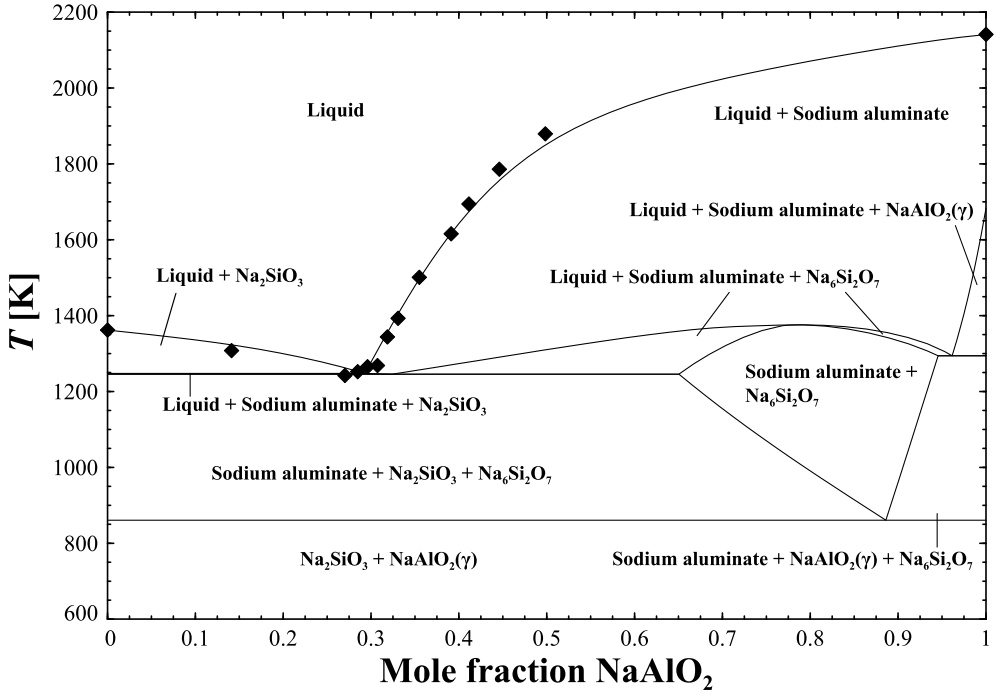

Fig. 3.12. Computed Na_2SiO_3-$NaAlO_2$ isoplethal section with experimental measurements shown as points. Data: ◆[74]

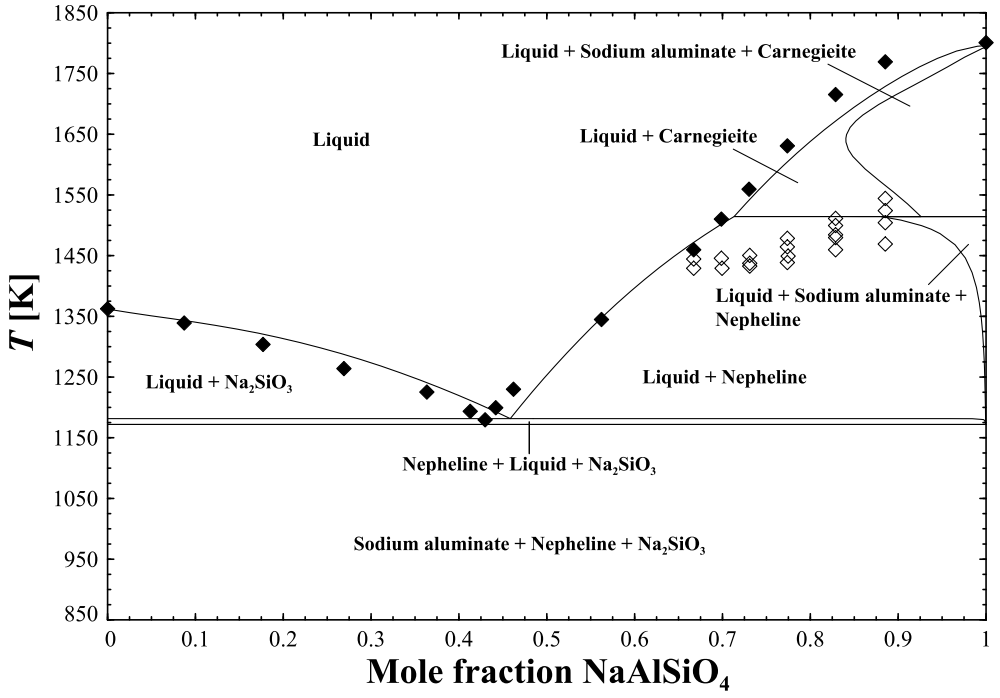

Fig. 3.13. Computed Na_2SiO_3-$NaAlSiO_4$ isoplethal section with experimental measurements shown as points. Data: ◆113 ◇113

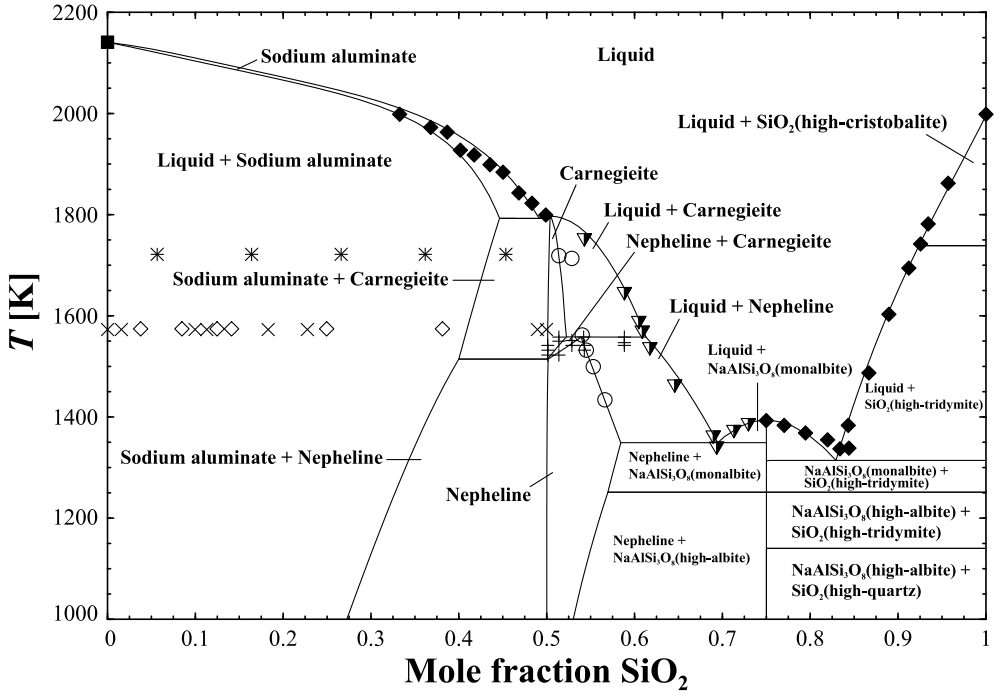

Fig. 3.14. Computed $NaAlO_2$-SiO_2 isoplethal section with experimental measurements shown as points. Data: ◆74 ◯74 ✳146 ◇147 ×147 +114 ▽114

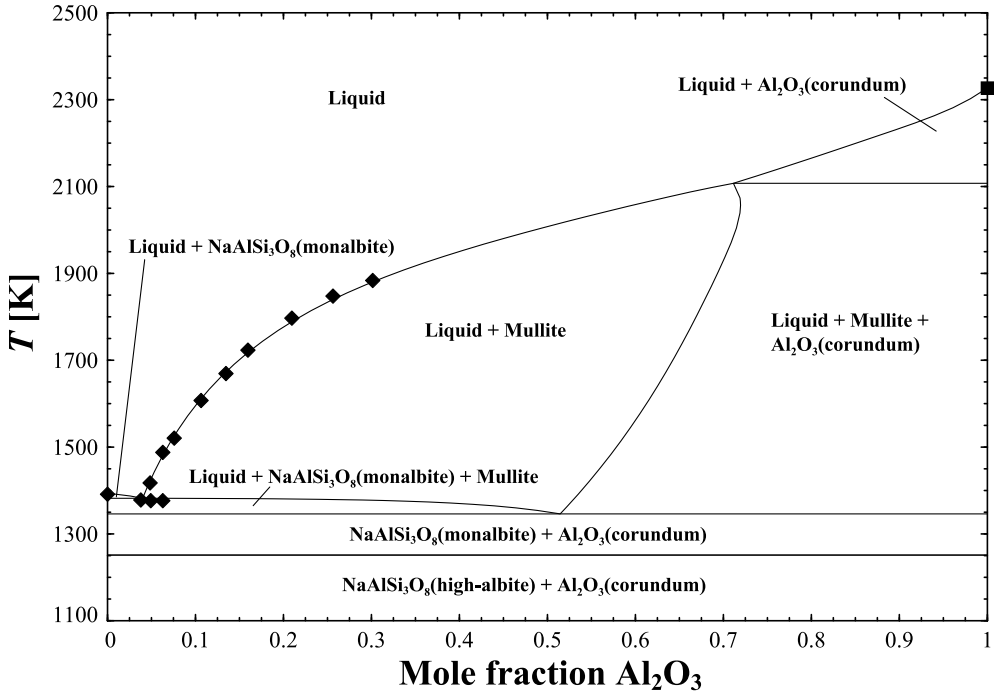

Fig. 3.15. Computed $NaAlSi_3O_8$-Al_2O_3 isoplethal section with experimental measurements shown as points. Data: ◆[74]

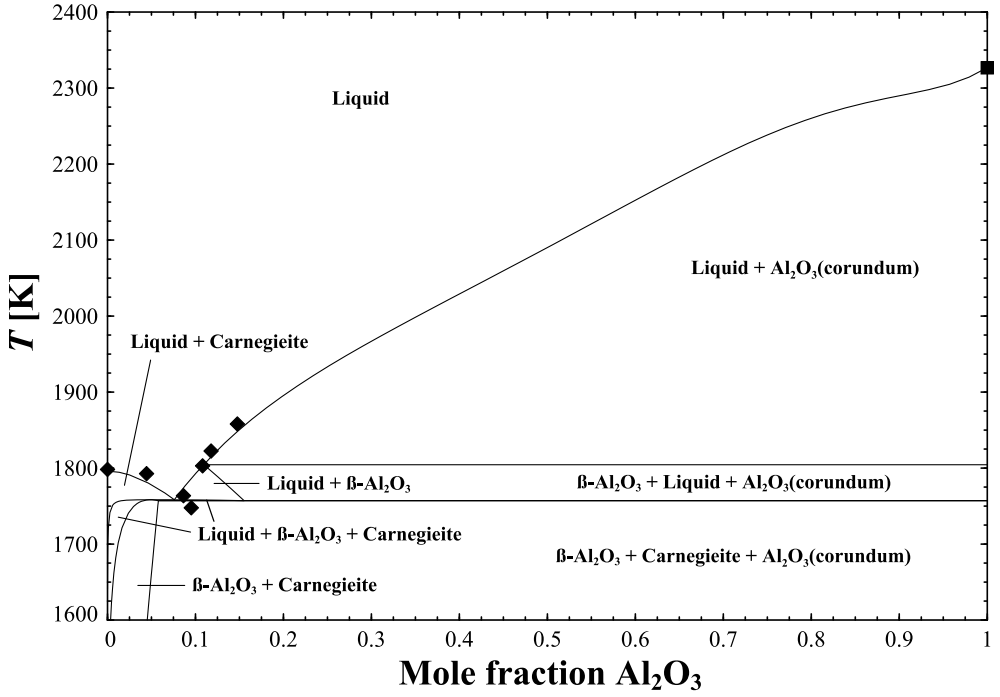

Fig. 3.16. Computed $NaAlSiO_4$-Al_2O_3 with experimental measurements shown as points. Data: ◆[74]

3.11. Copyright permission

JOHN WILEY AND SONS LICENSE TERMS AND CONDITIONS

Apr 08, 2019

This Agreement between University of South Carolina -- Stephen Utlak ("You") and John Wiley and Sons ("John Wiley and Sons") consists of your license details and the terms and conditions provided by John Wiley and Sons and Copyright Clearance Center.

License Number	4564220804226
License date	Apr 08, 2019
Licensed Content Publisher	John Wiley and Sons
Licensed Content Publication	Journal of the American Ceramic Society
Licensed Content Title	Thermodynamic assessment of the pseudoternary Na2O–Al2O3–SiO2 system
Licensed Content Author	Stephen A. Utlak,Theodore M. Besmann
Licensed Content Date	Sep 27, 2017
Licensed Content Pages	21
Type of use	Dissertation/Thesis
Requestor type	Author of this Wiley article
Format	Print and electronic
Portion	Full article
Will you be translating?	No
Title of your thesis / dissertation	Modeling complex oxides: Thermochemical behavior of nepheline-forming Na-Al-Si-B-K-Li-Ca-Mg-Fe-O and hollandite-forming Ba-Cs-Ti-Cr-Al-Fe-Ga-O systems
Expected completion date	Apr 2019
Expected size (number of pages)	275
Requestor Location	University of South Carolina
	Attn: University of South Carolina
Publisher Tax ID	EU826007151
Total	0.00 USD
Terms and Conditions	

TERMS AND CONDITIONS

This copyrighted material is owned by or exclusively licensed to John Wiley & Sons, Inc. or one of its group companies (each a"Wiley Company") or handled on behalf of a society with which a Wiley Company has exclusive publishing rights in relation to a particular work (collectively "WILEY"). By clicking "accept" in connection with completing this licensing transaction, you agree that the following terms and conditions apply to this transaction (along with the billing and payment terms and conditions established by the Copyright Clearance Center Inc., ("CCC's Billing and Payment terms and conditions"), at the time that

you opened your RightsLink account (these are available at any time at http://myaccount.copyright.com).

Terms and Conditions

- The materials you have requested permission to reproduce or reuse (the "Wiley Materials") are protected by copyright.

- You are hereby granted a personal, non-exclusive, non-sub licensable (on a stand-alone basis), non-transferable, worldwide, limited license to reproduce the Wiley Materials for the purpose specified in the licensing process. This license, **and any CONTENT (PDF or image file) purchased as part of your order,** is for a one-time use only and limited to any maximum distribution number specified in the license. The first instance of republication or reuse granted by this license must be completed within two years of the date of the grant of this license (although copies prepared before the end date may be distributed thereafter). The Wiley Materials shall not be used in any other manner or for any other purpose, beyond what is granted in the license. Permission is granted subject to an appropriate acknowledgement given to the author, title of the material/book/journal and the publisher. You shall also duplicate the copyright notice that appears in the Wiley publication in your use of the Wiley Material. Permission is also granted on the understanding that nowhere in the text is a previously published source acknowledged for all or part of this Wiley Material. Any third party content is expressly excluded from this permission.

- With respect to the Wiley Materials, all rights are reserved. Except as expressly granted by the terms of the license, no part of the Wiley Materials may be copied, modified, adapted (except for minor reformatting required by the new Publication), translated, reproduced, transferred or distributed, in any form or by any means, and no derivative works may be made based on the Wiley Materials without the prior permission of the respective copyright owner.**For STM Signatory Publishers clearing permission under the terms of the STM Permissions Guidelines only, the terms of the license are extended to include subsequent editions and for editions in other languages, provided such editions are for the work as a whole in situ and does not involve the separate exploitation of the permitted figures or extracts,** You may not alter, remove or suppress in any manner any copyright, trademark or other notices displayed by the Wiley Materials. You may not license, rent, sell, loan, lease, pledge, offer as security, transfer or assign the Wiley Materials on a stand-alone basis, or any of the rights granted to you hereunder to any other person.

- The Wiley Materials and all of the intellectual property rights therein shall at all times remain the exclusive property of John Wiley & Sons Inc, the Wiley Companies, or their respective licensors, and your interest therein is only that of having possession of and the right to reproduce the Wiley Materials pursuant to Section 2 herein during the continuance of this Agreement. You agree that you own no right, title or interest in or to the Wiley Materials or any of the intellectual property rights therein. You shall have no rights hereunder other than the license as provided for above in Section 2. No right, license or interest to any trademark, trade name, service mark or other branding ("Marks") of WILEY or its licensors is granted hereunder, and you agree that you shall not assert any such right, license or interest with respect thereto

- NEITHER WILEY NOR ITS LICENSORS MAKES ANY WARRANTY OR REPRESENTATION OF ANY KIND TO YOU OR ANY THIRD PARTY, EXPRESS, IMPLIED OR STATUTORY, WITH RESPECT TO THE MATERIALS OR THE ACCURACY OF ANY INFORMATION CONTAINED IN THE

MATERIALS, INCLUDING, WITHOUT LIMITATION, ANY IMPLIED WARRANTY OF MERCHANTABILITY, ACCURACY, SATISFACTORY QUALITY, FITNESS FOR A PARTICULAR PURPOSE, USABILITY, INTEGRATION OR NON-INFRINGEMENT AND ALL SUCH WARRANTIES ARE HEREBY EXCLUDED BY WILEY AND ITS LICENSORS AND WAIVED BY YOU.

- WILEY shall have the right to terminate this Agreement immediately upon breach of this Agreement by you.

- You shall indemnify, defend and hold harmless WILEY, its Licensors and their respective directors, officers, agents and employees, from and against any actual or threatened claims, demands, causes of action or proceedings arising from any breach of this Agreement by you.

- IN NO EVENT SHALL WILEY OR ITS LICENSORS BE LIABLE TO YOU OR ANY OTHER PARTY OR ANY OTHER PERSON OR ENTITY FOR ANY SPECIAL, CONSEQUENTIAL, INCIDENTAL, INDIRECT, EXEMPLARY OR PUNITIVE DAMAGES, HOWEVER CAUSED, ARISING OUT OF OR IN CONNECTION WITH THE DOWNLOADING, PROVISIONING, VIEWING OR USE OF THE MATERIALS REGARDLESS OF THE FORM OF ACTION, WHETHER FOR BREACH OF CONTRACT, BREACH OF WARRANTY, TORT, NEGLIGENCE, INFRINGEMENT OR OTHERWISE (INCLUDING, WITHOUT LIMITATION, DAMAGES BASED ON LOSS OF PROFITS, DATA, FILES, USE, BUSINESS OPPORTUNITY OR CLAIMS OF THIRD PARTIES), AND WHETHER OR NOT THE PARTY HAS BEEN ADVISED OF THE POSSIBILITY OF SUCH DAMAGES. THIS LIMITATION SHALL APPLY NOTWITHSTANDING ANY FAILURE OF ESSENTIAL PURPOSE OF ANY LIMITED REMEDY PROVIDED HEREIN.

- Should any provision of this Agreement be held by a court of competent jurisdiction to be illegal, invalid, or unenforceable, that provision shall be deemed amended to achieve as nearly as possible the same economic effect as the original provision, and the legality, validity and enforceability of the remaining provisions of this Agreement shall not be affected or impaired thereby.

- The failure of either party to enforce any term or condition of this Agreement shall not constitute a waiver of either party's right to enforce each and every term and condition of this Agreement. No breach under this agreement shall be deemed waived or excused by either party unless such waiver or consent is in writing signed by the party granting such waiver or consent. The waiver by or consent of a party to a breach of any provision of this Agreement shall not operate or be construed as a waiver of or consent to any other or subsequent breach by such other party.

- This Agreement may not be assigned (including by operation of law or otherwise) by you without WILEY's prior written consent.

- Any fee required for this permission shall be non-refundable after thirty (30) days from receipt by the CCC.

- These terms and conditions together with CCC's Billing and Payment terms and conditions (which are incorporated herein) form the entire agreement between you and WILEY concerning this licensing transaction and (in the absence of fraud) supersedes all prior agreements and representations of the parties, oral or written. This Agreement

may not be amended except in writing signed by both parties. This Agreement shall be binding upon and inure to the benefit of the parties' successors, legal representatives, and authorized assigns.

- In the event of any conflict between your obligations established by these terms and conditions and those established by CCC's Billing and Payment terms and conditions, these terms and conditions shall prevail.

- WILEY expressly reserves all rights not specifically granted in the combination of (i) the license details provided by you and accepted in the course of this licensing transaction, (ii) these terms and conditions and (iii) CCC's Billing and Payment terms and conditions.

- This Agreement will be void if the Type of Use, Format, Circulation, or Requestor Type was misrepresented during the licensing process.

- This Agreement shall be governed by and construed in accordance with the laws of the State of New York, USA, without regards to such state's conflict of law rules. Any legal action, suit or proceeding arising out of or relating to these Terms and Conditions or the breach thereof shall be instituted in a court of competent jurisdiction in New York County in the State of New York in the United States of America and each party hereby consents and submits to the personal jurisdiction of such court, waives any objection to venue in such court and consents to service of process by registered or certified mail, return receipt requested, at the last known address of such party.

WILEY OPEN ACCESS TERMS AND CONDITIONS

Wiley Publishes Open Access Articles in fully Open Access Journals and in Subscription journals offering Online Open. Although most of the fully Open Access journals publish open access articles under the terms of the Creative Commons Attribution (CC BY) License only, the subscription journals and a few of the Open Access Journals offer a choice of Creative Commons Licenses. The license type is clearly identified on the article.

The Creative Commons Attribution License

The Creative Commons Attribution License (CC-BY) allows users to copy, distribute and transmit an article, adapt the article and make commercial use of the article. The CC-BY license permits commercial and non-

Creative Commons Attribution Non-Commercial License

The Creative Commons Attribution Non-Commercial (CC-BY-NC)License permits use, distribution and reproduction in any medium, provided the original work is properly cited and is not used for commercial purposes.(see below)

Creative Commons Attribution-Non-Commercial-NoDerivs License

The Creative Commons Attribution Non-Commercial-NoDerivs License (CC-BY-NC-ND) permits use, distribution and reproduction in any medium, provided the original work is properly cited, is not used for commercial purposes and no modifications or adaptations are made. (see below)

Use by commercial "for-profit" organizations

Use of Wiley Open Access articles for commercial, promotional, or marketing purposes requires further explicit permission from Wiley and will be subject to a fee.

Further details can be found on Wiley Online Library

http://olabout.wiley.com/WileyCDA/Section/id-410895.html

Other Terms and Conditions:

v1.10 Last updated September 2015

Questions? customercare@copyright.com or +1-855-239-3415 (toll free in the US) or +1-978-646-2777.

Chapter 4

Thermodynamic Assessment of the Na_2O-Al_2O_3-SiO_2-B_2O_3 Pseudo-Binary and -Ternary Systems[2]

4.1. Abstract

Thermodynamic assessments of the pseudo-binary and -ternary systems formed by B_2O_3 with Na_2O, Al_2O_3, and SiO_2 were conducted according to the CALPHAD methodology. The compound energy formalism and two-sublattice partially ionic liquid models were used to thermodynamically represent the solid solutions malinkoite and mullite and the liquid phase of each system, respectively. A comprehensive literature review of available phase equilibria and thermodynamic experimental data as well as a detailed discussion of the modeling approaches implemented to optimize each system is provided. Assessment results are then presented and discussed, and the future path forward is outlined. The addition of B_2O_3 to the Na_2O-Al_2O_3-SiO_2 system contributes to the development of a thermodynamic database that will ultimately predict the equilibrium behavior of nepheline formation in high-level radioactive waste glass.

---

[2] Utlak S. A., Besmann T. M., Thermodynamic Assessment of the Na_2O-Al_2O_3-SiO_2-B_2O_3 Pseudo-Binary and -Ternary Systems. *J. Chem. Thermodyn.* 2019;130:251-268. Reprinted here with permission of publisher.

4.2. Introduction

The thermodynamic assessments conducted in this work are a continuation of the development of a high-level radioactive waste (HLW) glass thermodynamic database with the ultimate goal of characterizing the equilibrium behavior of nepheline and related phases in a multicomponent oxide HLW glass system. Construction of this database was initiated with the publication of Utlak & Besmann[148] that presented a successful thermodynamic assessment of the nepheline-forming Na_2O-Al_2O_3-SiO_2 pseudo-ternary system. As summarized by Lambotte & Chartrand,[76] nepheline refers to the sodium endmember of the mineral nepheline, $NaAlSiO_4$, which is a tectosilicate mineral from the feldspathoid family.[149] A derivative of SiO_2(high-tridymite),[150] the stable nepheline crystalline structure has a $P6_3$ space group and consists of 8 $NaAlSiO_4$ per unit cell.[76, 151] As has been noted,[1] HLW glass with high mass fractions of Na_2O and Al_2O_3 can precipitate nepheline, which acts to remove the glass-former SiO_2 and glass-modifier Al_2O_3 from the host matrix consequently causing severe deterioration of glass durability. An accurate HLW glass thermodynamic database will be capable of predicting the equilibrium nepheline formation compositional region for HLW glass and thus will enable facilities such as the Hanford Tank Waste Treatment and Immobilization Plant to target HLW glass compositions that both optimize waste loading and avoid nepheline formation.

According to studies,[1, 4, 5, 8, 14-25] Li_2O, K_2O, Fe_2O_3, B_2O_3, CaO, and MgO are HLW glass oxides that can go into solution and thus influence the precipitation of nepheline. For instance, studies conducted by Li et al.[8, 24] experimentally observed that the influence of glass oxide components on increasing nepheline precipitation could be ranked as Al_2O_3 > Na_2O > Li_2O ≈ K_2O ≈ Fe_2O_3 > B_2O_3 > CaO > SiO_2 and that glass liquidus temperatures

were increased by oxides in the order of Al_2O_3 > Na_2O > K_2O > CaO and decreased in the order of B_2O_3 > SiO_2 > Li_2O. Fe_2O_3 was determined to have minimal effect on glass liquidus temperatures.[24] Vienna et al.[47] conducted a literature review of available canister-centerline cooled HLW glass compositional data and reported the oxide compositional range of 657 HLW glass samples fabricated for experimental analysis. When neglecting five extreme glass compositions, the maximum B_2O_3 and Al_2O_3 mole fractions were approximately equal at of 9.38% and 9.39%, respectively, while the other previously listed nepheline solutes were 8 mol% or less. In progressing the thermochemical database, it was thus seen that boron plays an important role warranting attention in the next phase of the effort with the addition of B_2O_3 to the assessed Na_2O-Al_2O_3-SiO_2 pseudo-ternary system.[148] Thus, assessments of the pseudo-binary and -ternary systems formed from B_2O_3 with Na_2O, Al_2O_3, and SiO_2 were addressed.

Thermodynamic assessments of the Na_2O-B_2O_3, B_2O_3-Al_2O_3, B_2O_3-SiO_2, Na_2O-B_2O_3-SiO_2, Na_2O-B_2O_3-Al_2O_3, and Al_2O_3-B_2O_3-SiO_2 systems were conducted according to the calculation of phase diagrams (CALPHAD) methodology[26] using the two-sublattice partially ionic liquid (TSPIL) model[42, 152] and compound energy formalism (CEF)[12, 41, 153-156] to characterize the equilibrium behavior of the solid solutions and liquid phase, respectively. Model optimizations were conducted utilizing the OptiSage module of the FactSage software.

4.3. Literature review of experimental data

4.3.1. Na_2O-B_2O_3 pseudo-binary system

A reassessment of the Na_2O-B_2O_3 system was conducted to simplify the TSPIL model used in previous assessments[157-162] by excluding the $B_4O_7^{-2}$ species as discussed in

Section 4.4.4. Wang et al.[157] performed a comprehensive review of the phase equilibria and thermodynamic data as part of an assessment of the Na_2O-B_2O_3 system. Thus, this effort need not be repeated here but rather a summary is provided. Experimental efforts by Morey & Merwin,[163] Milman & Bouaziz,[164] and Liang et al.[165] indicated the formation of the following intermediate stoichiometric compounds for the Na_2O-B_2O_3 system: $NaBO_2$, NaB_3O_5, NaB_5O_8, NaB_9O_{14}, $Na_2B_4O_7$, $Na_2B_8O_{13}$, Na_3BO_3, and $Na_4B_2O_5$. The two polymorphs of $NaBO_2$ and three polymorphs of NaB_5O_8 as well as NaB_9O_{14} are based on Milman & Bouaziz.[164] Liquidus data from these experimental studies were also included in this assessment.

Optimization of values for the phases in the Na_2O-B_2O_3 system utilized enthalpy of mixing data reported by Shartsis & Capps[166] at 298 K, Navrotsky et al.[167] at 974 K, and Fan[137] at 1299 K as well as the activity of B_2O_3 in liquid measured by Itoh et al.[168, 169] at 1137 K and 1123 K. The measured activity of Na_2O in liquid reported by Park & Min[170] at 1373 K differed from that of Itoh et al.[169] with the latter's data showing consistency with multiple other studies.[168, 171, 172] As such, the Itoh et al.[169] Na_2O in liquid activity data was adopted in this assessment. Relative partial molar free energies of Na_2O in liquid measured by Itoh et al.[168, 169] at 1137 K and 1123 K, Stegmaier & Dietzel[171] at 1123 K, and Sato et al.[172] at 1123 K all referred to 0.05 Na_2O + 0.95 B_2O_3 were the final data sets used to assess the Na_2O-B_2O_3 system.

4.3.2. B_2O_3-Al_2O_3 pseudo-binary system

The B_2O_3-Al_2O_3 system has previously been assessed by Decterov et al.[173] using the Modified Quasichemical Model (MQM)[174, 175] and, as such, will be used as the basis for the reassessment of the system using the TSPIL model. The same intermediate

stoichiometric compounds, $Al_{18}B_4O_{33}$ and $Al_4B_2O_9$, chosen by Decterov et al.[173] based on Baumann & Moore,[176] Scholze,[177] Kim & Hummel,[178] Gielisse,[179] Gielisse & Foster,[180] Rymon-Lipinski,[181] and Mazza et al.[182] were included in this assessment. The melting temperatures selected by Decterov et al.[173] for $Al_{18}B_4O_{33}$ and $Al_4B_2O_9$ of 2223 K[176] and 1463 K,[181] respectively, were retained in the current assessment.

Liquidus measurements reported by Gielisse & Foster[180] were used to optimize the TSPIL model while the data reported by Narushima et al. as cited by Decterov et al.[173] was neglected as this data is listed as a private communication and thus could not be adequately reviewed.

4.3.3. B2O3-SiO2 pseudo-binary system

A reassessment of the B_2O_3-SiO_2 system was conducted with the TSPIL model as the previous assessment completed by Decterov et al.[173] used the MQM. Decterov et al.[173] optimized the B_2O_3-SiO_2 system with liquidus data from Rockett & Foster,[183] Pichavant,[184] and Charles & Wagstaff[185] as well as enthalpy of mixing and activity data. As explained in Section 4.4.4.1, the B_2O_3-SiO_2 system could not be isolated for assessment using the currently implemented TSPIL model. However, the B_2O_3-SiO_2 phase equilibria data was included as part of the Na_2O-B_2O_3-SiO_2 and Al_2O_3-B_2O_3-SiO_2 assessments. B_2O_3-SiO_2 thermodynamic data was neglected as this data could not be optimized to with ternary interaction parameters that included either a Na_2O or Al_2O_3 species as discussed in Section 4.4.4.1.

4.3.4. Na_2O-B_2O_3-SiO_2 pseudo-ternary system

Liquidus and invariant point measurements reported by Morey[186] for the Na_2O-B_2O_3-SiO_2 system served as the main data source for optimization of phase equilibria

behavior. After synthesizing samples across the Na_2O-B_2O_3-SiO_2 compositional space, Morey[186] heated, quenched, crushed, and then examined the powdered samples with a petrographic microscope. Results of this analysis indicated phase relations and liquidus/invariant point temperatures for the pseudo-ternary system. Phase equilibria data generated by Ghanbari-Ahari & Cameron[187] as well as Rockett & Foster[188] for the isopleths $Na_2B_4O_7$-SiO_2 and $Na_2B_8O_{13}$-SiO_2, respectively, were also used in assessing the Na_2O-B_2O_3-SiO_2 system.

Morey[186] and Ghanbari-Ahari & Cameron[187] reported synthesizing the pseudo-ternary compound malinkoite, $Na_2O.B_2O_3.2SiO_2$ or $NaBSiO_4$, with acknowledged difficulty, but neither could determine with confidence the compositional formation region of the phase. Morey[186] reported four liquidus composition measurements with malinkoite as a primary phase while Ghanbari-Ahari & Cameron[187] synthesized malinkoite at one of the compositions reported by Morey[186] reaffirming the melting temperature of the phase at that composition. Thus, the malinkoite CEF model developed in this work utilizes the four liquidus measurements with malinkoite as the primary phase reported by Morey.[186]

Thermodynamic data available for use in the optimization were partial molar free energies of Na_2O in the melt at 1200 K referred to $Na_2O + 2B_2O_3$ reported by Asai & Yokokawa[189] as well as at 1223 K referred to pure Na_2O as measured by Konakov et al.[190] The partial molar free energies of Na_2O in liquid at 1300 K referred to $Na_2O + 2B_2O_3$ reported by Kozhina & Shultz[191] have been neglected due to a labeling conflict in their Fig. 2.c. The figure caption indicates that the mole fraction of B_2O_3 is held constant at 40 and 60% yet the figure abscissa shows a variable B_2O_3 mole fraction. Interpretation of the figure intention is not necessary as data from Asai & Yokokawa[189] is superimposed

showing good agreement between data sets and, consequently, it is only necessary to include data from Asai & Yokokawa.[189]

4.3.5. Na_2O-B_2O_3-Al_2O_3 pseudo-ternary system

Binev et al.[192] determined liquidus temperatures and phase crystallization regions for the Na_2O-B_2O_3-Al_2O_3 system in the composition space 20 – 55 mol% Na_2O, 0 – 35 mol% Al_2O_3, and 25 – 55 mol% B_2O_3. They also identified a $Na_2Al_2B_2O_7$ phase while failing to detect the double borate $NaAlB_2O_5$ phase described by Abdullaev et al.[193] $Na_2Al_2B_2O_7$ was also observed by Peshev et al.,[194] He et al.,[195-197] Perras & Bryce,[198] Meng et al.,[199] and Salman et al.[200] and, thus, has been included in the optimization of the Na_2O-B_2O_3-Al_2O_3 system. Additional liquidus measurements conducted by Wakasugi et al.[201, 202] as well as $NaBO_2$-Al_2O_3 isopleth data reported by Peshev et al.[194] that included a 1119 K $NaBO_2$-$Na_2Al_2B_2O_7$ eutectic and 1259 K $Na_2Al_2B_2O_7$-Al_2O_3 peritectic point were considered. The 1259 K $Na_2Al_2B_2O_7$-Al_2O_3 peritectic is equivalent to the 1259 K melting temperature of $Na_2Al_2B_2O_7$ reported by He et al.[195] and consequently was adopted as the $Na_2Al_2B_2O_7$ melting point.

4.3.6. Al_2O_3-B_2O_3-SiO_2 pseudo-ternary system

The Al_2O_3-B_2O_3-SiO_2 system was reassessed with the TSPIL model as the previous assessment conducted by Swamy et al.[88] utilized the MQM. A comprehensive literature review of available phase equilibria data for the pseudo-ternary Al_2O_3-B_2O_3-SiO_2 system was documented by Swamy et al.,[88] which discussed liquidus data measured by Dietzel & Scholze[203] as well as Gielisse[179] in the high SiO_2-low Al_2O_3 and high B_2O_3-low SiO_2 composition regions, respectively. Additionally, Gielisse,[179] Mazza et al.,[182] and multiple other studies as cited by Swamy et al.[88] have concluded that B_2O_3 is soluble in mullite. A

mullite-$Al_{18}B_4O_{33}$ phase boundary was indicated by Gielisse to exist at ~15 wt% SiO_2 over a range of 30 – 100 wt% B_2O_3, which was adopted as the phase boundary location by Swamy et al.[88] as well as in this assessment.

4.4. Thermodynamic modeling and optimization

The following sections summarize the CEF and TSPIL modeling approaches as well as discuss modeling and optimization of the stoichiometric compounds, solid solutions, and liquid phase in the assessed pseudo-binary and -ternary systems of B_2O_3 with Na_2O, Al_2O_3, and SiO_2.

4.4.1. CEF and TSPIL models

The CEF and TSPIL models were implemented through the FactSage software to optimize the solid solutions and liquid phase. Utlak & Besmann[148] provided a detailed review of the models, and readers may also consult the primary source publications for the CEF[12, 41, 153-156] and TSPIL[42, 152] models. As such, only a brief summary of the modeling approaches will herein be given.

The CEF is a sublattice-based model that can account for the non-stoichiometry of a substitutional solution based on lattice site occupancies, which can include vacancies. A CEF three sublattice structure could have the form:

$(A,B)_k(D,E,F)_l(G)_m$

where *A*, *B*, *D*, *E*, and *G* represent solid solution constituents, and the subscripts k, l, and m the sublattice stoichiometric coefficients. Definition of the Gibbs energy function can be found in Hillert.[41]

As stated in Utlak & Besmann,[148] the TSPIL model is based on the concept that in ionic phases each atom bears a charge and thus are surrounded by unlike atoms resulting

in chemical ordering. This ordering can be treated as two sublattices, one containing only cations and the other anions, vacancies, and neutral species:

$$\left(C_i^{+\nu_i}\right)_P\left(A_j^{-\nu_j}, Va, B_k^0\right)_Q$$

where *C*, *A*, *Va*, and *B* denote cations, anions, vacancies, and neutral species, respectively, while the indices i, j, and k represent specific sublattice constituents. The superscripts $+\nu_i$ and $-\nu_j$ represent the charge of the i^{th} or j^{th} cation or anion, respectively, while 0 indicates a neutral species. Electroneutrality is maintained by allowing the stoichiometric coefficients (P and Q) to vary as a function of site fractions. The TSPIL model Gibbs energy function is discussed in Utlak & Besmann as well.[148]

Of final note, both CEF and TSPIL approaches incorporate excess Gibbs energy terms that contain interaction parameters often expressed as a Redlich-Kister (RK) power series expansion in terms of site fractions. As an example, a binary interaction between the A and B species on the first sublattice of a three sublattice CEF model can be described by

$$L_{A,B:D:G} = \sum_{k=0}^{n} {}^{k}L_{A,B:D:G}\left(y_A - y_B\right)^k \tag{4.1}$$

where *y* represents the site fraction of the subscripted sublattice constituent and k the order of the expansion. The *L* term on the right-hand side of eq. (4.1) can be expressed as a polynomial that varies as a function of temperature with the form:

$${}^{k}L_{A,B:D:G} = A + B{\cdot}T + C{\cdot}T\ln(T) + D{\cdot}T^2 + E{\cdot}T^3 + F{\cdot}T^{-1} \tag{4.2}$$

where *T* is the temperature in kelvin and the variables *A*, *B*, *C*, *D*, *E*, and *F* are coefficients that can be empirically determined by optimizing the model Gibbs energy function to thermochemical or phase equilibria data. In practice, only the *A* and *B* coefficients of eq.

(4.2) are generally included in an assessment unless experimental data can justify the assignment of an empirically derived value to an additional coefficient.[26]

4.4.2. Stoichiometric compounds

44 stoichiometric compounds were required to assess the Na_2O-Al_2O_3-SiO_2-B_2O_3 pseudo-binary and -ternary systems (Table 4.1). The Gibbs energy functions assigned to 29 of the 44 compounds were adopted from referenced sources (Table 4.1) whereas the remaining 15 were to some extent optimized in this work. Compound thermodynamic values sourced from Bale et al.[43] were obtained from the FTOxid FactSage[43] database.

4.4.2.1. Optimization of select stoichiometric compounds

The standard formation enthalpy and standard entropy of $NaBO_2(\beta)$, $NaB_5O_8(\beta)$, $NaB_5O_8(\gamma)$, $NaB_9O_{14}(\beta)$, and $NaB_9O_{14}(\gamma)$ were derived in this work as these polymorphs were not reported (Table 4.1). Values were obtained by optimizing the standard formation enthalpy and standard entropy of these compounds to the phase equilibria reported by Liang et al.[165] Additionally, the standard enthalpy of formation of $NaBO_2(\alpha)$, $NaB_3O_5(s)$, $NaB_5O_8(\alpha)$, $NaB_9O_{14}(\alpha)$, $Na_2B_4O_7(s)$, $Na_2B_8O_{13}(s)$, and $Na_3BO_3(s)$ as well as $Al_{18}B_4O_{33}$ and $Al_4B_2O_9$ that formed in the Al_2O_3-B_2O_3 pseudo-binary system were minimally adjusted from the values contained in the FactSage FTOxid database to best fit melting temperatures.

The final compound included in the Na_2O-Al_2O_3-SiO_2-B_2O_3 assessed database was the $Na_2Al_2B_2O_7(s)$ phase that has been observed. It was necessary to derive all terms of the Gibbs energy function for the phase as it had not previously been considered. Thus, the heat capacity as a function of temperature was approximated by the Neumann-Kopp rule[204] where the heat capacities of $Na_2O(\alpha)$, $B_2O_3(s)$, and Al_2O_3(corundum) were summed. The

$Na_2Al_2B_2O_7$(s) standard entropy was initially estimated via Latimer's method[205] with updated entropic contribution values of species as summarized by Spencer.[64] The standard formation enthalpy and standard entropy were then optimized using phase equilibria reported by Binev et al.,[192] Peshev et al.,[194] and He et al.[195] with the resulting values listed in Table 4.1.

4.4.3. Solid solutions

The three solid solutions malinkoite, β-Al_2O_3, and mullite were incorporated into the Na_2O-B_2O_3-SiO_2, Na_2O-B_2O_3-Al_2O_3, and Al_2O_3-B_2O_3-SiO_2 assessments, respectively, with malinkoite and mullite requiring optimization as part of conducting the assessments.

4.4.3.1. Malinkoite

The malinkoite phase was modeled using the same approach as applied to the nepheline phase that was optimized as part of the Na_2O-Al_2O_3-SiO_2 pseudo-ternary assessment conducted by Utlak & Besmann.[148] Schneider et al.[206] and McCloy et al.[5] refer to the nepheline structure as a stuffed tridymite derivative composed of six-membered stacked ring layers, which form channels perpendicular to the layers that are filled with various cations. Layers adjacent to these rings along the c-axis create an eclipsed or *cis* structure in the case of tridymite and nepheline, whereas adjacent layers that are rotated 180° and shifted laterally generate a staggered or *trans* structure such as kalsilite and malinkoite.[5] Thus, as the type and quantity of crystallographic lattice sites does not differ between malinkoite and nepheline, the three sublattice CEF model implemented by Utlak & Besmann[148] to thermodynamically characterize nepheline could also be applied to describe malinkoite. As such, the nepheline three sublattice CEF model implemented by Utlak & Besmann[148] was modified by replacing the $(Na - Al)^{+4}$ species on the first

sublattice with a $(Na - B)^{+4}$ species, thus representing the substitution of an Al^{+3} cation with a B^{+3} cation:

$$((Na - B)^{+4},(Va - Si)^{+4})_8^{\alpha}\left[Si^{+4}\right]_8\left\{O^{-2}\right\}_{32}$$

4.4.3.1.1. Optimization of the malinkoite CEF model

An initial Gibbs energy function of the malinkoite endmember, $Na_8B_8Si_8O_{32}$, was generated by proportionally summing the values for $Na_2O(\alpha)$, $B_2O_3(s)$, and SiO_2(high-cristobalite) (Table 4.1) . The enthalpy of formation of the malinkoite endmember was then derived by optimizing the malinkoite CEF model with liquidus data reported by Morey[186] such that the malinkoite phase formation boundary in the pseudo-ternary Na_2O-B_2O_3-SiO_2 was in agreement with the liquidus measurements as addressed in Section 4.5.4. Eq. (3) defines the CEF model molar Gibbs energy expression used to characterize the malinkoite equilibrium behavior with parameter values listed in Table 4.2, where R is the ideal gas law constant.

$$G_{\mathrm{m}}^{\mathrm{malinkoite}} = y_{\mathrm{NaB}^{+4}}^{\alpha} \,{}^{\mathrm{o}}G_{\mathrm{Na_8B_8Si_8O_{32}}} + y_{\mathrm{VaSi}^{+4}}^{\alpha} \,{}^{\mathrm{o}}G_{\mathrm{Si_{16}O_{32}}} + 8RT\left(y_{\mathrm{NaB}^{+4}}^{\alpha}\ln y_{\mathrm{NaB}^{+4}}^{\alpha} + y_{\mathrm{VaSi}^{+4}}^{\alpha}\ln y_{\mathrm{VaSi}^{+4}}^{\alpha}\right) \quad (4.3)$$

4.4.3.2. β-Al_2O_3

The CEF β-Al_2O_3 model of Utlak & Besmann[148] was retained in this work (Table 4.2). This three sublattice model was not modified to incorporate B_2O_3 on the second sublattice to substitute with Al_2O_3 as it is known that the two hypothetical endmembers that would have resulted from this sublattice structure, $Na_2B_2O_{34}$ and $Na_4B_2O_{35}$, do not form at equilibrium in the Na_2O-B_2O_3 pseudo-binary system.[163-165]

4.4.3.3. Mullite

The mullite CEF model of Utlak & Besmann[148] was used as the initial model in this work. Similar to the approach applied by Swamy et al.,[88] a B^{+3} species was added to the second sublattice to substitute for Al^{+3}:

$$\left(Al^{+3}\right)_2\left[Al^{+3},B^{+3}Si^{+4}\right]_1^{\alpha}\left\{O^{-2},Va\right\}_5^{\beta}$$

yielding the two new endmembers Al_2BO_5 and Al_2B.

4.4.3.3.1. Optimization of the mullite CEF model

The mullite CEF model was optimized along with the oxide liquid TSPIL model as part of the Al_2O_3-B_2O_3-SiO_2 pseudo-ternary system assessment. An excess enthalpy and entropy value in the form of one zeroth-order RK parameter interacting the B^{+3} and Si^{+4} species on the second sublattice with Al^{+3} and O^{-2} on the first and third sublattices, respectively, were introduced to obtain a mullite-$Al_{18}B_4O_{33}$ phase boundary at 15 wt% SiO_2 over the range of approximately 30 – 100 wt% B_2O_3. The resulting molar Gibbs energy relation for the mullite phase is expressed in eq. (4.4) with values listed in Table 4.2:

$$\begin{aligned} G_{\mathrm{m}}^{\mathrm{mullite}} = {} & y_{\mathrm{Al}^{+3}}^{\alpha} y_{\mathrm{O}^{-2}}^{\beta} \, {}^{\mathrm{o}}G_{\mathrm{Al}_3\mathrm{O}_5^{-1}} \\ & + y_{\mathrm{Al}^{+3}}^{\alpha} y_{\mathrm{Va}}^{\beta} \, {}^{\mathrm{o}}G_{\mathrm{Al}_3^{+9}} + y_{\mathrm{B}^{+3}}^{\alpha} y_{\mathrm{O}^{-2}}^{\beta} \, {}^{\mathrm{o}}G_{\mathrm{Al}_2\mathrm{BO}_5} + y_{\mathrm{B}^{+3}}^{\alpha} y_{\mathrm{Va}}^{\beta} \, {}^{\mathrm{o}}G_{\mathrm{Al}_2\mathrm{B}^{+9}} \\ & + y_{\mathrm{Si}^{+4}}^{\alpha} y_{\mathrm{O}^{-2}}^{\beta} \, {}^{\mathrm{o}}G_{\mathrm{Al}_2\mathrm{SiO}_5} + y_{\mathrm{Si}^{+4}}^{\alpha} y_{\mathrm{Va}}^{\beta} \, {}^{\mathrm{o}}G_{\mathrm{Al}_2\mathrm{Si}^{+10}} \\ & + RT\left(y_{\mathrm{Al}^{+3}}^{\alpha} \ln y_{\mathrm{Al}^{+3}}^{\alpha} + y_{\mathrm{B}^{+3}}^{\alpha} \ln y_{\mathrm{B}^{+3}}^{\alpha} + y_{\mathrm{Si}^{+4}}^{\alpha} \ln y_{\mathrm{Si}^{+4}}^{\alpha} + 5 y_{\mathrm{O}^{-2}}^{\beta} \ln y_{\mathrm{O}^{-2}}^{\beta}\right. \\ & \left. + 5 y_{\mathrm{Va}}^{\beta} \ln y_{\mathrm{Va}}^{\beta}\right) + y_{\mathrm{Al}^{+3}}^{\alpha} y_{\mathrm{Si}^{+4}}^{\alpha} y_{\mathrm{O}^{-2}}^{\beta} \, {}^{0}L_{\mathrm{Al}^{+3}:\mathrm{Al}^{+3},\mathrm{Si}^{+4}:\mathrm{O}^{-2}} \\ & + y_{\mathrm{Al}^{+3}}^{\alpha} y_{\mathrm{Si}^{+4}}^{\alpha} y_{\mathrm{Va}}^{\beta} \, {}^{0}L_{\mathrm{Al}^{+3}:\mathrm{Al}^{+3},\mathrm{Si}^{+4}:\mathrm{Va}} + y_{\mathrm{B}^{+3}}^{\alpha} y_{\mathrm{Si}^{+4}}^{\alpha} y_{\mathrm{O}^{-2}}^{\beta} \, {}^{0}L_{\mathrm{Al}^{+3}:\mathrm{B}^{+3},\mathrm{Si}^{+4}:\mathrm{Va}} \end{aligned} \tag{4.4}$$

4.4.4. Oxide liquid

The TSPIL model implemented in this work to assess the pseudo-binary and -ternary systems of B_2O_3 with Na_2O, Al_2O_3, and SiO_2 follows that of Utlak & Besmann:[148]

$$\left(Al^{+3},Na^{+1}\right)_P\left(AlO_2^{-1},O^{-2},SiO_4^{-4},SiO_2^{0}\right)_Q$$

Thus, it was only required to introduce B_2O_3 species into the liquid sublattice model. Towards this effort, the approach initially developed by Yu et al.[160] to assess the Li_2O-B_2O_3 system and then subsequently applied by Yu et al.[158, 159, 207] as well as Wang et al.[157] to assess the BaO-B_2O_3,[159] Li_2O-BaO-B_2O_3,[190] CaO-B_2O_3,[158] and Na_2O-B_2O_3[157] systems was generally adopted in this work, which was to add the BO^{-3}, $B_4O_7^{-2}$, and $B_3O_{4.5}$ species to the second sublattice of the TSPIL model. A detailed explanation of the basis for this modeling approach is presented in Yu et al.[160] In brief, glassy B_2O_3 consists of BO_3 groups, hence the inclusion of the BO_3^{-3} species, and vitreous B_2O_3 has been observed to form randomly oriented boroxal rings with a stoichiometry of $B_3O_{4.5}$, which is captured by the inclusion of the neutral $B_3O_{4.5}$ species.[160] Yu et al.[160] also discussed the basis for the inclusion of the $B_4O_7^{-2}$ species but ultimately concluded that the reasoning was not well supported and the selection of this species was arbitrary. It was determined during the optimizations conducted in this work that the $B_4O_7^{-2}$ species minimally affected the equilibrium behavior of any system containing B_2O_3 and that the same result could be obtained without including $B_4O_7^{-2}$. Hence, the TSPIL model used to assess the Na_2O-Al_2O_3-SiO_2-B_2O_3 pseudo-binary and -ternary systems was:

$$\left(Al^{+3},Na^{+1}\right)_P\left(AlO_2^{-1},O^{-2},SiO_4^{-4},BO_3^{-3},B_3O_{4.5}^{0},SiO_2^{0}\right)_Q$$

4.4.4.1. Optimization of oxide liquid TSPIL model

As listed in Table 4.3, the TSPIL model endmembers $Al_3B_3O_9$, $NaAlO_2$, Na_4SiO_4, and Na_3BO_3 as well as 54 RK parameters were optimized to the phase equilibria and thermodynamic experimental data discussed in Section 4.3 to complete assessments of the Na_2O-Al_2O_3-SiO_2-B_2O_3 pseudo-binary and -ternary systems. Endmembers and parameters for solely Na_2O, Al_2O_3, and/or SiO_2 species are from Utlak & Besmann[148] whereas those with B_2O_3 species were generated in this work. The zeroth- and first-order quaternary reciprocal parameters comprised of Al^{+3}, Na^{+1}, AlO_2^{-1}, and BO_3^{-3} were needed to suppress a nonphysical miscibility gap that tended to form along the $NaBO_2$-Al_2O_3 isopleth.

[b] Units of all ^oG and L parameters are $(J/mol)^{-1}$

As the TSPIL sublattice structure used in this work contains all B_2O_3 and SiO_2 species on the second sublattice, the model could not be optimized to the B_2O_3-SiO_2 system. However, the phase equilibria data of the B_2O_3-SiO_2 system as discussed in Section 4.3.3 was incorporated into assessments of both the Na_2O-B_2O_3-SiO_2 and Al_2O_3-B_2O_3-SiO_2 systems, which enabled B_2O_3-SiO_2 phase diagrams to be generated assuming negligible mole fractions of Na_2O and Al_2O_3. The ternary RK parameters used to assess the Na_2O-B_2O_3-SiO_2 and Al_2O_3-B_2O_3-SiO_2 systems were required to include either a Na^{+1} or Al^{+3} species along with B_2O_3 and SiO_2 species, which prevented good optimizations from being obtained to B_2O_3-SiO_2 pseudo-binary thermodynamic data. Thus, enthalpy of mixing and activity measurements for the B_2O_3-SiO_2 system were not included in the assessments that contained this pseudo-binary system. The minimal effect of neglecting this data is discussed in Section 4.5.3.

The molar Gibbs energy of the oxide liquid in the TSPIL sublattice formalism is provided by Eq. (4.5) with parameter values listed in Table 4.3.

$$
\begin{aligned}
G_{\mathrm{m}}^{\mathrm{liquid}} = {} & y_{Al^{+3}} y_{AlO_2^{-1}} {}^{o}G_{Al_4O_6} + y_{Al^{+3}} y_{O^{-2}} {}^{o}G_{Al_2O_3} + y_{Al^{+3}} y_{SiO_4^{-4}} {}^{o}G_{Al_4Si_3O_{12}} \\
& + y_{Na^{+1}} y_{AlO_2^{-1}} {}^{o}G_{NaAlO_2} + y_{Na^{+1}} y_{O^{-2}} {}^{o}G_{Na_2O} + y_{Na^{+1}} y_{SiO_4^{-4}} {}^{o}G_{Na_4SiO_4} \\
& + y_{Na^{+1}} y_{BO_3^{-3}} {}^{o}G_{Na_3BO_3} + y_{Al^{+3}} y_{BO_3^{-3}} {}^{o}G_{Al_3B_3O_9} \\
& + (3y_{Al^{+3}} + y_{Na^{+1}}) \left(y_{SiO_2^0} {}^{o}G_{SiO_2^0} + y_{B_3O_{4.5}^0} {}^{o}G_{B_3O_{4.5}} \right) \\
& + (3y_{Al^{+3}} + y_{Na^{+1}}) RT (y_{Al^{+3}} \ln y_{Al^{+3}} + y_{Na^{+1}} \ln y_{Na^{+1}}) \\
& + \left(y_{AlO_2^{-1}} + y_{O_2^{-2}} + y_{SiO_4^{-4}} + y_{BO_3^{-3}} \right) RT \left(y_{AlO_2^{-1}} \ln y_{AlO_2^{-1}} + y_{O^{-2}} \ln y_{O^{-2}} \right. \\
& \left. + y_{SiO_4^{-4}} \ln y_{SiO_4^{-4}} + y_{SiO_2^0} \ln y_{SiO_2^0} + y_{B_3O_{4.5}^0} \ln y_{B_3O_{4.5}^0} \right) \\
& + y_{Na^{+1}} y_{O^{-2}} y_{BO_3^{-3}} \left({}^{0}L_{Na^{+1}:O^{-2},BO_3^{-3}} + {}^{1}L_{Na^{+1}:O^{-2},BO_3^{-3}} \left(y_{O^{-2}} - y_{BO_3^{-3}} \right)^1 \right) \\
& + y_{Na^{+1}} y_{BO_3^{-3}} y_{B_3O_{4.5}^0} \left({}^{0}L_{Na^{+1}:BO_3^{-3},B_3O_{4.5}^0} \right. \\
& + {}^{1}L_{Na^{+1}:BO_3^{-3},B_3O_{4.5}^0} \left(y_{BO_3^{-3}} - y_{B_3O_{4.5}^0} \right)^1 \\
& \left. + {}^{2}L_{Na^{+1}:BO_3^{-3},B_3O_{4.5}^0} \left(y_{BO_3^{-3}} - y_{B_3O_{4.5}^0} \right)^2 \right) + y_{Al^{+3}} y_{AlO_2^{-1}} y_{B_3O_{4.5}^0} {}^{0}L_{Al^{+3}:AlO_2^{-1},B_3O_{4.5}^0} \\
& + y_{Na^{+1}} y_{BO_3^{-3}} y_{SiO_2^0} \left({}^{0}L_{Na^{+1}:BO_3^{-3},SiO_2^0} + {}^{1}L_{Na^{+1}:BO_3^{-3},SiO_2^0} \left(y_{BO_3^{-3}} - y_{SiO_2^0} \right)^1 \right. \\
& \left. + {}^{2}L_{Na^{+1}:BO_3^{-3},SiO_2^0} \left(y_{BO_3^{-3}} - y_{SiO_2^0} \right)^2 \right) \\
& + y_{Na^{+1}} y_{:B_3O_{4.5}^0} y_{SiO_2^0} \left({}^{0}L_{Na^{+1}:B_3O_{4.5}^0,SiO_2^0} + {}^{1}L_{Na^{+1}:B_3O_{4.5}^0,SiO_2^0} \left(y_{:B_3O_{4.5}^0} - y_{SiO_2^0} \right)^1 \right. \\
& \left. + {}^{2}L_{Na^{+1}:B_3O_{4.5}^0,SiO_2^0} \left(y_{:B_3O_{4.5}^0} - y_{SiO_2^0} \right)^2 \right) \\
& + y_{Na^{+1}} y_{SiO_4^{-4}} y_{BO_3^{-3}} \left({}^{0}L_{Na^{+1}:SiO_4^{-4},BO_3^{-3}} + {}^{1}L_{Na^{+1}:SiO_4^{-4},BO_3^{-3}} \left(y_{SiO_4^{-4}} - y_{BO_3^{-3}} \right)^1 \right) \\
& + y_{Na^{+1}} y_{SiO_4^{-4}} y_{B_3O_{4.5}^0} {}^{0}L_{Na^{+1}:SiO_4^{-4},B_3O_{4.5}^0} \\
& + y_{Na^{+1}} y_{AlO_2^{-1}} y_{BO_3^{-3}} \left({}^{0}L_{Na^{+1}:AlO_2^{-1},BO_3^{-3}} + {}^{1}L_{Na^{+1}:AlO_2^{-1},BO_3^{-3}} \left(y_{AlO_2^{-1}} - y_{BO_3^{-3}} \right)^1 \right) \\
& + y_{Na^{+1}} y_{AlO_2^{-1}} y_{B_3O_{4.5}^0} \left({}^{0}L_{Na^{+1}:AlO_2^{-1},B_3O_{4.5}^0} \right. \\
& + {}^{1}L_{Na^{+1}:AlO_2^{-1},B_3O_{4.5}^0} \left(y_{AlO_2^{-1}} - y_{B_3O_{4.5}^0} \right)^1 \\
& \left. + {}^{2}L_{Na^{+1}:AlO_2^{-1},B_3O_{4.5}^0} \left(y_{AlO_2^{-1}} - y_{B_3O_{4.5}^0} \right)^2 \right) \\
& + y_{Al^{+3}} y_{Na^{+1}} y_{AlO_2^{-1}} y_{BO_3^{-3}} \left({}^{0}L_{Al^{+3},Na^{+1}:AlO_2^{-1},BO_3^{-3}} \right. \\
& \left. + {}^{1}L_{Al^{+3},Na^{+1}:AlO_2^{-1},BO_3^{-3}} \left(y_{AlO_2^{-1}} - y_{BO_3^{-3}} \right)^1 \right) \\
& + y_{Al^{+3}} y_{BO_3^{-3}} y_{SiO_2^0} \left({}^{0}L_{Al^{+3}:BO_3^{-3},SiO_2^0} + {}^{1}L_{Al^{+3}:BO_3^{-3},SiO_2^0} \left(y_{BO_3^{-3}} - y_{SiO_2^0} \right)^1 \right) \\
& + y_{Al^{+3}} y_{B_3O_{4.5}^0} y_{SiO_2^0} {}^{0}L_{Al^{+3}:B_3O_{4.5}^0,SiO_2^0}
\end{aligned}
\tag{4.5}
$$

As remarked by footnote a of Table 4.3, Eq. (4.5) only accounts for model parameters that contain a B_2O_3 species. The complete TSPIL model equation also includes model parameters consisting of only Na_2O, Al_2O_3, and/or SiO_2 species, which were reported in Utlak Besmann [1].

4.5. Results and discussion

4.5.1. Na_2O-B_2O_3 pseudo-binary system

All liquidus, melting, and invariant point temperatures and compositions reported by Morey & Merwin,[163] Milman & Bouaziz,[164] and Liang et al.[165] as well as polymorph transition temperatures of the phases $NaBO_2$, NaB_5O_8, and NaB_9O_{14} measured by Liang et al.[165] are generally well fit by the optimized models (Fig. 4.1 and Table 4.4) where the notation X_{oxide}, e.g., $X_{B_2O_3}$, indicates the molar amount of the specified oxide.

The two eutectic points sharing the $Na_2B_4O_7$ phase were optimized as well as the selected model parameters would allow, and a compromise was made between the $Na_2B_8O_{13}$ melting point and adjacent liquidus data. The discrepancies arising from this compromise are relatively minor and did not prevent good representations of pseudo-ternary systems containing Na_2O-B_2O_3 from being obtained. As noted for Na_2O-B_2O_3 by Wang et al.,[157] melt viscosity and volatility of B_2O_3 increase as B_2O_3 content increases, which may increase the uncertainty in liquidus measurements at a high B_2O_3 mole fraction. For instance, Morey & Merwin[163] were unable to crystallize B_2O_3 from the melt at B_2O_3 >80 mol% resulting in the conclusion that the lower portion of the $Na_2B_8O_{13}$ liquidus curve may be metastable. Thus, the overprediction of liquidus temperatures in this region both in the calculated diagram of Wang et al.[157] as well in this work (Fig. 4.1) is accepted due to the uncertainty in the high B_2O_3 mole fraction liquidus measurements.

TSPIL model calculations agreed well with the enthalpy of mixing, activity of B_2O_3 in the liquid, and partial free energy of Na_2O in the liquid data (Fig. 4.2-Fig. 4.4). Thus, the good fit of model calculations to thermodynamic and phase equilibria data indicates that an accurate assessment of the Na_2O-B_2O_3 system has been obtained.

4.5.2. B_2O_3-Al_2O_3 pseudo-binary system

As discussed in Section 4.3.2, the main source of experimental data to optimize the B_2O_3-Al_2O_3 system was phase equilibria data generated by Gielisse & Foster[180] as well as a series of melting temperatures for the intermediate stoichiometric compounds $Al_{18}B_4O_{33}$ and $Al_4B_2O_9$, which were ultimately assigned as 2223 K and 1463 K, respectively. The TSPIL model and standard formation enthalpies of the $Al_{18}B_4O_{33}$ and $Al_4B_2O_9$ compounds were accurately fit to this data as evidenced by the computed phase diagram (Fig. 4.5) as well as the calculated to measured data comparison displayed in Table A.1 indicating that the B_2O_3-Al_2O_3 systems was successfully assessed.

4.5.3. B_2O_3-SiO_2 pseudo-binary system

As addressed in Section 4.4.4.1, the B_2O_3-SiO_2 pseudo-binary system could not be explicitly assessed due to the B_2O_3 and SiO_2 TSPIL model species all residing on the second sublattice. However, the B_2O_3-SiO_2 phase equilibria data as reviewed in Section 4.3.3 was incorporated into both the Na_2O-B_2O_3-SiO_2 and Al_2O_3-B_2O_3-SiO_2 assessments. A B_2O_3-SiO_2 phase diagram was then able to be generated within both pseudo-ternary systems by setting the mole fractions of Na_2O and Al_2O_3 to a minimal value, 10^{-5} mol% (Fig. 4.6 & Fig. 4.7). Upon inspection of Fig. 4.6 & Fig. 4.7, the B_2O_3-SiO_2 phase equilibria measurements, which includes metastable miscibility gap data that corresponds to the calculated miscibility gaps represented as a dotted line in each figure, are well predicted

by the TSPIL model. While an ideal optimization would have also included the available thermodynamic measurements such as activity and enthalpy of mixing data, the ternary RK parameters used in the pseudo-ternary system assessments would not optimize to this type of data in a sufficiently accurate manner likely because of the mandatory inclusion of a Na_2O or Al_2O_3 TSPIL model cation sublattice species in the parameters that did not exist in the physical data. Regardless, a good representation of the phase equilibria data indicates that the models are consistent with thermodynamic data. Thus, it is considered that obtaining an accurate optimization of the B_2O_3-SiO_2 phase equilibria data within the successful Na_2O-B_2O_3-SiO_2 and Al_2O_3-B_2O_3-SiO_2 system assessments is sufficient.

4.5.4. Na_2O-B_2O_3-SiO_2 pseudo-ternary system

Fig. 4.8 displays the Na_2O-B_2O_3-SiO_2 calculated liquidus projection generated from the optimization of this system superimposed with liquidus/phase relations and invariant point data measured by Morey[186] as well as invariant points reported by Ghanbari-Ahari & Cameron.[187] The phase relations of Morey[186] are well represented in Fig. 4.8. The agreement of the TSPIL model calculations to data measurements of Ghanbari-Ahari & Cameron will be analyzed later in this section. The NaB_3O_5 phase is reported to exist in the region approaching 100 mol% B_2O_3, however $Na_2B_8O_{13}$ + SiO_2(quartz) liquidus measurements also were reported in this region. The model was optimized so that the $Na_2B_8O_{13}$ phase approximately formed at the $Na_2B_8O_{13}$ + SiO_2(quartz) points represented by the left half-filled circles. Morey did not identify the NaB_5O_8 and NaB_9O_{14} phases and thus did not report liquidus data for these compounds. However, these phases are known to form in the Na_2O-B_2O_3[163-165] system and consequently have been included in the Na_2O-B_2O_3-SiO_2 liquidus projection diagram (Fig. 4.8).

Concerning the malinkoite phase formation region in Fig. 4.8, Morey[186] did not explicitly define the phase boundary. However, as discussed in Section 4.4.3.3.1, the four liquidus measurements with malinkoite as the primary phase reported by Morey[186] were used as the guiding data for optimization of the malinkoite CEF model. The optimization to the data reported by Morey[186] effectively accounted for the malinkoite measurement of Ghanbari-Ahari & Cameron[187] as the composition of the sample was the same as a sample fabricated by Morey[186] and the temperatures were within 10 K. Thus, an optimization was obtained that resulted in the malinkoite phase boundary region aligning with three of the four Morey[186] liquidus measurements with the fourth residing in the phase formation region (Fig. 4.8). Additionally, the TSPIL model was refined to maximize the malinkoite melting temperature while retaining a reasonable phase region. The result is that the calculated liquidus temperatures are within 36 – 46 K of the four malinkoite liquidus temperatures reported by Morey[186] (Table 4.5). Additional increases in malinkoite region melting temperatures resulted in an expanded malinkoite liquidus compositional area and overall accuracy reduction of computed liquidus temperatures and compositions to the measurements of Morey.[186] While Morey[186] did not indicate an error limit associated with the malinkoite liquidus measurements, the one measurement conducted by Ghanbari-Ahari & Cameron[187] to synthesize malinkoite was reported with a confidence of ± 10 K. As both Morey[186] and Ghanbari-Ahari & Cameron[187] acknowledged difficulty in synthesizing malinkoite, it is not unreasonable to associate an approximate ± 10 K error with the four Morey[186] liquidus measurements herein being discussed. As these adjustments result in liquidus projections in agreement with the composition measurements of Morey,[186] and as

the calculated phase melting temperatures are within a reasonable range of the measured liquidus temperatures, the malinkoite phase is well-modeled.

Table 4.5 shows the calculated and measured temperatures for the 120 Fig. 4.8 liquidus data points. The differential between the Table 4.5 calculated and measured temperatures is 52 K or less for 79 of the data points and between 52 K and 134 K for an additional 30 data points, which indicates generally good agreement between TSPIL model calculations and measured data for a majority of the Fig. 4.8 liquidus points. One liquidus measurement at 2 mol% Na_2O, 16 mol% B_2O_3, and 82 mol% SiO_2 as well as five additional liquidus points between 68.5 – 82 mol% SiO_2 exceeded measured temperatures by341 K and between 151 – 171 K, respectively. This overprediction was the result of maximizing the malinkoite melt while maintaining good agreement between calculated and measured liquidus compositions and melt temperatures of adjacent phases. However, the calculated liquidus temperatures in the SiO_2-containing regions for <68.5 mol% SiO_2 as well as along the B_2O_3-SiO_2 pseudo-binary axis (Fig. 4.6) agree well with measured temperatures. Thus, increasing the melt temperatures for certain compositions in the SiO_2-containing region to obtain reasonable malinkoite melt temperatures was considered acceptable.

According to Morey,[186] some of the reported invariant points may have been metastable, so while all invariant points were included in the initial assessment of the Na_2O-B_2O_3-SiO_2 system, not all of the measured points agreed with the assessed liquidus projection (Fig. 4.8). Those invariant points measured by Morey[186] as well as Ghanbari-Ahari & Cameron[187] that disagreed with Na_2O-B_2O_3-SiO_2 liquidus projections due to the introduction of the malinkoite phase have been labeled as such in Table 4.6. Each of the Table 4.6 invariant point compositions and temperatures, however, are well fit with the

exception of the $NaBO_2$-$Na_2Si_2O_5$-Na_2SiO_3 calculated composition and $Na_2B_8O_{13}$-SiO_2-NaB_3O_5 calculated liquidus temperature. The former calculated invariant point deviated from the measured composition due to the addition of the malinkoite phase and the latter was due to the elevation of liquidus temperatures caused by targeting malinkoite melting temperatures. The latter invariant point is reported with a 50 K differential between measurements of Morey[186] and Ghanbari-Ahari & Cameron[187] indicating the variability associated with this measurement. Additionally, the phases reported by Ghanbari-Ahari & Cameron[187] at >62 mol% Na_2O did not include all the known stable phases in the Na_2O-B_2O_3[163-165] and Na_2O-SiO_2[148] systems such as Na_3BO_3 and $Na_{10}SiO_7$, which increases the concern with their data. Hence, the error generated in this region is considered of minimal consequence, and the Na_2O-B_2O_3-SiO_2 system representation is seen as well-representing behavior.

$Na_2B_4O_7$-SiO_2 and $Na_2B_8O_{13}$-SiO_2 phase equilibria data (Fig. 4.9 & Fig. 4.10) measured by Ghanbari-Ahari & Cameron[187] and Morey,[186] respectively, are adequately represented by model calculations. Preference was given to data reported by Morey[186] for the $Na_2B_4O_7$-SiO_2 isopleth, thus minor temperature differences exist between model calculations and experimental data measured by Ghanbari-Ahari & Cameron.[187] This region calculated by the TSPIL model, however, fits the data of Fig. 4.6 well indicating that a good optimization was obtained.

Finally, model calculations of the partial free energy of Na_2O in the oxide liquid at 1200 and 1223 K referred to $Na_2O + 2B_2O_3$ as shown in Fig. 4.11 & Fig. 4.12, respectively, well predict the experimental data for the specified constant Na_2O mole fractions.

4.5.5. Na_2O-B_2O_3-Al_2O_3 pseudo-ternary system

The calculated stability regions for the $Na_2B_2Al_2O_7$ phase within the Na_2O-B_2O_3-Al_2O_3 liquidus projection diagram (Fig. Fig. 4.13) agree well with the results reported by Binev et al.[192] Also, the calculated liquidus temperatures in Fig. Fig. 4.13 predict well the measured temperatures in Table 4.7. The $NaBO_2$-Al_2O_3 phase equilibria data generated by Peshev et al.[194] displayed in Fig. Fig. 4.14 are well reproduced by model calculations, including the $NaBO_2$-$Na_2Al_2B_2O_7$ eutectic and $Na_2Al_2B_2O_7$-β-Al_2O_3 peritectic compositions and temperatures (Table 4.4). While the $NaBO_2$(α) and $NaAlO_2$(γ) phases that share a boundary with the $Na_2Al_2B_2O_7$ compound are consistent with the experimental data of Binev et al.,[192] the boundary along the approximately 30 mol% Al_2O_3 region is shared by the β-Al_2O_3 and $Al_{18}B_4O_{33}$ phases as opposed to Al_2O_3 as indicated by Binev et al.[192] It is stated in Binev et al.[192] that Al_2O_3 crystallizes in this high B_2O_3 region, which is also true of the model (Fig. Fig. 4.13), but no mention is made of the additional phases β-Al_2O_3 and $Al_{18}B_4O_{33}$. It is necessary to include these phases in the Na_2O-B_2O_3-Al_2O_3 system as each exists in the respective pseudo-binary systems Na_2O-Al_2O_3[148] and B_2O_3-Al_2O_3. As the optimization was able to accurately converge to the liquidus data reported by Binev et al.[192] with the inclusion of β-Al_2O_3 and $Al_{18}B_4O_{33}$ (Fig. Fig. 4.13 & Table 4.7), the model calculations and measured data in other ways do not conflict, particularly as Al_2O_3(corundum) does form in the general region identified by Binev et al.[192] With no data

at >55 mol% B_2O_3, the remainder of the phase equilibria are based on the extrapolated models.

4.5.6. Al_2O_3-B_2O_3-SiO_2 pseudo-ternary system

The result of the Al_2O_3-B_2O_3-SiO_2 assessment is shown in the Fig. Fig. 4.15 pseudo-ternary liquidus projection diagram with superimposed liquidus data reported by Gielisse[179] and Dietzel & Scholze.[203] Table 4.8 indicates that all calculated temperatures differ by <49 K and 26 differ by <30 K of the measured values, which demonstrates good model to experimental data agreement. The Al_2O_3-B_2O_3-SiO_2 liquidus projection (Fig. 15) indicates that mullite forms at >15 wt.% SiO_2 while $Al_{18}B_4O_{33}$ exists at <15 wt.% SiO_2 over the approximate range of 30 – 100 wt.% B_2O_3, which agrees with the experimental phase equilibria determinations reported by Gielisse.[179]

4.6. Conclusion

As part of the development of a HLW glass database that will predict the equilibrium behavior for understanding nepheline formation, the Na_2O-B_2O_3, B_2O_3-Al_2O_3, B_2O_3-SiO_2, Na_2O-B_2O_3-SiO_2, Na_2O-B_2O_3-Al_2O_3, and Al_2O_3-B_2O_3-SiO_2 systems were successfully assessed, reproducing nearly all the reliable phase equilibria and thermochemical information for these systems. A comprehensive literature review of available phase equilibria and thermodynamic data for each optimized pseudo-binary and -ternary system was documented as was the modeling approach implemented to complete each optimization. This assessment effort effectively added the HLW glass oxide constituent B_2O_3 to the Na_2O-Al_2O_3-SiO_2 thermodynamic database developed by Utlak & Besmann[148] completing the development of a consistent base waste glass constituent

thermochemical database. The complex solid solutions malinkoite and mullite containing sodium and boron were thermodynamically modeled as were their oxide melts.

To next address minor waste constituents and to characterize/predict their behavior with respect to nepheline and related phase formation, the solutes Li_2O, K_2O, Fe_2O_3, B_2O_3, CaO, and MgO will be included in the melt and appropriate crystalline phases of subsystems and eventually the entire Na_2O-Al_2O_3-SiO_2-B_2O_3 base glass composition to obtain a sufficiently comprehensive thermodynamic database. Assessment of the Na_2O-Al_2O_3-SiO_2-B_2O_3 pseudo-quaternary system will occur as part of the overall database optimization and benchmarking process to HLW glass data.

Acknowledgements

The authors gratefully acknowledge the financial support provided by the U.S. Department of Energy Waste Treatment and Immobilization Plant Project. The authors also thank Albert Kruger, Michael Schweiger, and Chuck Henager for their involvement with this research project.

Funding: This work was supported by the Department of Energy Office of River Protection

4.7. Tables

Table 4.1. Enthalpy, entropy, and heat capacity constant values of specified compounds

Compound	T range / K	$\Delta H_{298.15\,K}$ / (J · mol^{-1})	$S_{298.15\,K}$ / (J · mol^{-1} · K^{-1})	C_p[a] constants							Reference
				a	b	c	d	e	f	g	
B_2O_3(s)	298.15 < T 1191.56 1191.56 < T < 2000	-1271936	53.95	187.065717 127.77936	6.228488	7.1088789		-2319.648372			Barin[208]
B_2O_3(ℓ)	298.15 < T 723 723 < T < 2000	-1247862.13	87.2665	196.430432 129.704				-2426.975391	1.790887896		"
Na_2O(γ)	298 < T < 1405 1405 < T < 1500	-417982	75.061	66.216001 104.6	43.865102	-8.1337002	-14087.5				Wu et al.[84]
Na_2O(β)	298 < T < 1405 1405 < T < 1500	-416224.72	76.7788	66.216001 104.6	43.865102	-8.1337002	-14087.5				"
Na_2O(α)	298 < T < 1405 1405 < T < 1500	-404300.32	86.372	66.216001 104.6	43.865102	-8.1337002	-14087.5				"
Na_2O(ℓ)	298 < T < 1405 1405 < T < 1500	-356602.72	120.3205	66.216001 104.6	43.865102	-8.1337002	-14087.5				"
$NaBO_2$(β)	298.15 < T 1500	-976000	72.76	122.522934	14.551			-1052.705187			$\Delta H_{298.15K}$ and $S_{298.15K}$ this work, C_p[208]
$NaBO_2$(α)	298.15 < T 1500	-975228	73.5296	122.522934	14.551			-1052.705187			$\Delta H_{298.15K}$ this work,[b] $S_{298.15K}$ and C_p[208]
NaB_3O_5(s)	298.15 < T 1500	-2301685	121.3537	321.462183	9.060921			-3505.054198			$\Delta H_{298.15K}$ this work,[b] $S_{298.15K}$ and C_p[208]
NaB_5O_8(γ)	298.15 < T 1250.23 1250.23 < T <1900	-3605590	171.576	637.259757 608.578898	-39.58115 -42.695393	44.8621645 41.3077251		-8477.216221 -7317.392035			$\Delta H_{298.15K}$ and $S_{298.15K}$ this work, C_p[43]
NaB_5O_8(β)	298.15 < T 1250.23 1250.23 < T <1900	-3603590	173.59	637.259757 608.578898	-39.58115 -42.695393	44.8621645 41.3077251		-8477.216221 -7317.392035			"
NaB_5O_8(α)	298.15 < T 1250.23 1250.23 < T <1900	-3601590	175.507	637.259757 608.578898	-39.58115 -42.695393	44.8621645 41.3077251		-8477.216221 -7317.392035			$\Delta H_{298.15K}$ this work,[b] $S_{298.15K}$ and C_p[43]
NaB_9O_{14}(γ)	298.15 < T 1250.23 1250.23 < T <1900	-6165000	281.091	1011.39119 867.986898	-27.124174 -42.695393	59.0799224 41.3077251		-13116.51296 -7317.392035			$\Delta H_{298.15K}$ and $S_{298.15K}$ this work, C_p[43]
NaB_9O_{14}(β)	298.15 < T 1250.23 1250.23 < T <1900	-6164000	282.763	1011.39119 867.986898	-27.124174 -42.695393	59.0799224 41.3077251		-13116.51296 -7317.392035			$\Delta H_{298.15K}$ and $S_{298.15K}$ this work, C_p[43]
NaB_9O_{14}(α)	298.15 < T 1250.23 1250.23 < T <1900	-6163410	283.407	1011.39119 867.986898	-27.124174 -42.695393	59.0799224 41.3077251		-13116.51296 -7317.392035			$\Delta H_{298.15K}$ this work,[b] $S_{298.15K}$ and C_p[43]
$Na_2B_4O_7$(s)	298.15 < T 1300	-3286766.08	189.5168	400.90256	57.64206			-3997.569676			$\Delta H_{298.15K}$, $S_{298.15K}$ and C_p[208]

Table 4.1 cont'd. Enthalpy, entropy, and heat capacity constant values of specified compounds

Compound	T range / K	$\Delta H_{298.15\,K}$ / (J · mol^{-1})	$S_{298.15\,K}$ / (J · mol^{-1} · K^{-1})	C_p[a] constants							Reference
				a	b	c	d	e	f	g	
$Na_2B_8O_{13}$(s)	298.15 < T 1900	-5911384	297.255	1087.453797	-85.390787	82.6154501		-14634.78407			$\Delta H_{298.15K}$ this work,[b] $S_{298.15K}$ and C_p[43]
Na_3BO_3(s)	298.15 < T 1400	-1503650	148.5906	188.738935	58.416103	-8.1337002	-14087.5	-1052.705187			$\Delta H_{298.15K}$ this work,[b] $S_{298.15K}$ and C_p[43]
$Na_4B_2O_5$(s)	298.15 < T 1400	-2485969.62	224.6285	311.261869	72.967103	-8.1337002	-14087.5	-2105.410374			$S_{298.15K}$ this work,[d] $\Delta H_{298.15K}$ and C_p[43]
Al_2O_3(corundum)	298.15 < T 600	-1676383.29	50.94	67.48039	134.9399	-18.77562	-85232.7				Chase[209]
	600 < T < 1500			116.2579	14.45137	-42.41404	-1671.19				
	1500 < T < 2327			156.0582	-14.18213	-247.3334	3776.41				
	2327 < T < 4000			192.464							
$Al_2O_3(\ell)$	298.15 < T < 600	-1564606.8	98.6775	67.4804	134.94	-18.7756	-85232.6				Taylor et al.[210]
	600 < T < 1500			116.258	14.4514	-42.414	-1671.19				
	1500 < T < 1912			156.058	-14.1821	-247.333	3776.41				
	1912 < T < 2327			-21987.1791	13991.05902	159768.7236	-2461357				
	2327 < T < 4000			192.464							
$Al_4B_2O_9$(s)	298.15 < T < 1500	-4652809.89	171.6068	506.4682		-77.22726		-4083.7494	9.9725608		$\Delta H_{298.15K}$ this work, $S_{298.15K}$ and C_p[211]
$Al_{18}B_4O_{33}$(s)	298.15 < T < 2300	-17764514.5	583.4399	1788.0308		-347.52267		-12309.434	40.399304		$\Delta H_{298.15K}$ this work, $S_{298.15K}$ and C_p[211]
$NaAlO_2$(β)	298.15 < T < 2140	-1134391.9	70.36	139.1606				-1143.4999	1.40428967		Lambotte & Chartrand[76]
$NaAlO_2$(γ)	298.15 < T < 2140	-1133094.9	72.1127	139.1606				-1143.4999	1.40428967		"
$NaAlO_2$(δ)	298.15 < T < 2140	-1131939.9	72.7989	139.1606				-1143.4999	1.40428967		"
$Na_2Al_{12}O_{19}$(s)	298.15 < T < 2000	-10690701.36	418.6424	1157.35601	19.93868	-34.89447	-6403.41	-10425.19423	3.73188145		$\Delta H_{298.15K}$[148], $S_{298.15K}$ and C_p[76]
$Na_2Al_2B_2O_7$(s)	298.15 < T < 600	-3627944.24	227.4986	320.762107	185.03349	-19.8004413	-99320.2	-2319.648372			This work
	600 < T < 1191.56			369.539617	64.54496	-43.4388613	-15758.7	-2319.648372			
	1191.56 < T < 1405			310.253261	58.31647	-50.5477402	-15758.7				
	1405 < T < 1500			348.63726	14.45137	-42.41404	-1671.19				
	1500 < T < 2000			388.43756	-14.18213	-247.3334	3776.41				
	2000 < T < 2327			388.43756	-14.18213	-247.3334	3776.41				
	2327 < T < 4000			424.84336							
SiO_2(low-quartz)	298.15 < T < 373	-910699.94	41.46	80.011992		-35.46684		-240.2759989	4.915683694		Wu et al.[84]
	373 < T < 848.02			80.011992	8.440022	-35.46684	-45212.7	-240.2759989	4.915683694	6.0550446	
	848.02 < T < 850			0.04184							
SiO_2(high-quartz)	298.15 < T < 1995.99	-908626.77	44.2068	80.011992		-35.46684		-240.2759989	4.915683694		"
	1995.99 < T < 3000			85.772							

Table 4.1 cont'd. Enthalpy, entropy, and heat capacity constant values of specified compounds

Compound	T range / K	$\Delta H_{298.15\,K}$ / (J · mol^{-1})	$S_{298.15\,K}$ / (J · mol^{-1} · K^{-1})	C_p[a] constants							Reference
				a	b	c	d	e	f	g	
SiO_2(high-tridymite)	298.15 < T < 1991.28 1991.28 < T < 3000	-907045.13	45.5237	75.372668 85.772		-59.5809508			9.582461229		"
SiO_2(high-quartz)	298.15 < T < 1995.99 1995.99 < T < 3000	-908626.77	44.2068	80.011992 85.772		-35.46684		-240.2759989	4.915683694		"
SiO_2(high-tridymite)	298.15 < T < 1991.28	-907045.13	45.5237	75.372668		-59.5809508			9.582461229		"
SiO_2(high-cristobalite)	298.15 < T < 1995.99 1995.99 < T < 3000	-906377.23	46.0288	83.513598 85.772		-24.5535998		-374.6929988	2.800721944		Wu et al.[84]
SiO_2(ℓ)	298.15 < T < 1995.99 1995.99 < T < 3000	-896795.87	50.8291	83.513598 85.772		-24.5535998		-374.6929988	2.800721944		"
Na_2SiO_3(s)	298.15 < T < 1363 1363 < T < 1450	-1561430	113.847	234.77 177.31792				-2218.900009	1.352999996		Wu et al.[84,b]
Na_4SiO_4(s)	298.15 < T < 1358 1358 < T < 1450	-2108979	195.811	162.59024 259.408	74.22416						"
$Na_{10}SiO_7$(s)	298.15 < T < 1358	-3327528.29	528.3676	361.238242	205.819466	-24.4011006	-42262.5				Utlak & Besmann[148]
$Na_2Si_2O_5$(α)	298.15 < T < 1148 1148 < T < 1250	-2470070	165.7	250.69 261.20712		-156.510001			22.17000012		Wu et al.[84,c]
$Na_2Si_2O_5$(β)	298.15 < T < 951 951 < T < 1148 1148 < T < 1250	-2469652	166.1395	250.69 292.88 261.20712		-156.510001			22.17000012		$\Delta H_{298.15K}$ and $S_{298.15K}$,[209,c] C_p[84]
$Na_2Si_2O_5$(γ)	298.15 < T < 951 951 < T < 1148 1148 < T < 1250	-2469024	166.7804	250.69 292.88 261.20712		-156.510001			22.17000012		"
$Na_6Si_2O_7$(s)	298.15 < T < 1397	-3617193.47	349.1774	461.006007		-203.6927012		-1005.180017	32.28358041		$\Delta H_{298.15K}$[148], $S_{298.15K}$[d] and C_p[84]
$Na_6Si_8O_{19}$(s)	298.15 < T < 1082	-9187800	636.5	987.691985		-355.4062985		-4020.719986	54.1059985		Wu et al.[84,c]

Table 4.1 cont'd. Enthalpy, entropy, and heat capacity constant values of specified compounds

Compound	T range / K	$\Delta H_{298.15\,K}$ / (J · mol^{-1})	$S_{298.15\,K}$ / (J · mol^{-1} · K^{-1})	C_p[a] constants					Reference
				a	b c	d e	f	g	
$NaAlSi_3O_8$(low-albite)	298.15 < T < 2000	-3935000	207.4	394.18993	-76.68033	-2438.11327	10.17706412		Lambotte & Chartrand[76]
$NaAlSi_3O_8$(high-albite)	298.15 < T < 2000	-3923302.7	219.6723	394.18993	-76.68033	-2438.11327	10.17706412		"
$NaAlSi_3O_8$(monalbite)	298.15 < T < 2000	-3915260.6	226.1	394.18993	-76.68033	-2438.11327	10.17706412		"

[a] $C_p/\left(\mathrm{J{\cdot}mol^{-1}{\cdot}K^{-1}}\right) = a + b\cdot 10^{-3}T + c\cdot 10^{5}T^{-2} + d\cdot 10^{-9}T^{2} + e\cdot T^{-0.5} + f\cdot 10^{8}T^{-3} + g\cdot T^{3}$

[b] $\Delta H_{298.15K}$ slightly modified in FTOxid FactSage database

[c] $\Delta H_{298.15K}$ and $S_{298.15K}$ slightly modified in FTOxid FactSage database

[d] $S_{298.15K}$ slightly modified in FTOxid FactSage database

Table 4.2. Model parameters for solid solution (all °G and L parameter units are J/mol)

Malinkoite $((Na - B)^{+4},(Va - Si)^{+4})_8[Si^{+4}]_8\{O^{-2}\}_{32}$

$^{\circ}G_{Na_8B_8Si_8O_{32}} = 4 \cdot {}^{\circ}G_{Na_2O(\alpha)} + 4 \cdot {}^{\circ}G_{B_2O_3(s)} + 8 \cdot {}^{\circ}G_{SiO_2(\text{high-cristobalite})} - 1.18 \cdot 10^6$

$^{\circ}G_{Si_{16}O_{32}} = 16\left({}^{\circ}G_{SiO_2(\text{high–tridymite})} + 6276.0\right)$

β-Al_2O_3 $(Na_2O)_1[Al_2O_3]_{11}\{Na_2O,Va\}_1$ (retained from Utlak & Besmann[148])

$^{\circ}G_{Na_4Al_{22}O_{35}} = 2{}^{\circ}G_{NaAl_{11}O_{17}} + {}^{\circ}G_{Na_2O(\alpha)} - 154808$

$^{\circ}G_{Na_2Al_{22}O_{34}} = 2{}^{\circ}G_{NaAl_{11}O_{17}}$

$^{0}L_{Na_2O:Al_2O_3:Na_2O,Va} = -271700 - 3T$

Mullite $\left(Al^{+3}\right)_2\left[Al^{+3},B^{+3},Si^{+4},\right]\{O^{-2},Va\}_5$

$^{\circ}G_{Al_3O_5^{-1}} = {}^{\circ}G_{Al_3Va^{+9}} = 0.5{}^{\circ}G_{Al_2O_3(\text{corundum})} + 86508.38 - 0.418T$

$^{\circ}G_{Al_2SiO_5} = {}^{\circ}G_{Al_2SiVa^{+10}} = {}^{\circ}G_{Al_2SiO_5(\text{sillimanite})} + 9957.92 - 3.347T$

$^{\circ}G_{Al_2BO_5^{-1}} = {}^{\circ}G_{Al_2BVa^{+9}} = 0.5{}^{\circ}G_{Al_4B_2O_9(s)} + 1024.84 + 20.92T$

$^{0}L_{Al^{+3}:Al^{+3},Si^{+4}:O^{-2}} = {}^{0}L_{Al^{+3}:Al^{+3},Si^{+4}:Va} = -92048.0$

$^{0}L_{Al^{+3}:B^{+3},Si^{+4}:O^{-2}} = 5000 - 56T$

Table 4.3. Model parameters for oxide liquid (all °G and L parameter units are J/mol)

Oxide liquid[a] $\left(Al^{+3},Na^{+1}\right)_P\left(AlO_2^{-1},O^{-2},SiO_4^{-4},BO_3^{-3},B_3O_{4.5}^0,SiO_2^0\right)_Q$

$^{\circ}G_{Al^{+3}:BO_3^{-3}} = 1.5\,^{\circ}G_{B_2O_3(\ell)} + 1.5\,^{\circ}G_{Al_2O_3(\ell)} + 21653.682 + 25.88113T$

$^{\circ}G_{Al^{+3}:B_3O_{4.5}^0} = 4.5\,^{\circ}G_{B_2O_3(\ell)}$

$^{\circ}G_{Na^{+1}:BO_3^{-3}} = 1.5\,^{\circ}G_{Na_2O(\ell)} + 0.5\,^{\circ}G_{B_2O_3(\ell)} - 320809.298 + 51.48266T$

$^{\circ}G_{Na^{+1}:B_3O_{4.5}^0} = 1.5\,^{\circ}G_{B_2O_3(\ell)}$

$^0L_{Na^{+1}:O^{-2},BO_3^{-3}} = -74488 + 31.27T$

$^1L_{Na^{+1}:O^{-2},BO_3^{-3}} = -26891.7$

$^0L_{Na^{+1}:BO_3^{-3},B_3O_{4.5}^0} = -248431 - 65.55T$

$^1L_{Na^{+1}:BO_3^{-3},B_3O_{4.5}^0} = -85047 + 98.92T$

$^2L_{Na^{+1}:BO_3^{-3},B_3O_{4.5}^0} = -63847 + 59.34T$

$^0L_{Al^{+3}:AlO_2^{-1},B_3O_{4.5}^0} = 18800$

$^0L_{Na^{+1}:BO_3^{-3},SiO_2^0} = 32768 - 153T$

$^1L_{Na^{+1}:BO_3^{-3},SiO_2^0} = -19933 + 111.5T$

$^2L_{Na^{+1}:BO_3^{-3},SiO_2^0} = 32590$

$^0L_{Na^{+1}:B_3O_{4.5}^0,SiO_2^0} = 220954 - 255T$

$^1L_{Na^{+1}:B_3O_{4.5}^0,SiO_2^0} = -62887 + 45T$

$^2L_{Na^{+1}:B_3O_{4.5}^0,SiO_2^0} = 30T$

$^0L_{Na^{+1}:SiO_4^{-4},BO_3^{-3}} = -92775 - 10T$

$^1L_{Na^{+1}:SiO_4^{-4},BO_3^{-3}} = -30T$

$^0L_{Na^{+1}:SiO_4^{-4},B_3O_{4.5}^0} = -328622$

$^0L_{Na^{+1}:AlO_2^{-1},BO_3^{-3}} = -69894$

$^1L_{Na^{+1}:AlO_2^{-1},BO_3^{-3}} = -31493$

$^0L_{Na^{+1}:AlO_2^{-1},B_3O_{4.5}^0} = -206353 - 10T$

$^1L_{Na^{+1}:AlO_2^{-1},B_3O_{4.5}^0} = -131712 + 10T$

$^2L_{Na^{+1}:AlO_2^{-1},B_3O_{4.5}^0} = -110597$

$^0L_{Al^{+3},Na^{+1}:AlO_2^{-1},BO_3^{-3}} = -100T$

$^1L_{Al^{+3},Na^{+1}:AlO_2^{-1},BO_3^{-3}} = -100T$

$^0L_{Al^{+3}:BO_3^{-3},SiO_2^0} = 126779 - 170T$

$^1L_{Al^{+3}:BO_3^{-3},SiO_2^0} = -2289 - 96.8T$

$^0L_{Al^{+3}:B_3O_{4.5}^0,SiO_2^0} = 54261 - 51.8T$

$^{AlO_2^{-1}}L_{Al^{+3}:AlO_2^{-1},BO_3^{-3},SiO_2^0} = -682389$

$^{BO_3^{-3}}L_{Al^{+3}:AlO_2^{-1},BO_3^{-3},SiO_2^0} = -289894$

$^{SiO_2^0}L_{Al^{+3}:AlO_2^{-1},BO_3^{-3},SiO_2^0} = -180968$

$^{AlO_2^{-1}}L_{Al^{+3}:AlO_2^{-1},B_3O_{4.5}^0,SiO_2^0} = -780417 - 220.6T$

$^{B_3O_{4.5}^0}L_{Al^{+3}:AlO_2^{-1},B_3O_{4.5}^0,SiO_2^0} = 103224 + 71.1T$

$^{SiO_2^0}L_{Al^{+3}:AlO_2^{-1},B_3O_{4.5}^0,SiO_2^0} = -287290 - 104.7T$

[a] Model endmember and RK interaction parameters consisting of only Na_2O, Al_2O_3, and/or SiO_2 species are reported in Utlak & Besmann.[148]

Table 4.4. Invariant points of Na_2O, Al_2O_3, and SiO_2 pseudo-binary subsystems with B_2O_3 as well as $NaBO_2$-Al_2O_3 system

Invariant point	Calculated		Measured		References
Na_2O-B_2O_3 system (Fig. 4.1)	$X_{B_2O_3}$ [a]	T / K	$X_{B_2O_3}$	T / K	
$Na_2O(\gamma)$ + Na_3BO_3 eutectic	0.183	724	0.202	728	Milman & Bouaziz[164]
Na_3BO_3 + $Na_4B_2O_5$ eutectic	0.296	851	0.301	843	"
$Na_4B_2O_5$ + $NaBO_2$ eutectic	0.350	899	0.348	905	"
$NaBO_2$ + $Na_2B_4O_7$ eutectic	0.640	1006	0.654	1013	Morey & Merwin[163]
			0.665	1016	Milman & Bouaziz[164]
$Na_2B_4O_7$ + NaB_3O_5 eutectic	0.680	1010	0.699	995	Morey & Merwin[163]
			0.708	1001	Milman & Bouaziz[164]
NaB_3O_5 + $Na_2B_8O_{13}$ peritectic	0.727	1038	0.740	1038	"
$Na_2B_8O_{13}$ + NaB_5O_8 peritectic	0.847	1058	0.931	1058	"
NaB_5O_8 + NaB_9O_{14} peritectic	0.963	955	0.869	955	"
$Na_2O(\alpha)$ T_m [b]		1405		1405	Wu et al.[84]
Na_3BO_3 T_m		950		948	Milman & Bouaziz[164]
$Na_4B_2O_5$ T_m		908			
$NaBO_2$ T_m		1241		1203	Burgess & Holt[212]
				1239	van Klooster[213]
				1238	Cole et al.[214]
				1239	Morey & Merwin[163]
$Na_2B_4O_7$ T_m		1011		1015	Day & Allen[215]
				1005	Ponomareff[216]
				1008	Cole et al.[214]
				1011	Menzel[217]
				1064	Burgess & Holt[212]
				1016	Morey & Merwin[163]
				1015	Liang et al.[165]
				1015	Ghanbari-Ahari & Cameron[187]
NaB_3O_5 T_m	0.727	1038	0.738	1039	Morey & Merwin[163]
			0.75	1038	Liang et al.[165]
				967	Ponomareff[216]
				993	Cole et al.[214]
$Na_2B_8O_{13}$ T_m		1071		1131	Burgess & Holt[212]
				1083	Cole et al.[214]
				1089	Morey & Merwin[163]
				1088	Liang et al.[165]
				1089	Rockett & Foster[188]
NaB_5O_8	0.847	1058	0.833	1077	Liang et al. [165]
				1058	Milman & Bouaziz[164]
B_2O_3 T_m		724		724	Barin[208]

[a] $X_{compound}$ = mole fraction of specified compound
[b] T_m = melting temperature in inverse kelvin

Table 4.4 cont'd. Invariant points of Na_2O, Al_2O_3, and SiO_2 pseudo-binary subsystems with B_2O_3 as well as $NaBO_2$-Al_2O_3 system

Invariant point	Calculated		Measured		References
B_2O_3-Al_2O_3 system (Fig. 4.5)	$X_{B_2O_3}$	T / K	$X_{B_2O_3}$	T / K	
$Al_{18}B_4O_{33}$ T_m		2224		1713	Scholze[177]
				1713	Kim & Hummel[178]
				2223	Baumann &
$Al_4B_2O_9$ T_m		1463		1323	Scholze[177]
				1303	Kim & Hummel[178]
				1308	Gielisse & Foster[180]
				1463	Rymon-Lipinski[181]
Al_2O_3(corundum) T_m		2327		2327	Eriksson et al.[80]
B_2O_3-SiO_2 system (Fig. 4.6 & Fig. 4.7)	$X_{B_2O_3}$	T / K	$X_{B_2O_3}$	T / K	
SiO_2(high-cristobalite) T_m		1996		1996	Weber & Venero [218]
$NaBO_2$-Al_2O_3 (Fig. Fig. 4.14)	$X_{Al_2O_3}$	T / K	$X_{Al_2O_3}$	T /K	
$NaBO_2$-$Na_2Al_2B_2O_7$ eutectic	0.187	1119.6	0.182	1119	Peshev et al.[194]
$Na_2Al_2B_2O_7$-β-Al_2O_3 peritectic	0.333	1259.0	0.315	1259	"

Table 4.5. Liquidus temperatures of Na_2O-B_2O_3-SiO_2 system (Fig. 4.8)

X_{Na_2O}	$X_{B_2O_3}$	X_{SiO_2}	T^m/K[186,a]	T^c/K[b]	X_{Na_2O}	$X_{B_2O_3}$	X_{SiO_2}	T^m/K[186]	T^c/K	X_{Na_2O}	$X_{B_2O_3}$	X_{SiO_2}	T^m/K[186]	T^c/K
0.499	0.339	0.163	1185	1167	0.227	0.717	0.056	1037	1052	0.496	0.092	0.412	1239	1163
0.498	0.288	0.214	1165	1155	0.234	0.71	0.056	1031	1048	0.36	0.137	0.503	1042	981.7
0.498	0.246	0.256	1135	1135	0.031	0.855	0.114	893	995.9	0.423	0.163	0.414	1057	1085
0.498	0.224	0.278	1118	1122	0.094	0.808	0.097	970	1045	0.484	0.156	0.36	1138	1127
0.441	0.44	0.118	1172	1155	0.178	0.71	0.112	1059	1062	0.457	0.164	0.379	1144	1115
0.419	0.419	0.162	1133	1138	0.193	0.698	0.109	1056	1058	0.475	0.172	0.353	1135	1117
0.392	0.392	0.216	1103	1099	0.214	0.673	0.114	1029	1047	0.496	0.186	0.318	1130	1110
0.369	0.351	0.28	1015	1046	0.174	0.648	0.177	1036	1047	0.508	0.149	0.343	1153	1127
0.294	0.296	0.41	866	984	0.213	0.62	0.167	982	1032	0.25	0.25	0.5	1040	1004
0.564	0.246	0.19	1093	1080	0.084	0.719	0.197	952	1036	0.249	0.273	0.478	1039	1003
0.514	0.274	0.212	1149	1145	0.162	0.623	0.215	1040	1038	0.278	0.244	0.478	1038	994.3
0.464	0.303	0.234	1165	1151	0.033	0.744	0.224	929	1006	0.342	0.258	0.4	1012	965.6
0.413	0.331	0.256	1136	1110	0.074	0.644	0.282	943	1012					
0.397	0.34	0.263	1072	1089	0.125	0.592	0.283	992	1018					
0.336	0.374	0.29	1035	990	0.142	0.572	0.286	973	1014					
0.294	0.399	0.307	900	985	0.178	0.549	0.273	955	1011					
0.311	0.369	0.321	964	980	0.211	0.517	0.272	931	1006					
0.411	0.291	0.299	1074	1084	0.096	0.603	0.301	961	1010					
0.35	0.321	0.329	1015	999	0.099	0.585	0.316	949	1005					
0.309	0.341	0.35	935	972	0.163	0.521	0.317	954	998.6					
0.299	0.346	0.354	903	976	0.134	0.538	0.328	963	999.3					
0.289	0.351	0.36	887	979	0.216	0.451	0.334	901	985.9					
0.335	0.601	0.064	967	1006	0.054	0.61	0.336	940	986.9					
0.327	0.558	0.115	944	1009	0.073	0.568	0.358	944	986.1					
0.43	0.173	0.397	1045	1088	0.032	0.596	0.373	905	965.3					
0.397	0.182	0.421	1053	1041	0.169	0.46	0.371	998	999.6					
0.378	0.16	0.462	1005	1013	0.124	0.497	0.379	979	1005					
0.317	0.207	0.476	917	975	0.204	0.411	0.386	1020	996.1					
0.355	0.224	0.421	1039	974	0.062	0.545	0.393	950	990.9					
0.356	0.189	0.455	992	972	0.198	0.403	0.399	1040	1005					
0.349	0.203	0.448	975	971	0.123	0.456	0.422	1063	1032					
0.334	0.208	0.458	950	973	0.231	0.342	0.428	874	998.8					
0.324	0.211	0.465	939	972	0.177	0.295	0.528	1060	1074					
0.312	0.209	0.479	911	978	0.215	0.277	0.508	1042	1041					
0.314	0.458	0.228	973	1003	0.223	0.253	0.524	1033	1038					
0.383	0.226	0.391	1063	1011	0.192	0.237	0.571	1044	1073					
0.328	0.616	0.057	985	1007	0.022	0.393	0.586	1098	1140					
0.299	0.59	0.11	969	1010	0.212	0.212	0.576	1057	1055					
0.313	0.523	0.164	914	1011	0.264	0.114	0.622	949	996.3					
0.286	0.527	0.187	908	1009	0.091	0.27	0.639	1015	1199					
0.292	0.418	0.29	901	989	0.197	0.16	0.643	1211	1060					
0.247	0.698	0.055	1017	1039	0.063	0.253	0.685	1125	1268					
0.267	0.678	0.055	1005	1030	0.065	0.208	0.727	1146	1317					
0.28	0.604	0.116	967	1018	0.079	0.106	0.815	1371	1399					
0.287	0.658	0.055	991	1021	0.059	0.123	0.817	1323	1457					
0.267	0.567	0.166	926	1017	0.04	0.141	0.819	1310	1498					
0.24	0.566	0.193	946	1021	0.02	0.159	0.821	1180	1521					
0.215	0.592	0.194	971	1026	0.308	0.141	0.551	979	981.2					
0.264	0.517	0.219	907	1008	0.312	0.132	0.557	1028	984					
0.217	0.564	0.219	952	1020	0.281	0.101	0.618	983	988.7					
0.251	0.503	0.246	892	1006	0.298	0.088	0.614	1028	980.8					
0.264	0.47	0.266	898	997	0.336	0.053	0.611	1078	1007					
0.188	0.753	0.06	1083	1066	0.499	0.191	0.31	1127	1107					
0.207	0.736	0.057	1062	1062	0.497	0.136	0.367	1189	1137					

[a] T^m = measured temperature
[b] T^c = calculated temperature

Table 4.6. Invariant points of Na_2O-B_2O_3-SiO_2 system (Fig. 4.8)

Invariant point	Measured				Calculated				References
	X_{Na_2O}	$X_{B_2O_3}$	X_{SiO_2}	T / K	X_{Na_2O}	$X_{B_2O_3}$	X_{SiO_2}	T / K	
$NaBO_2$-Na_2SiO_3	0.5	0.196	0.304	1105	0.498	0.214	0.289	1106	Morey[186]
$NaBO_2$-SiO_2	metastable				0.275	0.283	0.443	803	"
$Na_2B_8O_{13}$-SiO_2	0.129	0.518	0.353	991	0.129	0.518	0.353	948	"
$NaBO_2$-$Na_2Si_2O_5$-Na_2SiO_3	0.346	0.228	0.425	965	0.331	0.161	0.508	913	"
$NaBO_2$-$Na_2Si_2O_5$-SiO_2	metastable				0.273	0.225	0.501	793	"
$NaBO_2$-$Na_2B_4O_7$-SiO_2	metastable				0.277	0.301	0.423	793	"
$Na_2B_4O_7$-SiO_2-NaB_3O_5	metastable				0.248	0.378	0.374	843	"
NaB_3O_5-SiO_2-$Na_2B_8O_{13}$	0.185	0.470	0.345	984	0.218	0.417	0.365	873	"
B_2O_3-$Na_2B_8O_{13}$-SiO_2	metastable				0.022	0.955	0.023	713	Ghanbari-Ahari & Cameron[187]
$Na_2B_8O_{13}$-SiO_2-NaB_3O_5	0.185	0.470	0.345	984	0.218	0.417	0.365	923	"
NaB_3O_5-SiO_2-$Na_2B_4O_7$	metastable				0.233	0.392	0.374	893	"
$Na_2B_4O_7$-SiO_2-$NaBO_2$	metastable				0.258	0.354	0.388	783	"
$NaBO_2$-SiO_2-$Na_2Si_2O_5$	metastable				0.273	0.216	0.511	783	"
$NaBO_2$-$Na_2Si_2O_5$-Na_2SiO_3	0.346	0.228	0.425	965	0.326	0.152	0.522	913	"
$NaBO_2$-Na_2SiO_3-$Na_4B_2O_5$[a]	0.621	0.274	0.105	933	0.617	0.256	0.127	873	"
$Na_4B_2O_5$-Na_2SiO_3-Na_4SiO_4[b]	0.651	0.287	0.062	842	0.65	0.219	0.132	873	"
$Na_4B_2O_5$-Na_4SiO_4-Na_2O[c]	0.699	0.256	0.045	815	0.697	0.219	0.084	873	"

[a] Calculated invariant point consists of $NaBO_2$-Na_2SiO_3-Na_4SiO_4 phases
[b] Calculated invariant point consists of $NaBO_2$-$Na_4B_2O_5$-Na_4SiO_4 phases
[c] Calculated invariant point consists of $Na_4B_2O_5$-Na_3BO_3-Na_4SiO_4 phases

Table 4.7. Liquidus temperatures of Na_2O-B_2O_3-Al_2O_3 system (Fig. Fig. 4.13)

X_{Na_2O}	$X_{B_2O_3}$	$X_{Al_2O_3}$	T^m / K	T^c / K	References
0.5	0.5	0	1240	1241	Wakasugi et al.[201]
0.46	0.46	0.079	1211	1200	"
0.45	0.45	0.1	1183	1191	"
0.44	0.44	0.12	1173	1180	"
0.43	0.43	0.14	1158	1166	"
0.42	0.42	0.159	1131	1150	"
0.41	0.41	0.18	1117	1129	"
0.40	0.40	0.20	1149	1136	"
0.39	0.39	0.22	1172	1163	"
0.38	0.38	0.24	1195	1188	"
0.37	0.37	0.260	1207	1211	"
0.36	0.36	0.279	1236	1231	"
0.35	0.35	0.30	1253	1248	"
0.34	0.34	0.32	1252	1259	"
0.339	0.341	0.321	1265	1264	"
0.4	0.6	0	1164	1115	Wakasugi et al.[202]
0.36	0.54	0.099	1101	1090	"
0.34	0.51	0.149	1069	1081	"
0.32	0.48	0.199	1086	1098	"
0.3	0.45	0.25	1119	1139	"
0.284	0.424	0.292	1206	1188	"
0.448	0.272	0.28	1093	1158	Binev[192]
0.434	0.276	0.289	1133	1136	"
0.413	0.283	0.304	1173	1167	"
0.376	0.291	0.333	1213	1335	"
0.358	0.322	0.321	1253	1251	"
0.337	0.359	0.304	1253	1251	"
0.309	0.405	0.286	1213	1209	"
0.283	0.444	0.273	1173	1143	"
0.258	0.48	0.262	1133	1062	"
0.24	0.505	0.254	1093	1165	"
0.385	0.441	0.174	1093	1115	"
0.396	0.425	0.179	1093	1117	"
0.441	0.364	0.195	1093	1112	"
0.455	0.345	0.2	1093	1092	"

Table 4.8. Liquidus temperatures of Al_2O_3-B_2O_3-SiO_2 system (Fig. Fig. 4.15)

$W_{B_2O_3}$ [a]	$W_{Al_2O_3}$	W_{SiO_2}	T^m / K	T^c / K	References
0.7	0.2	0.1	1723	1748	Gielisse[179]
0.65	0.2	0.15	1723	1716	"
0.6	0.2	0.2	1723	1721	"
0.5	0.2	0.3	1773	1741	"
0.4	0.2	0.4	1788	1774	"
0.75	0.15	0.1	1698	1707	"
0.7	0.15	0.15	1703	1684	"
0.5	0.15	0.35	1738	1708	"
0.8	0.1	0.1	1613	1661	"
0.7	0.1	0.2	1633	1653	"
0.6	0.1	0.3	1673	1657	"
0.4	0.1	0.5	1723	1696	"
0.8	0.05	0.15	1598	1575	"
0.65	0.05	0.3	1598	1587	"
0.9	0.025	0.075	1463	1455	"
0.6625	0.025	0.3125	1513	1495	"
0.104	0.053	0.846	1758	1751	Dietzel & Scholze[203]
0.125	0.095	0.783	1813	1817	"
0.09	0.202	0.708	1928	1932	"
0.175	0.057	0.765	1713	1722	"
0.175	0.095	0.726	1783	1788	"
0.158	0.201	0.645	1878	1890	"
0.134	0.309	0.553	1993	1964	"
0.076	0.45	0.476	2048	2067	"
0.241	0.065	0.688	1658	1707	"
0.196	0.116	0.692	1793	1801	"
0.209	0.209	0.579	1848	1867	"
0.099	0.349	0.556	2008	2003	"
0.302	0.06	0.634	1638	1671	"
0.282	0.115	0.601	1733	1757	"

[a] $W_{compound}$ = weight fraction of specified compound

4.8. Figures

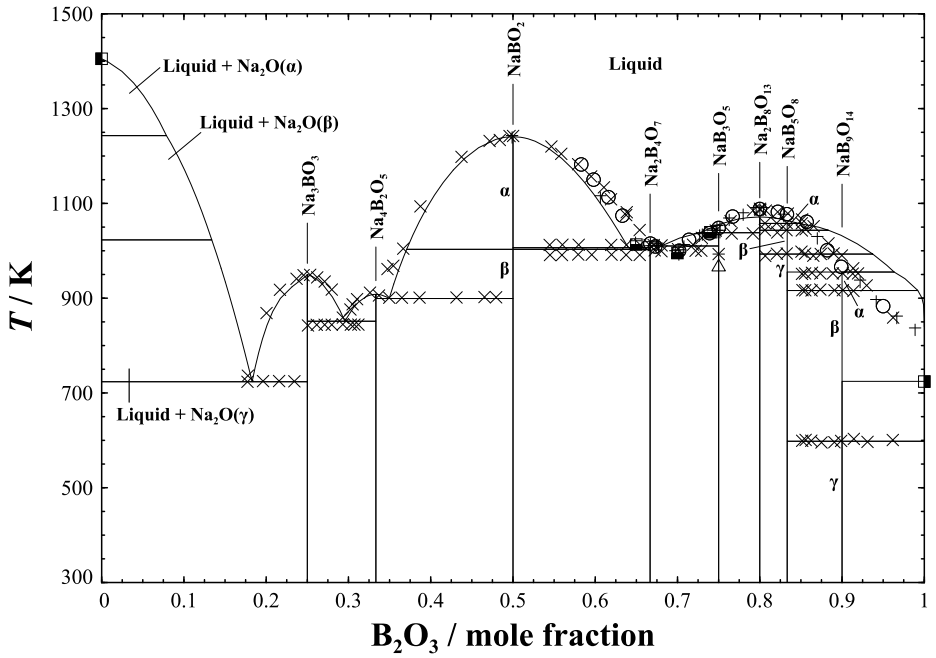

Fig. 4.1. Computed Na_2O-B_2O_3 pseudo-binary phase diagram with experimental measurements shown as points. Data: ×[164] +[163] ○[165] ▬[186] ◧[84] ◨[208] △[216] ✳[214]

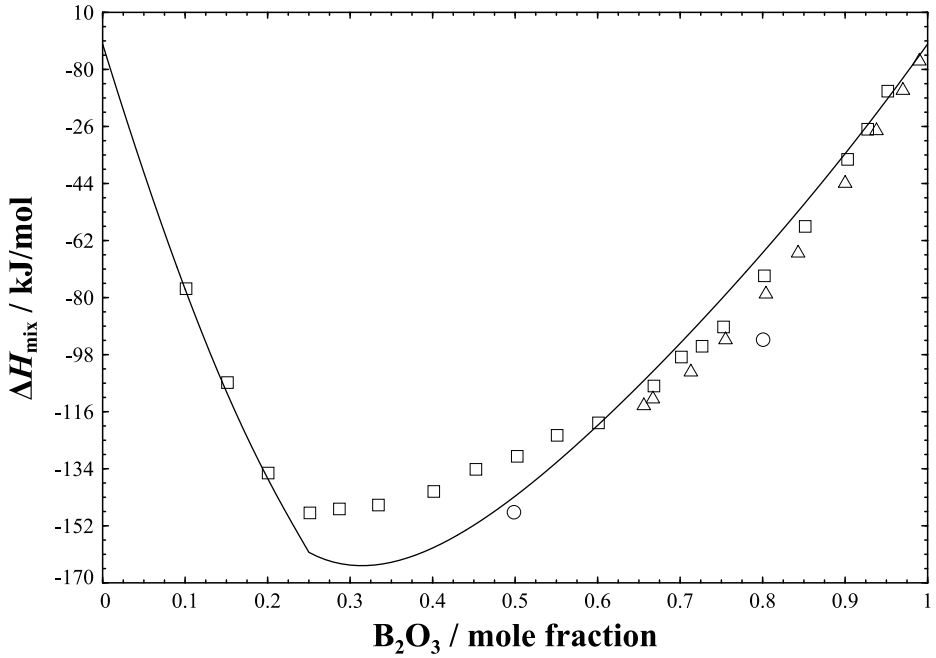

Fig. 4.2. Computed curve of enthalpy of mixing for Na_2O-B_2O_3 with experimental measurements shown as points. Data: □ 1299 K[137] ○ 974 K[167] △ 298 K[166]

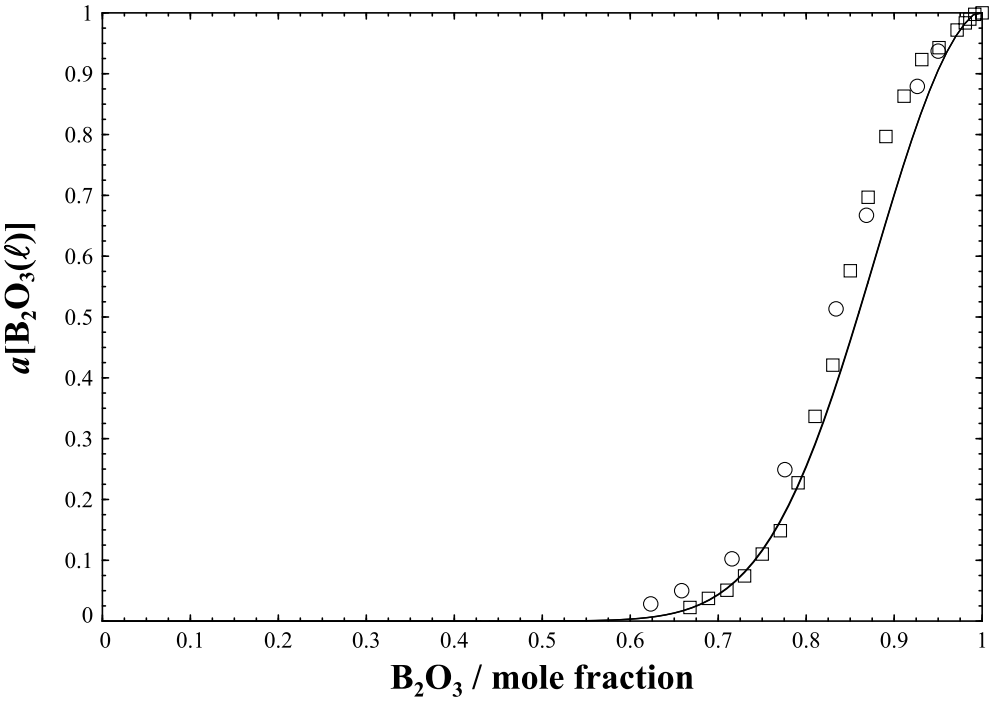

Fig. 4.3. Computed activity curve of liquid B_2O_3 in Na_2O-B_2O_3 system with experimental measurements shown as points. Data: ○ 1137 K[168] □ 1123 K[169]

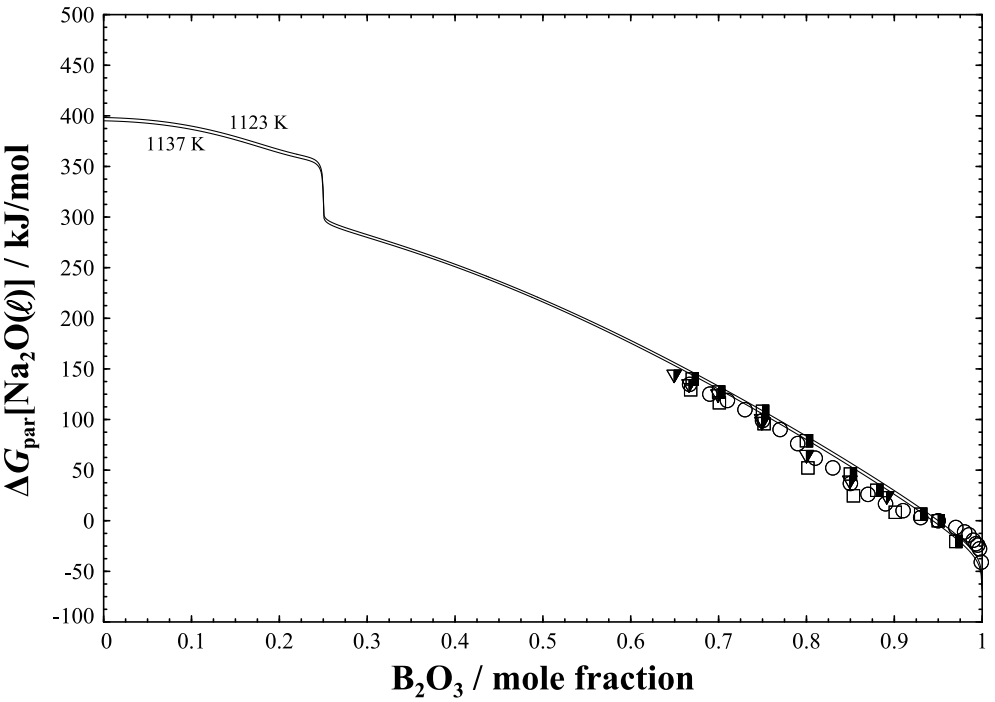

Fig. 4.4. Partial Gibbs energy of liquid Na_2O in Na_2O-B_2O_3 system referred to $0.5Na_2O + 0.95B_2O_3$ with experimental measurements shown as points. Data: ○ 1137 K[169] □ 1123 K[171] ▽ 1123 K[172] ◨ 1123K[168]

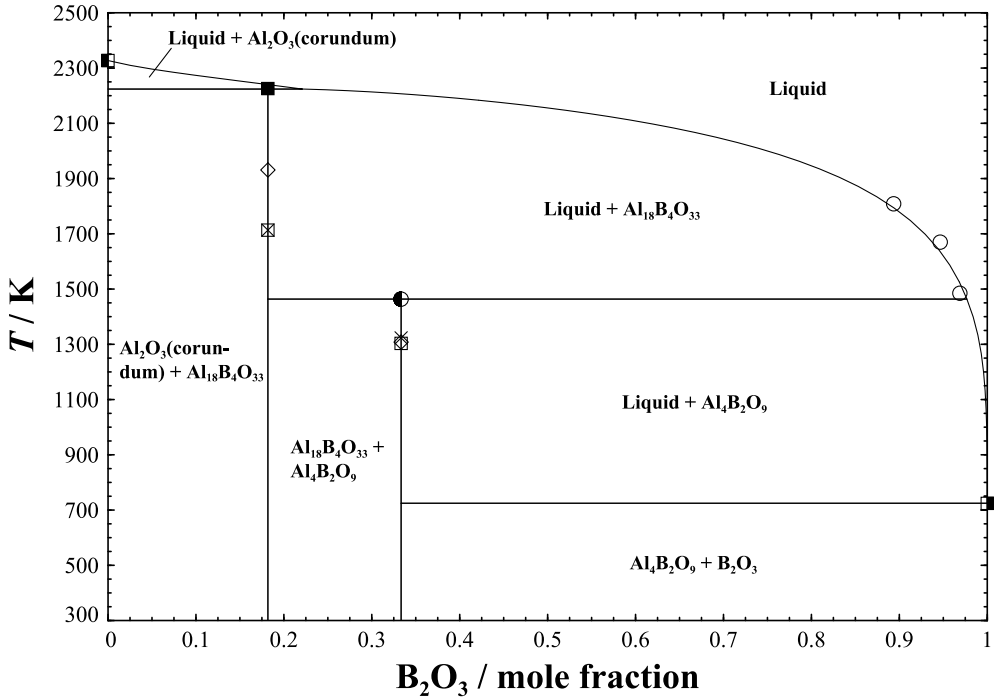

Fig. 4.5. Computed B_2O_3-Al_2O_3 pseudo-binary phase diagram with experimental measurements shown as points. Data: ○[180] □[178] ◇[219] ×[177] ◐[181] ■[176] ◧[80] ◨[208]

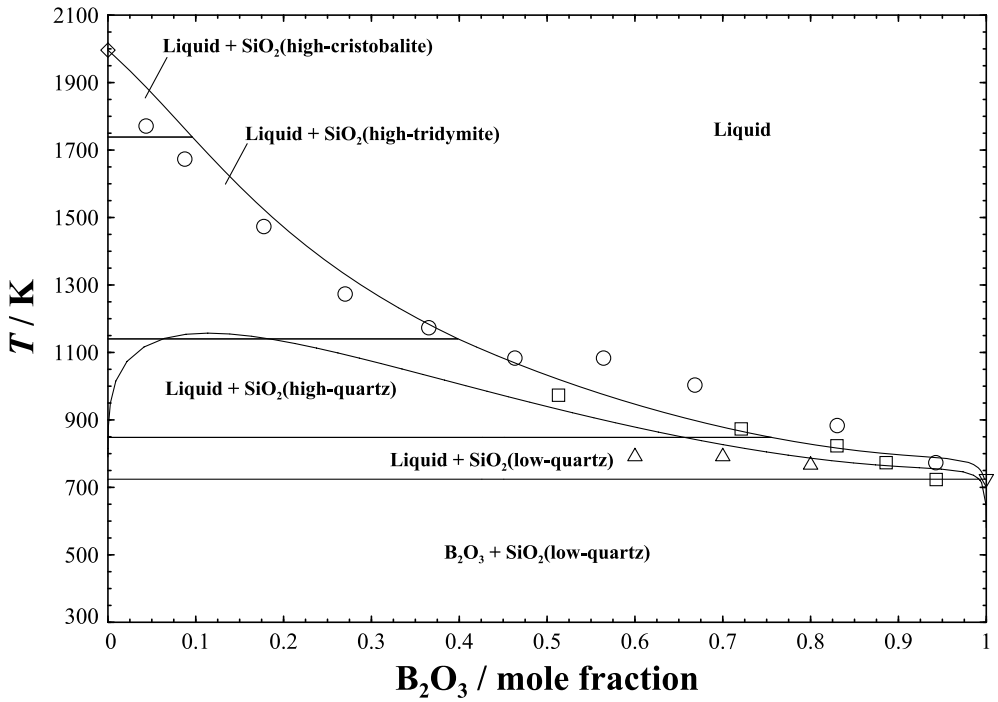

Fig. 4.6. Computed Na_2O-B_2O_3-SiO_2 isopleth with Na_2O mole fraction of 10^{-7} and experimental measurements shown as points. Data: ○[183] □[184] △[185] ◇[103] ▽[208]

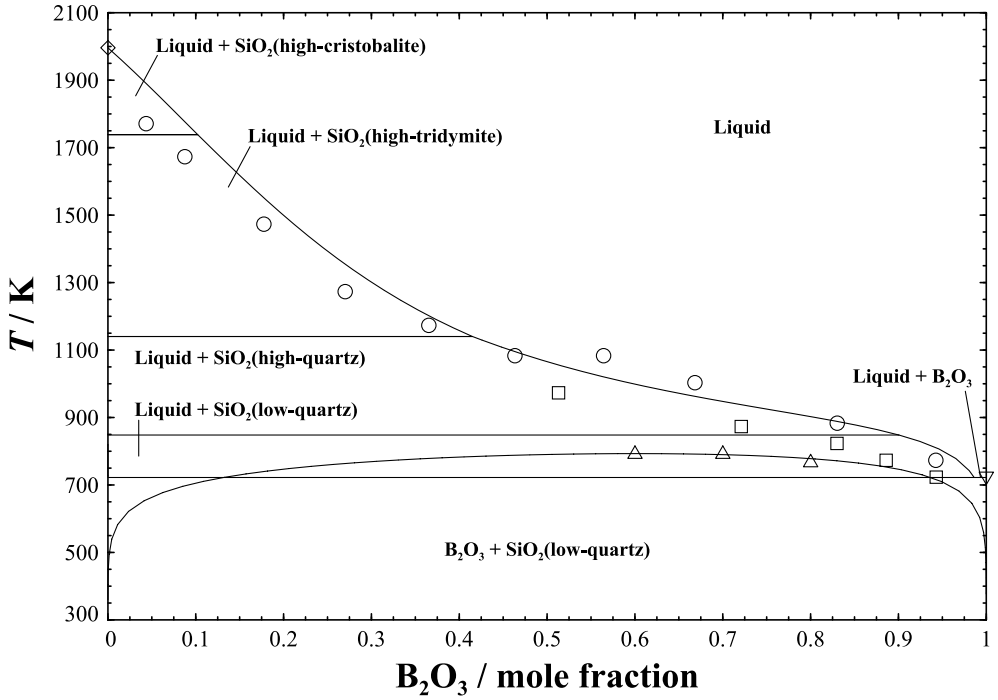

Fig. 4.7. Computed B_2O_3-Al_2O_3-SiO_2 isopleth with Na_2O mole fraction of 10^{-7} and experimental measurements shown as points. Data: ○[183] □[184] △[185] ◇[103] ▽[208]

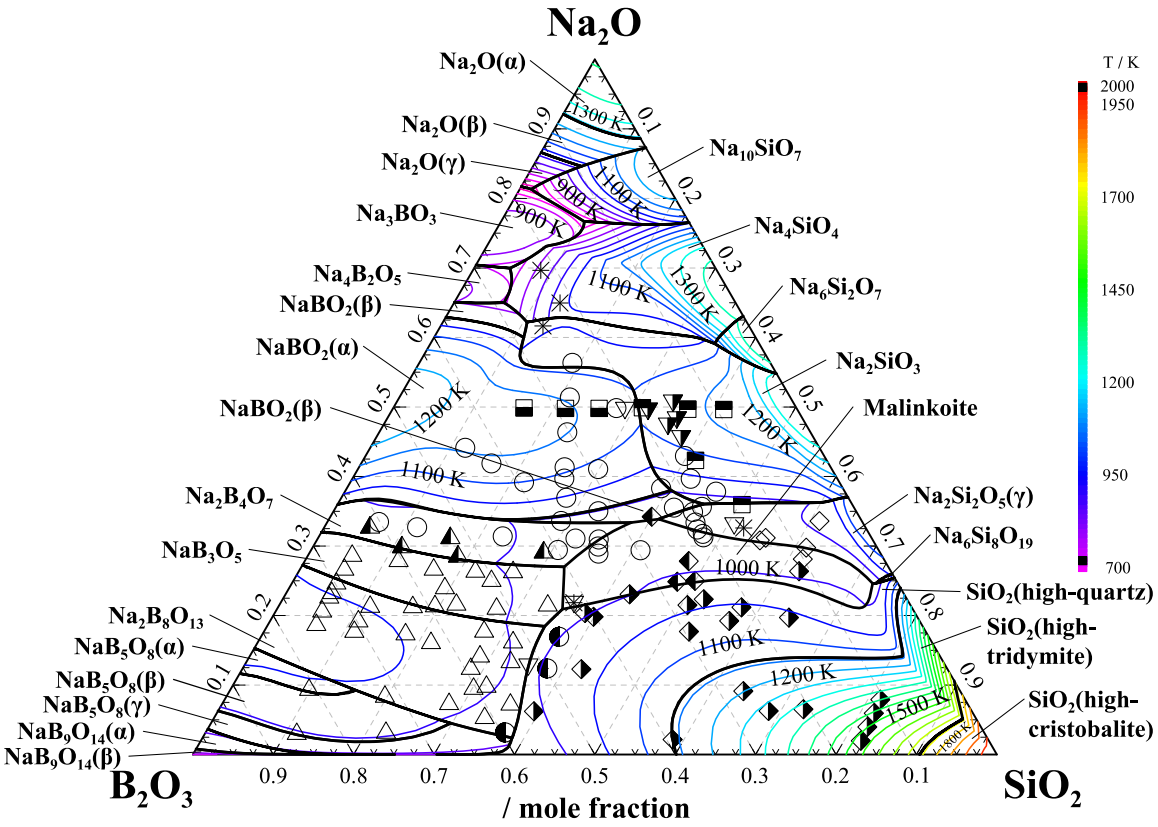

Fig. 4.8. Computed Na_2O-B_2O_3-SiO_2 system liquidus projections with liquidus and phase composition experimental measurements shown as points. Data: Morey[186]: ⬓ $NaBO_2$, ○ $NaBO_2$ + Na_2SiO_3, ◭ $Na_2B_4O_7$, △ NaB_3O_5, ◐ $Na_2B_8O_{13}$ + SiO_2(quartz), ◆ $Na_2B_8O_{13}$ + SiO_2(quartz), ◇ $Na_2Si_2O_5$, ⬒ Na_2SiO_3, ◥ Na_2SiO_3 + $NaBO_2$, ◆ malinkoite, ▽ invariant points. Ghanbari-Ahari & Cameron[187]: ✳ invariant points.

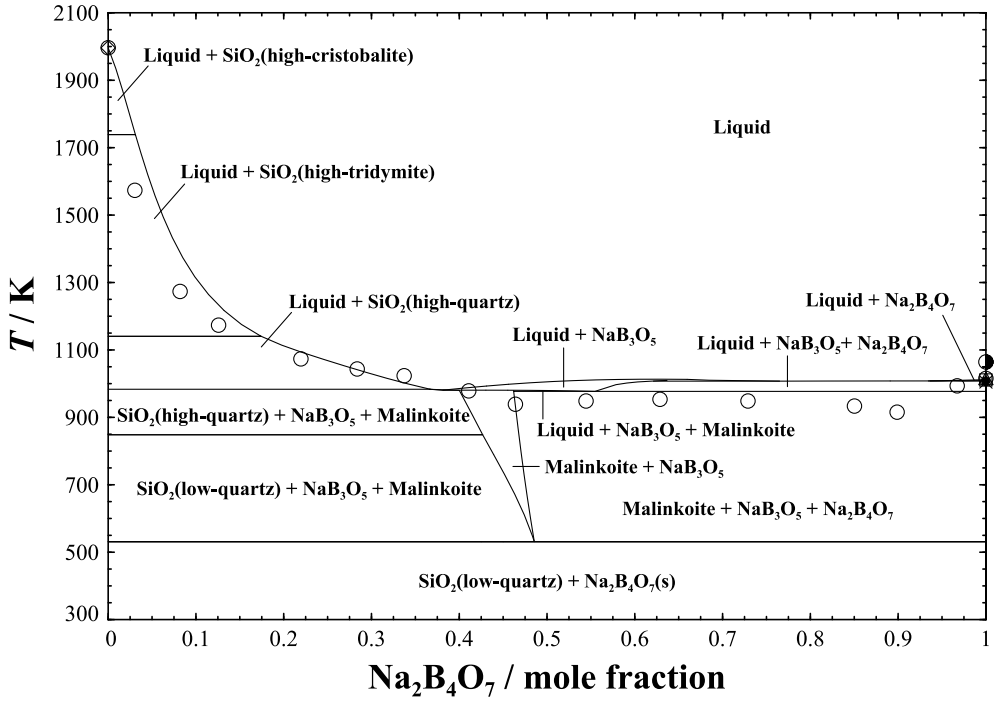

Fig. 4.9. Computed $Na_2B_4O_7$-SiO_2 pseudo-binary phase diagram with experimental measurements shown as points. Data: ◯187 □163, 165, 187, 215 ◇103 ✳216 ●214 △217 ◑212

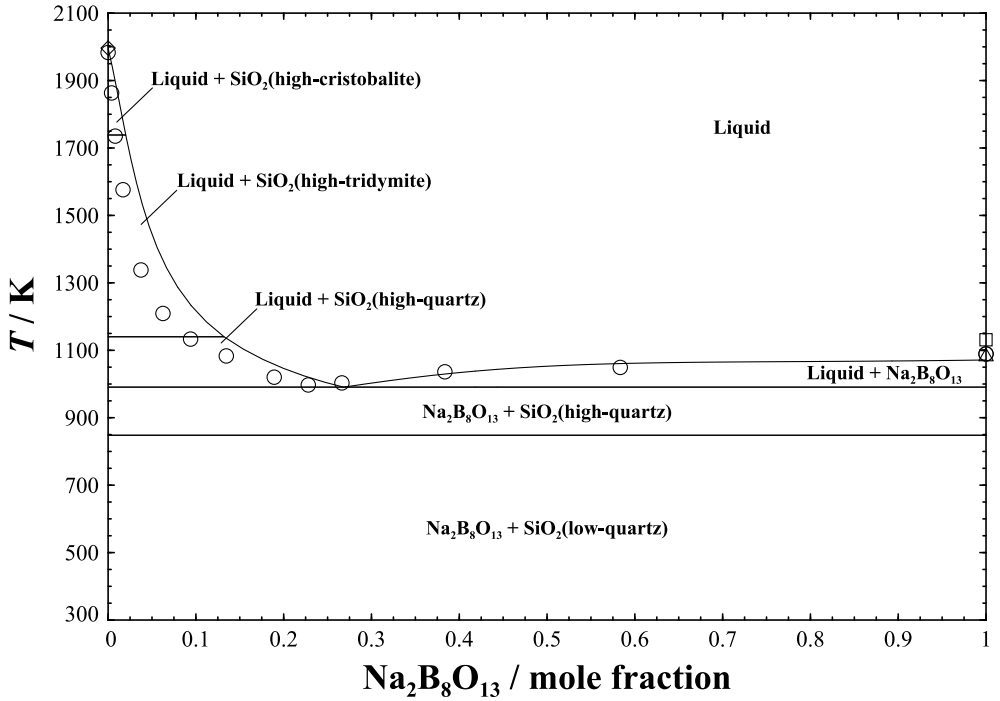

Fig. 4.10. Computed $Na_2B_8O_{13}$-SiO_2 pseudo-binary phase diagram with experimental measurements shown as points. Data: ◯188 ◇103 □212 △214

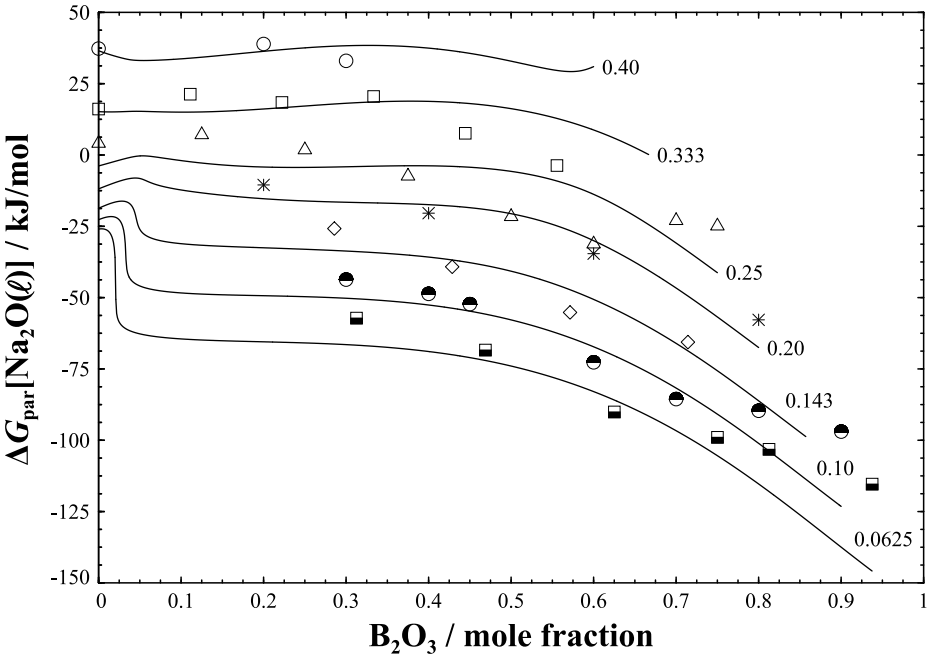

Fig. 4.11. Partial Gibbs energy of liquid Na_2O at 1200 K and specified Na_2O constant mole fractions in the Na_2O-B_2O_3-SiO_2 system referred to $Na_2O + 2B_2O_3$ with experimental measurements shown as points. Data[189]: ○ 40 mol% Na_2O, □ 33.3 mol% Na_2O, △ 25 mol% Na_2O, ✳ 20 mol% Na_2O, ◇ 14.3 mol% Na_2O, ◓ 10 mol% Na_2O, ◒ 6.25 mol% Na_2O

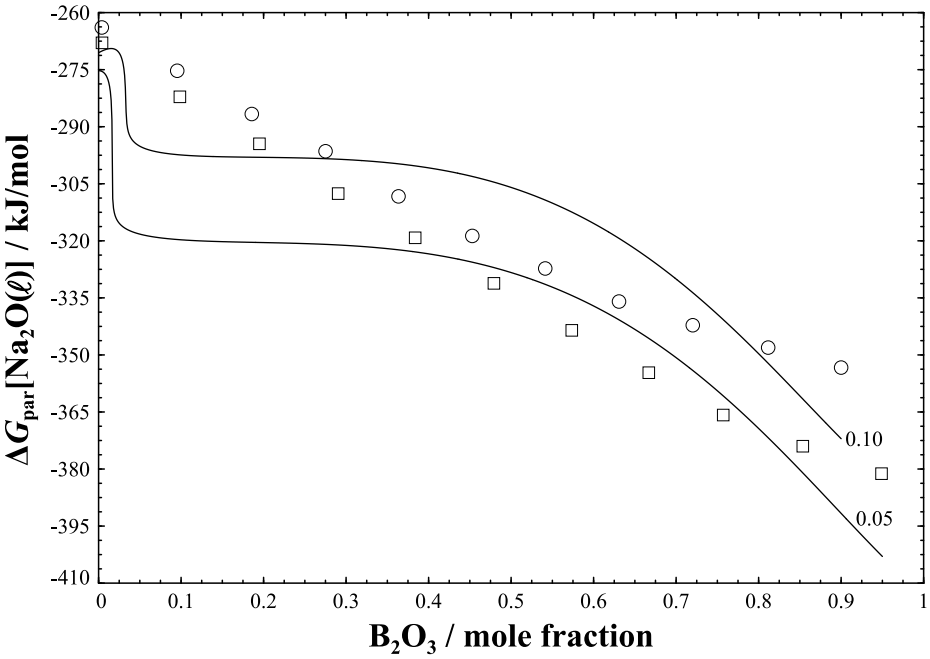

Fig. 4.12. Partial Gibbs energy of liquid Na_2O at 1223 K and 5 and 10% Na_2O constant mole fractions in the Na_2O-B_2O_3-SiO_2 system referred to pure Na_2O with experimental measurements shown as points. Data[190]: ○ 10 mol% Na_2O, □ 5 mol% Na_2O

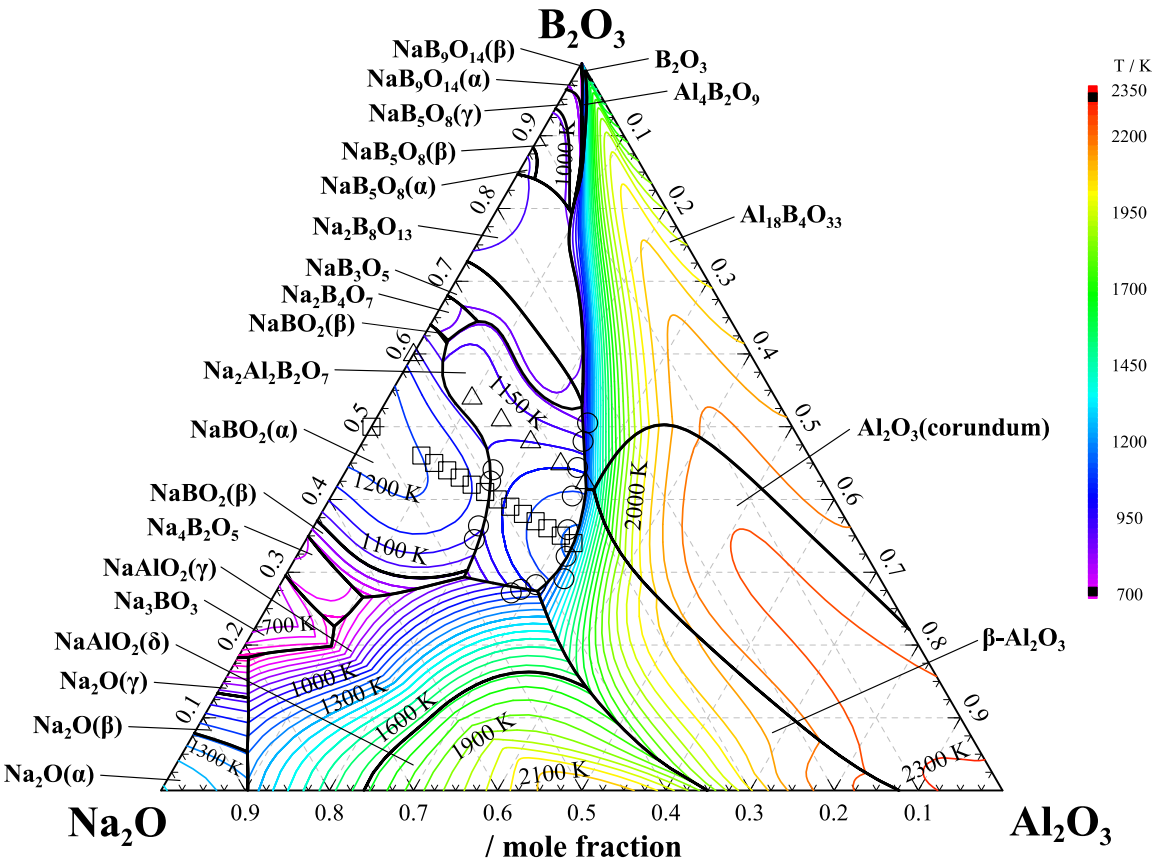

Fig. 4.13. Computed Na_2O-B_2O_3-Al_2O_3 system liquidus projections with liquidus experimental measurements shown as points. Data: ◯[192] □[201] △[202]

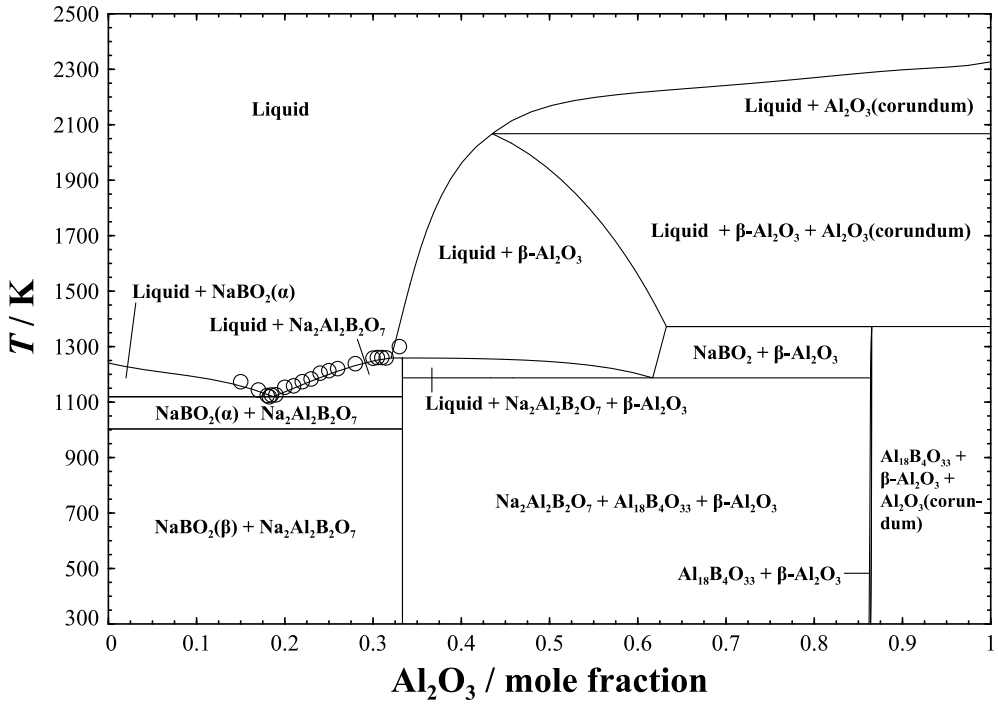

Fig. 4.14. Computed $NaBO_2$-Al_2O_3 pseudo-binary phase diagram with experimental measurements shown as points. Data: ◯ 194 □ 163, 213, 214 △ 212 ◇ 80

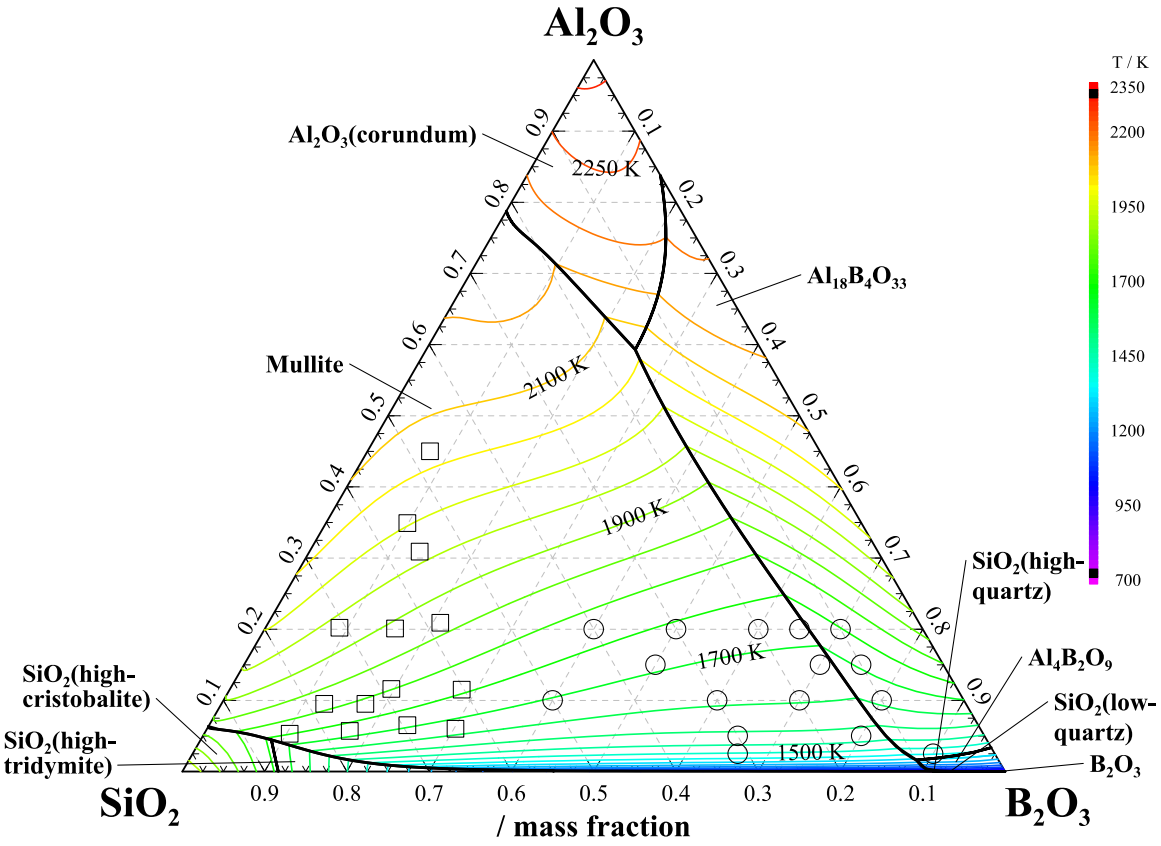

Fig. 4.15. Computed Al_2O_3-B_2O_3-SiO_2 system liquidus projections with liquidus experimental measurements shown as points. Data: ◯[179] □[203]

4.9. Copyright permission

In the case of the Accepted Manuscript and the Published Journal Article the Author Rights exclude Commercial Use (unless expressly agreed in writing by Elsevier Ltd), other than use by the author in a subsequent compilation of the author's works or to extend the Article to book length form or re-use by the author of portions or excerpts in other works (with full acknowledgment of the original publication of the Article).

AUTHOR REPRESENTATIONS / ETHICS AND DISCLOSURE / SANCTIONS

I affirm the Author Representations noted below, and confirm that I have reviewed and complied with the relevant Instructions to Authors, Ethics in Publishing policy, Declarations of Interest disclosure and information for authors from countries affected by sanctions (Iran, Cuba, Sudan, Burma, Syria, or Crimea). Please note that some journals may require that all co-authors sign and submit Declarations of Interest disclosure forms. I am also aware of the publisher's policies with respect to retractions and withdrawal (https://www.elsevier.com/about/our-business/policies/article-withdrawal).
For further information see the publishing ethics page at https://www.elsevier.com/about/our-business/policies/publishing-ethics and the journal home page. For further information on sanctions, see https://www.elsevier.com/about/our-business/policies/trade-sanctions

Author representations

- The Article I have submitted to the journal for review is original, has been written by the stated authors and has not been previously
- The Article was not submitted for review to another journal while under review by this journal and will not be submitted to any other
- The Article and the Supplemental Materials do not infringe any copyright, violate any other intellectual property, privacy or other righ entity, or contain any libellous or other unlawful matter.
- I have obtained written permission from copyright owners for any excerpts from copyrighted works that are included and have credit Article or the Supplemental Materials.
- Except as expressly set out in this Journal Publishing Agreement, the Article is not subject to any prior rights or licenses and, if my o institution has a policy that might restrict my ability to grant the rights required by this Journal Publishing Agreement (taking into acc permitted hereunder, including Internal Institutional Use), a written waiver of that policy has been obtained.
- If I and/or any of my co-authors reside in Iran, Cuba, Sudan, Burma, Syria, or Crimea, the Article has been prepared in a personal, a capacity and not as an official representative or otherwise on behalf of the relevant government or institution.
- If I am using any personal details or images of patients, research subjects or other individuals, I have obtained all consents required complied with the publisher's policies relating to the use of such images or personal information. See https://www.elsevier.com/abou business/policies/patient-consent for further information.
- Any software contained in the Supplemental Materials is free from viruses, contaminants or worms.
- If the Article or any of the Supplemental Materials were prepared jointly with other authors, I have informed the co-author(s) of the t Publishing Agreement and that I am signing on their behalf as their agent, and I am authorized to do so.

GOVERNING LAW AND JURISDICTION

This Agreement will be governed by and construed in accordance with the laws of the country or state of Elsevier Ltd ("the Governing State"), without regard to conflict of law principles, and the parties irrevocably consent to the exclusive jurisdiction of the courts of the Governing State.

For information on the publisher's copyright and access policies, please see http://www.elsevier.com/copyright.
For more information about the definitions relating to this agreement click here.

☑ **I have read and agree to the terms of the Journal Publishing Agreement.**

11th September 2018 T-copyright-v22/2017

Chapter 5

Expansion of Database to Include K_2O, Li_2O, CaO, Fe_2O_3, FeO, and MgO

5.1. Introduction

All pseudo-binary systems of K_2O, Li_2O, CaO, Fe_2O_3, FeO, and MgO with Na_2O, Al_2O_3, SiO_2, and B_2O_3 have been previously assessed (Table 5.1) with the exception of K_2O-B_2O_3, which required a new assessment. Experimental data available in literature for these systems was reviewed in the previous assessments and thus won't be repeated here. While a majority of these systems have been assessed prior to this work, it was necessary to reassess the systems to obtain a self-consistent database. The assessments listed in Table 5.1 were used as bases for the reassessments, and the solutions and stoichiometric compounds added to the database as part of these reassessments are discussed in Sections 5.2, 5.3, and 5.4. Overall, all new assessments agreed very well with data (Fig. 5.1 - Fig. 5.38). A select few diagrams showed minor discrepancies, which will be addressed in the subsections of Section 5.6. Also discussed in this section are notes of interest as it relates to conducting the assessments.

In addition to expanding the database by assessing additional pseudo-binary systems, the nepheline and carnegieite CEF models were expanded by adding minor oxide species to the sublattice formalisms. Details of this expansion process are discussed in Section 5.7 including assessments of the $NaAlSiO_4$-$NaFeSiO_4$ and $NaAlSiO_4$-$NaFeSi_2O_6$ systems as part of adding Fe to the CEF models.

5.2. Expanded liquid phase

The TSPIL model was expanded to account for the oxides K_2O, Li_2O, CaO, MgO, Fe_2O_3, and FeO by adding the species K^{+1}, Li^{+1}, M^{+2}, Ca^{+2}, and Fe^{+2} to the first sublattice and $FeO^0_{1.5}$ to the second. The inclusion of the alkaline earth cations and Fe^{+2} was straightforward as each combined with the O^{-2} anionic species on the second sublattice generated the desired oxide endmember. Addition of the neutral $FeO^0_{1.5}$ species on the second sublattice to obtain a scaled down Fe_2O_3 endmember enabled Selleby,[220] Fabrichnaya & Sundman,[221] and Dreval et al.[222] to successfully assess the FeO-Fe_2O_3-SiO_2[220, 221] and FeO-Fe_2O_3-Al_2O_3[222] systems; hence, this approach was also adopted in this work to ultimately yield the TSPIL model:

$$\left(Al^{+3}, Na^{+1}, K^{+1}, Li^{+1}, Mg^{+2}, Ca^{+2}, Fe^{+2}\right)_P\left(AlO_2^{-1}, O^{-2}, SiO_4^{-4}, BO_3^{-3}, B_3O^0_{4.5}, FeO^0_{1.5}, SiO^0_2\right)_Q.$$

The endmember Gibbs energy functions as well as the 106 RK interaction parameters required to assess the pseudo-binary major-minor oxide systems are displayed in Table 5.2. An additional 5 RK parameters were needed to complete assessments of the $NaAlSiO_4$-$NaFeSiO_4$ and $NaAlSiO_4$-$NaFeSi_2O_6$ systems (Table 5.2). Gibbs energies of the liquid oxide components that contributed to the TPSIL endmember Gibbs energies are displayed in Table 5.3.

5.3. Solid solutions in major-minor oxide systems

6 solid solutions were added to the database, and the β-Al_2O_3 model was expanded from the previous assessment of the Na_2O-Al_2O_3 system (Section 3.6.2) as part of assessing the major-minor pseudo-binary oxide systems (Table 5.4).

The nepheline and carnegieite CEF models resulting from the assessment of the Na_2O-Al_2O_3-SiO_2 system (Section 3.6.4) were expanded to include minor oxide species as discussed in detail in Section 5.7.

5.3.1.1. Wustite

The one-lattice polynomial model structure was adopted from Moosavi-Khoonsari & Jung.[223] However, as this assessment employed the Modified Quasichemical Model[175] to characterize the liquid phase of the Na_2O-FeO-Fe_2O_3 system, the wustite model required reoptimization to experimental data. Also, the Fe_2O_3 species included by Moosavi-Khoonsari & Jung[223] was removed from the model lattice as wustite is not stable in the Na_2O-Fe_2O_3 system.

5.3.2. Fe-Spinel, Mg-Spinel, & Mg-Halite

Endmember Gibbs energies were initially adopted from Dreval et al[222] and Zienert & Fabrichnaya[224] for the Fe- and Mg-Spinel solid solutions, respectively. However, as the TSPIL models used by Dreval et al[222] and Zienert & Fabrichnaya[224] contained the $AlO_{1.5}$ species instead of the AlO_2 species used in this work, the liquid model parameters differed. This resulted in the need to reoptimize the Fe- and Mg-Spinel as well as Mg-Halite solid solutions to experimental data. Revised endmember Gibbs energies in the form of standard enthalpies and entropies of formation and heat capacities are listed in Table 5.5 while the RK parameters for these solutions are in Table 5.4.

5.4. Stoichiometric compounds of expanded database

Table 5.6 lists all the stoichiometric compounds added to the database from the expansion process, which totals to 148. 85 were added from assessing the pseudo-binary major-minor oxide systems. The remaining 63 consist of all the ternary and higher order phases available in the FactSage[43] FToxid, FactPS, and TDnucl databases that were composed of oxides contained in the database, which were added to be comprehensive and to account for the formation of secondary phases such as pyroxene that have been observed to form in HLW glass samples.[54]

The Gibbs energy descriptions of 20 compounds were obtained from references external to FactSage, and 10 were developed in this work, the latter contributing to assessments of the K_2O-B_2O_3, Fe_2O_3-B_2O_3, and FeO-B_2O_3 systems. Derivation of the Gibbs energy functions followed the same method as discussed in Sections 3.4.1 and 4.4.2, where the Neumann-Kopp rule[204, 225] was initially applied to estimate heat capacities and then standard enthalpies of formation were optimized to experimental data.

5.5. Addition of O_2 molecule

The gaseous O_2 molecule was added to the database to enable assessment of systems containing Fe as experimental measurements were often made with samples exposed to air. Thermodynamic values for O_2(g) are listed in Table 5.7.

5.6. Assessments of major-minor oxide pseudo-binary systems

5.6.1. Na_2O with alkali earth metals

Rankin & Merwin[226] observed that in all fused mixtures of CaO and MgO, the two oxides crystallized out and showed no evidence of forming a stable compound in contact with the melt indicating the tendency for alkali and alkali earth metals to favor separation

as opposed to intermediate compound formation. Pseudo-ternary thermodynamic studies[87, 227-235] containing various combinations of Na_2O, K_2O, Li_2O, and/or MgO as two of the three oxides considered have confirmed this result with no intermediate compound consisting exclusively of Na_2O with K_2O, Li_2O, or MgO reported as stable. Due to this, similar to the approach applied by Vedishcheva & Shakhmatkin,[228] the liquid phase of the pseudo-binary systems of Na_2O with K_2O, Li_2O, and MgO were treated as ideal solutions.

5.6.2. K_2O-Al_2O_3

As noted by Eriksson et al.,[80] the phase equilibria data reported by Moya et al.[236] conflicts with Eliezer & Howald[237] and Roth,[238] hence the Moya et al. data was neglected in the optimization of the K_2O-Al_2O_3 system. As noted by Eriksson et al.[80] and indicated by Fig. 3.2, studies indicate that β-Al_2O_3 has a narrow solubility range in the $NaAl_9O_{14}$ to $Na_2Al_{12}O_{19}$ composition region, which conflicts with the experimental data available for the similar K-containing β-Al_2O_3 solution (Fig. 5.2). Thus, while this led Eriksson et al.[80] to treat β-Al_2O_3 as a line compound with the composition KAl_9O_{14}, the present assessment added K_2O to the existing β-Al_2O_3 solid solution CEF model (Table 5.4) and was optimized to have a solubility range similar to Fig. 3.2.

5.6.3. K_2O-SiO_2

Due to a lack of experimental data, the liquidus boundary of Fig. 5.3 at > 50 mol% SiO_2 required estimation. While Zhang et al. did not include the K_4SiO_4 compound in their assessment of the K_2O-SiO_2 system, the TSPIL model in this work required the inclusion of this compound to reasonably represent the phase equilibrium behavior in this region. The intermediate compound Na_4SiO_4 is known to form in the similar Na_2O-SiO_2 system (Fig. 3.3) and thus provides a strong basis for the inclusion of K_4SiO_4 in Fig. 5.3.

5.6.4. K_2O-B_2O_3

The K_2O-B_2O_3 system required a new assessment. Phase equilibria data from Rollet,[239, 240] Polyakova & Tokareva,[241] and Kaplun & Meshalkin[242] were considered when conducting the assessment. The more recent experimental studies of Polyakova & Tokareva,[241] and Kaplun & Meshalkin[242] were more self-consistent than the data reported by Rollet,[239, 240] hence the former data was included in the system optimization. The assessment compromised between the $K_2B_4O_7$-$K_2B_6O_{10}$ eutectic and $K_{10}B_{38}O_{62}$ melting temperatures, ultimately obtaining reasonable agreement with both.

5.6.5. Fe_2O_3-Na_2O at 0.21 atm O_2 partial pressure

Similar to the assessment of the K_2O-SiO_2 system, the liquidus boundary in the Fe_2O_3-Na_2O system in air at > 50 mol% Na_2O required estimation due to lack of equilibria data. While the estimated liquidus curve in Fig. 5.22 differs from the previous assessment,[223] the shape of the curve at > 50 mol% Na_2O was required to obtain the overall fit to experimental data.

5.6.6. Fe_2O_3-SiO_2

Experimental data was not exclusively available for Fe_2O_3-SiO_2. The previous assessment conducted by Selleby[220] generated the Fe_2O_3-SiO_2 diagram from the assessment of the Fe_2O_3-FeO-SiO_2 pseudo-ternary system. The new assessment of the system incorporated the invariant points calculated by Selleby[220] and obtained good agreement.

5.6.7. FeO-B_2O_3 saturated with solid Fe

Fig. 5.32 displays better agreement with liquidus curve reported by Koch et al. in the Slag Atlas[243] than the data measured by Fujiwara et al.[244] As expected, discrepancy also

exists between database calculations of solid and liquid FeO activity with the activity data of Fujiwara et al.[244] as the authors used the activity measurements as a basis for the liquidus boundary points. As noted by Jakobsson et al.[245] in a previous assessment of the $FeO-B_2O_3$ system, experimental data is limited, and thus obtaining good agreement with phase equilibrium data from one of the two available studies is considered sufficient.

5.6.8. $MgO-B_2O_3$

Similar to the assessment by Chen et al.,[162] the calculated activity curves of Fig. 5.38 have better agreement with Zhang & Ji[246] than Wang et al.[247]

5.7. Expansion of nepheline solid solution CEF model

The nepheline solid solution CEF model was expanded to incorporate K, Ca, and Fe, which are elements known to go into solution with nepheline,[5, 6, 248-253] in sublattice form:

$(NaAl^{+4},KAl^{+4},NaFe^{+4},Ca_{0.5}Al^{+4},Mg_{0.5}Al^{+4},VaSi^{+4})_8[Si^{+4}]_8\{O^{-2}\}_{32}$.

Addition of the $Ca_{0.5}Al^{+4}$ species allowed the necessary generation of the anorthite, $CaAl_2Si_2O_8$, endmember, which is stable in the $Ca_2O-Al_2O_3-SiO_2$ system.[100, 254] For this endmember as well as for $KAlSiO_4$, Gibbs energies were available in the FToxid database of FactSage[255] and thus were adopted as initial descriptions. As the $MgAl_2Si_2O_8$ endmember produced from the $Mg_{0.5}Al^{+4}$ species is not stable in the $MgO-Al_2O_3-SiO_2$ system,[256] the Gibbs energy of the stoichiometrically similar $Mg_2Al_4Si_5O_{18}$ compound from FToxid was used as the primary energetic function. No such Gibbs energy values were available for $NaFeSiO_4$, which necessitated conducting novel assessments of the $NaAlSiO_4-NaFeSiO_4$ and $NaAlSiO_4-NaFeSi_2O_6$ systems as part of the endmember optimization..

Li and B were not incorporated in the sublattice model as experimental studies have established that Li is not observed to go into solution in nepheline,[6, 257-260] and B is unlikely to go into solution in a system composed of oxides common to HLW glass systems.[259, 260] As summarized by Marcial et al[259] and Pierce et al,[3] possible explanations for the resistance of these elements to go into solution in nepheline is the preferred eucryptite crystal structure,[258] and the interaction of Na and Al in nepheline is more energetically favored than between Na and B, which results in the formation of Na-[AlO_4] and BO_3 moieties at the expense of Na-[BO_4] moieties.[261-263] While Li and B are not included in the nepheline model, the thermodynamic effect of Li and B on nepheline precipitating from the liquid phase are accounted for in computing equilibria through inclusion of pseudo-binary and -ternary systems containing Li_2O and B_2O_3 in the current database.

5.7.1. Assessment of $NaAlSiO_4$-$NaFeSiO_4$ and $NaAlSiO_4$-$NaFeSi_2O_6$ systems

Experimental phase equilibria data reported in studies[250-252] were used to conduct assessments of the $NaAlSiO_4$-$NaFeSiO_4$ and $NaAlSiO_4$-$NaFeSi_2O_6$ systems with the resulting diagrams displayed in Fig. 5.39 and Fig. 5.40, respectively. The calculated liquidus curve of each diagram agree well with measurements while the nepheline to carnegieite computed transition temperatures are somewhat elevated in comparison to measurements. Regardless, as discussed in Section 6.2, these assessments resulted in the nepheline model well representing data with for compositions containing Fe.

5.8. Conclusion

Assessments of major-minor oxide pseudo-binary systems were successfully completed thus expanding the database to include the oxides K_2O, Li_2O, CaO, MgO, Fe_2O_3, and FeO. Additionally, species were added to the first sublattice of the nepheline CEF

model to obtain endmembers representing solubility of K, Ca, Mg, and Fe in nepheline. The inclusion of Fe necessitated assessing the $NaAlSiO_4$-$NaFeSiO_4$ and $NaAlSiO_4$-$NaFeSi_2O_6$ systems to obtain an accurate Gibbs energy description of the $NaFeSiO_4$ nepheline model endmember. As the database now contains the HLW glass oxides identified by Li et al.[8] to affect nepheline precipitation, experimental HLW glass data can now be used to validate the accuracy of database calculations.

5.9. Tables

Table 5.1. Previous assessments used as a bases for assessments conducted in this work

System	Previous assessment
K_2O-Al_2O_3	Eriksson et al[80]
K_2O-SiO_2	Zhang et al[82]
K_2O-B_2O_3	Kaplun & Meshalkin[242]
CaO-Al_2O_3	Hallstedt[264]
CaO-SiO_2	Eriksson et al[265]
CaO-B_2O_3	Yu et al[158]
Li_2O-Al_2O_3	Kulkarni & Besmann[266]
Li_2O-SiO_2	Konar et al[267]
Li_2O-B_2O_3	Yu et al[160]
Fe_2O_3-Na_2O	Moosavi-Khoonsari & Jung[223]
Fe_2O_3-Al_2O_3	Dreval et al[222]
Fe_2O_3-SiO_2	Selleby[220]
Fe_2O_3-B_2O_3	Jakobsson et al[245]
FeO-Na_2O	Moosavi-Khoonsari & Jung[223]
FeO-Al_2O_3	Dreval et al[222]
FeO-SiO_2	Fabrichnaya & Sundman[221]
FeO-B_2O_3	Jakobsson et al[245]
MgO-Al_2O_3	Zienert & Fabrichnaya[224]
MgO-SiO_2	Fabrichnaya[268]
MgO-B_2O_3	Chen et al[162]

Table 5.2. TSPIL model parameters for assessments of the major-minor oxide, $NaAlSiO_4$- $NaFeSiO_4$, and $NaAlSiO_4$-$NaFeSi_2O_6$ systems

---

Oxide liquid $\left(Al^{+3}, Na^{+1}, K^{+1}, Li^{+1}, Mg^{+2}, Ca^{+2}, Fe^{+2}\right)_P \left(AlO_2^{-1}, O^{-2}, SiO_4^{-4}, BO_3^{-3}, B_3O_{4.5}^0, FeO_{1.5}^0, SiO_2^0\right)_Q$

$^{o}G_{Fe_3O_{4.5}} = 1.5\,^{o}G_{Fe_2O_3(L)}$
$^{o}G_{FeO_{1.5}} = 0.5\,^{o}G_{Fe_2O_3(L)}$
$^{o}G_{KAlO_2} = 0.5\,^{o}G_{K_2O(L)} + 0.5\,^{o}G_{Al_2O_3(L)} - 153287.55 - 16.766T$
$^{o}G_{K_2O} = {}^{o}G_{K_2O(L)}$
$^{o}G_{K_4SiO_4} = {}^{o}G_{SiO_2(L)} + 2\,^{o}G_{K_2O(L)} - 476973.24 - 31.792T$
$^{o}G_{K_3BO_3} = 1.5\,^{o}G_{K_2O(L)} + 0.5\,^{o}G_{B_2O_3(L)} - 173515.5602 - 83.972T$
$^{o}G_{B_3O_{4.5}} = 1.5\,^{o}G_{B_2O_3(L)}$
$^{o}G_{FeO_{1.5}} = 0$
$^{o}G_{SiO_2} = {}^{o}G_{SiO_2(L)}$
$^{o}G_{AlLiO_2} = 0.5\,^{o}G_{Li_2O(L)} + 0.5\,^{o}G_{Al_2O_3(L)} - 77787.49 + 4.702T$
$^{o}G_{Li_2O} = {}^{o}G_{Li_2O(L)}$
$^{o}G_{Li_4SiO_4} = 2\,^{o}G_{Li_2O(L)} + {}^{o}G_{SiO_2(L)} - 242322.25 - 1.408T$
$^{o}G_{Li_3BO_3} = 1.5\,^{o}G_{Li_2O(L)} + 0.5\,^{o}G_{B_2O_3(L)} - 185579.42 + 3.613T$
$^{o}G_{B_3O_{4.5}} = 1.5\,^{o}G_{B_2O_3(L)}$
$^{o}G_{FeO_{1.5}} = 0$
$^{o}G_{SiO_2} = {}^{o}G_{SiO_2(L)}$
$^{o}G_{Al_2MgO_4} = {}^{o}G_{MgO(L)} + {}^{o}G_{Al_2O_3(L)} + 318474.4 - 153.682T$
$^{o}G_{Mg_2O_2} = 2\,^{o}G_{MgO(L)}$
$^{o}G_{Si_2Mg_4O_8} = 4\,^{o}G_{MgO(L)} + 2\,^{o}G_{SiO_2(L)} + -340980.44 + 67.287T$
$^{o}G_{Mg_3B_2O_6} = 3\,^{o}G_{MgO(L)} + {}^{o}G_{B_2O_3(L)} - 198373.63 + 21.882T$
$^{o}G_{B_6O_9} = 3\,^{o}G_{B_2O_3(L)}$
$^{o}G_{Fe_2O_3} = 0$
$^{o}G_{Si_2O_4} = 2\,^{o}G_{SiO_2(L)}$
$^{o}G_{CaAl_2O_4} = {}^{o}G_{CaO(L)} + {}^{o}G_{Al_2O_3(L)} - 164688.88 + 33.804T$
$^{o}G_{Ca_2O_2} = 2\,^{o}G_{CaO(L)}$
$^{o}G_{Ca_4Si_2O_8} = 4\,^{o}G_{CaO(L)} + 2\,^{o}G_{SiO_2(L)} - 426285.48 + 25.734T$
$^{o}G_{Ca_3B_2O_6} = {}^{o}G_{B_2O_3(L)} + 3\,^{o}G_{CaO(L)} - 338108 + 2.215T$
$^{o}G_{B_6O_9} = 3\,^{o}G_{B_2O_3(L)}$
$^{o}G_{Fe_2O_3} = 0$
$^{o}G_{Si_2O_4} = 2\,^{o}G_{SiO_2(L)}$
$^{o}G_{FeAl_2O_4} = {}^{o}G_{FeO(L)} + {}^{o}G_{Al_2O_3(L)} + 125000 - 85T$
$^{o}G_{Fe_2O_2} = 2\,^{o}G_{FeO(L\_1)}$
$^{o}G_{Fe_4Si_2O_8} = 4\,^{o}G_{FeO(L\_1)}\mathrm{F} + 2\,^{o}G_{SiO_2(L)} + 12806.46 - 13.693T$
$^{o}G_{Fe_3B_2O_6} = 3\,^{o}G_{FeO(L\_1)} + {}^{o}G_{B_2O_3(L)}$
$^{o}G_{B_6O_9} = 3\,^{o}G_{B_2O_3(L)}$
$^{o}G_{Fe_2O_3} = {}^{o}G_{Fe_2O_3(L)}$
$^{o}G_{Si_2O_4} = 2\,^{o}G_{SiO_2(L)}$

$^{0}L_{Ca^{+2}:O^{-2},SiO_2^0} = -30622 - 12.2T$

$^{1}L_{Ca^{+2}:O^{-2},SiO_2^0} = -139424 + 67.4T$

$^{2}L_{Ca^{+2}:O^{-2},SiO_2^0} = -33547 + 22.5T$

$^{3}L_{Ca^{+2}:O^{-2},SiO_2^0} = -97015 + 24.6T$

$^{0}L_{Ca^{+2}:SiO_4^{-4},SiO_2^0} = 2\ ^{0}L_{Ca^{+2},O^{-2},SiO_2^0}$

$^{1}L_{Ca^{+2}:SiO_4^{-4},SiO_2^0} = 2\ ^{1}L_{Ca^{+2},O^{-2},SiO_2^0}$

$^{2}L_{Ca^{+2}:SiO_4^{-4},SiO_2^0} = 2\ ^{2}L_{Ca^{+2},O^{-2},SiO_2^0}$

$^{3}L_{Ca^{+2}:SiO_4^{-4},SiO_2^0} = 2\ ^{3}L_{Ca^{+2},O^{-2},SiO_2^0}$

$^{0}L_{Ca^{+2}:O^{-2},SiO_4^{-4}} = 41317$

$^{0}L_{Ca^{+2}:O^{-2},BO_3^{-3}} = 12758 - 11.1T$

$^{1}L_{Ca^{+2}:O^{-2},BO_3^{-3}} = -32073 + 12T$

$^{2}L_{Ca^{+2}:O^{-2},BO_3^{-3}} = 35481$

$^{0}L_{Ca^{+2}:O^{-2},B_3O_{4.5}^0} = 187599 - 104.5T$

$^{1}L_{Ca^{+2}:O^{-2},B_3O_{4.5}^0} = 12513 + 103.5T$

$^{2}L_{Ca^{+2}:O^{-2},B_3O_{4.5}^0} = -151861$

$^{0}L_{Ca^{+2}:BO_3^{-3},B_3O_{4.5}^0} = -82869 - 125.8T$

$^{1}L_{Ca^{+2}:BO_3^{-3},B_3O_{4.5}^0} = -238727 + 87.1T$

$^{2}L_{Ca^{+2}:BO_3^{-3},B_3O_{4.5}^0} = 26206 + 39.3T$

$^{0}L_{Fe^{+2}:O^{-2},SiO_2^0} = -68426 + 60.8T$

$^{1}L_{Fe^{+2}:O^{-2},SiO_2^0} = -118041 + 44.9T$

$^{2}L_{Fe^{+2}:O^{-2},SiO_2^0} = 82003$

$^{0}L_{Fe^{+2}:SiO_4^{-4},SiO_2^0} = 64793 - 25.1T$

$^{1}L_{Fe^{+2}:SiO_4^{-4},SiO_2^0} = -149655 + 79.2TT$

$^{2}L_{Fe^{+2}:SiO_4^{-4},SiO_2^0} = 81725$

$^{0}L_{Fe^{+2}:O^{-2},SiO_4^{-4}} = 38191 - 5T$

$^{0}L_{Mg^{+2}:O^{-2},SiO_2^0} = 190605 - 93.04T$

$^{1}L_{Mg^{+2}:O^{-2},SiO_2^0} = -212.38$

$^{2}L_{Mg^{+2}:O^{-2},SiO_2^0} = 164928 - 54.98T$

$^{3}L_{Mg^{+2}:O^{-2},SiO_2^0} = -2500$

$^{0}L_{Mg^{+2}:SiO_4^{-4},SiO_2^0} = 2\ ^{0}L_{Mg^{+2}:O^{-2},SiO_2^0}$

$^{1}L_{Mg^{+2}:SiO_4^{-4},SiO_2^0} = 2\ ^{1}L_{Mg^{+2}:O^{-2},SiO_2^0}$

$^{2}L_{Mg^{+2}:SiO_4^{-4},SiO_2^0} = 2\ ^{2}L_{Mg^{+2}:O^{-2},SiO_2^0}$

$^{3}L_{Mg^{+2}:SiO_4^{-4},SiO_2^0} = 2\ ^{3}L_{Mg^{+2}:O^{-2},SiO_2^0}$

$^{0}L_{Fe^{+2}:FeO_{1.5}^0,SiO_2^0} = 80465 - 22.95T$

$^{1}L_{Fe^{+2}:FeO_{1.5}^0,SiO_2^0} = 32129 - 19.24T$

$^{0}L_{Mg^{+2}:AlO_2^{-1},O^{-2}} = -25000 - 15T$

$^{0}L_{Al^{+3},Mg^{+2}:AlO_2^{-1}} = -90000$

$^{0}L_{Al^{+3},Mg^{+2}:AlO_2^{-1},O^{-2}} = -600000 - 3.5T$

$^{0}L_{Mg^{+2}:O^{-2},B_3O_{4.5}^0} = 40014 - 26.67T$

$^{1}L_{Mg^{+2}:O^{-2},B_3O_{4.5}^0} = -56390 + 5.1T$

$^{2}L_{Mg^{+2}:O^{-2},B_3O_{4.5}^0} = 6822.5$

$^{0}L_{Mg^{+2}:BO_3^{-3},B_3O_{4.5}^{0}} = 75229 - 63.7T$

$^{1}L_{Mg^{+2}:BO_3^{-3},B_3O_{4.5}^{0}} = -143825 + 18.2T$

$^{2}L_{Mg^{+2}:BO_3^{-3},B_3O_{4.5}^{0}} = -10185$

$^{0}L_{Li^{+1}:O^{-2},BO_3^{-3}} = -60956 + 39.24T$

$^{1}L_{Li^{+1}:O^{-2},BO_3^{-3}} = -2209.8$

$^{2}L_{Li^{+1}:O^{-2},BO_3^{-3}} = 19085$

$^{0}L_{Li^{+1}:BO_3^{-3},B_3O_{4.5}^{0}} = -140554 - 52.9T$

$^{1}L_{Li^{+1}:BO_3^{-3},B_3O_{4.5}^{0}} = -46837$

$^{2}L_{Li^{+1}:BO_3^{-3},B_3O_{4.5}^{0}} = -31712$

$^{0}L_{Al^{+3},Li^{+1}:AlO_2^{-1}} = -248420 + 101.4T$

$^{1}L_{Al^{+3},Li^{+1}:AlO_2^{-1}} = 35511 - 22.2T$

$^{2}L_{Al^{+3},Li^{+1}:AlO_2^{-1}} = 61564 - 33.75T$

$^{0}L_{Li^{+1}:AlO_2^{-1},O^{-2}} = -134221 + 66.9T$

$^{0}L_{Li^{+1}:O^{-2},SiO_2^{0}} = -62724 + 9.65T$

$^{1}L_{Li^{+1}:O^{-2},SiO_2^{0}} = -30777 + 18.6T$

$^{2}L_{Li^{+1}:O^{-2},SiO_2^{0}} = 2909 - 0.85T$

$^{3}L_{Li^{+1}:O^{-2},SiO_2^{0}} = -32475 + 11.8T$

$^{0}L_{Li^{+1}:O^{-2},SiO_4^{-4}} = 90581 - 92T$

$^{1}L_{Li^{+1}:O^{-2},SiO_4^{-4}} = -43796 + 6.73T$

$^{0}L_{Li^{+1}:SiO_4^{-4},SiO_2^{0}} = 2\ ^{0}L_{Li^{+1}:O^{-2},SiO_2^{0}}$

$^{1}L_{Li^{+1}:SiO_4^{-4},SiO_2^{0}} = 2\ ^{1}L_{Li^{+1}:O^{-2},SiO_2^{0}}$

$^{2}L_{Li^{+1}:SiO_4^{-4},SiO_2^{0}} = 2\ ^{2}L_{Li^{+1}:O^{-2},SiO_2^{0}}$

$^{3}L_{Li^{+1}:SiO_4^{-4},SiO_2^{0}} = 2\ ^{3}L_{Li^{+1}:O^{-2},SiO_2^{0}}$

$^{0}L_{K^{+1}:O^{-2},BO_3^{-3}} = 3575 - 26.44T$

$^{1}L_{K^{+1}:O^{-2},BO_3^{-3}} = 15201 - 15.63T$

$^{0}L_{K^{+1}:BO_3^{-3},B_3O_{4.5}^{0}} = -458426 - 53.95T$

$^{1}L_{K^{+1}:BO_3^{-3},B_3O_{4.5}^{0}} = -18250 - 7.9T$

$^{2}L_{K^{+1}:BO_3^{-3},B_3O_{4.5}^{0}} = 22316 - 24.1T$

$^{3}L_{K^{+1}:BO_3^{-3},B_3O_{4.5}^{0}} = 31888 - 54.3T$

$^{0}L_{Al^{+3},K^{+1}:AlO_2^{-1}} = -75373 + 40T$

$^{1}L_{Al^{+3},K^{+1}:AlO_2^{-1}} = -14060 + 10.5T$

$^{0}L_{K^{+1}:AlO_2^{-1},O^{-2}} = 20064$

$^{0}L_{K^{+1}:O^{-2},SiO_2^{0}} = -86676 - 13.8T$

$^{1}L_{K^{+1}:O^{-2},SiO_2^{0}} = 118130 - 63.7T$

$^{2}L_{K^{+1}:O^{-2},SiO_2^{0}} = 31645 - 47.7T$

$^{3}L_{K^{+1}:O^{-2},SiO_2^{0}} = -37079$

$^{0}L_{K^{+1}:SiO_4^{-4},SiO_2^{0}} = 2\ ^{0}L_{K^{+1}:O^{-2},SiO_2^{0}}$

$^{1}L_{K^{+1}:SiO_4^{-4},SiO_2^{0}} = 2\ ^{1}L_{K^{+1}:O^{-2},SiO_2^{0}}$

$^{2}L_{K^{+1}:SiO_4^{-4},SiO_2^{0}} = 2\ ^{2}L_{K^{+1}:O^{-2},SiO_2^{0}}$

$^{3}L_{K^{+1}:SiO_4^{-4},SiO_2^{0}} = 2\ ^{3}L_{K^{+1}:O^{-2},SiO_2^{0}}$

$^{0}L_{K^{+1}:O^{-2},SiO_4^{-4}} = -9403$

$^{0}L_{Fe^{+2}:O^{-2},B_3O_{4.5}^{0}} = 53996 - 57T$

$^{1}L_{Fe^{+2}:O^{-2},B_3O_{4.5}^{0}} = -59726 - 45T$

$^{2}L_{Fe^{+2}:O^{-2},B_3O_{4.5}^{0}} = 21933 - 40T$

$^{0}L_{Fe^{+2}:BO_3^{-3},B_3O_{4.5}^{0}} = 50000$

$^{0}L_{Na^{+1},Fe^{+2}:O^{-2}} = -135623 - 27.8T$

$^{1}L_{Na^{+1},Fe^{+2}:O^{-2}} = -17049 - 74.2T$

$^{2}L_{Na^{+1},Fe^{+2}:O^{-2}} = 12019 - 76.3T$

$^{3}L_{Na^{+1},Fe^{+2}:O^{-2}} = -121399 + 26.5T$

$^{0}L_{Na^{+1}:O^{-2},FeO_{1.5}^{0}} = -252281 + 66.4T$

$^{1}L_{Na^{+1}:O^{-2},FeO_{1.5}^{0}} = 102329 - 49.6T$

$^{2}L_{Na^{+1}:O^{-2},FeO_{1.5}^{0}} = 88294 - 44.1T$

$^{3}L_{Na^{+1}:O^{-2},FeO_{1.5}^{0}} = -52294.5 - 86.8T$

$^{0}L_{Al^{+3},Fe^{+2}:AlO_2^{-1}} = 6.5T$

$^{0}L_{Fe^{+2}:AlO_2^{-1},O^{-2}} = 3433.54 + 20T$

$^{1}L_{Fe^{+2}:AlO_2^{-1},O^{-2}} = 2677.85$

$^{0}L_{Fe^{+2}:AlO_2^{-1},FeO_{1.5}^{0}} = 25T$

$^{0}L_{Al^{+3}:AlO_2^{-1},FeO_{1.5}^{0}} = 20T$

$^{2}L_{Fe^{+2}:FeO_{1.5}^{0}SiO_2^{0}} = 25259 - 6.59T$

$^{0}L_{Ca^{+2}:AlO_2^{-1},O^{-2}} = -55518 - 9.87T$

$^{1}L_{Ca^{+2}:AlO_2^{-1},O^{-2}} = 28481 - 5.69T$

$^{2}L_{Ca^{+2}:AlO_2^{-1},O^{-2}} = 32805.6 + 1.49T$

$^{0}L_{Al^{+3},Ca^{+2}:AlO_2^{-1}} = -46401 + 1.93T$

$^{1}L_{Al^{+3},Ca^{+2}:AlO_2^{-1}} = 1057$

$^{2}L_{Al^{+3},Ca^{+2}:AlO_2^{-1}} = 760$

$^{0}L_{Na^{+1}:AlO_2^{-1},FeO_{1.5}^{0}} = 77283 - 55.8T$

$^{1}L_{Na^{+1}:AlO_2^{-1},FeO_{1.5}^{0}} = 7231.2 + 14.94T$

$^{0}L_{Na^{+1}:FeO_{1.5}^{0},SiO_2^{0}} = 140367 - 93.36T$

$^{1}L_{Na^{+1}:FeO_{1.5}^{0},SiO_2^{0}} = 15T$

$^{0}L_{Na^{+1}:SiO_4^{-4},FeO_{1.5}^{0}} = -30T$

Table 5.3. Gibbs energy functions of liquid oxides

Oxide	*T* range (K)	Gibbs energy function (J/mol)						Reference
$CaO(\ell)$	298-2845	-571766.658	T^0	348.735802	T	573572.991	T^-1	Bale et al.[43]
		-535.615998	T^0.5	-17163131.3	T^-2	-58.7911706	Tln(T)	
	2845-3500	-596946.671	T^0	379.180084	T	-62.76	Tln(T)	
$Fe_2O_3(\ell)$	298-700	-790405.918	T^0	837.082867	T	0.01841615	T^2	"
		1573510	T^-1	-1.2042E-05	T^3	-143.718	Tln(T)	
	700-955	-1024615.17	T^0	4083.09189	T	0.48202345	T^2	
		22374620	T^-1	-9.35382E-05	T^3	-638.059	Tln(T)	
	955-970	3270153331	T^0	-34689563	T	-3454.0955	T^2	
		-3.97896E+11	T^-1	0.4437025	T^3	5041690	Tln(T)	
	970-1050	23618923.1	T^0	-239921.242	T	-21.754045	T^2	
		-3228093000	T^-1	0.002566407	T^3	34422.16	Tln(T)	
	1050-1812	-725640.027	T^0	376.873946	T	-0.02791235	T^2	
		-8342755	T^-1	2.06076E-06	T^3	-80.37801	Tln(T)	
	1812-4000	-821058.176	T^0	1018.03098	T	-165	Tln(T)	
$FeO(\ell)$	298-1644	-290958.454	T^0	-349.657168	T	-0.01530403	T^2	Fabrichnaya[268]
		1266650	T^-1	6003.60001	T^0.5	18.0244741	Tln(T)	
	1644-2000	-268094.665	T^0	398.288735	T	-68.1992	Tln(T)	
$K_2O(\ell)$	298-1013	-359688.062	T^0	388.245328	T	-0.008573	T^2	Bale et al.[43]
		295819.992	T^-1	-75.9470015	Tln(T)			
	1013-1300	-381763.356	T^0	616.548762	T	-107.000001	Tln(T)	
$Li_2O(\ell)$	298-600	-582532.74	T^0	388.975332	T	-0.011613776	T^2	"
		747837.604	T^-1	-64.0131075	Tln(T)			
	600-4000	-597700.724	T^0	642.231109	T	-100.416	Tln(T)	
$MgO(\ell)$	298-1700	-548234.128	T^0	275.724634	T	-0.00232681	T^2	Fabrichnaya[268]
		516900	T^-1	4.5043E-08	T^3	-47.4817	Tln(T)	
	1700-2450	-584295.443	T^0	506.068248	T	0.0097344	T^2	
		8591550	T^-1	-8.60338E-07	T^3	-78.3772	Tln(T)	
	2450-3100	9111293.97	T^0	-42013.7634	T	-1.30122485	T^2	
		-3240374160	T^-1	5.82626E-05	T^3	5298.548	Tln(T)	
	3100-5100	-631800.291	T^0	589.239565	T	-84	Tln(T)	
$FeAl_2O_4(\ell)$	298-600	-1597434.4	T^0	-158.38391	T	-0.06747	T^2	This work
		938780	T^-1	1.42054E-05	T^3	-30.2989	Tln(T)	
	600-1500	-1614969.17	T^0	148.45157	T	-0.0072257	T^2	
		2120700	T^-1	2.78532E-07	T^3	-79.0765	Tln(T)	
	1500-1912	-1662246.3	T^0	447.049802	T	0.00709105	T^2	
		12366650	T^-1	-6.29402E-07	T^3	-118.8765	Tln(T)	
	1912-2327	29188458.9	T^0	-168924.873	T	-6.9955295	T^2	
		-7988436200	T^-1	0.000410226	T^3	22024.361	Tln(T)	
	2327-6000	-1747285.82	T^0	780.905007	T	-155.2825	Tln(T)	

Table 5.4. Solid solution model parameters assessed as part of expanded database

---

β-Al_2O_3 $(K_2O)_1[Al_2O_3]_{11}\{Va, Na_2O, K_2O\}_1$

${}^{o}G_{K_2Na_2Al_{22}O_{35}} = 0$

${}^{o}G_{Na_2Al_{22}O_{35}} = 2\,{}^{o}G_{KAl_9O_{14}(K\_beta\_alumina)} + {}^{o}G_{K_2O(s)} + 2\,{}^{o}G_{Al_2O_3(corundum)} - 50T$

${}^{o}G_{Na_2Al_{22}O_{34}} = 2\,{}^{o}G_{KAl_9O_{14}(K\_beta\_alumina)} + 2\,{}^{o}G_{Al_2O_3(corundum)}$

${}^{0}L_{K_2O:Al_2O_3:Na_2O,Va,K_2O} = -650000 + 80T$

${}^{1}L_{K_2O:Al_2O_3:Na_2O,Va,K_2O} = 55T$

Nepheline $((Na - Al)^{+4}, (K - Al)^{+4}, (Va - Si)^{+4}, (Na - Fe)^{+4}, (Ca_{0.5} - Al)^{+4}, (Mg_{0.5} - Al)^{+4})_8[Si^{+4}]_8\{O^{-2}\}_{32}$

${}^{o}G_{K_8Al_8Si_8O_{32}} = 8\,{}^{o}G_{KAlSiO_4(hexagonal)} + 119480$

${}^{o}G_{Na_8Fe_8Si_8O_{32}} = 4\,{}^{o}G_{Na_2O(\alpha)} + 4\,{}^{o}G_{Fe_2O_3(hematite)} + 8\,{}^{o}G_{SiO_2(high-cristobalite)} - 8\cdot10^5 - 75.2T$

${}^{o}G_{Ca_4Al_8Si_8O_{32}} = 4\,{}^{o}G_{CaAl_2Si_2O_8(anorthite)} + 1.2\cdot10^5$

${}^{o}G_{Mg_4Al_8Si_8O_{32}} = 2\,{}^{o}G_{Mg_2Al_4Si_5O_{18}(cordierite)} + 2.003\cdot10^6$

${}^{0}L_{NaAl^{+4},NaFe^{+4}:Si^{+4}:O^{-2}} = -150000$

${}^{0}L_{VaSi^{+4},NaFe^{+4}:Si^{+4}:O^{-2}} = -50000$

Carnegieite $((Na - Al)^{+4}, (K - Al)^{+4}, (Va - Si)^{+4}, (Na - Fe)^{+4}, (Ca_{0.5} - Al)^{+4})_4[Si^{+4}]_4\{O^{-2}\}_{16}$

${}^{o}G_{K_4Al_4Si_4O_{16}} = 4\,{}^{o}G_{KAlSiO_4(orthorhombic)} + 59740$

${}^{o}G_{Na_4Fe_4Si_4O_{16}} = 2\,{}^{o}G_{Na_2O(\alpha)} + 2\,{}^{o}G_{Fe_2O_3(hematite)} + 4\,{}^{o}G_{SiO_2(high-cristobalite)} - 369096 - 84.8T$

${}^{o}G_{Ca_2Al_4Si_4O_{16}} = 2\,{}^{o}G_{CaAl_2Si_2O_8(hexagonal)} + 6\cdot10^4$

Mg-Spinel[a] $(Al^{+3}, Mg^{+2})_1[Al^{+3}, Mg^{+2}, Va]_2\{Mg^{+2}, Va\}_2\langle O^{-2}\rangle_4$

${}^{o}G_{Al_3Mg_2O_4^{+5}} = {}^{o}G_{Mg-Spinel\_1}$

${}^{o}G_{Al_3O_4^{+1}} = {}^{o}G_{Mg-Spinel\_2}$

${}^{o}G_{AlMg_4O_4^{+3}} = {}^{o}G_{Mg-Spinel\_3}$

${}^{o}G_{AlMg_2O_4^{-1}} = {}^{o}G_{Mg-Spinel\_4}$

${}^{o}G_{AlMg_2O_4^{-1}} = {}^{o}G_{Mg-Spinel\_5}$

${}^{o}G_{AlO_4^{-5}} = {}^{o}G_{Mg-Spinel\_6}$

${}^{o}G_{Al_2Mg_3O_4^{+4}} = {}^{o}G_{Mg-Spinel\_7}$

${}^{o}G_{Al_2MgO_4} = {}^{o}G_{Mg-Spinel\_8}$

${}^{o}G_{Mg_5O_4^{+2}} = {}^{o}G_{Mg-Spinel\_9}$

${}^{o}G_{Mg_3O_4^{-2}} = {}^{o}G_{Mg-Spinel\_10}$

${}^{o}G_{Mg_3O_4^{-2}} = {}^{o}G_{Mg-Spinel\_11}$

${}^{o}G_{MgO_4^{-6}} = {}^{o}G_{Mg-Spinel\_12}$

${}^{0}L_{Al^{+3}:Al^{+3},Va:Va:O^{-2}} = 64655 + 60.74T$

${}^{1}L_{Al^{+3}:Al^{+3},Va:Va:O^{-2}} = -79056 - 34.81T$

${}^{2}L_{Al^{+3}:Al^{+3},Va:Va:O^{-2}} = -252333 - 110T$

${}^{0}L_{Mg^{+2}:Mg^{+2},Va:Mg^{+2}:O^{-2}} = 35000$

${}^{0}L_{Mg^{+2}:Al^{+3},Mg^{+2}:Mg^{+2}:O^{-2}} = -250000 - 50T$

${}^{1}L_{Mg^{+2}:Al^{+3},Mg^{+2}:Mg^{+2}:O^{-2}} = -40T$

Mg-Halite[a] $(Al^{+3}, Mg^{+2}, Va)_1[O^{-2}]_1$

${}^{o}G_{AlO^{+1}} = {}^{o}G_{AlO}$

${}^{o}G_{MgO} = {}^{o}G_{MgO(s)}$

${}^{o}G_{O^{-2}} = 0$

${}^{0}L_{Al^{+3},Mg^{+2}:O^{-2}} = 114145 - 20.53T$

${}^{1}L_{Al^{+3},Mg^{+2}:O^{-2}} = -84998 + 30.97T$

${}^{0}L_{Al^{+3},Va:O^{-2}} = 100T$

Wustite (FeO, Na_2O)

${}^{o}G_{FeO} = {}^{o}G_{FeO(s)}$

${}^{o}G_{Na_2O} = {}^{o}G_{Na_2O(\alpha)}$

${}^{11}q_{FeO,Na_2O} = 114145 - 20.53T$

${}^{31}q_{FeO,Na_2O} = -35762.74 - 29.02T$

Fe-Corund_soln $(Al^{+3}, Fe^{+3})_2[O^{-2}]_3$ (adopted from Dreval et al.[222])

${}^{o}G_{Al_2O_3} = {}^{o}G_{Al_2O_3(Fe-Corund\_soln)}$

${}^{o}G_{Fe_2O_3} = {}^{o}G_{Fe_2O_3(Fe-Corund\_soln)}$, $\tau = 2.5$, $T_N = 948$ K

${}^{0}L_{Al^{+3},Fe^{+3}:O^{-2}} = 95000 - 18.5T$

${}^{1}L_{Al^{+3},Fe^{+3}:O^{-2}} = -11511.15 + 10T$

FeAl_soln $(Fe^{+2}, Al^{+3}, Va)_1[O^{-2}]_1$

${}^{o}G_{FeO} = {}^{o}G_{FeO(s)} + 5 \cdot 10^4$, $\tau = 3.5$, $T_C = 570$ K

${}^{o}G_{AlO^{+1}} = 0.5\,{}^{o}G_{Al_2O_3(corundum)} + 85300 + 46.332T$

${}^{o}G_{O^{-2}} = {}^{o}G_{FeO(s)} - {}^{o}G_{Fe(bcc)} + 5 \cdot 10^4$

${}^{0}L_{Fe^{+2},Al^{+3}:O^{-2}} = 15000 - 33T$

Fe-Spinel[a] $(Al^{+3}, Fe^{+2}, Fe^{+3})_1[Al^{+3}, Fe^{+2}, Fe^{+3}, Va]_2\{Va\}_2\langle O^{-2}\rangle_4$

${}^{o}G_{Al_3O_4^{+1}} = {}^{o}G_{Fe-Spinel\_1}$

${}^{o}G_{AlO_4^{-5}} = {}^{o}G_{Fe-Spinel\_2}$

${}^{o}G_{Fe_2AlO_4^{-1}} = {}^{o}G_{Fe-Spinel\_3}$

${}^{o}G_{Fe_2AlO_4^{+1}} = {}^{o}G_{Fe-Spinel\_4}$

${}^{o}G_{FeAl_2O_4} = {}^{o}G_{Fe-Spinel\_5}$

${}^{o}G_{FeAl_2O_4^{+1}} = {}^{o}G_{Fe-Spinel\_6}$

${}^{o}G_{FeO_4^{-6}} = {}^{o}G_{Fe-Spinel\_7}$, $\tau = 44.54$, $T_C = 848$ K

${}^{o}G_{FeO_4^{-5}} = {}^{o}G_{Fe-Spinel\_8}$, $\tau = 44.54$, $T_C = 848$ K

${}^{o}G_{Fe_3O_4^{-2}} = {}^{o}G_{Fe-Spinel\_9}$, $\tau = 44.54$, $T_C = 848$ K

${}^{o}G_{Fe_3O_4^{+1}} = {}^{o}G_{Fe-Spinel\_10}$, $\tau = 44.54$, $T_C = 848$ K

${}^{o}G_{Fe_3O_4} = {}^{o}G_{Fe-Spinel\_11}$, $\tau = 44.54$, $T_C = 848$ K

${}^{o}G_{Fe_3O_4^{-1}} = {}^{o}G_{Fe-Spinel\_12}$, $\tau = 44.54$, $T_C = 848$ K

${}^{0}L_{Al^{+3},Fe^{+2}:Al^{+3}:Va:O^{-2}} = 81928.63 - 8.1T$

${}^{0}L_{Al^{+3}:Al^{+3},Fe^{+2}:Va:O^{-2}} = -57148.27 - 30T$

${}^{0}L_{Al^{+3},Fe^{+2}:Fe^{+2}:Va:O^{-2}} = 19660.93$

${}^{0}L_{Fe^{+2}:Al^{+3},Fe^{+2}:Va:O^{-2}} = -7088.79 + 3.63T$

${}^{0}L_{Al^{+3}:Fe^{+3},Va:Va:O^{-2}} = 10^6$

${}^{0}L_{Fe^{+2}:Al^{+3},Fe^{+3}:Va:O^{-2}} = 15000$

[a] Endmember thermodynamic values defined in Table 5.5.

Table 5.5. Thermodynamic values for Fe-Spinel, Mg-Spinel, and halite solid solution endmembers

Solution endmember	$\Delta H_{298.15K}$ (J/mol)	$S_{298.15K}$ (J/mol·K)	C_p (J/mol·K)	T range (K)
$^{o}G_{Fe-Spinel\_1}$	-2514574.965	-25.15006816	95.652585 +0.197310962T -2854708/T^2 -0.000125863482T^2	298-600
			168.81885 +0.016578167T -6400471/T^2 -5.21247E-7T^2	600-1000
			165.97995 +0.021081256T -6099201/T^2 -2.486442E-6T^2	1000-1500
			225.6804 -0.021868992T -36837104/T^2 +5.6849595E-6T^2	1500-2327
			280.2891 -0.000595798T +262905/T^2 +2.0343E-8T^2	2327-3300
			279.2192 -0.000425243T +4383200/T^2 +3.2163E-8T^2	3300-6000
$^{o}G_{Fe-Spinel\_2}$	533049.9893	-351.221181	61.580275 +0.09296519T -746940/T^2 -5.2543374E-5T^2	298-600
			85.96975 +0.032720364T -1928845/T^2 -1.0763301E-5T^2	600-1000
			100.16425 +0.010204915T -3435195/T^2 -9.37326E-7T^2	1000-1500
			120.062 -0.004111835T -13680875/T^2 +1.7864985E-6T^2	1500-2327
			-152.9815 -0.11047781T -199180924/T^2 +0.0000301095817T^2	2327-3000
			-243.43539 +0.00297899T -1314525/T^2 -1.01715E-7T^2	3000-3300
			-238.08589 +0.002126215T -21916000/T^2 -1.60815E-7T^2	3300-6000
$^{o}G_{Fe-Spinel\_3}$	-1077687.507	-332.0854213	215.13502 -0.145010962T -3412924/T^2 +0.000125863482T^2	298-600
			141.96875 +0.035721832T +132839/T^2 +5.21247E-7T^2	600-1000
			144.80765 +0.031218744T -168431/T^2 +2.486442E-6T^2	1000-1500
			85.1072 +0.074168994T +30569472/T^2 -5.6849595E-6T^2	1500-2327
			30.4985 +0.052895798T -6530537/T^2 -2.0343E-8T^2	2327-3300
			31.5684 +0.052725242T -10650832/T^2 -3.2163E-8T^2	3300-6000
$^{o}G_{Fe-Spinel\_4}$	-1149513.507	-304.8194213	215.13502 -0.145010962T -3412924/T^2 +0.000125863482T^2	298-600
			141.96875 +0.035721832T +132839/T^2 +5.21247E-7T^2	600-1000
			144.80765 +0.031218744T -168431/T^2 +2.486442E-6T^2	1000-1500
			85.1072 +0.074168994T +30569472/T^2 -5.6849595E-6T^2	1500-2327
			30.4985 +0.052895798T -6530537/T^2 -2.0343E-8T^2	2327-3300
			31.5684 +0.052725242T -10650832/T^2 -3.2163E-8T^2	3300-6000
$^{o}G_{Fe-Spinel\_5}$	-1954112.187	-114.414003	155.3938 +0.02615T -3133816/T^2	298.15-6000
$^{o}G_{Fe-Spinel\_6}$	-1950908.187	-87.14800298	155.3938 +0.02615T -3133816/T^2	298.15-6000
$^{o}G_{Fe-Spinel\_7}$	-643216.3349	-147.7111075	124.9395 +0.011952256T -2065200/T^2	298.15-3000
			160.5668	3000-6000
$^{o}G_{Fe-Spinel\_8}$	-690042.3349	-120.4451075	124.9395 +0.011952256T -2065200/T^2	298.15-3000
			160.5668	3000-6000

Table 5.5 cont'd. Thermodynamic values for Fe-Spinel, Mg-Spinel, and halite solid solution endmembers

Solution endmember	$\Delta H_{298.15K}$ (J/mol)	$S_{298.15K}$ (J/mol·K)	C_p (J/mol·K)	T range (K)
$^{o}G_{Fe-Spinel\_9}$	-1022698.869	-205.9187505	174.9153 +0.0167331584T -2891280/T^2	298.15-3000
			224.79352	3000-6000
$^{o}G_{Fe-Spinel\_10}$	-1116350.869	-151.3867505	174.9153 +0.0167331584T -2891280/T^2	298.15-3000
$^{o}G_{Fe-Spinel\_11}$	-1069524.869	-182.1527505	174.9153 +0.0167331584T -2891280/T^2	298.15-3000
			224.79352	3000-6000
$^{o}G_{Fe-Spinel\_12}$	-1069524.869	-178.6527505	174.9153 +0.0167331584T -2891280/T^2	298.15-3000
			224.79352	3000-6000
$^{o}G_{Mg-Spinel\_1}$	-3587648.968	124.6958635	221.46229 +0.17691541·T -4250476/T^2 -0.00011792133·T^2 -592.398/T^0.5 +11689224/T^3	298.15-600
			294.62855 -0.003817385·T -7796239/T^2 +7.420905E-6·T^2 -592.398/T^0.5 +11689224/T^3	600-1000
			280.43405 +0.018698065·T -6289889/T^2 -2.40507E-6·T^2 -592.398/T^0.5 +11689224/T^3	1000-1500
			340.1345 -0.024252186·T -37027794/T^2 +5.7663315E-6·T^2 -592.398/T^0.5 +11689224/T^3	1500-2327
			394.7432 -0.00297899·T +72216.992/T^2 +1.01715E-7·T^2 -592.398/T^0.5 +11689224/T^3	2327-3097.91
			441.418 -0.00297899·T +5041449/T^2 +1.01715E-7·T^2 +1777.194/T^0.5 -35067672/T^3	3097.91-3098
			406.4119 -0.00297899·T +1314525/T^2 +1.01715E-7·T^2	3098-3300
			401.0624 -0.002126215·T +21916000/T^2 +1.60815E-7·T^2	3300-6000
$^{o}G_{Mg-Spinel\_2}$	-2444694.532	-48.84547816	95.652585 +0.197310962·T -2854708/T^2 -0.000125863482·T^2	298.18-600
			168.81885 +0.016578167·T -6400471/T^2 -5.21247E-7·T^2	600-1000
			165.97995 +0.021081256·T -6099201/T^2 -2.486442E-6·T^2	1000-1500
			225.6804 -0.021868992·T -36837104/T^2 +5.6849595E-6·T^2	1500-2327
			280.2891 -0.000595798·T +262905/T^2 +2.0343E-8·T^2	2327-3300
			279.2192 -0.000425243·T +4383200/T^2 +3.2163E-8·T^2	3300-6000
$^{o}G_{Mg-Spinel\_3}$	-3182239.076	34.74597529	278.7164 +0.052173286·T -3538492/T^2 -3.66597258E-5·T^2 -1184.796/T^0.5 +23378448/T^3	298.15-600
			303.10515 -0.008070979·T -4720413/T^2 +5.12101902E-6·T^2 -1184.796/T^0.5 +23378448/T^3	600-1000
			294.58845 +0.005438291·T -3816603/T^2 -7.7456598E-7·T^2 -1184.796/T^0.5 +23378448/T^3	1000-1500
			314.4886 -0.008878459·T -14062571/T^2 +1.94923452E-6·T^2 -1184.796/T^0.5 +23378448/T^3	1500-2327
			332.6915 -0.001787394·T -1695901.02/T^2 +6.1029E-8·T^2 -1184.796/T^0.5 +23378448/T^3	2327-3097.91
			379.3663 -0.001787394·T +3273331/T^2 +6.1029E-8·T^2 +1184.796/T^0.5 -23378448/T^3	3097.91-3098
			356.0289 -0.001787394·T +788715/T^2 +6.1029E-8·T^2	3098-3300
			352.8192 -0.001275729·T +13149600/T^2 +9.6489E-8·T^2	3300-6000

Table 5.5 cont'd. Thermodynamic values for Fe-Spinel, Mg-Spinel, and halite solid solution endmembers

Solution endmember	$\Delta H_{298.15K}$ (J/mol)	$S_{298.15K}$ (J/mol·K)	C_p (J/mol·K)	T range (K)
$^{o}G_{Mg-Spinel\ 4}$	-1999165.072	-75.10001984	152.9067 +0.072568838·T -2142724/T^2 -4.46018778E-5·T^2 -592.398/T^0.5 +11689224/T^3	298.15-600
			177.29545 +0.012324573·T -3324645/T^2 -2.82113298E-6·T^2 -592.398/T^0.5 +11689224/T^3	600-1000
			180.13435 +0.007821483·T -3625915/T^2 -8.5593798E-7·T^2 -592.398/T^0.5 +11689224/T^3	1000-1500
			200.0345 -0.006495267·T -13871883/T^2 +1.86786252E-6·T^2 -592.398/T^0.5 +11689224/T^3	1500-2327
			218.2374 +0.000595798·T -1505213/T^2 -2.0343E-8·T^2 -592.398/T^0.5 +11689224/T^3	2327-3098
			229.9061 +0.000595798·T -262905/T^2 -2.0343E-8·T^2	3098-3300
			230.976 +0.000425243·T -4383200/T^2 -3.2163E-8·T^2	3300-6000
$^{o}G_{Mg-Spinel\ 5}$	-1911265.205	-36.96958691	187.3899 +0.072568838·T -2142724/T^2 -4.46018778E-5·T^2 -592.398/T^0.5 +11689224/T^3	298.15-600
			211.77865 +0.012324573·T -3324645/T^2 -2.82113298E-6·T^2 -592.398/T^0.5 +11689224/T^3	600-1000
			214.61755 +0.007821483·T -3625915/T^2 -8.5593798E-7·T^2 -592.398/T^0.5 +11689224/T^3	1000-1500
			234.5177 -0.006495267·T -13871883/T^2 +1.86786252E-6·T^2 -592.398/T^0.5 +11689224/T^3	1500-2327
			252.7206 +0.000595798·T -1505213/T^2 -2.0343E-8·T^2 -592.398/T^0.5 +11689224/T^3	2327-3097.91
			299.3954 +0.000595798·T +3464019/T^2 -2.0343E-8·T^2 +1777.194/T^0.5 -35067672/T^3	3097.91-3098
			264.3893 +0.000595798·T -262905/T^2 -2.0343E-8·T^2	3098-3300
			265.4592 +0.000425243·T -4383200/T^2 -3.2163E-8·T^2	3300-6000
$^{o}G_{Mg-Spinel\ 6}$	-783191.2723	-236.8155685	61.580195 +0.09296439·T -746956/T^2 -5.25440298E-5·T^2	298.15-600
			85.96895 +0.032720124·T -1928877/T^2 -1.07632848E-5·T^2	600-1000
			100.16345 +0.010204675·T -3435227/T^2 -9.3730998E-7·T^2	1000-1500
			120.0636 -0.004112075·T -13681195/T^2 +1.78649052E-6·T^2	1500-2327
			138.2665 +0.00297899·T -1314525/T^2 -1.01715E-7·T^2	2327-3300
			143.616 +0.002126215·T -21916000/T^2 -1.60815E-7·T^2	3300-6000
$^{o}G_{Mg-Spinel\ 7}$	-3375446.874	68.59365297	250.08934 +0.114544348·T -3894484/T^2 -7.729053E-5·T^2 -888.597/T^0.5 +17533836/T^3	298.15-600
			298.86685 -0.005944182·T -6258326/T^2 +6.2709618E-6·T^2 -888.597/T^0.5 +17533836/T^3	600-1000
			287.51125 +0.012068178·T -5053246/T^2 -1.58981802E-6·T^2 -888.597/T^0.5 +17533836/T^3	1000-1500
			327.31155 -0.016565322·T -25545182/T^2 +3.85778298E-6·T^2 -888.597/T^0.5 +17533836/T^3	1500-2327
			363.71735 -0.002383192·T -811842.02/T^2 +8.1372E-8·T^2 -888.597/T^0.5 +17533836/T^3	2327-3097.91
			410.39215 -0.002383192·T +4157390/T^2 +8.1372E-8·T^2 +1480.995/T^0.5 -29223060/T^3	3097.91-3098
			381.2204 -0.002383192·T +1051620/T^2 +8.1372E-8·T^2	3098-3300
			376.9408 -0.001700972·T +17532800/T^2 +1.28652E-7·T^2	3300-6000
$^{o}G_{Mg-Spinel\_8}$	-2362372.969	-67.25237216	124.27964 +0.1349399·T -2498716/T^2 -8.5232682E-5·T^2 -296.199/T^0.5 +5844612/T^3	298.15-600
			173.05715 +0.01445137·T -4862558/T^2 -1.67119002E-6·T^2 -296.199/T^0.5 +5844612/T^3	600-1500
			212.85745 -0.01418213·T -25354494/T^2 +3.77641098E-6·T^2 -296.199/T^0.5 +5844612/T^3	1500-2327
			249.26325 -621154/T^2 -296.199/T^0.5 +5844612/T^3	2327-3098
			255.0976	3098-6000

Table 5.5 cont'd. Thermodynamic values for Fe-Spinel, Mg-Spinel, and halite solid solution endmembers

Solution endmember	$\Delta H_{298.15K}$ (J/mol)	$S_{298.15K}$ (J/mol·K)	C_p (J/mol·K)	T range (K)
$^{o}G_{Mg-Spinel\_9}$	-2970036.982	-21.35633531	307.34345 -0.010197776·T -3182500/T^2 +3.971076E-6·T^2 -1480.995/T^0.5 +29223060/T^3	298.15-1000
			301.66565 -0.001191596·T -2579960/T^2 +4.06860006E-8·T^2 -1480.995/T^0.5 +29223060/T^3	1000-2327
			301.66565 -0.001191596·T -2579960/T^2 +4.0686E-8·T^2 -1480.995/T^0.5 +29223060/T^3	2327-3097.91
			348.34045 -0.001191596·T +2389272/T^2 +4.0686E-8·T^2 +888.597/T^0.5 -17533836/T^3	3097.91-3098
			330.8374 -0.001191596·T +525810/T^2 +4.0686E-8·T^2	3098-3300
			328.6976 -0.000850486·T +8766400/T^2 +6.4326E-8·T^2	3300-6000
$^{o}G_{Mg-Spinel\_10}$	-1786962.977	-131.2023306	181.53375 +0.010197776·T -1786732.02/T^2 -3.971076E-6·T^2 -888.597/T^0.5 +17533836/T^3	298.15-1000
			187.21155 +0.001191596·T -2389272/T^2 -4.06860006E-8·T^2 -888.597/T^0.5 +17533836/T^3	1000-2327
			187.21155 +0.001191596·T -2389272/T^2 -4.0686E-8·T^2 -888.597/T^0.5 +17533836/T^3	2327-3098
			204.7146 +0.001191596·T -525810/T^2 -4.0686E-8·T^2	3098-3300
			206.8544 +0.000850486·T -8766400/T^2 -6.4326E-8·T^2	3300-6000
$^{o}G_{Mg-Spinel\_11}$	-1651271.011	-186.8748976	216.01695 +0.010197776·T -1786732.02/T^2 -3.971076E-6·T^2 -888.597/T^0.5 +17533836/T^3	298.15-1000
			221.69475 +0.001191596·T -2389272/T^2 -4.06859988E-8·T^2 -888.597/T^0.5 +17533836/T^3	1000-2327
			221.69475 +0.001191596·T -2389272/T^2 -4.0686E-8·T^2 -888.597/T^0.5 +17533836/T^3	2327-3097.91
			268.36955 +0.001191596·T +2579960/T^2 -4.0686E-8·T^2 +1480.995/T^0.5 -29223060/T^3	3097.91-3098
			239.1978 +0.001191596·T -525810/T^2 -4.0686E-8·T^2	3098-3300
			241.3376 +0.000850486·T -8766400/T^2 -6.4326E-8·T^2	3300-6000
$^{o}G_{Mg-Spinel\_12}$	-523197.0863	-292.9178626	90.20725 +0.030593328·T -390964/T^2 -1.1913228E-5·T^2 -296.199/T^0.5 +5844612/T^3	298.15-1000
			107.24065 +0.003574788·T -2198584/T^2 -1.22058E-7·T^2 -296.199/T^0.5 +5844612/T^3	1000-3098
			113.075 +0.003574788·T -1577430/T^2 -1.22058E-7·T^2	3098-3300
			119.4944 +0.002551458·T -26299200/T^2 -1.92978E-7·T^2	3300-6000
$^{o}G_{AlO}$	-757139.0401	-78.15563114	33.740195 +0.06746995·T -938781/T^2 -4.26163398E-5·T^2	298.15-600
			58.12895 +0.007225685·T -2120702/T^2 -8.3559498E-7·T^2	600-1500
			78.0291 -0.007091065·T -12366670/T^2 +1.88820552E-6·T^2	1500-2327
			96.232	2327-4000

Table 5.6. Gibbs energy functions of stoichiometric solid oxides

Compound	*T* range (K)	Gibbs energy function (J/mol)						Reference
$Al_2Fe_2O_6$	298-1591	-2524091.23	T^0	1959.90518	T	-0.001640856	T^2	Bale et al.[43]
		4719072.53	T^-1	-155785255	T^-2	-3313.54792	T^0.5	
		-299.877284	Tln(T)					
	1591-2500	-2523119.76	T^0	1971.4282	T	4719072.53	T^-1	
		-155785255	T^-2	-3313.54792	T^0.5	-301.877282	Tln(T)	
$LiAl_5O_8(\beta)$	298-600	-4672667.02	T^0	1361.8075	T	-0.1652665	T^2	Kulkarni et al[266]
		2812550	T^-1	0.000033217	T^3	-207.034	Tln(T)	
	600-1500	-4716504.06	T^0	2128.89658	T	-0.014656	T^2	
		5767350	T^-1	-1.60033E-06	T^3	-328.978	Tln(T)	
	1500-2173	-4834696.57	T^0	2875.39176	T	0.021136	T^2	
		31382200	T^-1	-3.87017E-06	T^3	-428.478	Tln(T)	
	2173-3000	-5046138.41	T^0	3784.73347	T	-529.695	Tln(T)	
$LiAl_5O_8(\alpha)$	298-600	-4667926.12	T^0	1358.80903	T	-0.1652665	T^2	"
		2812550	T^-1	0.000033217	T^3	-207.034	Tln(T)	
	600-1500	-4711763.16	T^0	2125.89812	T	-0.014656	T^2	
		5767350	T^-1	-1.60033E-06	T^3	-328.978	Tln(T)	
	1500-2173	-4829955.67	T^0	2872.3933	T	0.021136	T^2	
		31382200	T^-1	-3.87017E-06	T^3	-428.478	Tln(T)	
	2173-3000	-5041397.51	T^0	3781.73501	T	-529.695	Tln(T)	
$LiAl_{11}O_{17}$	298-600	3998603.5	T^0	864.330718	T	-0.18083655	T^2	"
		8379050	T^-1	0.000033217	T^3	-559.504	Tln(T)	
	600-1500	3954766.4	T^0	1631.4187	T	-0.030226	T^2	
		11333900	T^-1	-1.60033E-06	T^3	-681.44784	Tln(T)	
	1500-2173	3836573.95	T^0	2377.91394	T	0.005566	T^2	
		36948700	T^-1	-3.87017E-06	T^3	-780.94785	Tln(T)	
	2173-2327	3625131.78	T^0	3287.25695	T	-0.01557	T^2	
		5566500	T^-1	-882.165	Tln(T)			
	2327-3000	3190833.01	T^0	5182.35891	T	-1107.087	Tln(T)	
Li_5AlO_4	298-600	-2495652.92	T^0	1432.7679	T	-0.0166935	T^2	"
		2797350	T^-1	-4.3805E-06	T^3	-225.405	Tln(T)	
	600-1500	-2504419.85	T^0	1586.17946	T	0.013429	T^2	
		3388350	T^-1	-0.000011344	T^3	-249.793	Tln(T)	
	1500-3000	-2528058.32	T^0	1735.47842	T	0.0205875	T^2	
		8511300	T^-1	-0.000011798	T^3	-269.693	Tln(T)	
$Ca_2Al_2SiO_7$	298-698	-4031807.92	T^0	2584.76721	T	2389233.03	T^-1	Bale et al.[43]
		-9107.01992	T^0.5	-79651965.6	T^-2	-373.087401	Tln(T)	
	698-1600	-3925619.73	T^0	1115.40557	T	-0.184750001	T^2	
		-6256406.96	T^-1	2.44833E-05	T^3	-9107.01992	T^0.5	
		-79651965.6	T^-2	-151.347401	Tln(T)			
	1600-2500	-4018818.24	T^0	2573.29903	T	2389233.03	T^-1	
		-9107.01992	T^0.5	-79651965.6	T^-2	-373.087401	Tln(T)	
$CaAl_2B_2O_8$	298-1850	-4532261.43	T^0	2271.91585	T	-0.020414504	T^2	"
		4192216.05	T^-1	-3849.16392	T^0.5	-85343739	T^-2	
		-343.576019	Tln(T)					
	1850-2327	-4598480.42	T^0	2831.251	T	2504254.5	T^-1	
		-3849.16392	T^0.5	-85343739	T^-2	-418.123292	Tln(T)	
$Ca_2B_2O_5(\beta)$	298-804	-2805279.01	T^0	1120.12627	T	-0.024053975	T^2	"
		2235973.85	T^-1	-183.019375	Tln(T)			
	804-1850	-2816136.2	T^0	1360.77442	T	-0.00501996	T^2	
		-218.744757	Tln(T)					
$Ca_2B_2O_5(\alpha)$	298-804	-2800677.01	T^0	1114.40239	T	-0.024053975	T^2	"
		2235973.85	T^-1	-183.019375	Tln(T)			
	804-1850	-2811534.2	T^0	1355.05054	T	-0.00501996	T^2	
		-218.744757	Tln(T)					

Table 5.6 cont'd. Gibbs energy functions of stoichiometric solid oxides

Compound	*T* range (K)	Gibbs energy function (J/mol)						Reference
$Ca_2B_2SiO_7$	298-2150	-3751833.86	T^0	1812.64691	T	-0.020414504	T^2	Bale et al.[43]
		3517635.54	T^-1	-2761.17992	T^0.5	-80724903.6	T^-2	
		-278.838627	Tln(T)					
$Ca_2Fe_2O_5$	298-1721	-2220525.65	T^0	1481.02667	T	-0.002438372	T^2	"
		2399757.28	T^-1	-245.085491	Tln(T)			
$Ca_2FeSi_2O_7$	298-2000	-3699969.78	T^0	1769.203	T	7442145.23	T^-1	"
		-177252552	T^-2	2190.09622	T^0.5	-295.2345	Tln(T)	
$Ca_2Mg_2Al_{28}O_{46}$	298-6000	-26665168	T^0	16992.8976	T	28797841.1	T^-1	"
		-49830.4949	T^0.5	-990802974	T^-2	-2410.06599	Tln(T)	
$Ca_2MgSi_2O_7$	298-2000	-3880436.17	T^0	2721.30231	T	-11755.076	T^0.5	"
		6798413.33	T^-2	-387.063961	Tln(T)			
$Ca_2SiO_4(\gamma)$	298-2500	-2309731.15	T^0	1747.5334	T	-5126356.04	T^-2	"
		-8137.6857	T^0.5	-243.660206	Tln(T)			
$Ca_2SiO_4(\beta)$	298-1710	-2331645.86	T^0	1371.89957	T	3994699.94	T^-1	"
		-216246659	T^-2	-2807.60006	T^0.5	-210.488764	Tln(T)	
	1710-5000	-2246145.86	T^0	949.687163	T	3994699.94	T^-1	
		-216246659	T^-2	-2807.60006	T^0.5	-160.488767	Tln(T)	
$Ca_2SiO_4(\alpha)$	298-5000	-2241869.07	T^0	947.186107	T	3994699.94	T^-1	"
		-216246659	T^-2	-2807.60006	T^0.5	-160.488767	Tln(T)	
$Ca_3Al_2O_6$	298-1814	-3655463.3	T^0	2119.24615	T	2890650.08	T^-1	"
		-5021.59998	T^0.5	-110203331	T^-2	-321.580002	Tln(T)	
$Ca_3Al_2Si_3O_{12}$	298-2000	-6785285.07	T^0	3898.74051	T	9443584.02	T^-1	"
		-8157.61994	T^0.5	-386551978	T^-2	-573.430421	Tln(T)	
$Ca_3B_2O_6$	298-1850	-3522132.7	T^0	1441.32444	T	-0.021794993	T^2	"
		2723328.3	T^-1	-236.105452	Tln(T)			
$Ca_3Fe_2Si_3O_{12}$	298-3000	-5754773.02	T^0	5943.95922	T	0.0351255	T^2	"
		339450	T^-1	-29612	T^0.5	-809.24	Tln(T)	
$Ca_3MgAl_4O_{10}$	298-6000	-6086252.2	T^0	3750.01087	T	5892658.99	T^-1	"
		-9418.73984	T^0.5	-188824711	T^-2	-547.520926	Tln(T)	
$Ca_3MgSi_2O_8$	298-2500	-4580726.46	T^0	3167.16334	T	-13000	T^0.5	"
		57371666.7	T^-2	-453.62	Tln(T)			
$Ca_3Si_2O_7$	298-5000	-4019610.62	T^0	2723.09959	T	5329997.77	T^-1	"
		-8800.26331	T^0.5	-228931522	T^-2	-392.848756	Tln(T)	
Ca_3SiO_5	298-2500	-2902196.94	T^0	1229.21802	T	-2018.41164	T^0.5	"
		-209.98832	Tln(T)					
$Ca_5SiO_{10}B_2$	298-6000	-5881683.16	T^0	2180.6406	T	-0.0621015	T^2	"
		3563085	T^-1	3.28278E-06	T^3	-361.427	Tln(T)	
	6000-6001	-5278637.24	T^0	2138.45428	T	-397.36592	Tln(T)	
$Ca_{11}B_2Si_4O_{22}(\beta)$	298-1850	-12832553.9	T^0	8431.45955	T	-0.021794993	T^2	"
		2723328.3	T^-1	-20505424.2	T^-2	-32550.7428	T^0.5	
		-1210.74628	Tln(T)					
	1850-2500	-12901259	T^0	9023.76125	T	-20505424.2	T^-2	
		-32550.7428	T^0.5	-1289.79633	Tln(T)			
$Ca_{11}B_2Si_4O_{22}(\alpha)$	298-1710	-12865042.9	T^0	6928.93073	T	-0.021794993	T^2	"
		18702128.1	T^-1	-864986635	T^-2	-11230.4003	T^0.5	
		-1078.06051	Tln(T)					
	1710-1850	-12523042.9	T^0	5240.08112	T	-0.021794993	T^2	
		18702128.1	T^-1	-864986635	T^-2	-11230.4003	T^0.5	
		-878.060522	Tln(T)					
	1850-5000	-12591748	T^0	5832.38281	T	15978799.8	T^-1	
		-864986635	T^-2	-11230.4003	T^0.5	-957.110569	Tln(T)	
$CaAl_2B_2O_7$	298-1850	-3806588.77	T^0	1895.23928	T	-0.020414504	T^2	"
		3618643.06	T^-1	-3313.54792	T^0.5	-68180607.7	T^-2	
		-284.784848	Tln(T)					
	1850-2327	-3872807.76	T^0	2454.57443	T	1930681.51	T^-1	
		-3313.54792	T^0.5	-68180607.7	T^-2	-359.332122	Tln(T)	

Table 5.6 cont'd. Gibbs energy functions of stoichiometric solid oxides

Compound	*T* range (K)	Gibbs energy function (J/mol)						Reference
$CaAl_2O_4$	298-1877	-2336571.1	T^0	1603.12059	T	280400.007	T^-1	Bale et al.[43]
		-6676.39993	T^0.5	14256666.9	T^-2	-227.039999	Tln(T)	
$CaAl_2SiO_6$	298-3000	-3265591.3	T^0	1841.0616	T	-0.0013425	T^2	"
		2672000	T^-1	-160183333	T^-2	-27110	ln(T)	
		-280.08	Tln(T)					
$CaAl_4O_7$	298-2038	-4097286.08	T^0	2253.36407	T	6056300.04	T^-1	"
		-4088.79994	T^0.5	-251766670	T^-2	-337.980001	Tln(T)	
$CaAl_{12}O_{19}$	298-2106	-10888743.9	T^0	6990.90794	T	14073900.1	T^-1	"
		-21400.1207	T^0.5	-624501832	T^-2	-992.735002	Tln(T)	
CaB_2O_4	298-1850	-2086008.3	T^0	795.281075	T	-0.020414504	T^2	"
		1687961.55	T^-1	-129.765966	Tln(T)			
$CaB_2Si_2O_8$	298-1000	-3802256.8	T^0	3309.42042	T	-0.0905935	T^2	"
		-905700	T^-1	0.0000205	T^3	-20986.36	T^0.5	
		-425.295	Tln(T)					
CaB_4O_7	298-1850	-3450249.48	T^0	1368.01928	T	-0.040076014	T^2	"
		3589271.4	T^-1	-214.770622	Tln(T)			
$CaFe_2O_4$	298-2000	-1535407.08	T^0	1014.35	T	-0.008	T^2	"
		909486	T^-1	-170.988	Tln(T)			
$CaFe_4O_7$	298-1498	-2388710.27	T^0	1956.491	T	-0.0012193	T^2	"
		3375926	T^-1	-2.4E-11	T^3	-325.8761	Tln(T)	
$CaFeSi_2O_6$	298-3000	-2422037.82	T^0	2105.13531	T	-0.007025	T^2	"
		-15395000	T^-1	797666667	T^-2	-93220	ln(T)	
		-309.3	Tln(T)					
$CaMg_2Al_{16}O_{27}$	298-6000	-15701036.8	T^0	10016.4718	T	16640179.1	T^-1	"
		-29413.5914	T^0.5	-564556197	T^-2	-1421.16153	Tln(T)	
$CaMgO_2$	298-1800	-1278690	T^0	601.39896	T	-0.00382836	T^2	"
		912112	T^-1	-97.82192	Tln(T)			
	1800-1801	-1289066.96	T^0	699.638426	T	-111.04098	Tln(T)	
$CaMgSi_2O_6$	298-2000	-3254230.63	T^0	2117.64351	T	3582986.6	T^-1	"
		-6419.72408	T^0.5	-153639590	T^-2	-305.413331	Tln(T)	
CaO	298-2845	-651262.658	T^0	376.676564	T	573572.991	T^-1	"
		-535.615998	T^0.5	-17163131.3	T^-2	-58.7911706	Tln(T)	
	2845-3500	-676442.671	T^0	407.120846	T	-62.76	Tln(T)	
$CaOMgOSiO_2$	298-2000	-2272506.1	T^0	1593.2697	T	589854.504	T^-1	"
		-6170.96403	T^0.5	3880981.33	T^-2	-226.34225	Tln(T)	
$CaSiO_3(\beta)$	298-2000	-1664832.94	T^0	1013.06077	T	1829673.99	T^-1	"
		-2761.17992	T^0.5	-80724903.6	T^-2	-149.072661	Tln(T)	
	2000-2002	-1719540.35	T^0	959.109345	T	-146.44	Tln(T)	
$CaSiO_3(\alpha)$	298-1813	-1667838.65	T^0	927.913022	T	2928797.49	T^-1	"
		-1668.92799	T^0.5	-156789159	T^-2	-141.15611	Tln(T)	
	1813-1815	-1709861.48	T^0	952.40428	T	-146.44	Tln(T)	
Fe(bcc)	298-1811	1225.7	T^0	124.134	T	-0.00439752	T^2	"
		77358.5	T^-1	-5.89269E-08	T^3	-23.5143	Tln(T)	
	1811-1812	-24287.8308	T^0	298.768006	T	-46	Tln(T)	
$Fe_2Al_4Si_5O_{18}$	298-1500	-8780752.4	T^0	5043.87601	T	24702746.5	T^-1	
		-2066.048	T^0.5	-1201307815	T^-2	-785.40228	Tln(T)	
Fe_2O_3	298-2500	-861183.055	T^0	828.050052	T	1453820	T^-1	"
		-137.00893	Tln(T)					
$Fe_2B_2O_5$	298-1192	-1928880.4	T^0	804.103973	T	-0.033722304	T^2	This work
		2177856.05	T^-1	2728.60654	T^0.5	-151.016768	Tln(T)	
	1192-1644	-2014555.9	T^0	183.321546	T	-0.03060806	T^2	
		2533299.99	T^-1	12007.2	T^0.5	-91.7304118	Tln(T)	
	1644-2000	-1968828.32	T^0	1679.21335	T	-264.17776	Tln(T)	

Table 5.6 cont'd. Gibbs energy functions of stoichiometric solid oxides

Compound	*T* range	Gibbs energy function (J/mol)						Reference
$Fe_2B_2O_6$	298-1192	-2121831.79	T^0	2293.5289	T	-0.003114244	T^2	This work
		1098376.05	T^-1	-9278.59349	T^0.5	-324.074647	Tln(T	
	1192-2000	-2207507.28	T^0	1672.74647	T	1453820	T^-1	
		-264.78829	Tln(T					
	2000-2500	-2207507.28	T^0	1672.74647	T	1453820	T^-1	
		-264.78829	Tln(T					
Fe_2SiO_4	298-1500	-1542696.95	T^0	1048.25766	T	0.004404	T^2	Fabrichnaya & Sundman[221]
		1944500	T^-1	-4.11833E-	T^3	-176.02	Tln(T	
$Fe_3Al_2Si_3O_1$	298-3000	-4733460.21	T^0	4833.14609	T	0.04425	T^2	Bale et al.[43]
		-7290000	T^-1	-0.0000026	T^3	-149600	ln(T)	
		-713	Tln(T					
$Fe_3Ca_2O_5$	298-3172	-2189313.8	T^0	1468.7848	T	-0.0149906	T^2	"
		1357103.4	T^-1	-4.8E-11	T^3	-250.07292	Tln(T	
	3172-6000	-719178.56	T^0	-3165.29991	T	-0.10332293	T^2	
		-696808600	T^-1	2.34239E-06	T^3	307.6742	Tln(T	
	6000-6001	-2879521.59	T^0	3361.30778	T	-464.95717	Tln(T	
Fe_3O_4	298-848	-1200277.81	T^0	1282.9585	T	-0.019017282	T^2	"
		3621668.52	T^-1	3.9679E-05	T^3	-3.1046E-08	T^4	
		-110726059	T^-2	-207.93083	Tln(T			
	848-1870	-1186819.15	T^0	1260.56231	T	3621668.52	T^-1	
		-110726059	T^-2	-207.93083	Tln(T			
$Fe_6B_2O_9$	298-1192	-3241380.57	T^0	-518.645769	T	-0.094938424	T^2	This work
		7244456.04	T^-1	26743.0066	T^0.5	-78.9188719	Tln(T	
	1192-1644	-3327056.06	T^0	-1139.4282	T	-0.09182418	T^2	
		7599899.98	T^-1	36021.6001	T^0.5	-19.6325154	Tln(T	
	1644-2000	-3189873.33	T^0	3348.24722	T	-536.97456	Tln(T	
$Fe_6B_2O_{12}$	298-1192	-3835519.51	T^0	3938.64849	T	-0.003114244	T^2	"
		4006016.05	T^-1	-9278.59349	T^0.5	-598.092507	Tln(T	
	1192-2000	-3921195	T^0	3317.86606	T	4361460	T^-1	
		-538.80615	Tln(T					
	2000-2500	-3921195	T^0	3317.86606	T	4361460	T^-1	
		-538.80615	Tln(T					
FeO	298-1644	-322147.542	T^0	-330.687435	T	-0.01530403	T^2	Bale et al.[43]
		1266650	T^-1	6003.60001	T^0.5	18.0244741	Tln(T	
	1644-2000	-299283.753	T^0	417.258468	T	-68.1992	Tln(T	
FeB_4O_7	298-1192	-2850138.18	T^0	2600.27025	T	-0.021532518	T^2	This work
		555762.105	T^-1	-12553.587	T^0.5	-356.106959	Tln(T	
	1192-1644	-3021489.16	T^0	1358.7054	T	-0.01530403	T^2	
		1266650	T^-1	6003.60001	T^0.5	-237.534246	Tln(T	
	1644-2000	-2998625.37	T^0	2106.6513	T	-323.75792	Tln(T	
$FeSiO_3$	298-2500	-1237141.38	T^0	555.709899	T	-0.0076095	T^2	Fabrichnaya & Sundman[221]
		-4170800	T^-1	9390.4	ln(T)	-152870833	T^-2	
		-110.148	Tln(T					
$K_2B_4O_7$	298-1088	-1312385.63	T^0	-8206.01151	T	-0.087092749	T^2	Bale et al.[43]
		-21301951.1	T^-1	-704021.751	ln(T)	187179.694	T^0.5	
		709.373468	Tln(T					
	1088-1500	2690647.79	T^0	-5095.3387	T	-138620093	T^-1	
		-1509731.11	ln(T)	229304.079	T^0.5	296.804103	Tln(T	
$K_2B_6O_{10}$	298-1000	-5353593	T^0	5916.83097	T	-0.050323691	T^2	"
		5970459.59	T^-1	229295.91	ln(T)	-75741.4515	T^0.5	
		-693.759394	Tln(T					
	1000-2000	-30517957.9	T^0	66016.774	T	550584644	T^-1	
		6927267.4	ln(T)	52.476067	T^1.5	-1385086.34	T^0.5	
		-6781.52311	Tln(T					

Table 5.6 cont'd. Gibbs energy functions of stoichiometric solid oxides

Compound	*T* range (K)	Gibbs energy function (J/mol)						Reference
$K_2B_8O_{13}$	298-700	-6024133.19	T^0	1275.39693	T	-0.182505684	T^2	Bale et al.[43]
		129639.412	T^-1	-625.163786	ln(T)	-217.500496	Tln(T)	
	700-1130	-68795815.6	T^0	251889.458	T	1.60695191	T^2	
		888238198	T^-1	19652003.1	ln(T)	-4931793.53	T^0.5	
		-24873.5593	Tln(T)					
	1130-2000	3624106.88	T^0	-3570.13324	T	-239063954	T^-1	
		-2283148.44	ln(T)	298614.88	T^0.5	11.0158607	Tln(T)	
K_2O	298-1013	-386888.05	T^0	415.096273	T	-0.008573	T^2	"
		295819.992	T^-1	-75.9470015	Tln(T)			
	1013-1300	-408963.344	T^0	643.399707	T	-107.000001	Tln(T)	
$K_2Si_2O_5(\gamma)$	298-1318	-2612211.83	T^0	1476.0817	T	7396700	T^-1	"
		-381535000	T^-2	-240.72	Tln(T)			
$K_2Si_2O_5(\beta)$	298-1318	-2610998.47	T^0	1473.70256	T	7396700	T^-1	"
		-381535000	T^-2	-240.72	Tln(T)			
$K_2Si_2O_5(\alpha)$	298-1318	-2609408.55	T^0	1471.86875	T	7396700	T^-1	"
		-381535000	T^-2	-240.72	Tln(T)			
$K_2Si_4O_9(\beta)$	298-373	-4499888.98	T^0	2555.94959	T	10943384	T^-1	"
		-545391123	T^-2	-1922.20799	T^0.5	-400.743984	Tln(T)	
	373-865	-4500085.06	T^0	2558.0503	T	-0.008440022	T^2	
		10943384	T^-1	1.50709E-05	T^3	-545391123	T^-2	
		-1.00917E-08	T^4	-1922.20799	T^0.5	-400.743984	Tln(T)	
	865-1038	-4499430.31	T^0	2446.78229	T	-0.00809604	T^2	
		-391.37136	Tln(T)					
$K_2Si_4O_9(\alpha)$	298-373	-4496677.2	T^0	2552.23655	T	10943384	T^-1	"
		-545391123	T^-2	-1922.20799	T^0.5	-400.743984	Tln(T)	
	373-865	-4496873.28	T^0	2554.33725	T	-0.008440022	T^2	
		10943384	T^-1	1.50709E-05	T^3	-545391123	T^-2	
		-1.00917E-08	T^4	-1922.20799	T^0.5	-400.743984	Tln(T)	
	865-1038	-4496218.53	T^0	2443.06925	T	-0.00809604	T^2	
		-391.37136	Tln(T)					
K_2SiO_3	298-1249	-1594048.44	T^0	671.804505	T	-0.024405272	T^2	"
		707723.6	T^-1	-118.900912	Tln(T)			
$K_4B_2O_5$	298-1013	-2459271.42	T^0	2295.67139	T	-0.020260244	T^2	This work
		236196.038	T^-1	-9278.59349	T^0.5	-338.95972	Tln(T)	
	1013-1192	-2503422	T^0	2752.27826	T	-0.003114244	T^2	
		-355443.946	T^-1	-9278.59349	T^0.5	-401.065718	Tln(T)	
	1192-1300	-2589097.5	T^0	2131.49583	T	-341.779362	Tln(T)	
	1300-2000	-2589097.5	T^0	2131.49583	T	-341.779362	Tln(T)	
$K_4B_6O_{11}$	298-1013	-5303261.12	T^0	5226.62913	T	-0.026488732	T^2	"
		-474691.854	T^-1	-27835.7805	T^0.5	-713.091153	Tln(T)	
	1013-1192	-5347411.71	T^0	5683.236	T	-0.009342731	T^2	
		-1066331.84	T^-1	-27835.7805	T^0.5	-775.197152	Tln(T)	
	1192-1300	-5604438.19	T^0	3820.88872	T	-597.338082	Tln(T)	
	1300-2000	-5604438.19	T^0	3820.88872	T	-597.338082	Tln(T)	
K_4SiO_4	298-1185	-2155463.08	T^0	1366.21789	T	-0.017146	T^2	Bale et al.[43]
		2364981.98	T^-1	-961.103996	T^0.5	-81928061.6	T^-2	
		-231.905995	Tln(T)					
$K_6B_2O_6$	298-1013	-2906159.47	T^0	2710.76766	T	-0.028833244	T^2	This work
		532016.03	T^-1	-9278.59349	T^0.5	-414.906721	Tln(T)	
	1013-1192	-2972385.35	T^0	3395.67797	T	-0.003114244	T^2	
		-355443.946	T^-1	-9278.59349	T^0.5	-508.065719	Tln(T)	
	1192-1300	-3058060.84	T^0	2774.89554	T	-448.779363	Tln(T)	
	1300-2000	-3058060.84	T^0	2774.89554	T	-448.779363	Tln(T)	

Table 5.6 cont'd. Gibbs energy functions of stoichiometric solid oxides

Compound	*T* range (K)	Gibbs energy function (J/mol)						Reference
$K_{10}B_{38}O_{62}$	298-1013	-28108534.3	T^0	29919.5794	T	-0.102035632	T^2	This work
		-5274335.02	T^-1	-176293.276	T^0.5	-3933.98362	Tln(T)	
	1013-1192	-28218910.8	T^0	31061.0966	T	-0.059170632	T^2	
		-6753434.98	T^-1	-176293.276	T^0.5	-4089.24862	Tln(T)	
	1192-1300	-29846745.2	T^0	19266.2305	T	-2962.80784	Tln(T)	
	1300-2000	-29846745.2	T^0	19266.2305	T	-2962.80784	Tln(T)	
$K_2B_{10}O_{16}$	298-723	-7129125.76	T^0	8117.69883	T	-8.57E-03	T^2	"
		295819.992	T^-1	-48539.5078	T^0.5	-149240658	T^-2	
		-1058.09916	Tln(T)					
	723-1013	-7541347.36	T^0	4685.81754	T	-8.57E-03	T^2	
		295819.992	T^-1	-724.467001	Tln(T)			
	1013-1300	-7563422.66	T^0	4914.12098	T	-755.520001	Tln(T)	
	1300-2000	-7563422.66	T^0	4914.12098	T	-755.520001	Tln(T)	
$KAlO_2(\beta)$	298-810	-1167128.76	T^0	399.063604	T	-0.0348505	T^2	Bale et al.[43]
		486065.991	T^-1	4.37928E-06	T^3	-68.6114997	Tln(T)	
	810-2600	-1170574.83	T^0	539.995886	T	-0.006	T^2	
		-91.9700019	Tln(T)					
$KAlO_2(\alpha)$	298-810	-1165833.76	T^0	397.464838	T	-0.0348505	T^2	"
		486065.991	T^-1	4.37928E-06	T^3	-68.6114997	Tln(T)	
	810-2600	-1169279.83	T^0	538.397121	T	-0.006	T^2	
		-91.9700019	Tln(T)					
$KAlSi_2O_6$	298-850	-3118627.78	T^0	979.620715	T	-0.14578413	T^2	"
		3928600.07	T^-1	7.16068E-05	T^3	-2.27069E-08	T^4	
		-159866672	T^-2	-160.616986	Tln(T)			
	850-918	13927105.2	T^0	-467460.634	T	-137.657668	T^2	
		3928600.62	T^-1	0.053260117	T^3	-1.03146E-05	T^4	
		-159866672	T^-2	78882.326	Tln(T)			
	918-2000	-3130719.74	T^0	1450.55472	T	-0.000733725	T^2	
		3191190.56	T^-1	-240.867967	Tln(T)			
$KAlSi_3O_8$(Microcline)	298-1473	-4047500.24	T^0	2609.56921	T	6018626.05	T^-1	"
		-7764.18002	T^0.5	-306070911	T^-2	-381.372311	Tln(T)	
$KAlSi_3O_8$(K-Feldspar)	298-1436	-3946203.49	T^0	4998.75393	T	0.078664999	T^2	"
		4208273.06	T^-1	-5.795E-06	T^3	-27089.6795	T^0.5	
		-306070911	T^-2	-664.355227	Tln(T)			
	1436-1473	-4036421.72	T^0	2594.5574	T	6018626.05	T^-1	
		-7764.18002	T^0.5	-306070911	T^-2	-381.372311	Tln(T)	
$KAlSi_3O_8$(Sanidine)	298-1473	-4036421.59	T^0	2594.55721	T	6018626.05	T^-1	"
		-7764.18002	T^0.5	-306070911	T^-2	-381.372311	Tln(T)	
KBO_2	298-1200	-1349368.6	T^0	4790.13635	T	3146492.37	T^-1	"
		144157.511	ln(T)	6.18454342	T^1.5	-57630.7431	T^0.5	
		-568.801196	Tln(T)					
	1200-2000	-850723.573	T^0	1114.4129	T	-11189169.9	T^-1	
		-19840.6711	ln(T)	-5879.89178	T^0.5	-151.396955	Tln(T)	
	2000-2001	-981563.544	T^0	427.47242	T	-80	Tln(T)	
Li_2O	298-1843	-669227.483	T^0	188.985206	T	-0.029072095	T^2	"
		1375700.37	T^-1	2.28388E-06	T^3	10344.7352	ln(T)	
		-34.2464863	Tln(T)					
	1843-3000	-655479.762	T^0	618.431454	T	-0.003136125	T^2	
		7107264.87	T^-1	-92.2890378	Tln(T)			

Table 5.6 cont'd. Gibbs energy functions of stoichiometric solid oxides

Compound	*T* range	Gibbs energy function (J/mol)						Reference
Li_3NaSiO_4	298-800	-2330306.34	T^0	979.793804	T	-0.04827802	T^2	Bale et al.[43]
		1223625	T^-1	-160.34756	Tln(T			
	800-984	-2544140.13	T^0	4321.13926	T	0.01967198	T^2	
		0.00013562	T^3	-1.27902E-	T^8	-640.64756	Tln(T	
	984-1358	-2416496.54	T^0	1003.47686	T	-0.05240302	T^2	
		2063550.56	T^-1	0.0000035	T^3	15517.1028	ln(T)	
		-166.94756	Tln(T					
	1358-1450	-2432255.97	T^0	1177.08742	T	-0.043125	T^2	
		2063550.56	T^-1	0.0000035	T^3	15517.1028	ln(T)	
		-191.152	Tln(T					
	1450-1550	-2432255.97	T^0	1177.08742	T	-0.043125	T^2	
		2063550.56	T^-1	0.0000035	T^3	15517.1028	ln(T)	
		-191.152	Tln(T					
$LiAlO_2$	298-500	-1199839.69	T^0	3.70264246	T	-0.1704815	T^2	Kulkarni et
		81050	T^-1	5.11098E-05	T^3	4.761	Tln(T	
	500-2058	-1224778.77	T^0	583.142878	T	-0.006067	T^2	
		1254850	T^-1	-1.72667E-	T^3	-92.379	Tln(T	
	2058-3000	-1283289.96	T^0	916.091389	T	-133.89	Tln(T	
$LiAlSi_2O_6$(α-Spodumene)	298-800	-3053631.59	T^0	2288.3625	T	-0.01302	T^2	Bale et al.[43]
		-11036	T^0.5	-312.1	Tln(T			
	800-1300	-3114254.6	T^0	1058.8021	T	-0.03888	T^2	
		-172.1	Tln(T					
$LiAlSi_2O_6$(β-Spodumene)	298-800	-2844710.96	T^0	-655.474357	T	-0.044205	T^2	"
		-98140	ln(T)	31568	T^0.5	-8.586	Tln(T	
	800-1800	-3093822.22	T^0	1184.88345	T	-0.026035	T^2	
		-195.2	Tln(T					
$LiAlSiO_4$(β)	298-1300	-2065456.25	T^0	1291.34455	T	-0.0043895	T^2	"
		72.8	T^-1	-24990	ln(T)	-195.4	Tln(T	
$LiAlSiO_4$(α)	298-1200	-2064810.41	T^0	1290.86539	T	-0.0043895	T^2	"
		72.8	T^-1	-24990	ln(T)	-195.4	Tln(T	
	1200-1900	-2167991.62	T^0	788.239488	T	-0.025105	T^2	
		-129.7	Tln(T					
$LiBO_2$	298-1117	-1059201.43	T^0	291.077487	T	-	T^2	"
		808667.014	T^-1	3696.90186	ln(T)	-49.133883	Tln(T	
	1117-2000	-1039568.2	T^0	325.756091	T	-	T^2	
		221318.486	T^-1	-53.3330599	Tln(T			
	2000-2001	-981708.087	T^0	444.087839	T	-80	Tln(T	
$LiFeO_2$	298-1000	-754301.511	T^0	933.833558	T	-0.01623	T^2	"
		-4216	T^0.5	-131	Tln(T			
$Mg_2Al_4Si_5O_{18}$	298-1750	-9187162.57	T^0	6914.09481	T	1158650	T^-1	"
		61701666.7	T^-2	-31849.2	T^0.5	-954.39	Tln(T	
$Mg_2B_2O_5$	298-1800	-2633936.35	T^0	230.822668	T	0.067078365	T^2	"
		794862.792	T^-1	-15.204624	T^1.5	1.7301859	Tln(T	
Mg_2SiO_4	298-3000	-2209753.81	T^0	1057.94573	T	-0.009275	T^2	Fabrichnaya[268]
		1985500	T^-1	-5610	ln(T)	-47683333.3	T^-2	
		-165.8	Tln(T					
$Mg_3Al_2Si_3O_{12}$	298-1700	-6336492.32	T^0	4577.46946	T	2350950.06	T^-1	Bale et al.[43]
		-18168.2803	T^0.5	-640.719978	Tln(T			
$Mg_3B_2O_6$	298-1850	-3277099.98	T^0	465.183604	T	0.071492201	T^2	"
		1198527.63	T^-1	-16.3139691	T^1.5	-32.7462529	Tln(T	
$Mg_4Al_{10}Si_2O_{23}$	298-2000	-13046195	T^0	8141.55575	T	16853810.6	T^-1	"
		-664214821	T^-2	-21306.9236	T^0.5	-1170.27835	Tln(T	
MgB_4O_7	298-1350	-3286144.29	T^0	-213.489561	T	0.121877714	T^2	"
		375277.718	T^-1	-27.2237978	T^1.5	108.311442	Tln(T	
$MgFe_2O_4$	298-2000	-1470263.4	T^0	783.433428	T	-0.01636	T^2	"
		-134	Tln(T					

Table 5.6 cont'd. Gibbs energy functions of stoichiometric solid oxides

Compound	*T* range (K)	Gibbs energy function (J/mol)						Reference
MgO	298-3098	-611541.379	T^0	420.064762	T	310577.002	T^-1	Bale et al.[43]
		-1184.796	T^0.5	-974102.005	T^-2	-61.1096505	Tln(T)	
	3098-3500	-662387.67	T^0	462.122764	T	-66.944	Tln(T)	
$MgSiO_3$(β-Orthopyroxene)	298-3000	-1500335.8	T^0	968.55269	T	-0.000941	T^2	Fabrichnaya[268]
		675000	T^-1	-76866666.7	T^-2	-19380	ln(T)	
		-144.45	Tln(T)					
$MgSiO_3$(α-Protopyroxene)	298-3000	-1496656.67	T^0	979.638578	T	-0.0009493	T^2	"
		687130	T^-1	-76404833.3	T^-2	-20162.6	ln(T)	
		-145.79	Tln(T)					
$Na_2Ca_2Si_2O_7$	298-3000	-3962397.3	T^0	2322.02358	T	7105241.06	T^-1	Bale et al.[43]
		-1071.232	T^0.5	-353741637	T^-2	-372.927677	Tln(T)	
$Na_2Ca_2Si_3O_9$	298-1300	-5051809.72	T^0	3272.3835	T	6344864.46	T^-1	"
		-7921.39482	T^0.5	-289630273	T^-2	-479.281384	Tln(T)	
$Na_2Ca_3Al_{16}O_{28}$	298-1405	-16850875.2	T^0	10531.0756	T	-0.021932551	T^2	"
		17572856	T^-1	2.34792E-06	T^3	-28115.2314	T^0.5	
		-596934256	T^-2	-1482.74057	Tln(T)			
	1405-1500	-16873954.4	T^0	10799.7269	T	17166171	T^-1	
		-28115.2314	T^0.5	-596934256	T^-2	-1521.12457	Tln(T)	
	1500-2327	-16873954.4	T^0	10799.7269	T	17166171	T^-1	
		-28115.2314	T^0.5	-596934256	T^-2	-1521.12457	Tln(T)	
	2327-2845	-18197433.1	T^0	13144.0598	T	1720718.97	T^-1	
		-1606.848	T^0.5	-51489393.9	T^-2	-1820.68551	Tln(T)	
	2845-3000	-18272973.1	T^0	13235.3926	T	-1832.592	Tln(T)	
	3000-3500	-18272973.1	T^0	13235.3926	T	-1832.592	Tln(T)	
$Na_2Ca_3Si_6O_{16}$	298-1373	-8683657.85	T^0	4465.4541	T	-0.021932551	T^2	"
		20001689.2	T^-1	2.34792E-06	T^3	-1009735517	T^-2	
		-1606.848	T^0.5	-694.82552	Tln(T)			
$Na_2Ca_8Al_6O_{18}$	298-1405	-11127559.8	T^0	6687.4304	T	-0.021932551	T^2	"
		10787313.5	T^-1	2.34792E-06	T^3	-14225.5717	T^0.5	
		-341846874	T^-2	-1001.60201	Tln(T)			
	1405-1500	-11150638.9	T^0	6956.08172	T	10380628.5	T^-1	
		-14225.5717	T^0.5	-341846874	T^-2	-1039.98601	Tln(T)	
	1500-2327	-11150638.9	T^0	6956.08172	T	10380628.5	T^-1	
		-14225.5717	T^0.5	-341846874	T^-2	-1039.98601	Tln(T)	
	2327-2845	-11646943.5	T^0	7835.20656	T	4588583.93	T^-1	
		-4284.92799	T^0.5	-137305050	T^-2	-1152.32136	Tln(T)	
	2845-3000	-11848383.6	T^0	8078.76082	T	-1184.072	Tln(T)	
	3000-3500	-11848383.6	T^0	8078.76082	T	-1184.072	Tln(T)	
$Na_2CaSi_5O_{12}$	298-1123	-6150055.26	T^0	3154.58396	T	-0.021932551	T^2	"
		15875495.7	T^-1	2.34792E-06	T^3	-815701567	T^-2	
		-535.615998	T^0.5	-501.870511	Tln(T)			
Na_2CaSiO_4	298-3000	-2352484.65	T^0	1530.62599	T	3552620.53	T^-1	"
		-535.615998	T^0.5	-176870818	T^-2	-238.763839	Tln(T)	
Na_2FeO_2	298-1600	-838530.863	T^0	55.3236417	T	-0.037236581	T^2	"
		1673335.01	T^-1	2.34792E-06	T^3	6003.60001	T^0.5	
		-48.1915266	Tln(T)					
Na_2FeSiO_4	298-1300	-1939536.29	T^0	535.519672	T	-0.037236581	T^2	"
		4652382.55	T^-1	2.34792E-06	T^3	6003.60001	T^0.5	
		-159707687	T^-2	-123.564195	Tln(T)			
$Na_2Mg_2Si_6O_{15}$	298-1200	-7464744.74	T^0	4926.98938	T	11542279.5	T^-1	"
		-13351.2747	T^0.5	-540204873	T^-2	-738.22496	Tln(T)	
$Na_2MgSi_4O_{10}$	298-1200	-4998940.4	T^0	3352.50982	T	8311434.41	T^-1	"
		-8685.99622	T^0.5	-400191413	T^-2	-504.469064	Tln(T)	
$Na_3Fe_5O_9$	298-1405	-3062437.55	T^0	2650.37592	T	-0.032898827	T^2	"
		4244577.51	T^-1	3.52188E-06	T^3	-441.846326	Tln(T)	

Table 5.6 cont'd. Gibbs energy functions of stoichiometric solid oxides

Compound	*T* range (K)	Gibbs energy function (J/mol)						Reference
Na_3FeO_3	298-1600	-1237614.77	T^0	1024.33145	T	-0.032898827	T^2	Bale et al.[43]
		1336937.51	T^-1	3.52188E-06	T^3	-167.828466	Tln(T)	
$Na_4CaSi_3O_9$	298-1423	-4764849.46	T^0	4414.32325	T	1829673.99	T^-1	"
		-20512.38	T^0.5	-125824903	T^-2	-618.612663	Tln(T)	
Na_4FeO_3	298-1600	-1258074.28	T^0	611.06001	T	-0.059169132	T^2	"
		2080020.02	T^-1	4.69583E-06	T^3	-0.0001127	T^0.5	
		-114.407527	Tln(T)					
Na_5FeO_4	298-1600	-1536285.43	T^0	1377.66073	T	-0.054831378	T^2	"
		1743622.52	T^-1	5.86979E-06	T^3	-234.044467	Tln(T)	
$Na_5FeSi_4O_{12}$	298-1200	-5901004.17	T^0	3300.67203	T	-0.054831378	T^2	"
		13659812.7	T^-1	5.86979E-06	T^3	-638830749	T^-2	
		-535.535139	Tln(T)					
$Na_8Ca_3Si_5O_{17}$	298-1373	-9483438.48	T^0	5030.36688	T	-0.087730204	T^2	"
		18242696.7	T^-1	9.39167E-06	T^3	-850027830	T^-2	
		-1606.848	T^0.5	-818.100855	Tln(T)			
$Na_8Fe_2O_7$	298-1600	-2843129	T^0	2237.49593	T	-0.040443454	T^2	"
		1776313.56	T^-1	-2.49612E-06	T^3	-392.782041	Tln(T)	
$Na_8Fe_6Si_{15}O_{40}$	298-850	-18922663.3	T^0	6768.9849	T	-0.179554384	T^2	"
		53912353.1	T^-1	9.39167E-06	T^3	36021.6001	T^0.5	
		-2395615307	T^-2	-1287.30718	Tln(T)			
$NaFe_2O_3$	298-1700	-1061763.83	T^0	276.064732	T	-0.026270305	T^2	"
		2196902.5	T^-1	1.17396E-06	T^3	6003.60001	T^0.5	
		-83.5879913	Tln(T)					
$NaFeO_2(\beta)$	870-1620	-739289.965	T^0	671.358406	T	-0.00384665	T^2	"
		1276100	T^-1	-110.95	Tln(T)			
$NaFeO_2(\alpha)$	1270-1620	-737114.285	T^0	669.645272	T	-0.00384665	T^2	"
		1276100	T^-1	-110.95	Tln(T)			
$NaFeSi_2O_6$	298-1263	-2641046.28	T^0	1039.32488	T	-0.074399644	T^2	"
		1805576.29	T^-1	9.93995E-06	T^3	-171.449479	Tln(T)	
	1263-5000	-2673924.39	T^0	1635.02116	T	-262	Tln(T)	
$Li_4B_2O_5(\beta)$	298-400	-2798414.17	T^0	1198.60811	T	-0.060352471	T^2	Yu et al.[160]
		2363564.62	T^-1	1.88316E-06	T^3	-188.982264	Tln(T)	
	400-723	-2801825.13	T^0	1257.01555	T	-0.049179518	T^2	
		2594979.57	T^-1	-8.1517E-07	T^3	-198.222711	Tln(T)	
	723-1726	-2834611.63	T^0	1821.08323	T	0.01363341	T^2	
		1862380	T^-1	-9.18659E-06	T^3	-283.03532	Tln(T)	
	1726-3000	-2872953.96	T^0	2247.56306	T	1.91193E-16	T^2	
		3.46897E-07	T^-1	-8.6391E-21	T^3	-337.704	Tln(T)	
	3000-4000	-2872953.96	T^0	2247.56306	T	1.91193E-16	T^2	
		3.46897E-07	T^-1	-8.6391E-21	T^3	-337.704	Tln(T)	
$Li_4B_2O_5(\alpha)$	298-400	-2785382.96	T^0	1183.98625	T	-0.060352471	T^2	"
		2363564.62	T^-1	1.88316E-06	T^3	-188.982264	Tln(T)	
	400-723	-2788793.93	T^0	1242.39369	T	-0.049179518	T^2	
		2594979.57	T^-1	-8.1517E-07	T^3	-198.222711	Tln(T)	
	723-1726	-2821580.42	T^0	1806.46137	T	0.01363341	T^2	
		1862380	T^-1	-9.18659E-06	T^3	-283.03532	Tln(T)	
	1726-3000	-2859922.75	T^0	2232.9412	T	1.91193E-16	T^2	
		3.46897E-07	T^-1	-8.6391E-21	T^3	-337.704	Tln(T)	
	3000-4000	-2859922.75	T^0	2232.9412	T	1.91193E-16	T^2	
		3.46897E-07	T^-1	-8.6391E-21	T^3	-337.704	Tln(T)	

Table 5.6 cont'd. Gibbs energy functions of stoichiometric solid oxides

Compound	*T* range (K)	Gibbs energy function (J/mol)						Reference
$Li_6B_2O_6$	298-400	-3502442.33	T^0	1695.89381	T	-0.053535766	T^2	Yu et al.[160]
		3294754.62	T^-1	-2.71013E-06	T^3	-265.647924	Tln(T)	
	400-723	-3505853.3	T^0	1754.30125	T	-0.042362813	T^2	
		3526169.57	T^-1	-5.40846E-06	T^3	-274.888371	Tln(T)	
	723-1726	-3538639.79	T^0	2318.36894	T	0.020450115	T^2	
		2793570	T^-1	-1.37799E-05	T^3	-359.70098	Tln(T)	
	1726-3000	-3596153.28	T^0	2958.08868	T	2.86789E-16	T^2	
		5.20346E-07	T^-1	-1.29586E-20	T^3	-441.704	Tln(T)	
	3000-4000	-3596153.28	T^0	2958.08868	T	2.86789E-16	T^2	
		5.20346E-07	T^-1	-1.29586E-20	T^3	-441.704	Tln(T)	
$Li_2B_4O_7$	298-3000	-3402275.81	T^0	932.398997	T	-0.0720525	T^2	"
		998000	T^-1	-158.812	Tln(T)			
$Li_6B_4O_9$	298-400	-4914495.4	T^0	1924.78336	T	-0.127521647	T^2	"
		3795939.25	T^-1	8.35962E-06	T^3	-301.298867	Tln(T)	
	400-723	-4921317.34	T^0	2041.59824	T	-0.10517574	T^2	
		4258769.14	T^-1	2.96295E-06	T^3	-319.779762	Tln(T)	
	723-1726	-4986890.33	T^0	3169.73361	T	0.020450115	T^2	
		2793570	T^-1	-1.37799E-05	T^3	-489.40498	Tln(T)	
	1726-3000	-5044403.82	T^0	3809.45335	T	2.86789E-16	T^2	
		5.20346E-07	T^-1	-1.29586E-20	T^3	-571.408	Tln(T)	
	3000-4000	-5044403.82	T^0	3809.45335	T	2.86789E-16	T^2	
		5.20346E-07	T^-1	-1.29586E-20	T^3	-571.408	Tln(T)	
$Li_2B_6O_{10}$	298-3000	-4732838.3	T^0	1903.95265	T	-0.044821	T^2	"
		2111000	T^-1	-311.808	Tln(T)			
$Li_2B_8O_{13}$	298-3000	-6065941.56	T^0	2645.55771	T	-0.049248	T^2"	Yu et al.[160]
		5807500	T^-1	-425.525	Tln(T)			
$Li_4B_{10}O_{17}$	298-3000	-8128860.43	T^0	2829.898	T	-0.1168735	T^2	"
		3109000	T^-1	-470.62	Tln(T)			
$Li_2Si_2O_5(\beta)$	298-1215	-2449151.76	T^0	1738.26556	T	-0.006585	T^2	Konar et al.[267]
		-813634.555	T^-1	-40510.6978	ln(T)	-258.27	Tln(T)	
$Li_2Si_2O_5(\alpha)$	1215-1405	-2449150.69	T^0	1738.26469	T	-0.006585	T^2	"
		-813634.555	T^-1	-40510.6978	ln(T)	-258.27	Tln(T)	
$Li_6Si_2O_7$	298-800	-4020644.71	T^0	2166.97728	T	-0.0614105	T^2	"
		2514900	T^-1	-3885.68	T^0.5	-330.95	Tln(T)	
	800-984	-4305756.42	T^0	6622.10456	T	0.0291895	T^2	
		883400	T^-1	0.000180833	T^3	-3885.68	T^0.5	
		-1.70536E-20	T^8	-971.35	Tln(T)			
	984-1452	-4135564.97	T^0	2198.55469	T	-0.0669105	T^2	
		3634800.75	T^-1	4.66667E-06	T^3	20689.4704	ln(T)	
		-3885.68	T^0.5	-339.75	Tln(T)			
	1452-1550	-4189987.76	T^0	2128.07712	T	-0.0575	T^2	
		2751400.75	T^-1	4.66667E-06	T^3	20689.4704	ln(T)	
		-340.747	Tln(T)					
Li_2SiO_3	298-1452	-1679303.35	T^0	1195.94541	T	-0.0094105	T^2	"
		883400	T^-1	-3885.68	T^0.5	-171.35	Tln(T)	
Li_4SiO_4	298-800	-2392051.35	T^0	1001.05747	T	-0.052	T^2	"
		1631500	T^-1	-159.6	Tln(T)			
	800-984	-2677163.07	T^0	5456.18475	T	0.0386	T^2	
		0.000180833	T^3	-1.70536E-20	T^8	-800	Tln(T)	
	984-1550	-2506971.61	T^0	1032.63489	T	-0.0575	T^2	
		2751400.75	T^-1	4.66667E-06	T^3	20689.4704	ln(T)	
		-168.4	Tln(T)					

Table 5.6 cont'd. Gibbs energy functions of stoichiometric solid oxides

Compound	*T* range (K)	Gibbs energy function (J/mol)						Reference
Li_8SiO_6	298-373	-3842448.51	T^0	1292.20617	T	-0.11628838	T^2	Konar et al.[267]
		7276143.5	T^-1	9.13552E-06	T^3	41378.9409	ln(T)	
		-961.103996	T^0.5	-81928061.6	T^-2	-216.997937	Tln(T)	
	373-1200	-3842253.53	T^0	1292.2091	T	-0.120508391	T^2	
		7276143.5	T^-1	1.6671E-05	T^3	41378.9409	ln(T)	
		-961.103996	T^0.5	-81928061.6	T^-2	-216.997937	Tln(T)	
$KAlSiO_4$(hexagonal)	298-810	-2209349.9	T^0	1159.86221	T	-2.52E-03	T^2	Bale et al.[43]
		6553350.46	T^-1	5.13E-06	T^3	-3.92E-09	T^4	
		-356488327	T^-2	-186	Tln(T)			
	810-2000	-2208089.9	T^0	1157.55021	T	6553350.04	T^-1	
		-356488327	T^-2	-186	Tln(T)			
$KAlSiO_4$(orthorhombic)	298-2000	-2206935.88	T^0	1156.1255	T	6553350.04	T^-1	"
		-356488327	T^-2	-186	Tln(T)			
$CaAl_2Si_2O_8$(hexagonal)	298-350	-4264064.79	T^0	1202.78457	T	-208.19584	Tln(T)	"
$CaAl_2Si_2O_8$(anorthite)	298-1828	-4235420.14	T^0	3179.03794	T	-14936.596	T^0.5	"
		52837204.7	T^-2	-439.369371	Tln(T)			
	1828-2500	-4447513.48	T^0	2505.38529	T	-380.744	Tln(T)	

Table 5.7. Gibbs energy function of gaseous O_2

Molecule	*T* (K)	Gibbs energy function (J/mol)						Reference
O_2(g)	298-1000	-5219.33235	T^0	-12.0704127	T	-0.008489341	T^2	Bale et al.[43]
		-114664.628	T^-1	1.12769E-06	T^3	-316.646634	T^0.5	
		-26.9240574	Tln(T)					
	1000-4000	-389938.784	T^0	638.786228	T	0.000723722	T^2	
		9341342.96	T^-1	-16506.1488	T^0.5	95803.9595	ln(T)	
		-89.6813271	Tln(T)					
	4000-6000	-8951197.09	T^0	2742.8706	T	592489211	T^-1	
		-139742.679	T^0.5	1674792.24	ln(T)	-249.173117	Tln(T)	

5.10. Figures

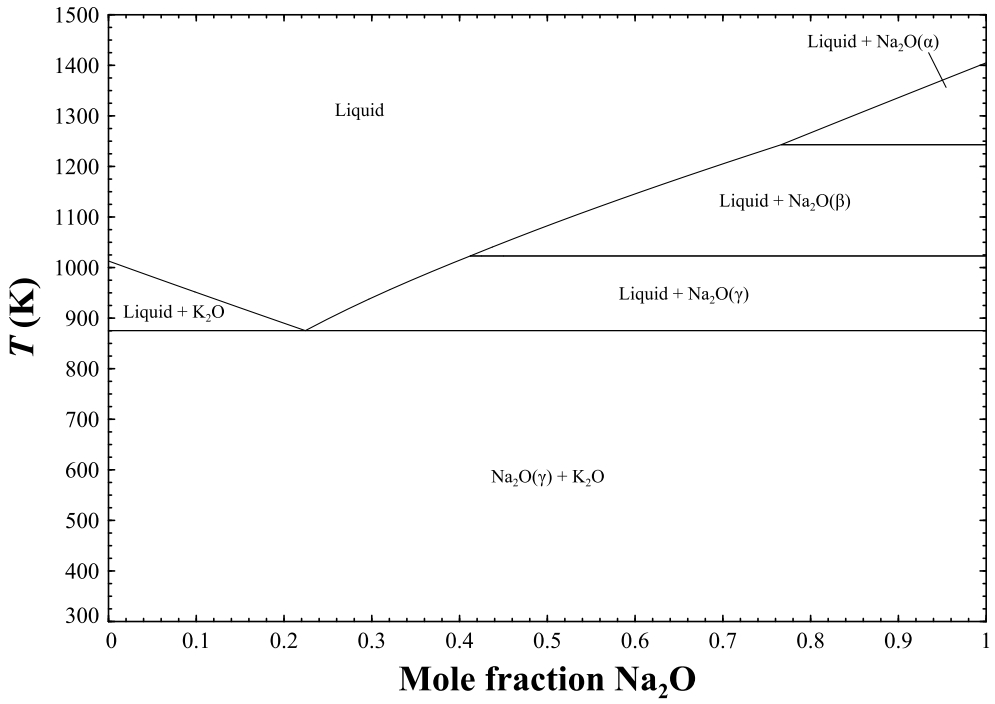

Fig. 5.1. Computed K_2O-Na_2O phase diagram.

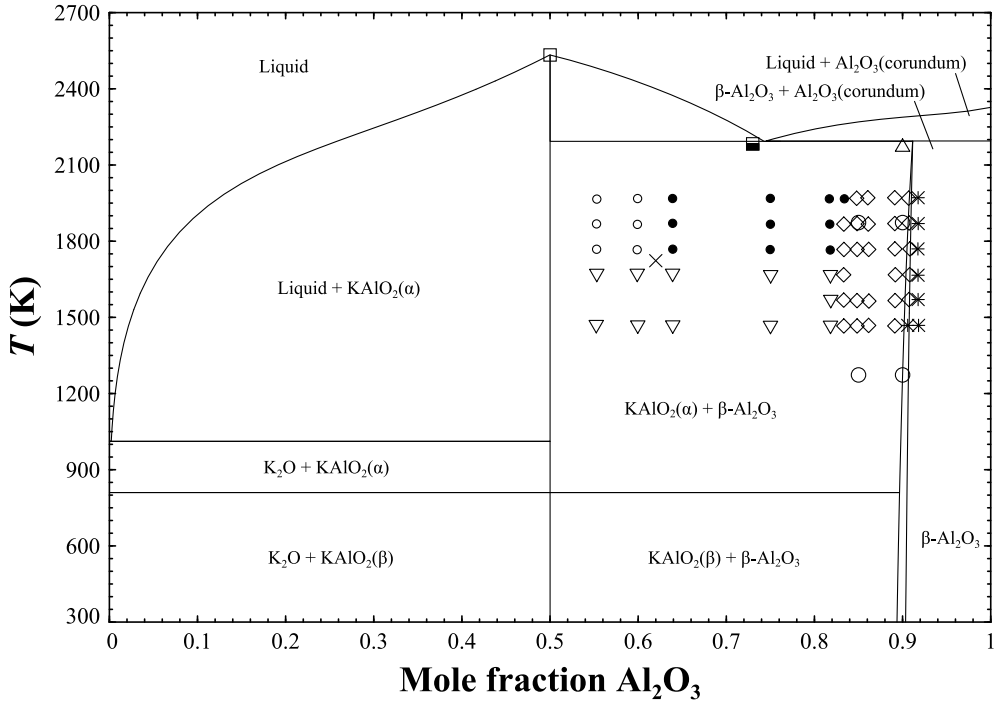

Fig. 5.2. Computed K_2O-Al_2O_3 phase diagram. Data: Eliezer & Howald[237]: △ melt + β-Al_2O_3. Roth[238]: ○ β-Al_2O_3 □ melt + $KAlO_2$ ⬓ melt + $KAlO_2$ + β-Al_2O_3. Moya et al.[236]: ▽ $KAlO_2$ + β-Al_2O_3 ○ melt + $KAlO_2$ ● melt + β-Al_2O_3 × melt + $KAlO_2$ + β-Al_2O_3 ◇ β-Al_2O_3 ✳ Al_2O_3(corundum) + β-Al_2O_3.

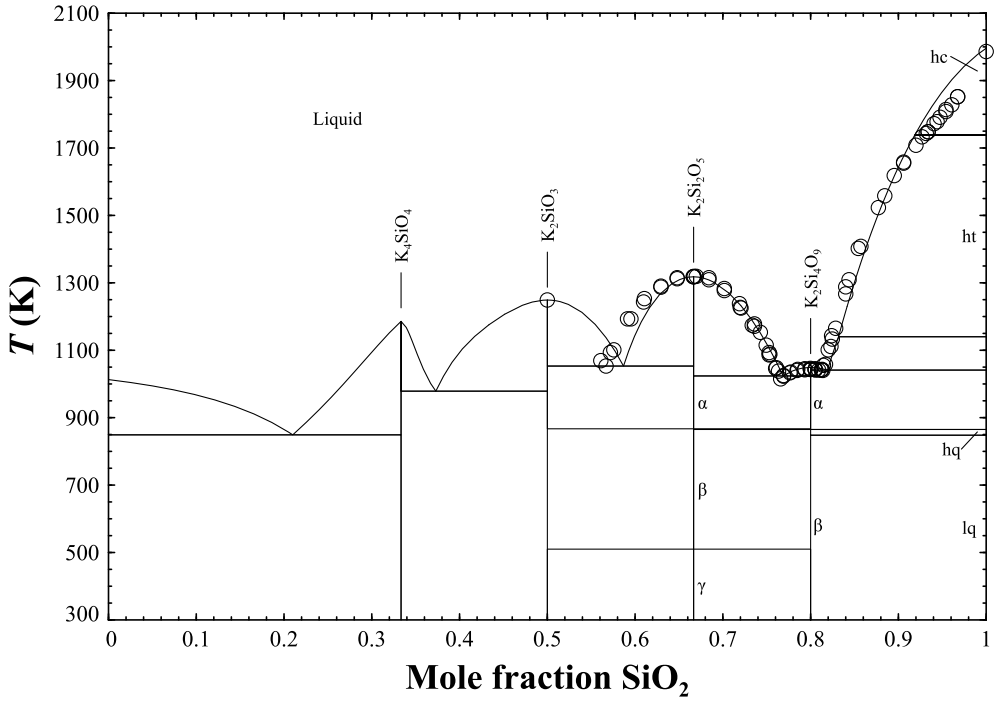

Fig. 5.3. Computed K_2O-SiO_2 phase diagram. Data: ◯[269]

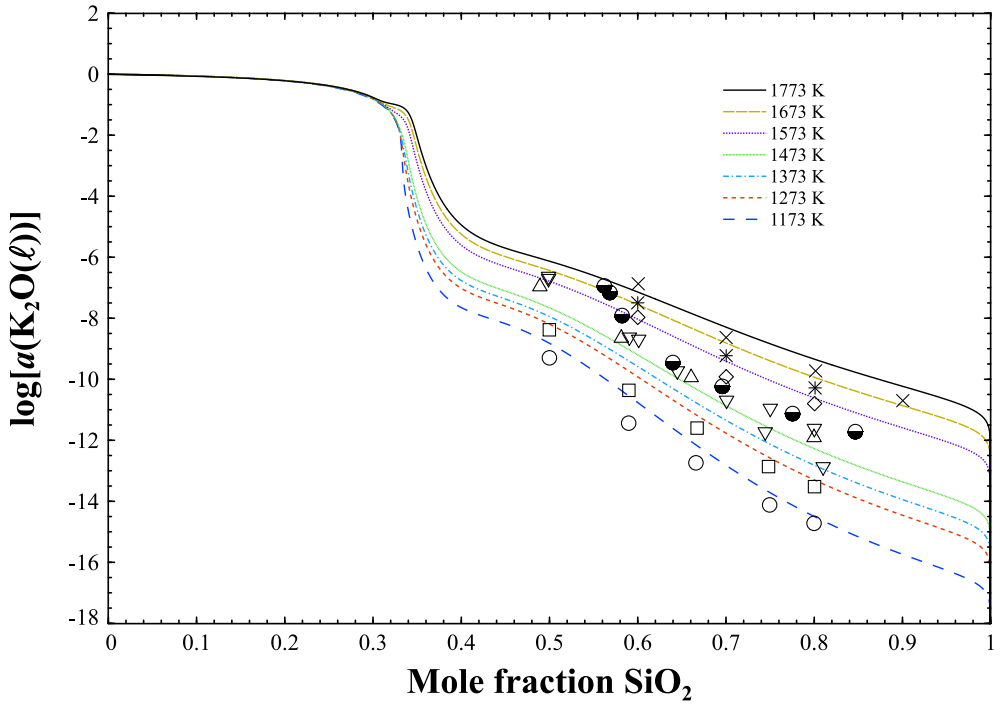

Fig. 5.4. Computed activity of $K_2O(\ell)$ in the K_2O-SiO_2 melt. Data: Zaitsev[270]: ╳ 1773 K ✳ 1673 K ◇ 1573 K ▽ 1373 K △ 1318 K □ 1273 K ◯ 1173 K. Steiler[271]: ◒ 1573 K.

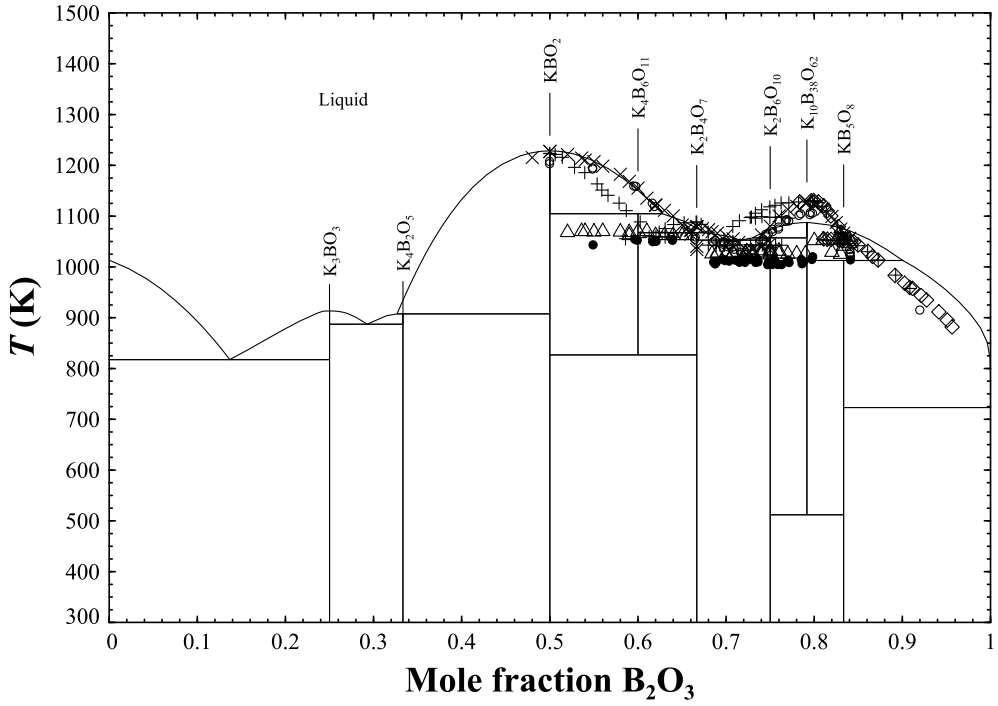

Fig. 5.5. Computed K_2O-B_2O_3 phase diagram. Data: Kaplun & Meshalkin[242]: × liquidus △ solidus. Polyakova & Tokareva[241]: ○ liquidus ● solidus. Rollet[239]: + liquidus. Rollet[240]: ◇ liquidus.

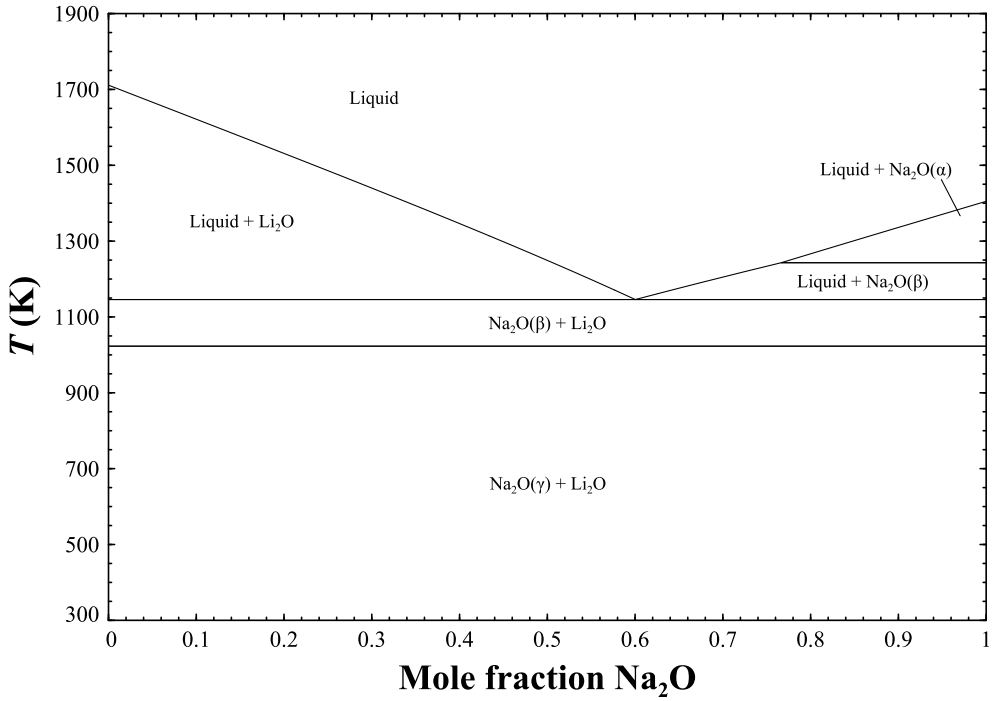

Fig. 5.6. Computed Li_2O-Na_2O phase diagram.

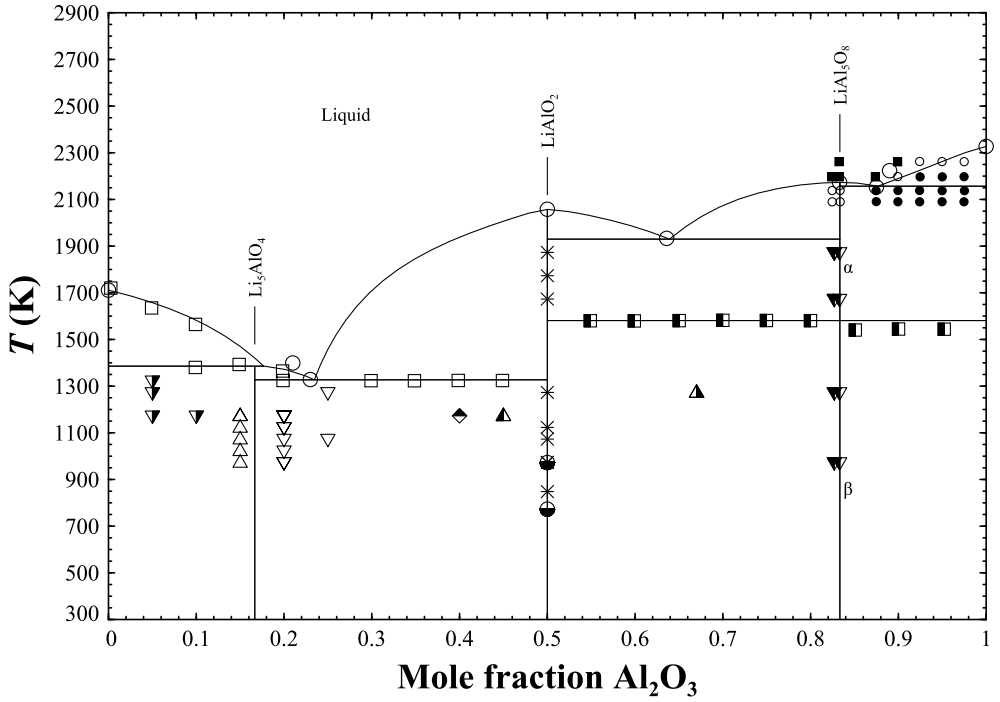

Fig. 5.7. Computed Li_2O-Al_2O_3 phase diagram. Data: Cook & Plante[272]: ▼ Li_2O + $LiAlO_2$ △ Li_5AlO_4 ▽ Li_5AlO_4 + $LiAlO_2$ ▼ $LiAl_5O_8$ ◆ $LiAlO_2$ + unidentified ✳ $LiAlO_2$ ◒ $LiAlO_2$ + Al_2O_3 ◭ $LiAlO_2$ + Li_5AlO_4 ◭ $LiAlO_2$ + $LiAl_5O_8$ □ quenched data ◧ DTA data ■ complete melt ○ partial melt ● no melt

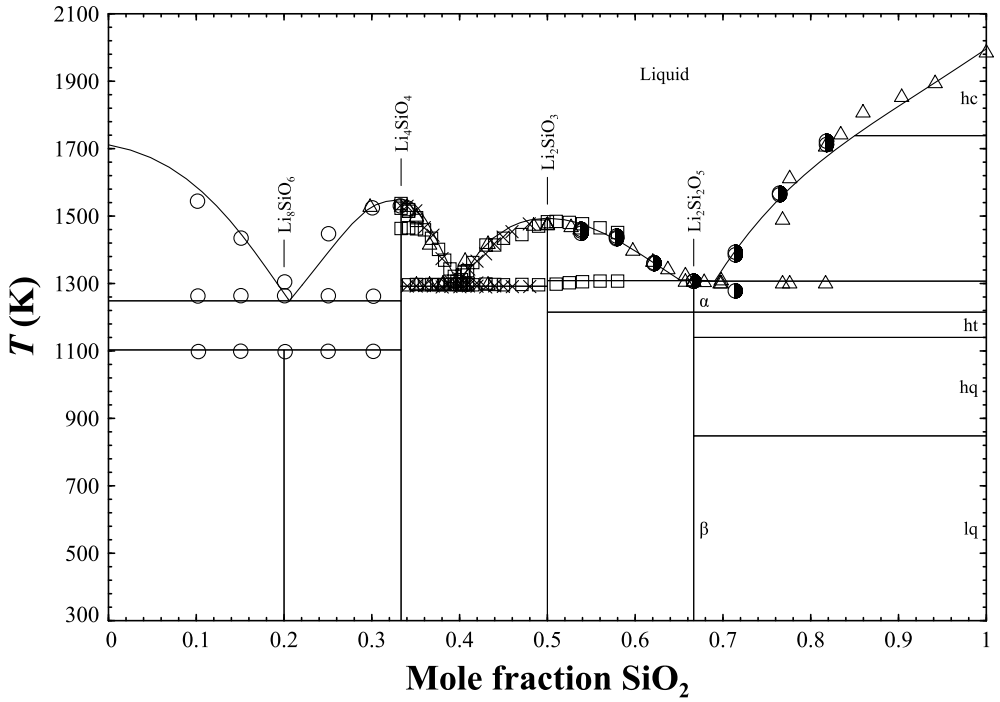

Fig. 5.8. Computed Li_2O-SiO_2 phase diagram. Data: ◯[273] ✕[274] □[275] △[276] ◑[277]

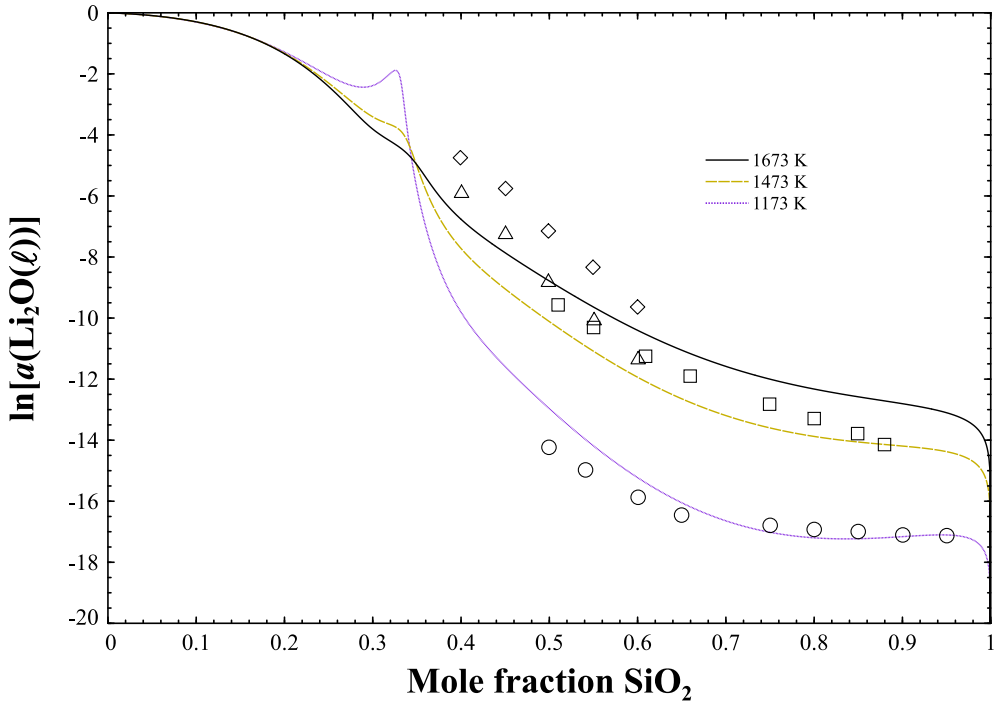

Fig. 5.9. Computed activity of $Li_2O(\ell)$ in the Li_2O-SiO_2 melt. Data: ◇ 1673 K[278] △ 1473 K[278] □ 1473 K[279] ○ 1173 K[279]

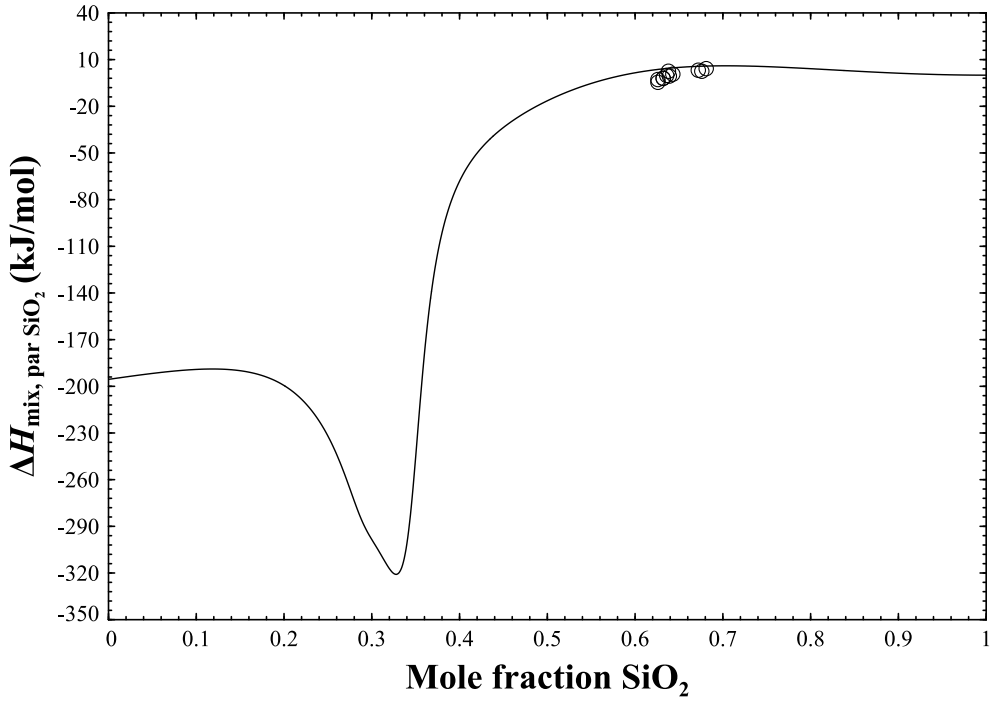

Fig. 5.10. Computed partial enthalpy of SiO_2 in the Li_2O-SiO_2 melt at 1663 K. Data: ○ 1663 K[280]

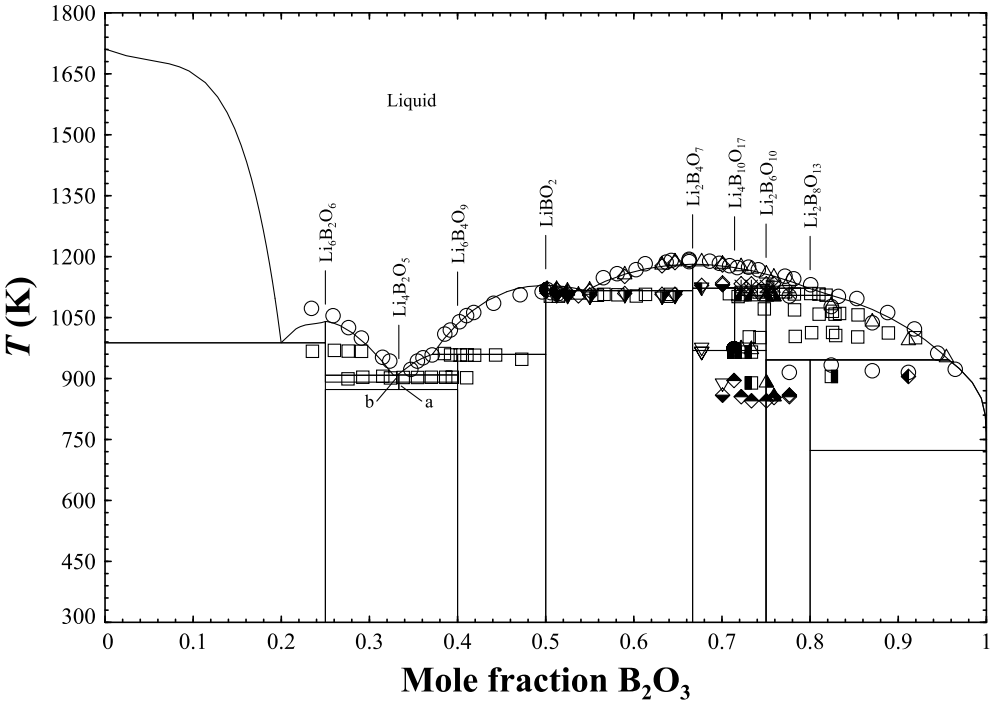

Fig. 5.11. Computed Li_2O-B_2O_3 phase diagram. Data: Rollet & Bouaziz[281]: ○ liquidus □ solidus. Sastry & Hummel[282]: △ melt ◇ melt + $Li_2B_4O_7$ ▼ $Li_2B_4O_7$ + $Li_4B_{10}O_{17}$ ▽ $Li_2B_4O_7$ + LiB_3O_5 ◥ $Li_2B_4O_7$ + $LiBO_2$ ◨ $Li_2B_8O_{13}$ ⬓ melt + $Li_2B_8O_{13}$ ◆ $Li_2B_8O_{13}$ + $Li_2B_4O_7$ ◓ $Li_4B_{10}O_{17}$ ✳ melt + $Li_4B_{10}O_{17}$ ◆ $Li_4B_{10}O_{17}$ + $Li_2B_4O_7$ ◭ $Li_4B_{10}O_{17}$ + LiB_3O_5 ◮ LiB_3O_5 × melt + LiB_3O_5 ◧ LiB_3O_5 + $Li_2B_4O_7$ ◆ LiB_3O_5 + $Li_2B_8O_{13}$ ◐ $LiBO_2$ ◆ melt + $LiBO_2$.

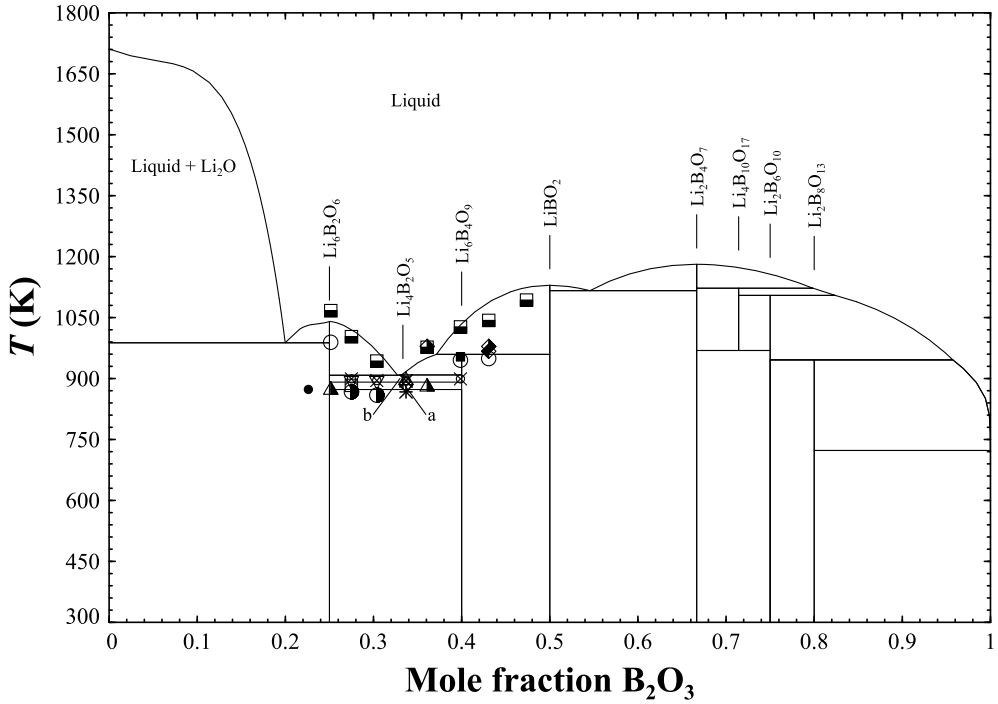

Fig. 5.12. Computed Li_2O-B_2O_3 phase diagram. Data: Sastry & Hummel[283]: ■ liquidus ○ incongruent melting ○ $Li_4B_2O_5$ inversion ◇ Li_3BO_3 ● Li_3BO_3 + Li_2O ✳ Li_3BO_3 + $Li_6B_4O_9$ ■ $Li_6B_4O_9$ ◆ melt + $LiBO_2$ ◆ $LiBO_2$ + $Li_6B_4O_9$ ◇ α-$Li_4B_2O_5$ □ α-$Li_4B_2O_5$ + Li_3BO_3 ◭ α-$Li_4B_2O_5$ + $Li_6B_4O_9$ △ β-$Li_4B_2O_5$ ▽ β-$Li_4B_2O_5$ + Li_3BO_3

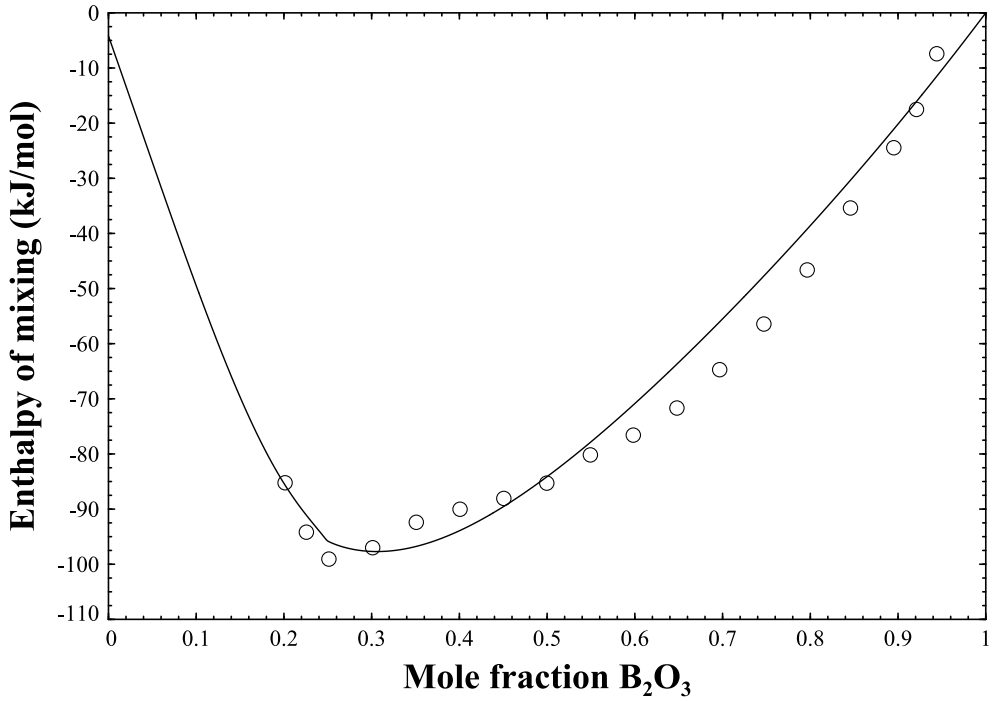

Fig. 5.13. Computed enthalpy of mixing in the Li_2O-B_2O_3 system at 1299 K. Data: ○ 1299 K[137]

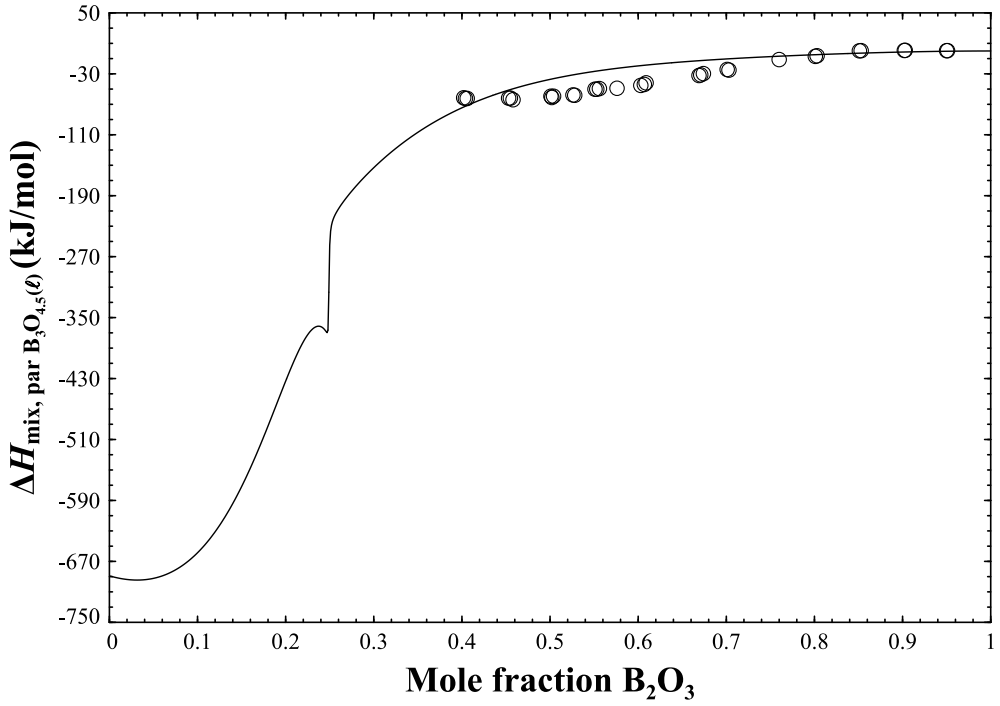

Fig. 5.14. Computed partial enthalpy of $B_3O_{4.5}$ in the Li_2O-B_2O_3 melt at 1213 K. Data: ○ 1213 K[284]

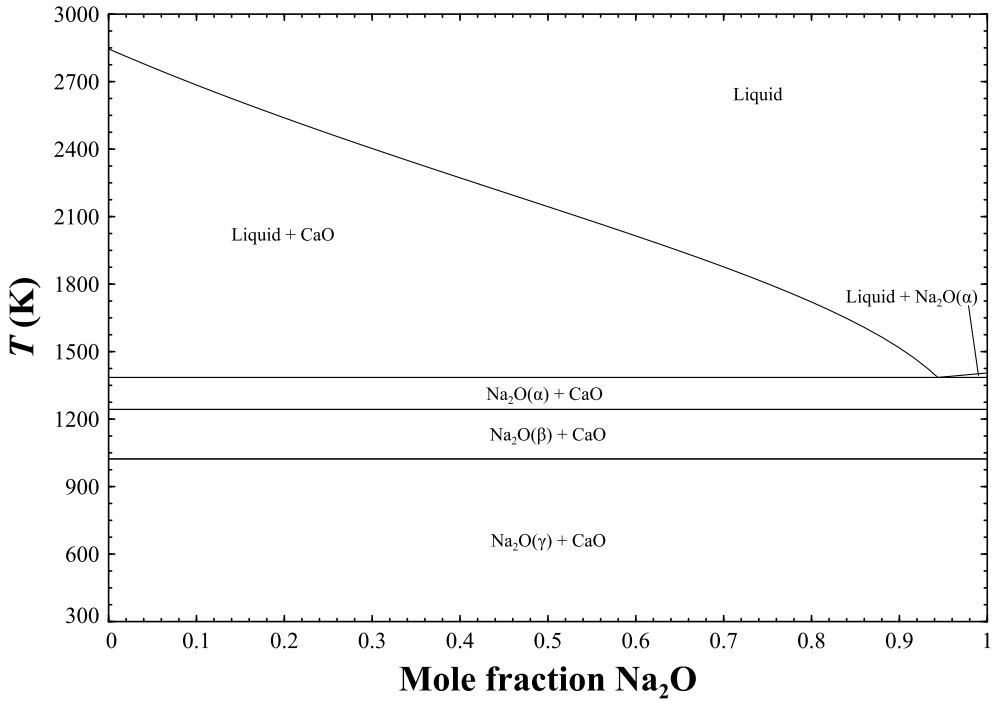

Fig. 5.15. Computed CaO-Na_2O phase diagram.

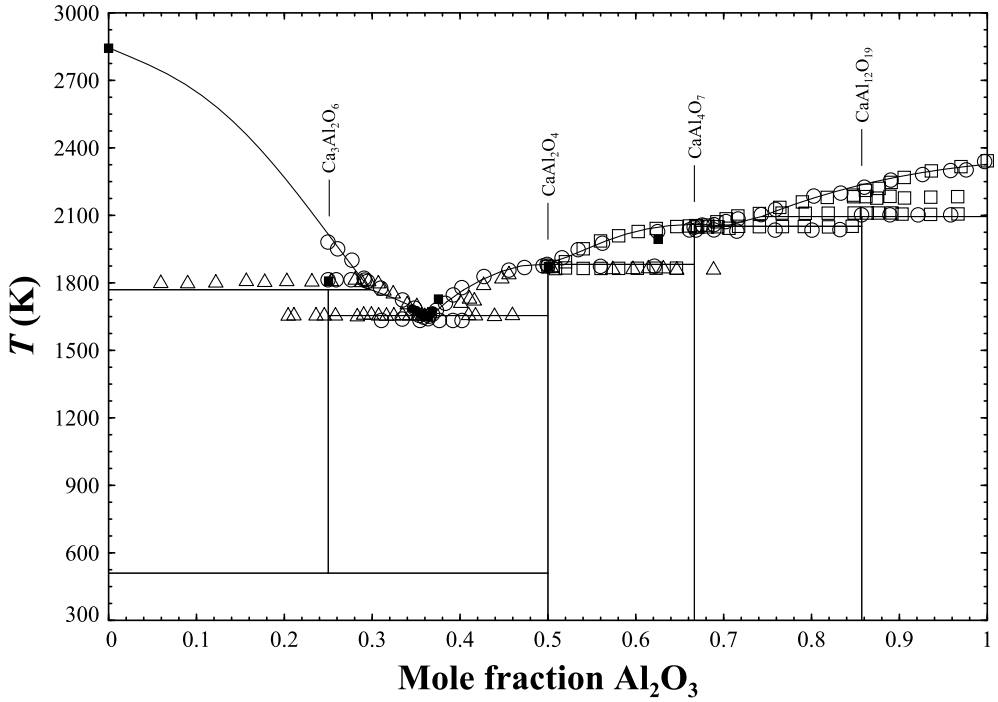

Fig. 5.16. Computed CaO-Al_2O_3 phase diagram. Data: ◯[285] □[286] ■[287] △[288] ●[289]

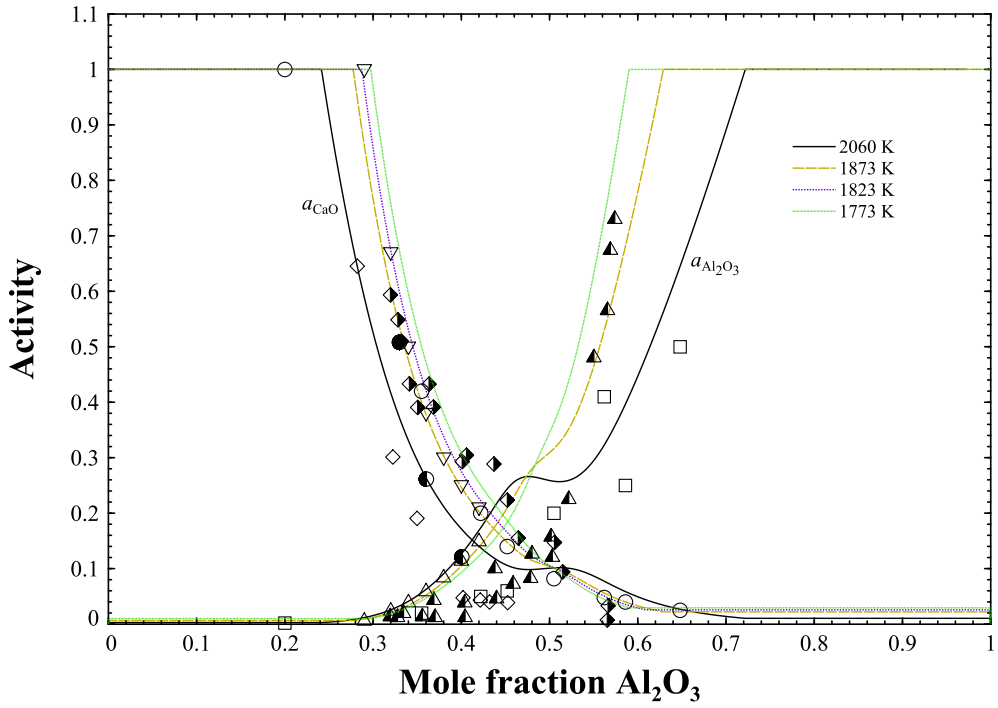

Fig. 5.17. Computed activity of CaO(s) and Al_2O_3(corundum) in the CaO-Al_2O_3 melt. Data: CaO(s) activity: ○ 2060 K[290] ◆ 1873 K[291] ◇ 1823 K[292] ▽ 1773 K[293] ◐ 1773 K[294]. Al_2O_3(corundum) activity: □ 2060 K[290] ◭ 1873 K[291] △ 1773 K[293]

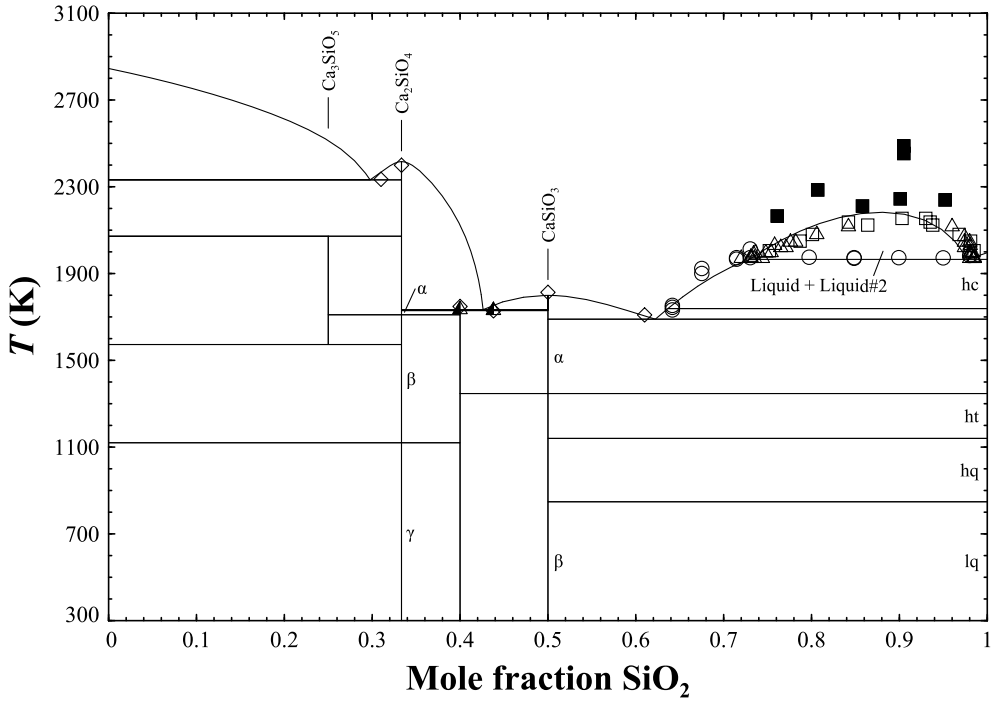

Fig. 5.18. Computed CaO-SiO_2 phase diagram. Data: ◯[295] □ two phase liquid immiscibility[296] ■ homogeneous liquid[296] △[297] ◇[287] ◭[298]

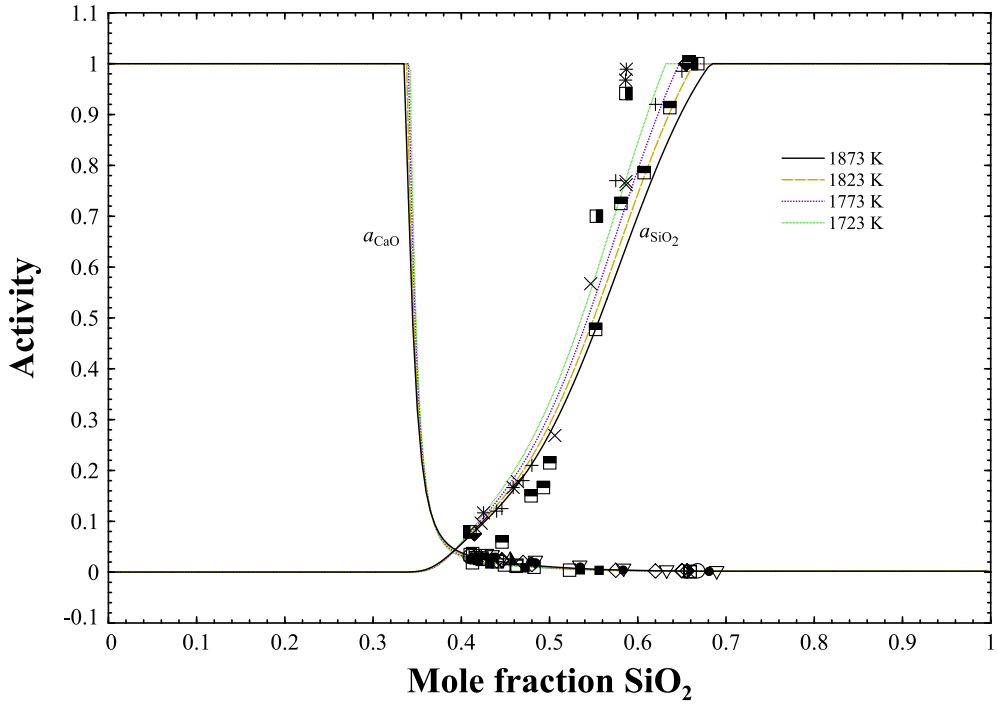

Fig. 5.19. Computed activity of SiO_2(cristobalite) and CaO(s) in the CaO-SiO_2 melt. Data: SiO_2(cristobalite) activity: ⬒ 1873 K[291] ◧ 1873 K[299] ⬙ 1823 K[299] + 1773 K[300] ✳ 1723 K[301] ◨ 1773 K[301] × 1823 K[301]. CaO(s) activity: □ 1873 K[291] ○ 1873 K[299] ⬗ 1823 K[299] ◇ 1773 K[300] ● 1773 K[301] ▽ 1823 K[301] ◭ 1723 K[301] ■ 1773 K[302] ⬓ 1823 K[302].

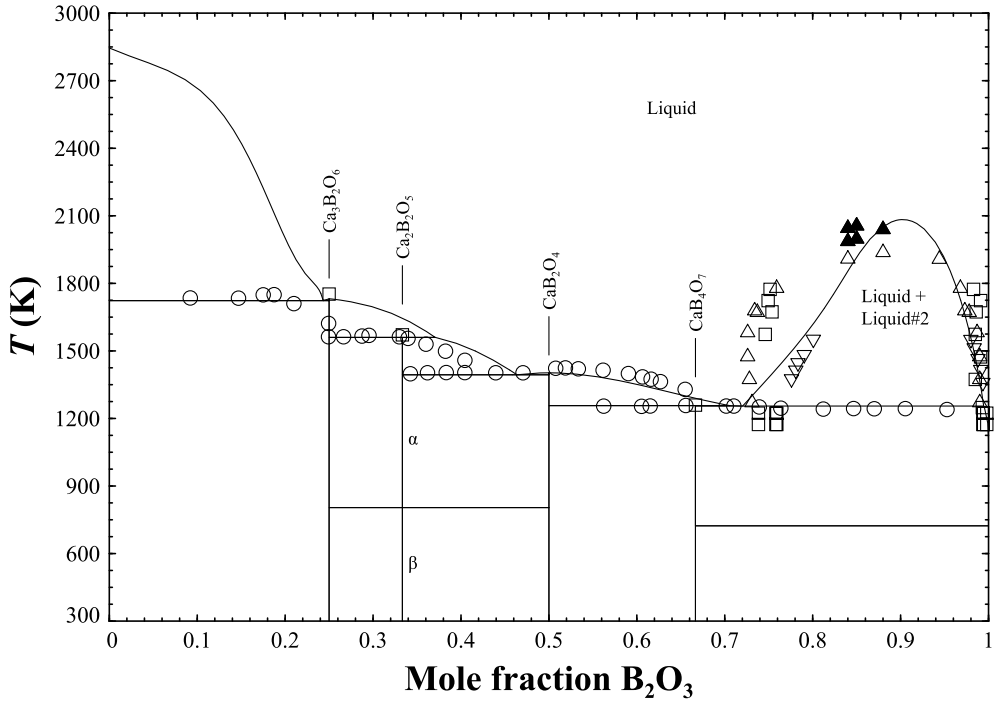

Fig. 5.20. Computed CaO-B_2O phase diagram. Data: ◯[303] □[303] △ immiscible liquid [304] ▲ homogeneous liquid [304] ▽[305]

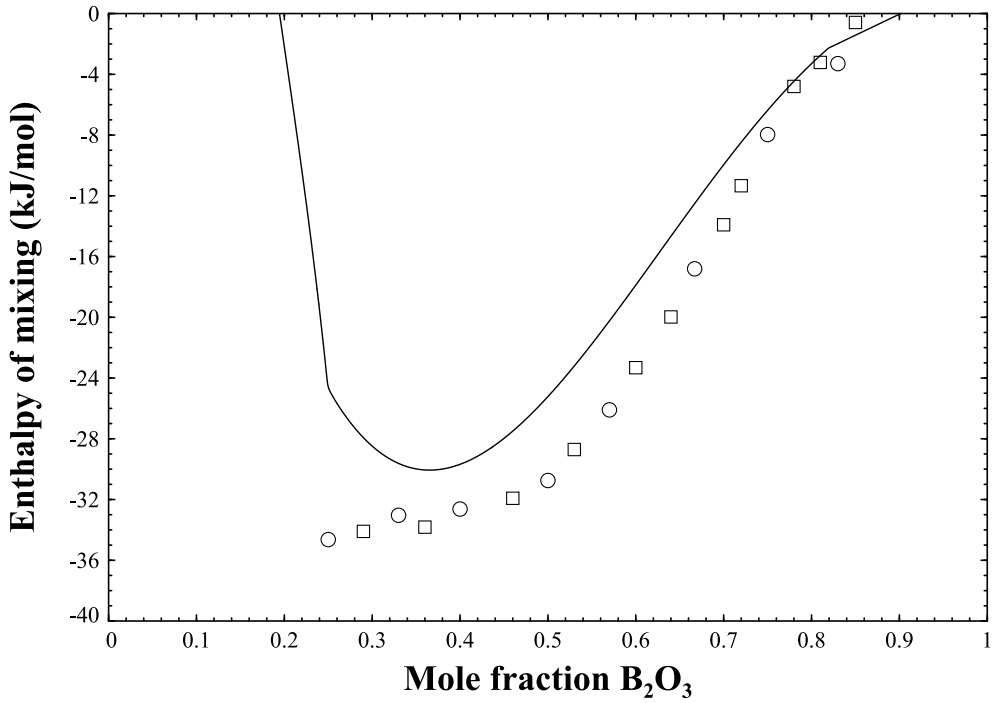

Fig. 5.21. Computed enthalpy of mixing in the CaO-B_2O_3 system at 1725 K. Data: ◯ 1725 K[306] □ 1725 K[307]

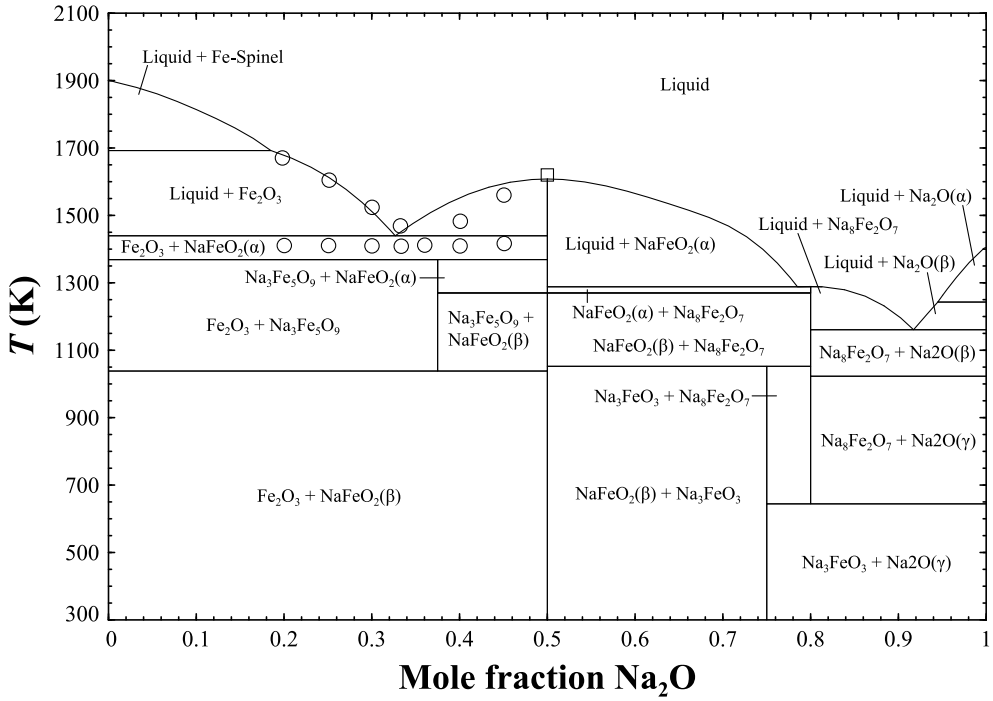

Fig. 5.22. Computed Fe_2O_3-Na_2O phase diagram at O_2(g) partial pressure of 0.21 atm. Data: ◯308 □127

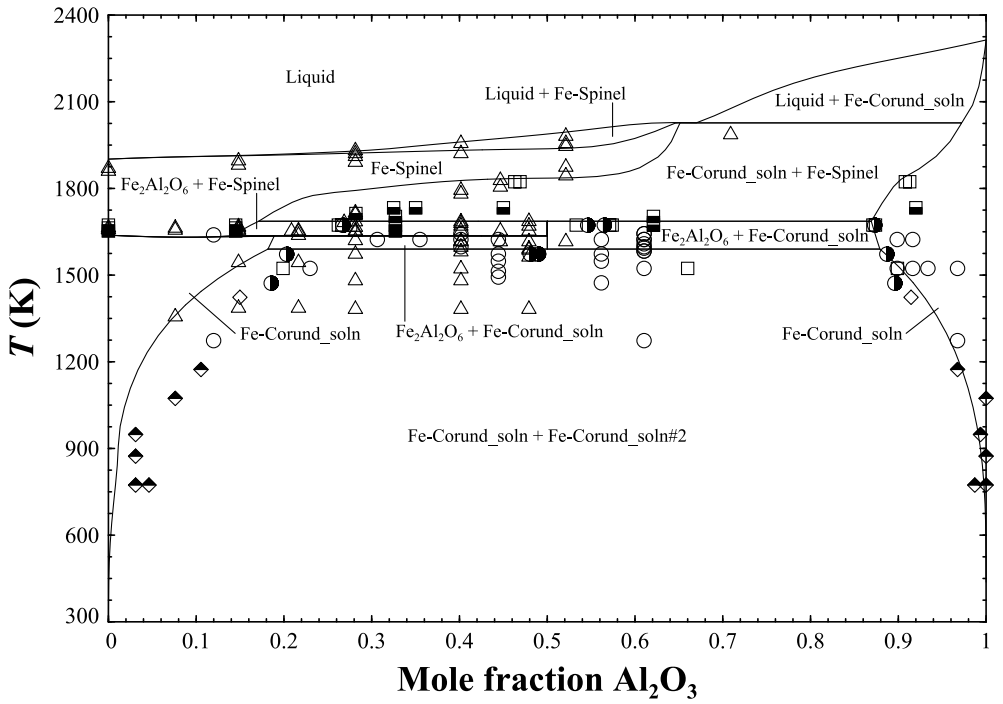

Fig. 5.23. Computed Fe_2O_3-Al_2O_3 phase diagram at O_2(g) partial pressure of 0.21 atm. Data: ◯309 □310 ◇311 △312 ◑313 ◒314 ◆315

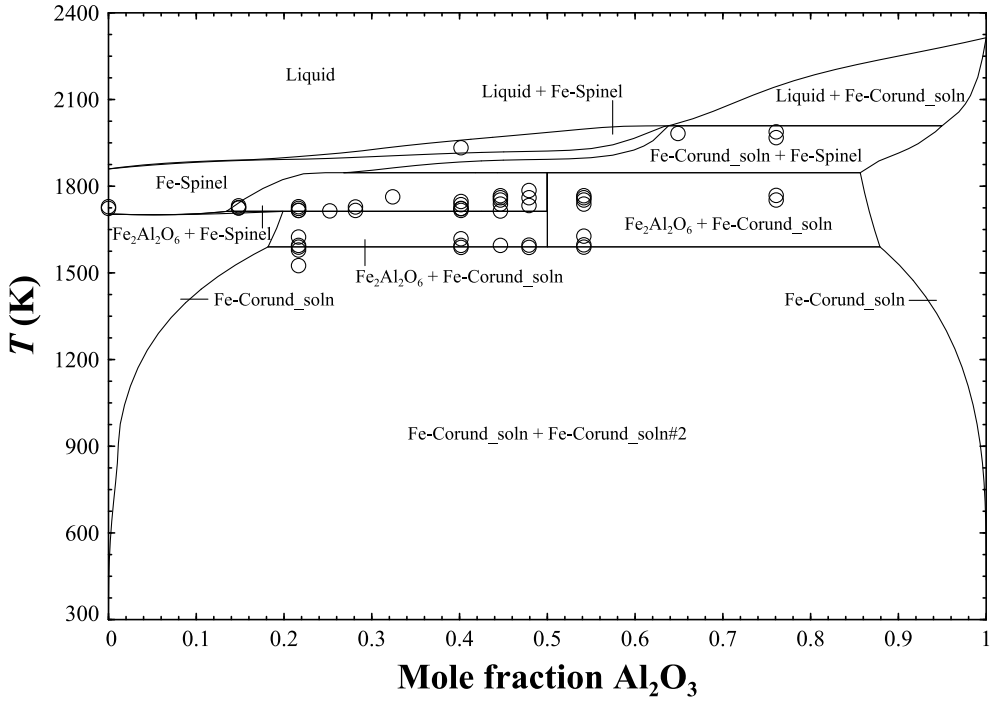

Fig. 5.24. Computed Fe_2O_3-Al_2O_3 phase diagram at O_2(g) partial pressure of 1 atm. Data: ◯[309]

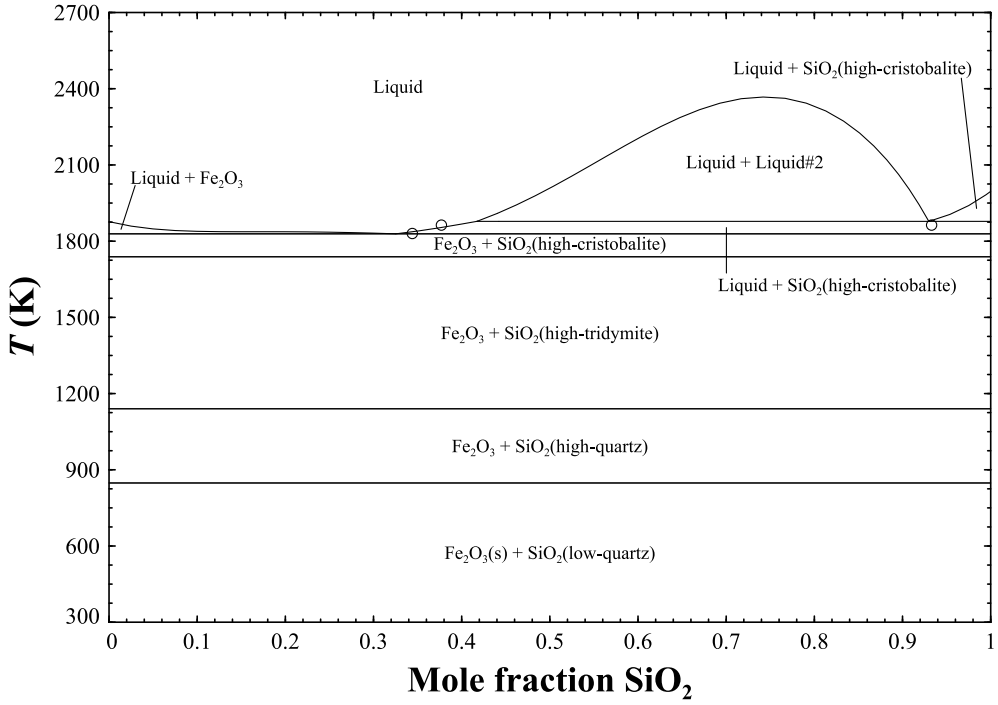

Fig. 5.25. Computed Fe_2O_3-SiO_2 phase diagram. Data calculated by Selleby[220]: ◯

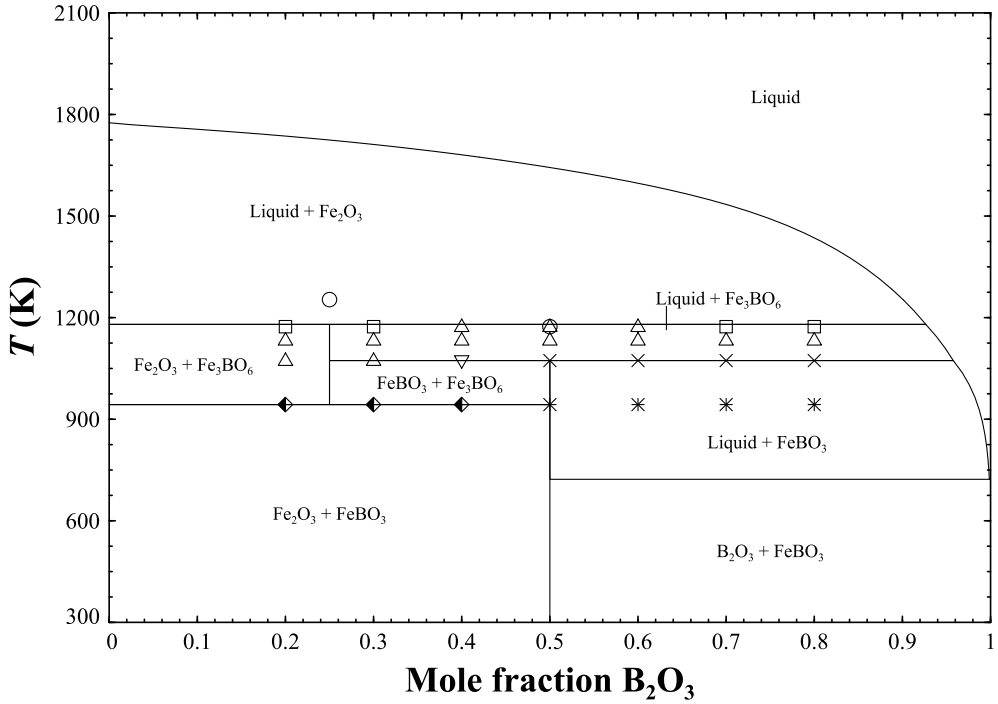

Fig. 5.26. Computed Fe_2O_3-B_2O_3 phase diagram at O_2(g) partial pressure of 0.21 atm. Data: Joubert et al.[316]: ○ incongruent melting. Makram et al.[317]: □ Fe_2O_3 △ Fe_2O_3 + Fe_3BO_6 ▽ Fe_3BO_6 + Fe_2O_3 + $FeBO_3$ ✳ $FeBO_3$ ◆ $FeBO_3$ + Fe_2O_3 ✕ $FeBO_3$ + Fe_3BO_6 + Fe_2O_3.

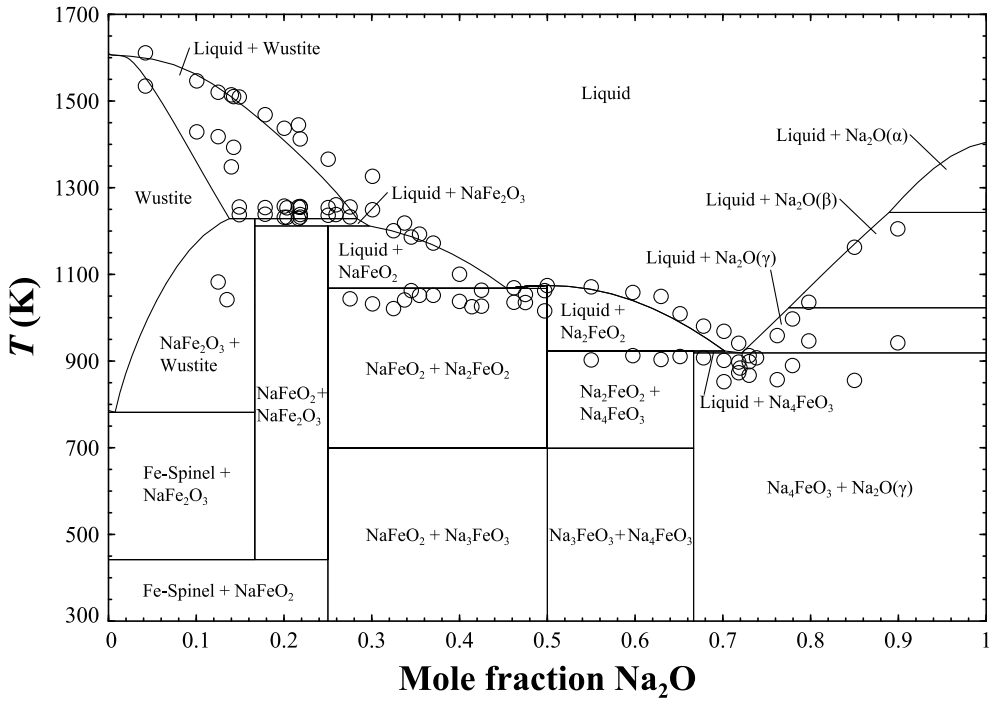

Fig. 5.27. Computed FeO-Na_2O phase diagram saturated with Fe(bcc). Data: ○[318]

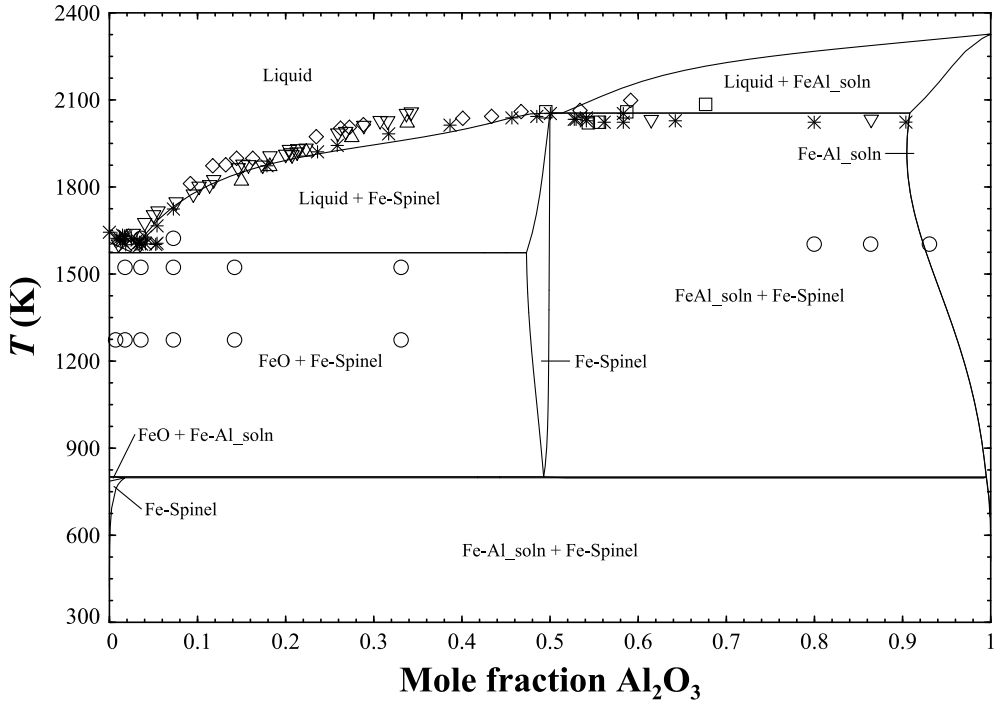

Fig. 5.28. Computed FeO-Al_2O_3 phase diagram saturated with Fe(bcc). Data: ◯309 □319 △320 ▽321 ✳322 ◇323

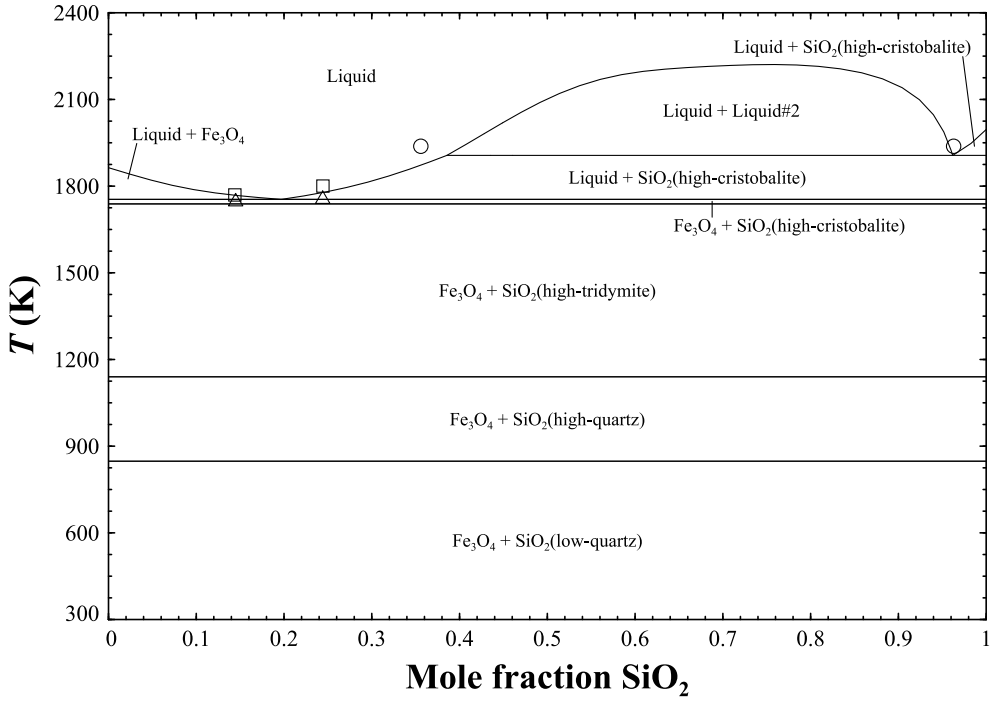

Fig. 5.29. Computed FeO-SiO_2 phase diagram at O_2(g) partial pressure of 0.21 atm. Data: ◯324 □325 △325

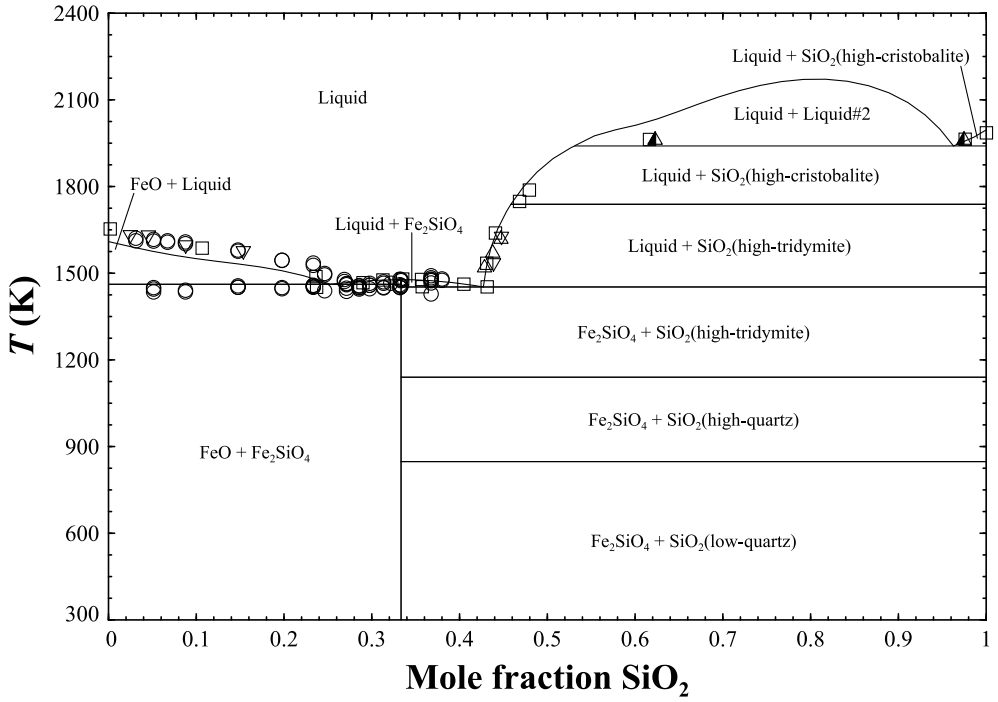

Fig. 5.30. Computed FeO-SiO_2 phase diagram saturated with Fe(bcc). Data: ◯[326] □[327] △[328] ▽[329] ◭[324]

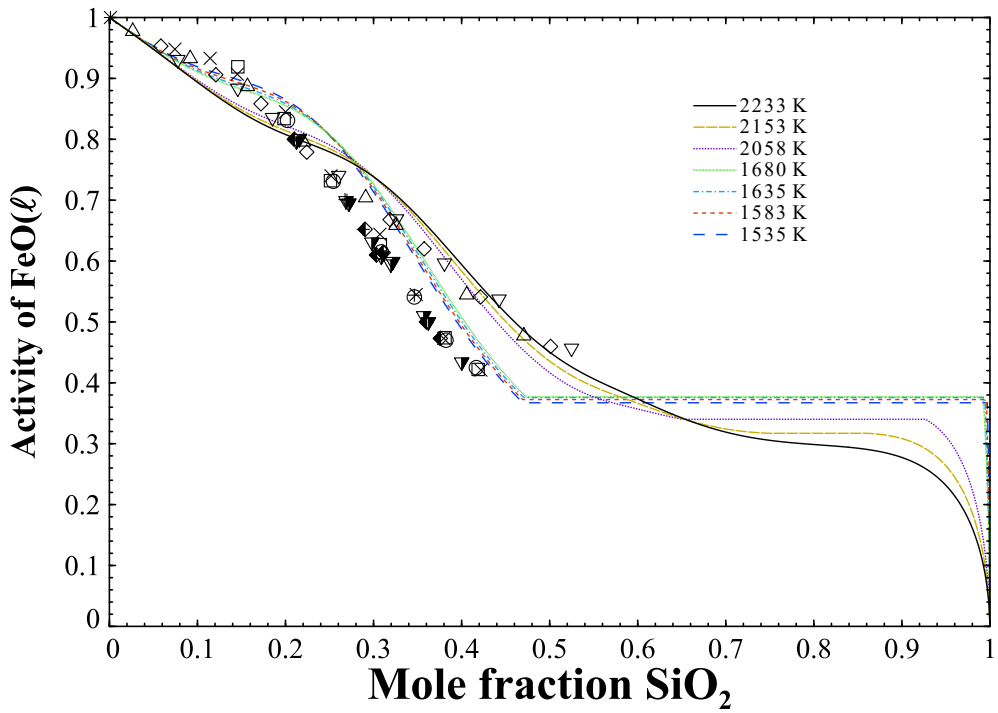

Fig. 5.31. Computed activity of FeO(ℓ) in the FeO-SiO_2 melt. Data: ◯ 1536 K[329] □ 1587 K[329] × 1638 K[329] ✳ 1680 K[329] + 1535 K[330] ◥ 1579 K[330] ◆ 1631 K[330] △ 2058 K[331] ◇ 2153 K[331] ▽ 2233 K[331]

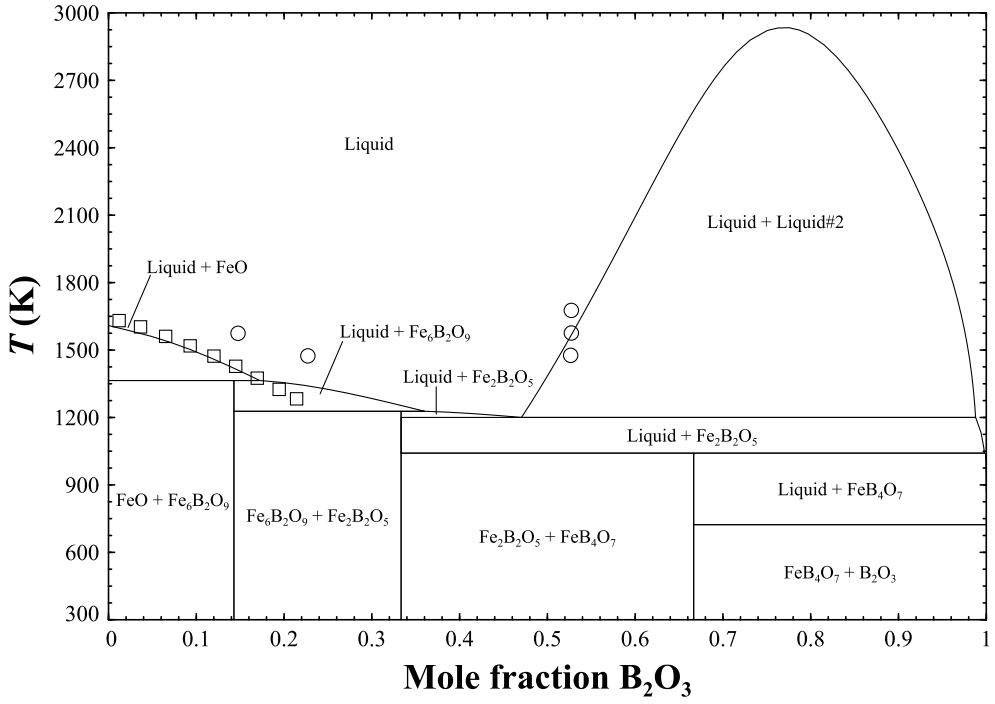

Fig. 5.32. Computed FeO-B_2O_3 phase diagram saturated with Fe(bcc). Data: ◯[244] □[243]

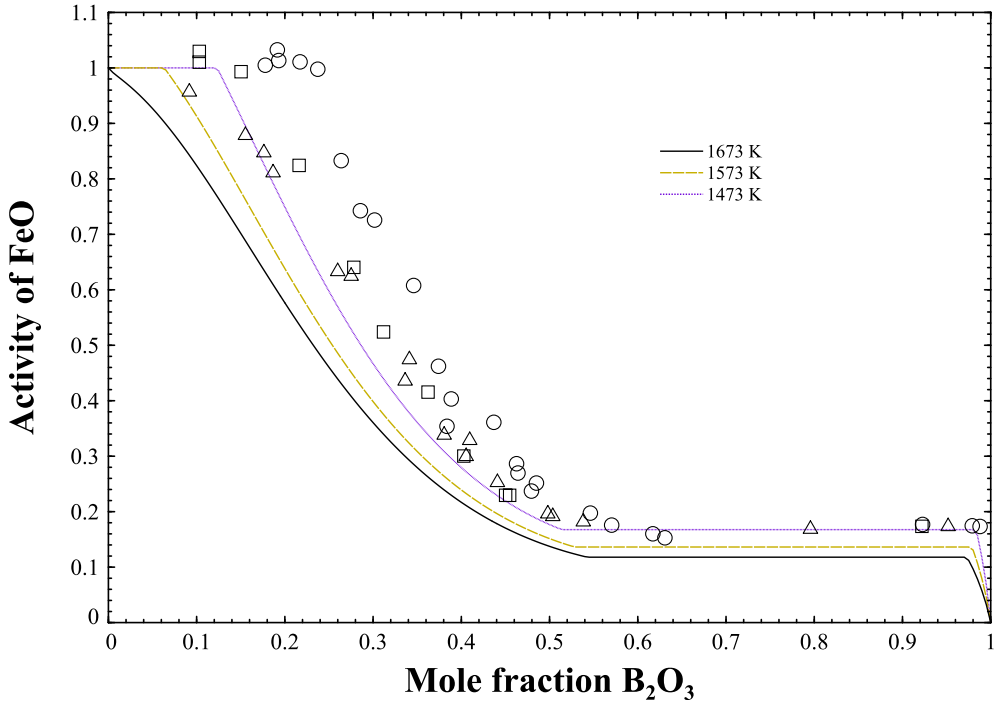

Fig. 5.33. Computed activity of FeO(s) at 1473 K and 1573 K and FeO(ℓ) at 1673 K in the FeO-B_2O_3 melt. Data: FeO(s) activity: ◯ 1473 K[244] □ 1573 K[244]. FeO(ℓ) activity: △ 1673 K[244]

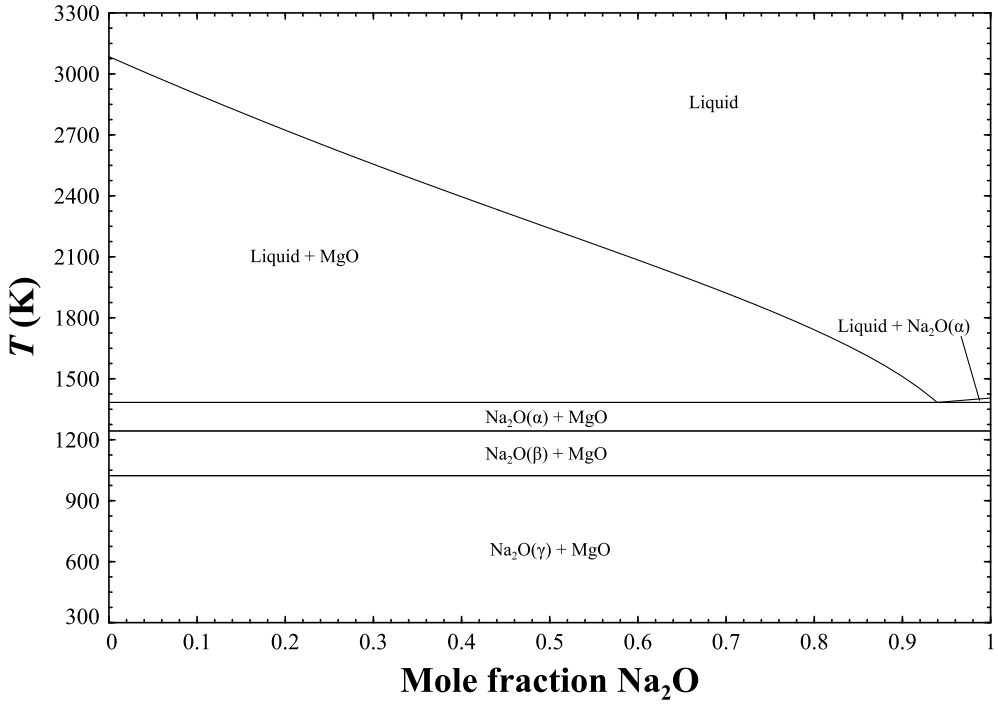

Fig. 5.34. Computed MgO-Na_2O phase diagram.

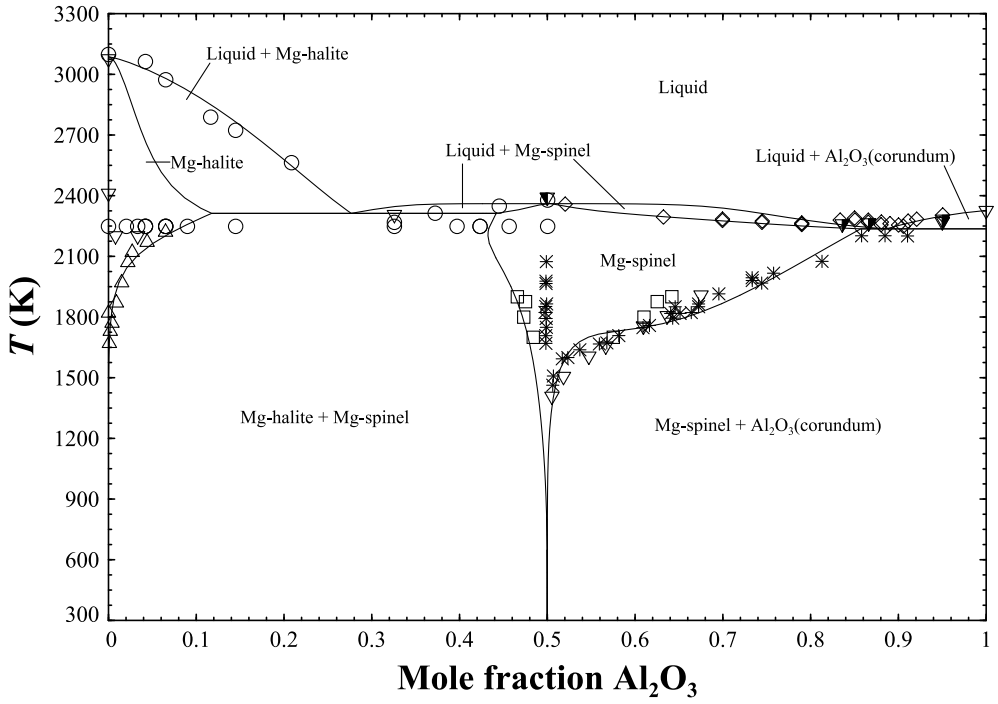

Fig. 5.35. Computed MgO-Al_2O_3 phase diagram. Data: ○332 □333 △334 ▽226 ◇335 ◥336 ▽337 ✳338 ◥224

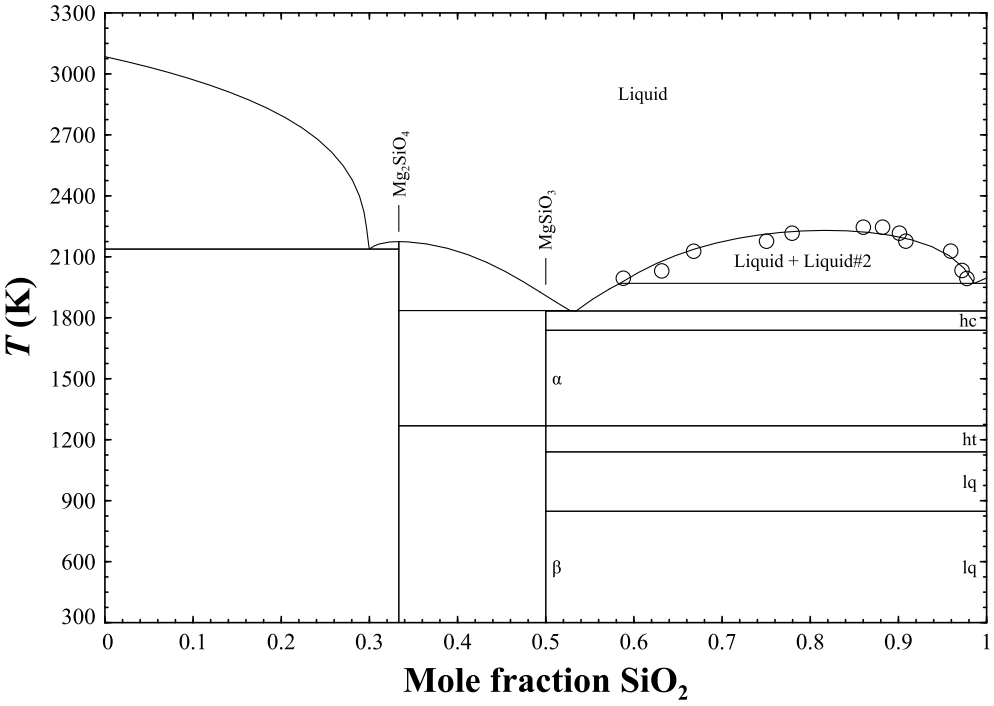

Fig. 5.36. Computed MgO-SiO_2 phase diagram. Data: ◯[339]

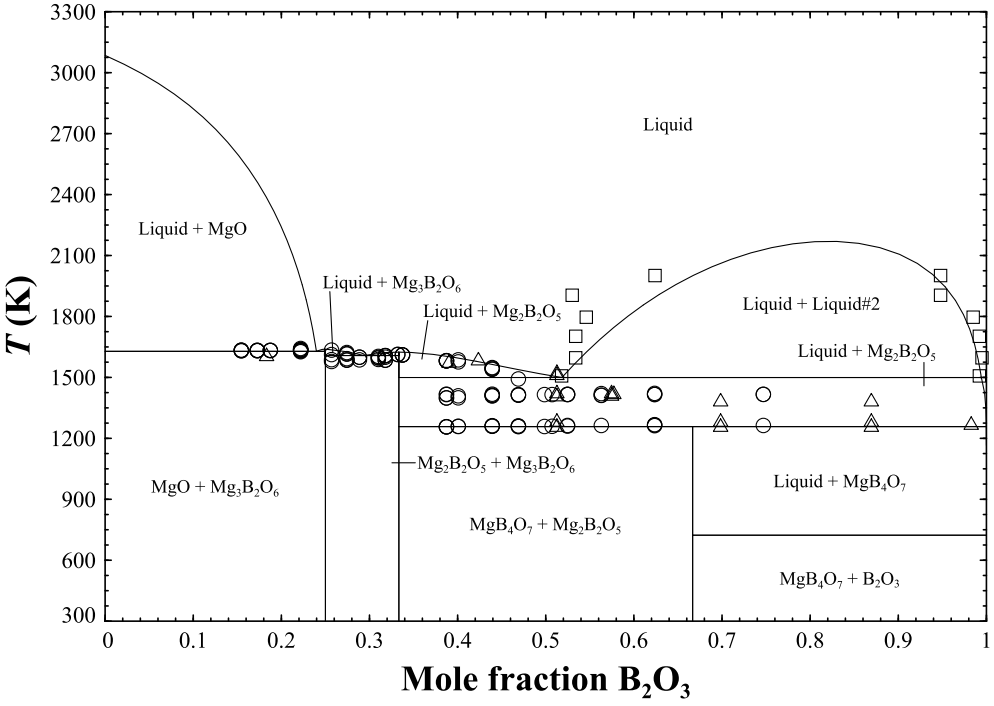

Fig. 5.37. Computed MgO-B_2O_3 phase diagram. Data: ◯[340] □[304] △[341]

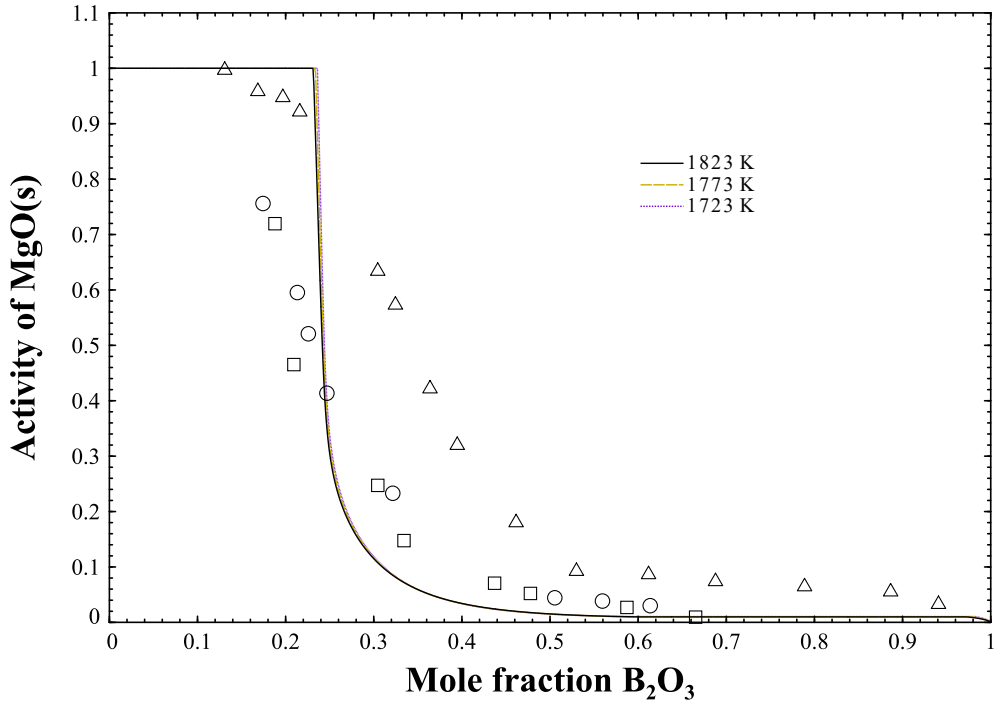

Fig. 5.38. Computed activity of MgO(s) in the MgO-B_2O_3 melt. Data: ○ 1823 K[246] □ 1773 K[246] △ 1723 K[247]

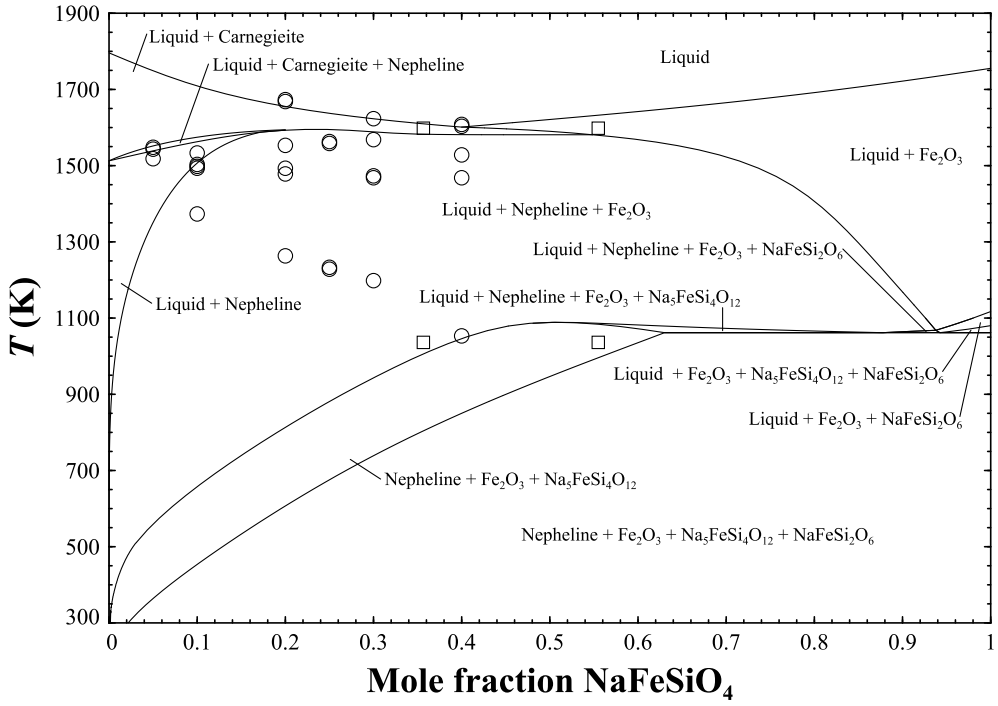

Fig. 5.39. $NaAlSiO_4$-$NaFeSiO_4$ phase diagram. Data: ○[250] □[252]

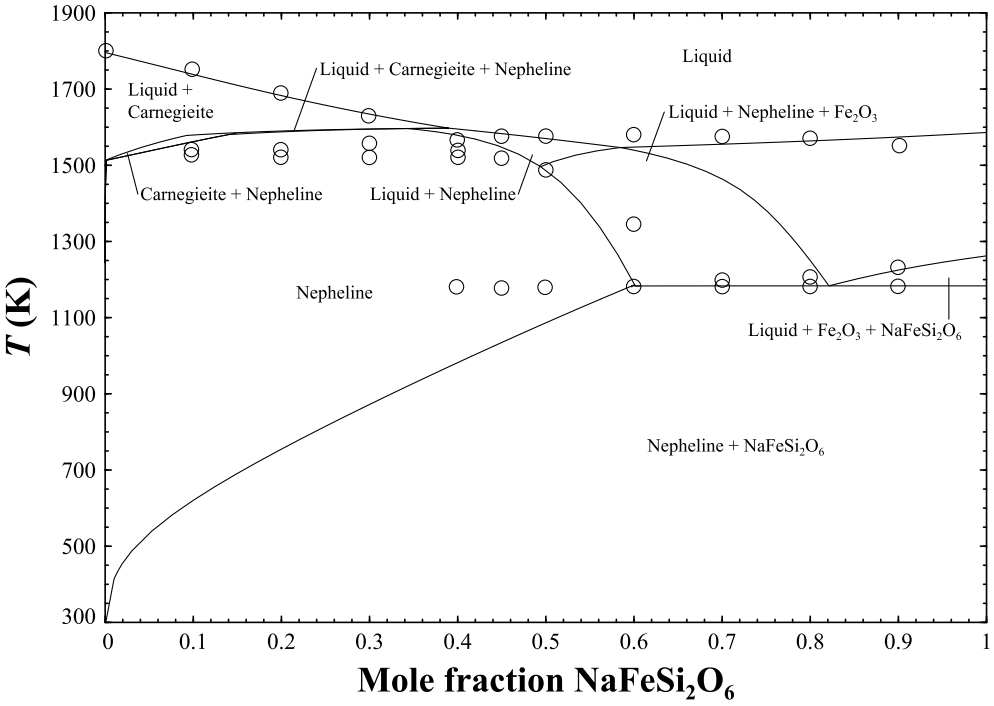

Fig. 5.40. $NaAlSiO_4$-$NaFeSi_2O_6$ phase diagram. Data: ◯[252]

Chapter 6

Validating HLW Thermodynamic Database to Experimental Data

6.1. Introduction

A thermodynamic database consisting of the oxides Na_2O, Al_2O_3, SiO_2, B_2O_3, K_2O, Li_2O, CaO, MgO, Fe_2O_3, and FeO has been developed to model the equilibrium behavior of nepheline crystallization in high-level waste (HLW) glass. As part of this process, the nepheline compound energy formalism (CEF) model was expanded to include the elements K, Ca, Mg, and Fe, which will be discussed in this report.

The final phase of the nepheline database development effort was to validate database calculations relative to HLW glass experimental data. Both annealed and canister centerline cooled (CCC) glass sample data were considered. Additionally, nepheline compositional data was included for comparison with database computations. Results of these comparisons indicate that the database agrees well with HLW glass experimental data. However, as phase precipitation in a CCC glass sample is dependent on kinetics, an approach that accounts for the kinetics of nucleation and growth such as phase field modeling will need to be utilized as it represents material morphological evolution with time. These models, however, often require accurate Gibbs energies of phases, which can effectively only be provided from equilibrated systems computed from a reliable thermodynamic database such as developed in this work.

6.2. Optimization of nepheline solid solution to compositional data

Ahmadzadeh et al.[248] and Marcial et al.[6] reported stoichiometric compositions of nepheline crystallized in HLW glass samples measured by electron probe microanalysis (EPMA), which was used to optimize the Gibbs energies of the nepheline CEF $KAlSiO_4$, $CaAl_2Si_2O_8$, $MgAl_2Si_2O_8$, and $NaFeSiO_4$ endmembers. Ahmadzadeh et al.[248] fabricated 5 glasses for analysis of the nepheline phase containing only Fe as a minor component with samples annealed for 7 hours at 775°C and then quenched. In contrast, Marcial et al.[6] subjected 5 glass samples with compositions adopted from previous studies to a CCC heat treatment. These compositions contained a complete profile of HLW glass oxides allowing for substitution of all oxides contained in the database with nepheline. Of note, the A4 composition was neglected in this effort as 4.47 wt.% of oxides in the sample are not considered in the current database, which was deemed too excessive to enable a productive benchmarking process. Table 6.1 & Table 6.2 display, respectively, the oxide composition and experimentally measured and calculated stoichiometry of nepheline for each glass sample, which show very good agreement. For the CCC samples fabricated by Marcial et al.,[6] the temperatures chosen to calculate the nepheline stoichiometry were at the centroids of the areas indicated in Fig. 6.1 – Fig. 6.10, which are explained in detail in Section 6.3.2. Details of this type of computation and how this temperature is estimated are also provided in Section 6.3.2. Those experimental nepheline compositions reported as $NaAlSiO_4$ in Table 6.2 were identified using x-ray diffraction. While this analysis was sufficient to conclude that nepheline with the base crystalline structure of $NaAlSiO_4$ precipitated in the sample, it is likely that the nepheline phase contains K, Ca, Mg, and/or Fe as seen in the results of

Ahmadzadeh et al.[248] and Marcial et al.[6] and as predicted by database calculations (Table 6.2).

6.3. Comparison of computed phases to those observed in HLW compositions

6.3.1. HLW glass annealed samples

Both CCC and annealing heat treatments were used to fabricate representative the HLW glass samples.[2, 8, 18, 19, 22, 23, 44, 54, 55, 57, 260, 342-354] The annealed samples were quenched after heat treatment at a constant temperature with techniques used such as contacting the glass-containing crucible with cold water[345] or pouring the molten glass on a stainless steel plate allowing for air cooling.[353, 354] Figure 2 of Billings & Edwards[353] as well as Figs. 3-1 & 3-2 of Billings & Edwards[354] are time-temperature-transformation (TTT) diagrams generated from experimental measurements conducted at SRNL. The referenced figures indicate that only trevorite formed during the CCC treatment whereas multiple other phases formed such as lithium silicate, acmite, krinovite, albite, and nepheline when samples were annealed for time periods ranging from 24 to 768 hours. For the C2-510 glass, nepheline did not start forming until 768 hours at 500°C. As expected, experimental results indicate that the CCC heat treatment affects the crystalline phases that form in HLW glass, and thus kinetics must be considered when modeling the precipitation of crystalline phases in CCC-treated HLW glass. This is evident in HLW studies[2, 8, 18, 19, 22, 23, 44, 54, 55, 57, 260, 342-352] in which the observed phases in annealed and CCC samples significantly differ.

Figure 2 of Billings & Edwards[353] and Figs. 3-1 & 3-2 of Billings & Edwards[354] indicates that trevorite ($NiFe_2O_4$) of the spinel group is a main secondary phase for the SB3-TTT, C2-510, and C4-418 glass compositions at the 768 hour anneal time. As the database does not currently contain Ni, calculations cannot be conducted to accurately

predict the behavior of the systems analyzed by Billings & Edwards.[353, 354] Additionally, anneal times in studies,[2, 8, 18, 19, 22, 23, 44, 54, 55, 57, 260, 342-352] which varied from 1 to 74 hours, were not ideal for comparison with calculations as Billings & Edwards[353, 354] indicate new crystalline phases formed at > 100 hours. Phase changes continued to occur between samples annealed for 384 and 768 hours, and nepheline did not form for the C2-510 composition at 500ºC until annealed for 768 hours.[353] Thus, any annealing experiments conducted for the purpose of benchmarking equilibrium calculations using the HLW database should only consider samples with a minimum anneal time of 100 hours and ideally the longest possible time, which in these studies was 768 hours. Also, anneal temperatures of studies[2, 8, 18, 19, 22, 23, 44, 54, 55, 57, 260, 342-352] typically ranged from 1250 to 800ºC, however as indicated by Billings & Edwards,[353, 354] nepheline and various other secondary phases can form in the temperature range of 500 to 700ºC. Hence, annealing experiments would also ideally analyze samples annealed at temperatures from 800 to 500ºC for comparison with database calculations.

6.3.2. CCC HLW glass samples that precipitated nepheline

Certain HLW glass compositions formed nepheline after a CCC heat treatment (Table 6.1), which indicates that nepheline precipitation kinetics for these samples differed from those that did not form nepheline following CCC. While the CCC times varied from 19.5 to 37.6 hours (Table 6.2), nepheline did not crystallize in the SB3-TTT, C2-510, or C4-418 compositions until annealing times exceeded 100 hours.[353, 354] Consequently, calculations were conducted for Table 6.1 samples to compare with experimental results. While being a comparison of computed results at equilibrium to experimental measurements obtained from a kinetically dependent heat treatment, the more rapid

formation of nepheline in these samples indicates they may be closer to an equilibrium state, at least as it concerns the nepheline phase, and, thus, may allow for a more useful data comparison.

Of HLW glass sample data in the literature,[2, 6, 8, 18, 19, 22, 23, 44, 54, 55, 57, 248, 260, 342-352] glass compositions were selected for this analysis if the sample precipitated nepheline under a CCC treatment and if the summation of the mass fractions of oxides not included in the database, e.g., ZrO_2, BaO, Ce_2O_3 and so forth, were approximately equal to or less than 3 wt.%. The latter criterion was applied so that phases not included in the database would be minimized. 10 compositions met these criteria (Table 6.1), and results are displayed in Fig. 6.1– Fig. 6.12.

Figures Fig. 6.1 – Fig. 6.10 display calculated mass fractions of stable phases for the CCC glass compositions listed in Table 6.1 over the temperature range of 500 to 1200°C. The maximum temperature of 1200°C bounds the nominal WTP and DWPF HLW glass melt pool temperature of 1150°C.[342, 344, 346, 347, 350, 355-357]

Analysis of Fig. 6.1 – Fig. 6.10 indicates that nepheline is consistently computed to form at high temperatures (> 1000°C) except for the CVS2-63 sample that had a high-B_2O_3 amount of 17.17 wt.%. The suppression of nepheline crystallization with increased B_2O_3 is consistent with the findings of Fox & Edwards[23] who concluded that increased B_2O_3 concentration significantly reduced the number of glass compositions where nepheline crystallized.

As the CCC heat treatment is a more rapid cooling process, crystalline phases have a more limited time period to form resulting in stable crystalline phases which precipitate at higher temperatures. Accordingly, areas have been indicated in Figs. Fig. 6.1 – Fig. 6.10

spanning from approximately 700 to 1000ºC, which represent the likely temperature ranges that phases were quenched in for the CCC samples. Comparison with phases experimentally observed in each glass sample agree well (Table 6.2). Also, as discussed in Section 6.2, the good agreement of the calculated nepheline stoichiometries in the temperature ranges specified in Figs. Fig. 6.1 – Fig. 6.10 with those compositions that were determined from EPMA (Table 6.2) further indicates the accuracy of the nepheline CEF model and by extension the overall database.

A minor caveat worth noting is the computed Ca-containing phase, $Na_2Ca_2Si_3O_9$, in Fig. 6.7 & Fig. 6.8 for CVS2-35 and CVS2-63, respectively, differs from the experimentally determined $Ca_2Al_2SiO_7$ phase (Table 6.2). To most accurately reproduce phase crystallization in CCC glass, a kinetic representation may be required.

6.3.3. Computed liquid-liquid immiscibility

Allowing the possibility of the formation of immiscible liquids was required in the equilibrium calculations as certain assessed pseudo-binary systems such as SiO_2 with CaO, MgO, Fe_2O_3, or FeO have experimentally observed miscibility gaps. As noted by Taylor[358] and Peeler & Hrma,[359] amorphous phase separation commonly occurs in borosilicate glass systems. Peeler & Hrma[359] fabricated and heat treated 24 simulated waste glass samples according to a CCC schedule selected from Hrma et al.[54] identifying 3 compositions with phase separation supporting the equilibrium calculational results of Figs. 3 – 12, which show a second liquid phase forms in all but the NE3-04 composition.

6.4. Scheil-Gulliver cooling compared to equilibrium calculations

Figures Fig. 6.11 & Fig. 6.12 compare results of direct equilibrium calculations with a Scheil-Gulliver cooling calculations for the NP-BL glass composition.[8] In Scheil-

Gulliver cooling, equilibrium calculations are performed at specified temperature steps between liquidus and solidus, where each subsequent calculation is performed only using the remaining liquid composition, thus removing precipitated phases from consideration and potentially more accurately representing finite cooling rates. Figure Fig. 6.12 indicates that the Scheil-Gulliver calculations indicated a negligible amount of Fe went into solution in nepheline, contradicting experimentally demonstrated solubility of Fe in nepheline as discussed in Section 5.7 (Fig. 5.39 & Fig. 5.40). Direct equilibrium calculations thus remain the best approach despite the obvious non-equilibrium cooling that is observed in CCC samples.

6.5. Suggested future work

The current set of elements and phases that have been modeled and provided in the current database are already useful for determining nepheline and related phase formation. Yet modeling of HLW systems would benefit from continued expansion of the current thermodynamic database to include additional oxides. Besides better representing systems with significant content of these elements, it would also contribute to any future development of kinetics models such as phase field. The oxides should consist of those that contribute to forming secondary phases that were observed to form in either annealed or CCC glass samples (Table 6.3): Oxides of Bi, C, Ce, Cr, Mn, Nd, Ni, P, Pb, Ru, Ti, Zn, and Zr. Most beneficial would be inclusion of the spinel-forming oxides, i.e., NiO, Cr_2O_3, MnO, and/or ZnO, as spinel is the most common secondary phase in both annealed and CCC samples.[2, 8, 18, 19, 22, 23, 44, 54, 55, 57, 260, 342-352] ZrO_2 and Nd_2O_3 as well as phosphates in the form of the ion PO_4^{-3} were also relatively common (Table 6.3) and hence should also receive priority consideration for inclusion in the database.

Development of accurate thermochemical models of HLW phases would also benefit from experimental work similar to that conducted by Billings & Edwards[353, 354] where HLW glass samples are fabricated that ideally only consist of the oxides contained in the database, annealed for > 100 hours at temperatures between glass melting temperatures and 500°C, quenched, and then analyzed to identify equilibrium crystalline phases. This type of heat treatment would allow near-equilibrium measurements that can be compared to database equilibrium calculations. Compositions may be selected to encompass the nepheline and surrounding region of the Na_2O-Al_2O_3-SiO_2 liquidus region with amounts of minor oxides varied to assess their influence on nepheline and secondary phase formation.

Phase field or other such time-dependent models will be required to fully understand the obvious non-equilibrium behavior which occurs during the cooling of HLW glass. Hence, approaches that combine thermochemical models with kinetic expressions for nucleation and growth are required to obtain the most accurate description of phase precipitation in HLW glass poured into canisters.

6.6. Tables

Table 6.1. Oxide compositions of HLW glass samples

Glass ID	Oxide amount [gm · 10^2]									
	Na_2O	Al_2O_3	SiO_2	B_2O_3	K_2O	Li_2O	CaO	MgO	Fe_2O_3	Others
Fe0.1_775-7[248]	21.634	33.909	41.115	0	0	0	0	0	3.482	-
Fe0.2_775-7[248]	21.133	30.417	39.851	0	0	0	0	0	8.93	-
Fe0.4_775-7[248]	20.198	24.912	40.987	0	0	0	0	0	13.792	-
Fe0.5_775-7[248]	20.168	23.447	40.805	0	0	0	0	0	20.168	-
Fe0.7_775-7[248]	19.9	20.279	40.35	0	0	0	0	0	19.352	-
NP-K-1[8]	19.69	13.36	37.27	7.77	3	4.37	1.09	0.66	9.65	3.06
NP-K-2[8]	19.08	12.95	36.12	7.53	6	4.23	1.05	0.64	9.35	2.96
NP-Ca-1[8]	20.51	13.92	38.82	8.09	0.1	4.55	0	0.69	10.05	3.18
NP-Ca-2[8]	18.46	12.52	34.94	7.28	0.09	4.1	10	0.62	9.05	2.86
NP-Fe-3[8]	19.62	13.31	37.14	7.74	0.1	4.35	1.08	0.66	12.95	3.04
NP-Li-2[8]	19.53	13.26	36.98	7.71	0.1	8	1.08	0.66	9.58	3.03
CVS2-35[54]	20	13.4	42	5	0	4.28	8	0	6.32	3.03
CVS2-63[54]	19	18	32.32	17.17	0	0.51	10	0	2	1
NP2-16[18]	14.76	13.87	43.32	5.05	0	4.07	2.15	0.3292	14.50	2.96
NE3-04[19]	17.52	13.79	48.36	4.63	0	4.90	0.2473	0.0087	11.39	0.353

Table 6.2. Stable crystalline phases and cooling times for CCC HLW glass samples[a]

Glass ID	Experimental crystalline phase(s)	Computed crystalline phase(s)[b]	CCC time [hr]
Fe0.1_775-7[248]	$Na_{1.004}Al_{0.957}Fe_{0.063}Si_{0.984}O_4$	$Na_{1.0}Al_{0.942}Fe_{0.058}Si_{1.0}O_4$	7[c]
Fe0.2_775-7[248]	$Na_{0.999}Al_{0.874}Fe_{0.164}Si_{0.971}O_4$	$Na_{1.0}Al_{0.869}Fe_{0.131}Si_{1.0}O_4$	7[c]
Fe0.4_775-7[248]	$Na_{0.972}Al_{0.728}Fe_{0.258}Si_{1.017}O_4$	$Na_{0.977}Al_{0.733}Fe_{0.245}Si_{1.023}O_4$	7[c]
Fe0.5_775-7[248]	$Na_{0.978}Al_{0.691}Fe_{0.289}Si_{1.02}O_4$	$Na_{0.979}Al_{0.692}Fe_{0.287}Si_{1.021}O_4$	7[c]
Fe0.7_775-7[248]	$Na_{0.978}Al_{0.606}Fe_{0.369}Si_{1.023}O_4$	$Na_{0.978}Al_{0.607}Fe_{0.370}Si_{1.022}O_4$	7[c]
NP-K-1[8]	$NaAlSiO_4$, Li_2SiO_3, SiO_2	$Na_{6.50}K_{1.47}Ca_{0.007}Mg_{0.008}Al_{6.49}Fe_{1.51}Si_{8.0}O_{32}$, Li_2SiO_3	19.5
NP-K-2[6, 8]	$Na_{5.94}K_{2.23}Mg_{0.03}Al_{6.82}Fe_{1.13}Si_{7.98}O_{32}$, Li_2SiO_3	$Na_{5.76}K_{2.21}Ca_{0.006}Mg_{0.007}Al_{6.80}Fe_{1.20}Si_{8.0}O_{32}$, Li_2SiO_3	19.5
NP-Ca-1[8]	$NaAlSiO_4$, Li_2SiO_3	$Na_{7.91}K_{0.053}Mg_{0.007}Al_{5.67}Fe_{2.31}Si_{8.01}O_{32}$, Li_2SiO_3	19.5
NP-Ca-2[6, 8]	$Na_{8.12}K_{0.01}Ca_{0.13}Mg_{0.07}Al_{6.89}Fe_{0.79}Si_{8.12}O_{32}$, spinel[d]	$Na_{7.49}K_{0.055}Ca_{0.155}Mg_{0.07}Al_{6.85}Fe_{1.15}Si_{8.0}O_{32}$	18.5
NP-Fe-3[6, 8]	$Na_{7.87}K_{0.05}Ca_{0.01}Mg_{0.02}Al_{6.2}Fe_{1.55}Si_{8.19}O_{32}$, Li_2SiO_3, Fe_2O_3, spinel[d]	$Na_{7.75}K_{0.083}Ca_{0.028}Mg_{0.05}Al_{5.99}Fe_{2.0}Si_{8.01}O_{32}$, Li_2SiO_3, Fe_2O_3	25.5
NP-Li-2[6, 8]	$Na_{8.03}K_{0.07}Ca_{0.01}Mg_{0.01}Al_{6.82}Fe_{0.96}Si_{8.13}O_{32}$, Li_2SiO_3, Li_8SiO_6, spinel[d]	$Na_{7.79}K_{0.165}Ca_{0.009}Mg_{0.011}Al_{6.37}Fe_{1.63}Si_{8.0}O_{32}$, Li_2SiO_3	17.5
CVS2-35[54]	$NaAlSiO_4$, $Ca_2Al_2SiO_7$	$Na_{7.84}Ca_{0.077}Al_{6.40}Fe_{1.59}Si_{8.0}O_{32}$, $Na_2Ca_2Si_3O_9$	33
CVS2-63[54]	$NaAlSiO_4$, $Ca_2Al_2SiO_7$	$Na_{7.93}Ca_{0.029}Al_{6.70}Fe_{1.29}Si_{8.01}O_{32}$, $Na_2Ca_2Si_3O_9$	25
NP2-16[18]	$NaAlSiO_4$, Fe_2O_3, Fe_3O_4, Li_2SiO_3	$Na_{7.14}Ca_{0.045}Mg_{0.119}Al_{5.21}Fe_{2.25}Si_{8.53}O_{32}$, Li_2SiO_3, Fe_2O_3	37.6[e]
NE3-04[19]	Nepheline,[d] Li_2SiO_3	$Na_{7.37}Ca_{0.012}Mg_{0.005}Al_{4.64}Fe_{2.77}Si_{8.59}O_{32}$, Li_2SiO_3	37.6[e]

[a] First phase listed in experimental and computed crystalline phase columns is nepheline
[b] Nepheline composition for each glass ID calculated at temperature of delineated area centroid in respective mass fraction diagram (Fig. 6.1 – Fig. 6.10)
[c] Samples were annealed for 7 hours and then quenched
[d] Elemental composition not reported
[e] CCC time obtained from Marra & Jantzen,[360] which was cited by Fox & Edwards[18]

Table 6.3. Secondary phases experimentally observed in annealed/quenched and CCC HLW glass samples[2, 8, 18, 19, 22, 23, 44, 54, 55, 57, 260, 342-352]

Quenched Phases	CCC Phases	
$Ca_2ZrSi_4O_{12}$	$Ca_2ZrSi_4O_{12}$	$NdPO_4$
$Ca_5(PO_4)_3F$	$Ca_5(PO_4)_3F$	Ni,Cr,Zn,Mn,Nd,Zr,Ce-spinel
$Li_{0.301}Ni_{1.699}O_2$	$CaFe_3Ti_4O_{12}$	NiO
Na_2CO_3	Ce_2O_3	Pb_2O_3
$NaMg_2CrSi_3O_{10}$	Cr_2O_3	RuO_2
$NaNdPO_4$	Li_3PO_4	$(Zn_{0.3}Al_{0.7})Al_{1.7}O_4$
NdZrO	$LiFe_3Cr_2O_8$	Zr,Ni-pyroxene
Ni,Cr,Zr,Ce,Nd-spinel	Na_2CO_3	ZrCeO
NiO	$Na_3Bi(PO_4)_2$	ZrO_2
RuO_2	$Na_3Nd(PO_4)_2$	$ZrSiO_4$
ZrO_2	$Na_8(AlSiO_4)_6(MnO_4)_2$	
$ZrSiO_4$	$NaMg_2CrSi_3O_{10}$	

6.7. Figures

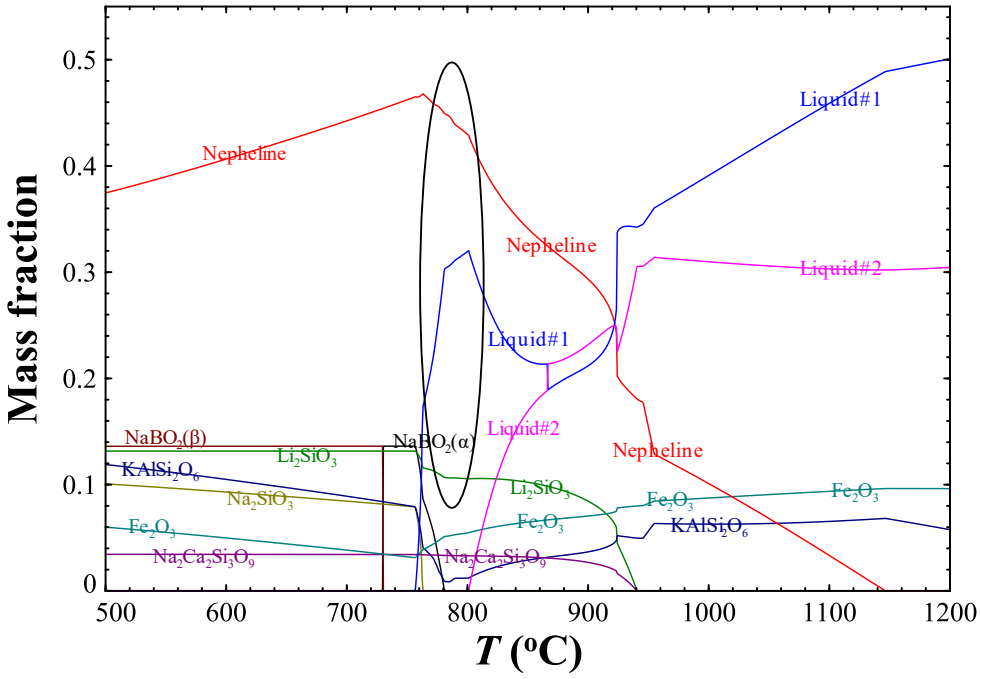

Fig. 6.1. Equilibrium mass fraction calculation for NP-K-1 glass with oval indicating the likely temperature range in which encompassed crystalline phases precipitated from CCC treatment.

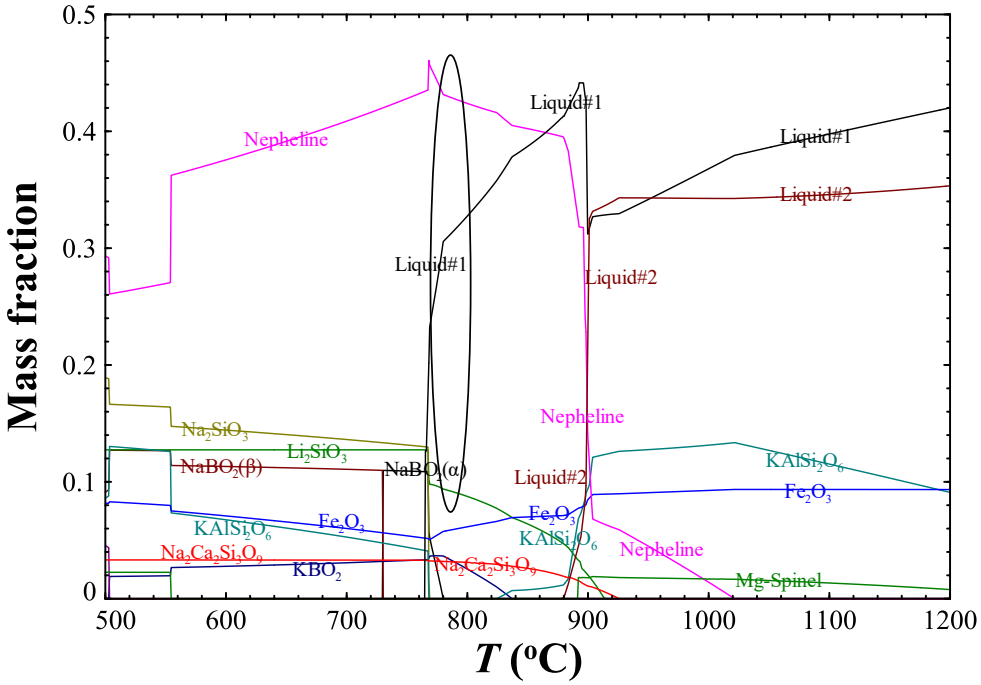

Fig. 6.2. Equilibrium mass fraction calculation for NP-K-2 glass with oval indicating the likely temperature range in which encompassed crystalline phases precipitated from CCC treatment.

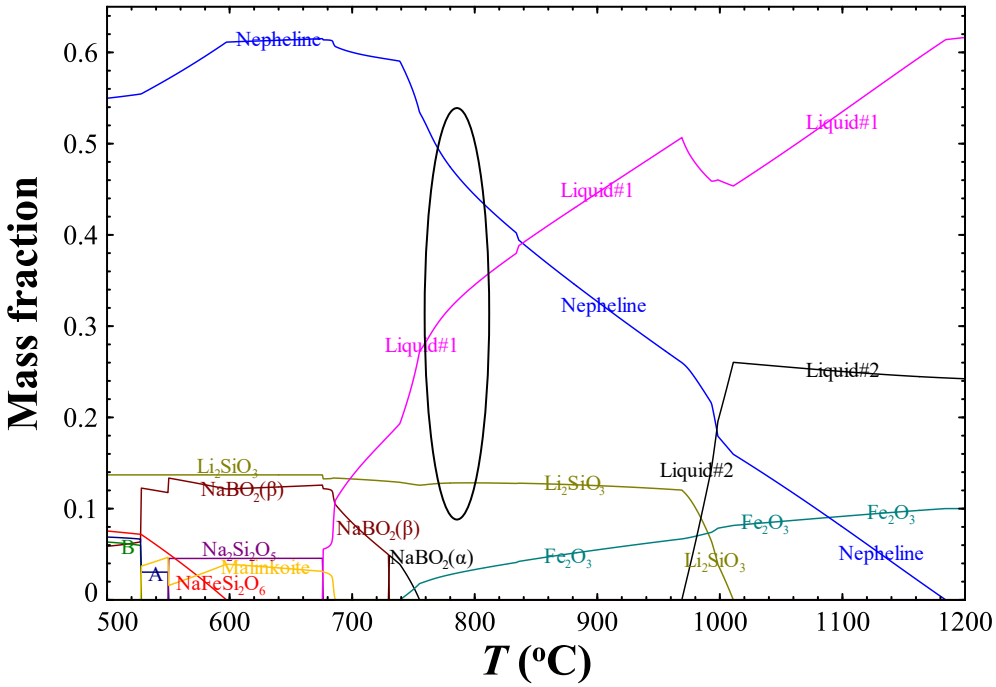

Fig. 6.3. Equilibrium mass fraction calculation for NP-Ca-1 glass with oval indicating the likely temperature range in which encompassed crystalline phases precipitated from CCC treatment. Phase labels A = Na_2SiO_3 and B = $Na_2B_4O_7$.

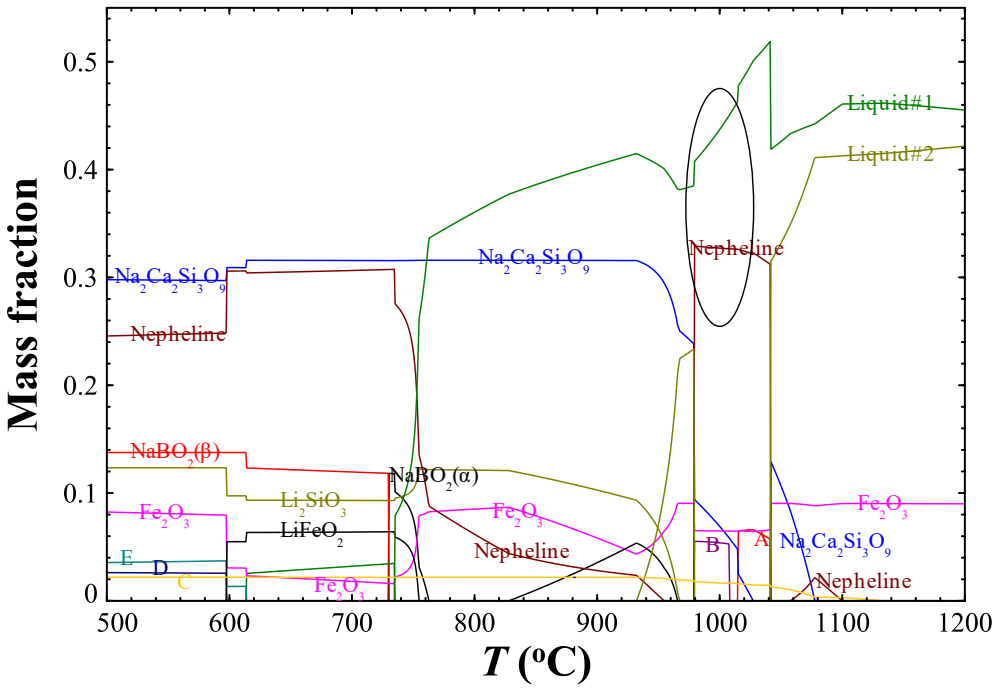

Fig. 6.4. Equilibrium mass fraction calculation for NP-Ca-2 glass with oval indicating the likely temperature range in which encompassed crystalline phases precipitated from CCC treatment. Phase labels A = $Ca_5SiO_{10}B_2$, B = $Ca_3B_2O_6$, C = Mg-Spinel, D = Na_2SiO_3, and E = $Na_2Ca_3Al_{16}O_{28}$.

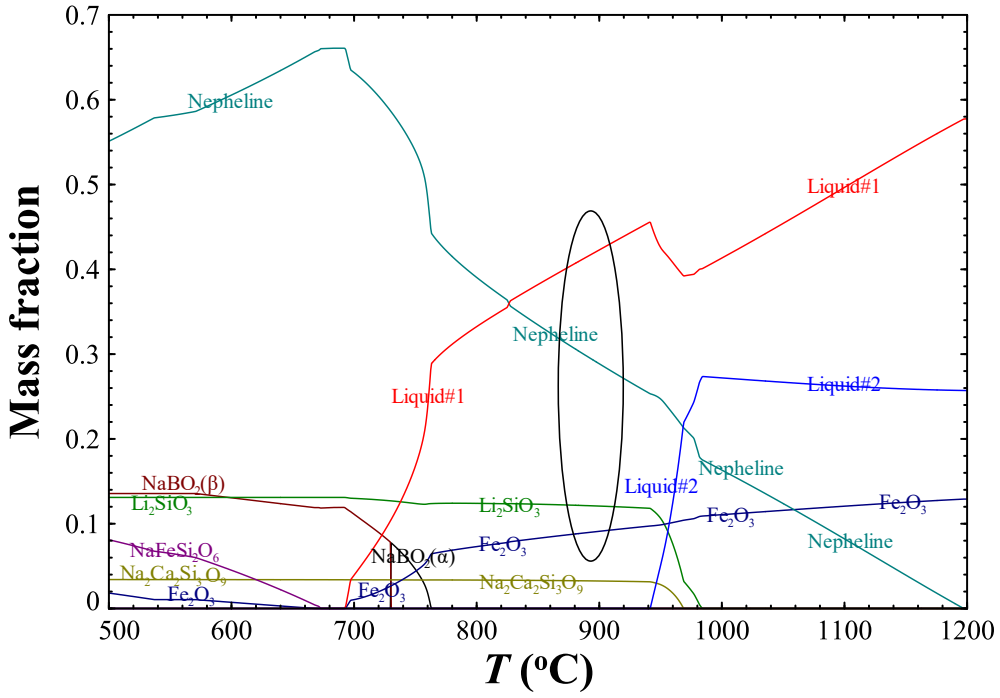

Fig. 6.5. Equilibrium mass fraction calculation for NP-Fe-3 glass with oval indicating the likely temperature range in which encompassed crystalline phases precipitated from CCC treatment.

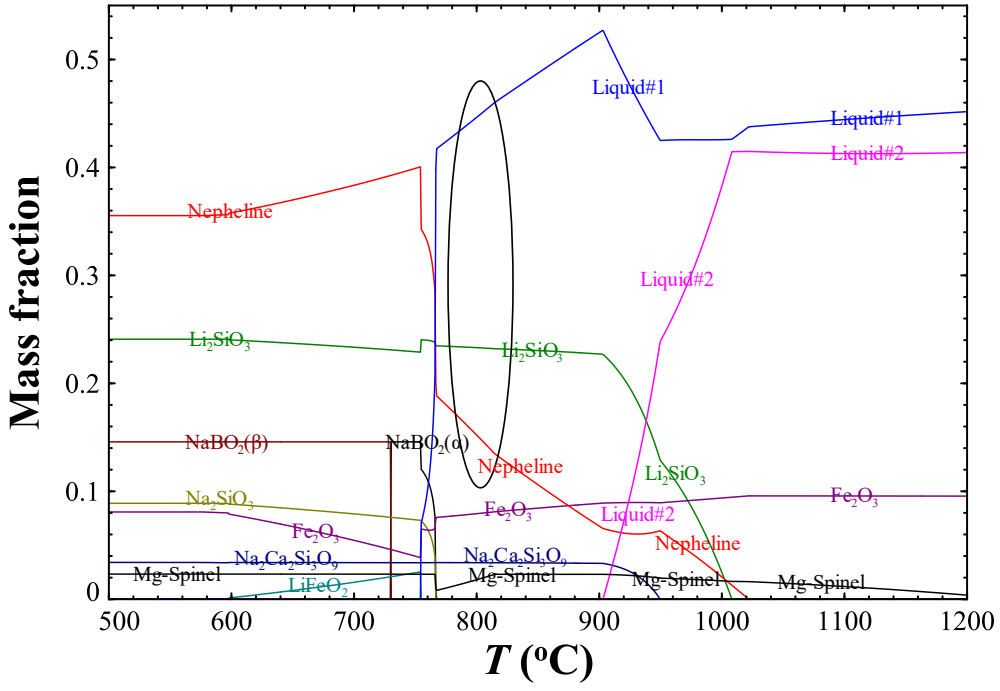

Fig. 6.6. Equilibrium mass fraction calculation for NP-Li-2 glass with oval indicating the likely temperature range in which encompassed crystalline phases precipitated from CCC treatment.

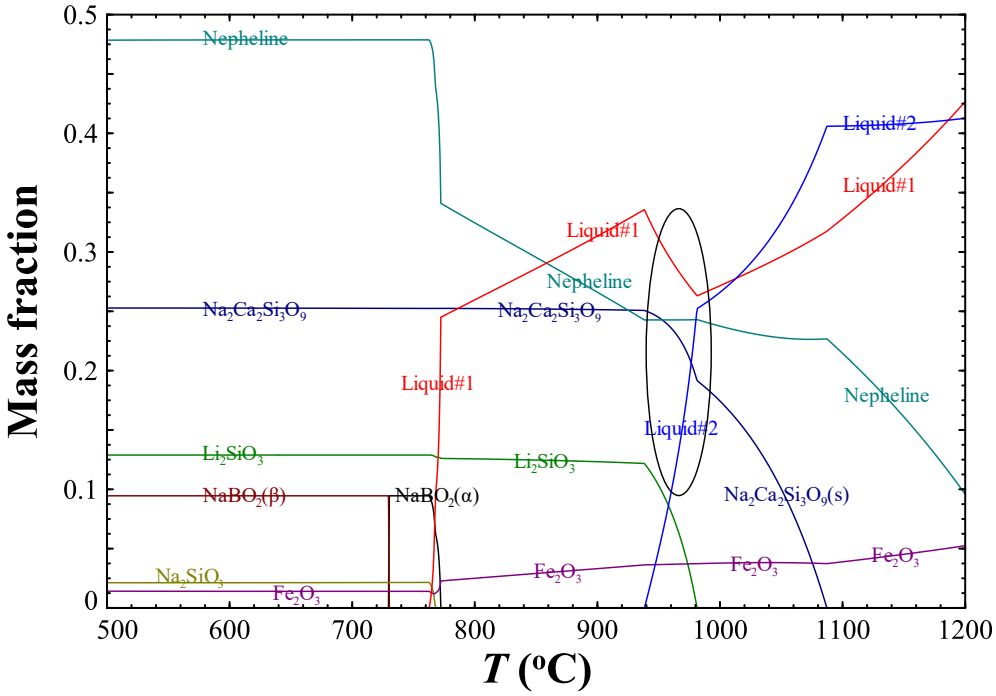

Fig. 6.7. Equilibrium mass fraction calculation for CVS2-35 glass with oval indicating the likely temperature range in which encompassed crystalline phases precipitated from CCC treatment.

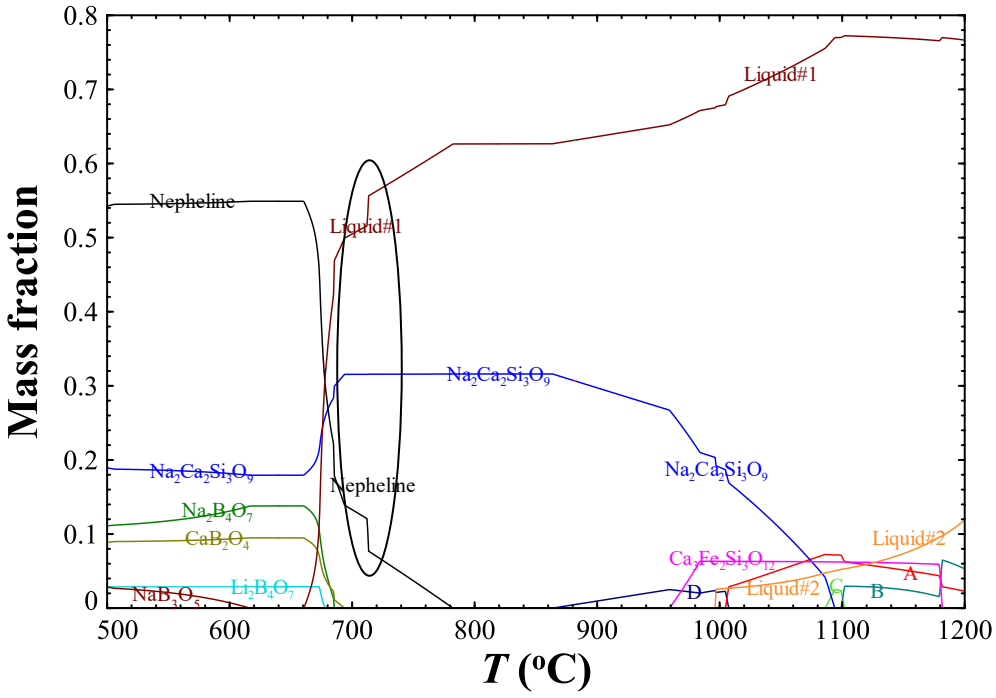

Fig. 6.8. Equilibrium mass fraction calculation for CVS2-63 glass with oval indicating the likely temperature range in which encompassed crystalline phases precipitated from CCC treatment. Phase labels A = $Ca_5SiB_2O_{10}$, B = $Ca_3Si_2O_7$, C = $CaSiO_3(\alpha)$, and D = $Ca_2B_2O_5(\alpha)$.

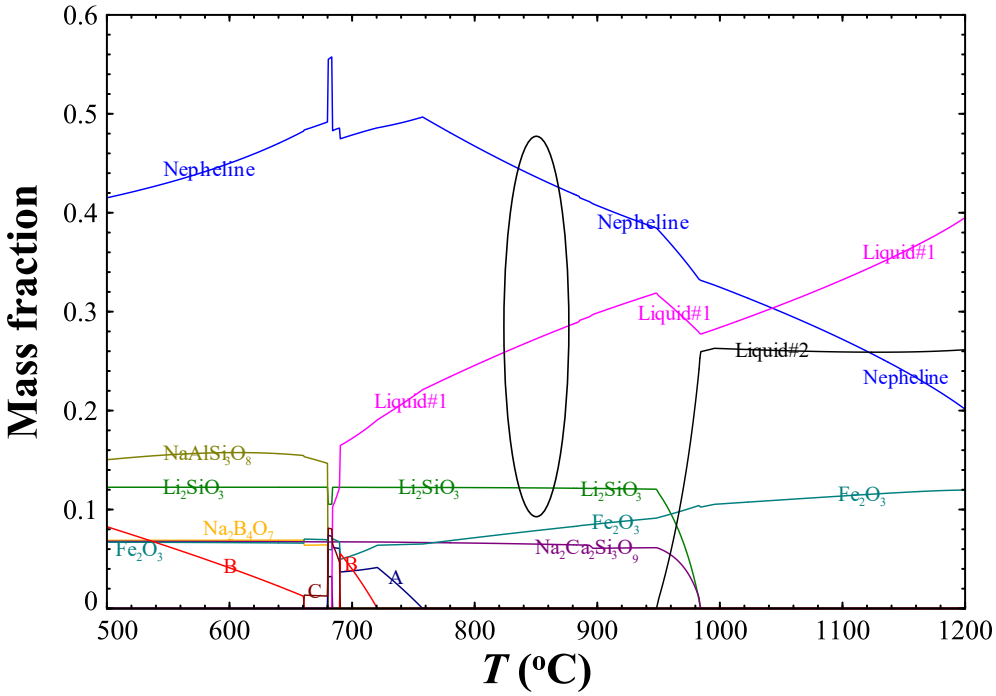

Fig. 6.9. Equilibrium mass fraction calculation for NP2-16 glass with oval indicating the likely temperature range in which encompassed crystalline phases precipitated from CCC treatment. Phase label A = $NaAlSi_3O_8$(high-albite), $NaFeSi_2O_6$, and C = Malinkoite.

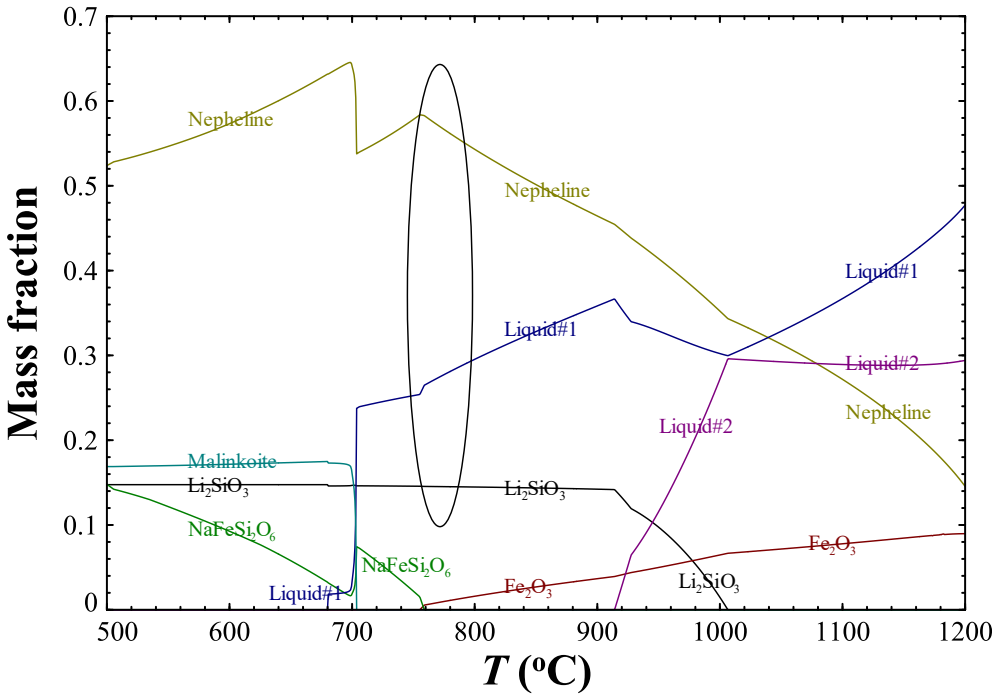

Fig. 6.10. Equilibrium mass fraction calculation for NE3-04 glass with oval indicating the likely temperature range in which encompassed crystalline phases precipitated from CCC treatment.

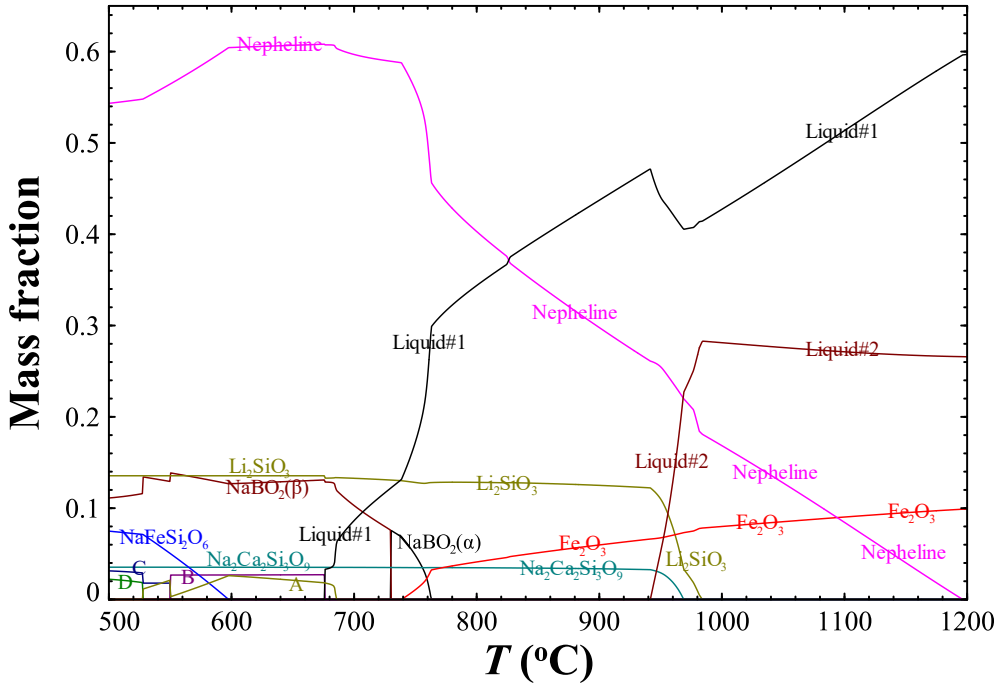

Fig. 6.11. Equilibrium mass fraction calculation for NP-BL glass. Phase labels A = Malinkoite, B = $Na_2Si_2O_5(\alpha)$, C = Na_2SiO_3, and D = $Na_2B_4O_7$.

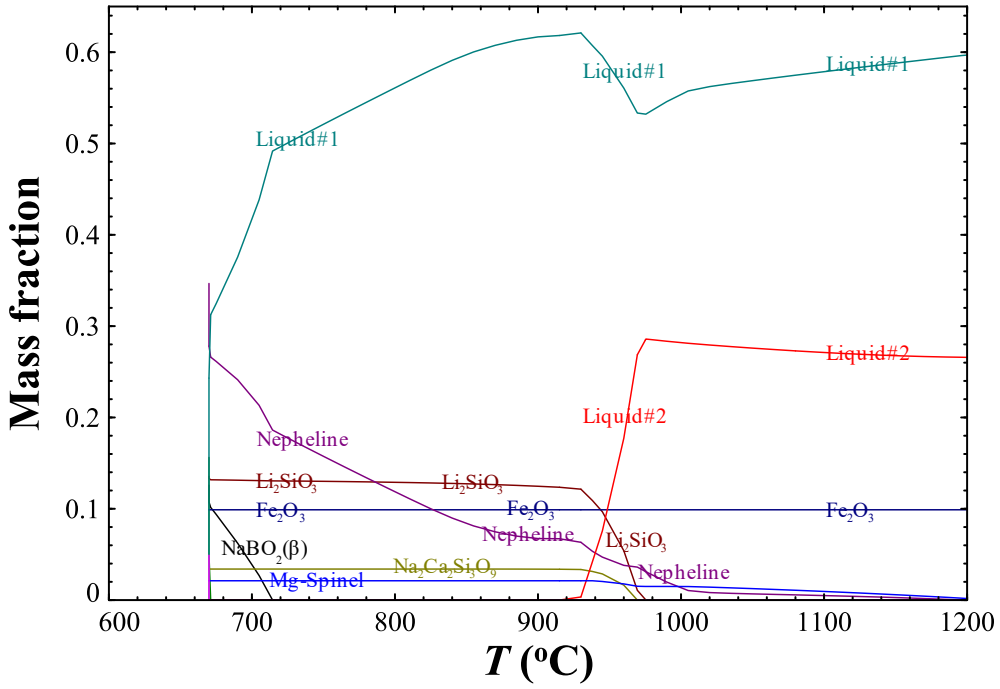

Fig. 6.12. Scheil-Gulliver cooling calculation for NP-BL glass.

Chapter 7

Thermodynamic Assessment of the Hollandite High-Level Radioactive Waste Form[3]

[3] Utlak S. A., Besmann T. M., Brinkman, K. S., Amoroso, J. W., Thermodynamic Assessment of the Hollandite High-Level Radioactive Waste Form. Accepted by *J. Am. Ceram. Soc.*, 03/08/2019. Reprinted here with permission of publisher.

7.1. Abstract

Hollandite has been studied as a candidate ceramic waste form for the disposal of high-level radioactive waste due to its inherent leach resistance and ability to immobilize alkaline-earth metals such as Cs and Ba at defined lattice sites in the crystallographic structure. The chemical and structural complexity of hollandite-type phases developed for high-level waste immobilization limits the systematic experimental research that is required to understand phase development due to the large number of potential additives and compositional ranges that must be evaluated. Modeling the equilibrium behavior of the complex hollandite-forming oxide waste system would aid in the design and processing of hollandite waste forms by predicting their thermodynamic stability. Thus, a BaO-Cs_2O-TiO_2-Cr_2O_3-Al_2O_3-Fe_2O_3-FeO-Ga_2O_3 thermodynamic database was developed in this work according to the CALPHAD methodology. The compound energy formalism was used to model solid solution phases such as hollandite while the two-sublattice partially ionic liquid model characterized the oxide melt. Results of model optimizations are presented and discussed including a 1473 K isothermal BaO-Cs_2O-TiO_2 pseudo-ternary diagram that extrapolates phase equilibrium behavior to regions not experimentally explored.

7.2. Introduction

Ceramic waste forms have been shown to accommodate nearly all constituents in the high-level nuclear waste (HLW) generated from reprocessing spent nuclear fuel including radioactive and non-radioactive components and are known to be resistant to hydrothermal leaching. Ceramic waste forms offer better durability and higher waste loadings for some species for which existing HLW glass formulations are inappropriate or

inefficient.[27-30] Specifically, titanate ceramics, e.g., SYNROC,[31] have been extensively studied for use in immobilizing nuclear wastes due to their inherent leach resistance.[32-34] Cs is one challenging radionuclide due to its thermal heat load, volatility at high temperatures, and tendency to form water-soluble compounds.[30] Ti-substituted hollandite, one of the SYNROC phases, is an alternative candidate for Cs immobilization. In these waste forms, ^{137}Cs (and other constituent radionuclides, i.e. ^{137}Ba, ^{87}Rb) is incorporated into the crystalline structure.[34, 38, 40] Notably, natural analogs of hollandite including ankagite are present in dolomitic marble in the Apuan Alps in Tuscany, Italy, which demonstrates the stability of the hollandite phase over geologic timescales of interest for nuclear waste immobilization.

Titanate hollandite ceramics can be generally expressed as $A_x(Ti^{+4},M)_8O_{16}$ where A represents alkali and alkaline earth metal cations such as Cs^{+1}, Ba^{+2}, Rb^{+1}, K^{+1}, and Sr^{+2} and M represents +2/+3 cations such as Al^{+3}, Fe^{+3}, Fe^{+2}, Ga^{+3}, Cr^{+3}, Zn^{+2}, and Mg^{+2}.[30, 35] The structure is composed of edge and corner sharing TiO_6 and MO_6 octahedra that form a framework consisting of tunnels parallel to the c-axis or b-axis for tetragonal or monoclinic hollandites, respectively.[35] The atom positions located within the tunnel sites can be occupied by A-site cations such as Cs^{+1} and Ba^{+2}, which is beneficial as both ^{137}Cs and its decay product ^{137}Ba can remain immobilized in the hollandite structure.[361]

Studies have been conducted to analyze the effect of M-site substitution on the crystallographic structure of hollandite and Cs incorporation.[28, 30, 36-40] Costa et al,.[361] for instance, determined that hollandite thermodynamic stability generally increased with decreasing average M-site cation radius while Aubin-Chevaldonnet et al.[36] demonstrated that various M-site substitutions for Ti^{+4} affects the fraction of Cs incorporated into the

hollandite tunnel sites. While experimentally assessing the effects of hollandite additives remains a focus of ongoing research, the complexity in the hollandite system limits the ability to evaluate large composition areas.

To reduce the magnitude of the possible experimental work and target specific hollandite formulations, a thermodynamic database is being developed to provide phase relations to guide development of compositions that are likely to form the hollandite phase as well as avoid secondary Cs parasitic phases. The database developed in this work according to the CALPHAD methodology[26] consists of the oxides BaO-Cs_2O-TiO_2-Cr_2O_3-Al_2O_3-Fe_2O_3-FeO-Ga_2O_3 and can calculate equilibrium behavior including extension to compositions/conditions that have not been experimentally determined. Solid solutions such as the hollandite phase were modeled with the compound energy formalism (CEF)[12, 41, 153-156] while the oxide liquid was characterized using the two-sublattice partially ionic liquid (TSPIL) model.[42, 152] The oxides of Cr, Al, Fe and Ga were considered in this initial development as experimental measurements have been reported for hollandite phases containing these constituents. The hollandite CEF model will subsequently be expanded to include additional elements of interest.

7.3. Identifying oxide systems to address

Table 7.1 provides synthesized hollandite compositions that were used to thermodynamically assess hollandite. The molar amount of TiO_2 averages ~70% of the hollandite-forming waste system. Thus, BaO, Cs_2O, and the additive oxides are dilute with respect to TiO_2, which assures that two non-TiO_2 oxides are unlikely to interact whereas all will warrant a description of energetic interactions with TiO_2. As such, Gibbs energies for the solid phases stable in the pseudo-binary systems of the oxides of substitutional

elements with TiO_2 were incorporated into the database except for Al_2O_3, Ga_2O_3, and Cr_2O_3. The Al_2O_3-TiO_2[362] and Ga_2O_3-TiO_2[363-365] systems were neglected as the intermediate compounds known to form in these systems, Al_4TiO_8, Al_2TiO_5, Ga_2TiO_5, and a series of $Ga_4Ti_{m-4}O_{2m-2}$ phases where $9 < m < 25$, are not stable at less than 1537 K, which is above temperatures of interest. Amoroso et al.[37] fabricated hollandites with Cr_2O_3 and did not report the formation of a chromium titanate minor phase, hence the Cr_2O_3-TiO_2 system was also neglected. The pseudo-binary system of Cs_2O-TiO_2 had not previously been assessed and, consequently, a new assessment of this system was conducted.

Minor phases that were observed to form[37] also led to the inclusion of intermediate compounds in the BaO-Fe_2O_3 and Al_2O_3-FeO systems.

7.4. Background

7.4.1. Cs_2O-TiO_2

Schmitz-Dumont & Reckhard[366] conducted liquidus measurements for the $Cs_2Ti_2O_5$-TiO_2 system, reporting the formation of one intermediate stoichiometric compound, $Cs_2Ti_4O_9$. Grey et al.,[367] however, did not observe the formation of $Cs_2Ti_4O_9$ but instead identified the compounds $Cs_2Ti_5O_{11}$ and $Cs_2Ti_6O_{13}$, which were subsequently confirmed by Grey et al.,[368] Kwiatkowska et al.,[369] Bursill et al.,[370] Peres et al.,[371] and Kobyakov et al.[372] Thus, the $Cs_2Ti_4O_9$ compound, and by extension the liquidus data reported by Schmitz-Dumont & Reckhard,[366] was neglected while $Cs_2Ti_5O_{11}$ and $Cs_2Ti_6O_{13}$ were included in the assessment of the Cs_2O-TiO_2 system. Grey et al.[367] were unable to experimentally determine the liquidus boundary in the analyzed 75-100 mol% TiO_2 region of the Cs_2O-TiO_2 system due to Cs volatilization, although phase transition temperatures were reported as follows: $Cs_2Ti_2O_5 + Cs_2Ti_5O_{11} \rightarrow Cs_2Ti_5O_{11}$ + melt = 1117

K, $Cs_2Ti_5O_{11}$ + melt → $Cs_2Ti_6O_{13}$ + melt = 1373 K, and $Cs_2Ti_6O_{13}$ + melt → TiO_2 + melt = 1405 K. Lu & Jin[373] summarized TiO_2 melting temperatures measured in varied atmospheres, ultimately adopting the 2185±10 K melting point measured for a near stoichiometric $TiO_{1.999}$ sample in a pure oxygen atmosphere. This melting point as well as the reported 763 K Cs_2O melting temperature[374, 375] were used in the Cs_2O-TiO_2 system assessment.

7.4.2. Hollandite

Amoroso et al.[28, 37] fabricated hollandite phases by melt processing to determine the impact of Cr, Al, and Fe additives on the stability and melting temperature in both single-phase[37] and multi-phase (MP) studies.[28] In both, the hollandite samples were heat treated at a constant temperature of 1773 K for 20 minutes and then allowed to cool in the powered off furnace,[28, 37] with cooling rates reported to drop from 60 K/min to 15 K/min by ~1473 K.[2] While the Fe-containing single phase hollandites (SPH) completely melted, Cr-Al-Fe (CAF) SPH samples only exhibited partial melting and Cr-SPH samples did not melt at all but were instead sintered at 1773 K (Section 7.5.4).[13] Dandeneau et al.[38] also fabricated a melt processed multi-phase waste form with a targeted composition equivalent to the CAF-MP composition of Amoroso et al.,[28] hence the ensuing discussion is applicable to both the Amoroso et al.[28] and Dandeneau et al.[38] studies. The SPH study targeted three hollandite nominal compositions that were fabricated in air and a 1% H_2 reducing atmosphere,[37] which will be designated as SPH and SPHR, respectively. Ti metal and TiO_2 were also added to some samples prior to synthesis,[37] which will be designated as SPH-Ti and SPHR-Ti, respectively. Amoroso et al.[37] determined the stoichiometry of the fabricated hollandite compositions through use of inductively coupled plasma (ICP) analysis as well

as the minor phases that formed in addition to hollandite. The MP hollandite study conducted by Amoroso et al.[28] differed from the SPH study[37] by incorporating additional oxides into samples that could be targeted by facilities operating to produce a MP ceramic waste form. The MP study targeted the same hollandite nominal compositions as the SPH study, and, consequently, the amounts of the oxides that formed the hollandite phase as listed in Table 5 of Amoroso et al.[28] were used as a basis in this work (Table 7.1). The ratio of $Fe^{+2}/(Fe^{+2} + Fe^{+3})$ for the CAF containing hollandites differed between the SPH and MP studies; thus, the SPH ratios were adopted in this work (Table 7.1). Also, the SPH Al_2O_3 quantities indicated in the Amoroso et al.[37] Table 2 footnotes were adopted. The waste compositions implemented in this work for the SPH hollandites[37] fabricated containing only the Fe additive were derived by adopting the Cr_2O_3 compositions used by Amoroso et al.[28] and then substituting Fe_2O_3 and FeO for Cr_2O_3 while retaining the $Fe^{+2}/(Fe^{+2} + Fe^{+3})$ ratio of the SPH study.[37]

Xu et al.[30, 35] used solid-state reaction and sol-gel methods to fabricate hollandites. Both studies employed final heat treatments of 1473 to 1523 K for 2 to 3 hours. Aubin-Chevaldonnet et al.[36] used a solid-state reaction to form oxide pellets that were calcined and sintered at 1473 K for 30 hours in air. Costa et al.[361] prepared hollandite samples by first mixing, heating, and evaporating citrate solutions before ultimately forming and heat treating pellets at 1523 K for 3 hours. Database calculations were conducted at each of these final heat treatment temperatures for comparison with the phase equilibria reported in these studies. Similarly, the reported 1473 K temperature at which the cooling rate of melt processed samples started slowing was adopted as defining the equilibrium state and, as such, calculations for comparison with melt processed sample results were conducted at

this temperature. Xu et al.,[30, 35, 40] Aubin-Chevaldonnet et al.,[36] and Costa et al.[361] synthesized hollandites with the additives Ga, Al, Cr, and Fe, hence the database was developed to include the oxides of these additives..

Wu et al.[35] derived a standard enthalpy of formation using drop solution calorimetry for a hollandite phase with the composition $Ba_{1.18}Cs_{0.21}Al_{2.44}Ti_{5.53}O_{16}$. Costa et al.[361] employed the same approach for the $Ba_{1.24}Al_{2.48}Ti_{5.52}O_{16}$ and $Ba_{1.24}Fe_{2.48}Ti_{5.52}O_{16}$ compositions. Xu et al.[30] and Wen et al.[39] used density functional theory (DFT)[65, 376] to calculate formation enthalpies at 0 K from the Ba to Cs endmember of two-thirds A-site occupied hollandites containing Al and Ga. The data reported by Xu et al.[30] was neglected as the DFT calculations were refined with improved computational parameterization by Wen et al.[39] Additionally, Wu et al.[377] measured heat capacities of a series of barium aluminotitanate hollandites including a Cs-substituted phase with the composition $Ba_{1.18}Cs_{0.21}Al_{2.44}Ti_{5.53}O_{16}$ at 1.2 mPa from 2 to 300 K.

7.5. Thermodynamic modeling and optimization

7.5.1. CEF and TSPIL models

The thermodynamic representations were optimized using the FactSage[43] software to obtain values for the CEF and TSPIL models for the solid solutions and liquid phases. The CEF is a sublattice-based model that can account for the non-stoichiometry of a substitutional or interstitial solid solution based on lattice site occupancies, which can include vacancies and interstitial sites. An example CEF three sublattice model can be represented as:

$(A,B)_k(D,E,F)_l(G)_m$

where *A*-*G* are elements distributed on one of the three possible lattice sites, and the subscripts k, l, and m are the sublattice stoichiometric coefficients. The CEF Gibbs energy function is defined in Hillert.[41]

The TSPIL model is based on the concept that in ionic liquid phases each atom bears a charge and thus is surrounded by unlike charged atoms resulting in atomic ordering. This ordering can be treated as two sublattices, one containing only cations and the other anions, vacancies, and neutral species (*C*, *A*, *Va*, and *B*, respectively) in:

$$\left(C_i^{+\nu_i}\right)_P\left(A_j^{-\nu_j}, Va, B_k^0\right)_Q$$

where the indices i, j, and k represent specific sublattice constituents. The superscripts $+\nu_i$ and $-\nu_j$ represent the charge of the i^{th} or j^{th} cation or anion, respectively, while 0 indicates a neutral species. Electroneutrality is maintained by allowing the stoichiometric coefficients (P and Q) to vary as a function of site fractions.

As noted in Utlak & Besmann,[148] the molar Gibbs energy of a phase modeled using the CEF can be expressed as:

$$G_m = \Sigma \Delta_f{}^o G_{end} \Pi y_J^s + RT\Sigma\Sigma n^s y_J^s \ln y_J^s + {}^E G_m \qquad (7.1)$$

where $\Delta_f{}^o G_{end}$ is the standard molar Gibbs energy of formation of an end-member, y_J^s is the site fraction of the J^{th} constituent in the n^{th} sublattice, and n^s is the stoichiometric coefficient of the n^{th} sublattice. The first, second, and third terms of eq. (7.1) are the Gibbs energy surface of reference, ideal entropy of mixing, and excess Gibbs energy of mixing, respectively.

The excess Gibbs energy, which accounts for the departure from ideal mixing of species on the same sublattice due to attraction or repulsion of the mixing constituents,[72] can be described with a generalized regular solution expression:

$$^{E}G_{m} = \Pi y_{J}^{s} \Sigma y_{B}^{t} L_{A,B:D:G} \ldots + \Pi y_{J}^{s} \Sigma\Sigma y_{B}^{t} y_{D}^{u} L_{A,B:D,E:G} \ldots + \ldots \quad (7.2)$$

where the subscripts A, B, D, E, and G as well as superscripts t and u refer to the constituents in a sublattice and the sublattice designations, respectively, in a generalized CEF formulation for a three sublattice phase $(A,B)_{k}^{t}(D,E,F)_{l}^{u}(G)_{m}^{v}$. The subscripts *k*, *l*, and *m* in the generalized formula represent the sublattice stoichiometric coefficients. The commas separating constituents in the interaction parameter designations of eq. (7.2) indicate the interactions between constituents on the same sublattice, whereas the colons separate sublattices. Equation (7.2) can be expanded to describe, in principle, constituent interactions of a multicomponent system of any order.

The interaction parameters of eq. (7.2) can be expressed as a Redlich-Kister (RK) power series[26] in terms of site fractions. As an example, for a binary interaction between the A and B species of eq. (7.2)

$$L_{A,B:D:G} = \sum_{k=0}^{n} {}^{k}L_{A,B:D:G}(y_{A} - y_{B})^{k} \quad (7.3)$$

where D and G are constituents on each of the second and third sublattices, *y* represents the site fraction of the subscripted sublattice constituent, and k is the order of the expansion. The interaction parameter *L* on the right-hand side of eq. (7.3) can be expressed as a polynomial in temperature with the form:

$$^{k}L_{A,B:D:G} = A + B{\cdot}T + C{\cdot}T\ln(T) + D{\cdot}T^{2} + E{\cdot}T^{3} + F{\cdot}T^{-1} \quad (7.4)$$

where *T* is the temperature in kelvin and the variables *A*, *B*, *C*, *D*, *E*, and *F* are coefficients determined by optimizing the model Gibbs energy function to thermochemical and/or phase equilibria data. In practice, only the *A* and *B* coefficients of eq. (7.4) are generally needed in an assessment unless experimental data can justify additional coefficients.[26]

The molar Gibbs energy in the TSPIL model is:

$$G_{\mathrm{m}} = \Sigma\Sigma y_{C_{\mathrm{i}}} y_{A_{\mathrm{j}}} {}^{\mathrm{o}}G_{C_{\mathrm{i}}:A_{\mathrm{j}}} + Q\left(y_{\mathrm{Va}}\Sigma y_{C_{\mathrm{i}}} {}^{\mathrm{o}}G_{C_{\mathrm{i}}} + \Sigma y_{B_{\mathrm{k}}} {}^{\mathrm{o}}G_{B_{\mathrm{k}}}\right) \quad (7.5)$$

$$+ RT\left[P\Sigma y_{C_{\mathrm{i}}}\ln y_{C_{\mathrm{i}}} + Q\left(\Sigma y_{A_{\mathrm{j}}}\ln y_{A_{\mathrm{j}}} + y_{Va}\ln y_{Va} + \Sigma y_{B_{\mathrm{k}}}\ln y_{B_{\mathrm{k}}}\right)\right] + {}^{\mathrm{E}}G_{\mathrm{m}}$$

where ${}^{\mathrm{o}}G_{C_{\mathrm{i}}:A_{\mathrm{j}}}$ is the Gibbs energy of formation for $\nu_{\mathrm{i}} + \nu_{\mathrm{j}}$ moles of atoms of the end-member $C_{\mathrm{i}}A_{\mathrm{j}}$ while ${}^{\mathrm{o}}G_{C_{\mathrm{i}}}$, and ${}^{\mathrm{o}}G_{B_{\mathrm{k}}}$ are the values for C_{i} and B_{k}, respectively. The first, second, and third terms of eq. (7.5) are the Gibbs energy surface of reference for all possible types of constituents, the random configurational entropy on each sublattice, and the excess Gibbs mixing energy, which can be expressed as:

$${}^{\mathrm{E}}G_{\mathrm{m}} = \Sigma\Sigma\Sigma y_{\mathrm{i}_1} y_{\mathrm{i}_2} y_{\mathrm{j}} L_{\mathrm{i}_1,\mathrm{i}_2:\mathrm{j}} + \Sigma\Sigma\Sigma y_{\mathrm{i}} y_{\mathrm{j}_1} y_{\mathrm{j}_2} L_{\mathrm{i}:\mathrm{j}_1,\mathrm{j}_2} + \Sigma\Sigma y_{\mathrm{i}} y_{\mathrm{j}_1} y_{\mathrm{Va}} L_{\mathrm{i}:\mathrm{j}_1,\mathrm{Va}} + \ldots \quad (7.6)$$

The interaction parameters again can be expressed as a Redlich-Kister power series (eq. (7.3)).

7.5.2. Stoichiometric phases

As observed by Hanaor & Sorrell[378] based on the results of cited studies, rutile is the equilibrium polymorph of TiO_2. Hence, a Gibbs energy description of the rutile polymorph has been incorporated in the database (Table 7.2). Intermediate stoichiometric phases for the BaO-TiO_2,[373] Cs_2O-TiO_2,[366, 367] FeO-TiO_2,[379] and Fe_2O_3-TiO_2[380] systems were included in the database. In addition, Amoroso et al.[37] observed the formation of the $BaFe_{12}O_{19}$ and $FeAl_2O_4$ phases. Consequently, these phases as well as the remaining intermediate line compounds known to be stable in the BaO-Fe_2O_3[381] system were also incorporated into the database (Table 7.2). While the only intermediate phase in the Al_2O_3-FeO[80, 222, 243, 323, 382, 383] system, $FeAl_2O_4$, has previously been represented as a stoichiometric compound and a solid solution, in this work a line compound was assumed, which is a sufficient approximation as $FeAl_2O_4$ is a minor phase due to the low of Al_2O_3

and FeO content in relevant waste compositions (Table 7.1). Values from the FactSage 7.2 databases cited in Table 7.2 from sources such as NIST-JANAF thermochemical tables[209] were used with slight modifications as necessary from the assessments.

The three stoichiometric compounds $Cs_2Ti_2O_5$, $Cs_2Ti_5O_{11}$, and $Cs_2Ti_6O_{13}$ were optimized as part of the Cs_2O-TiO_2 system assessment. The Neumann-Kopp rule[204] was applied to derive endmember heat capacities and estimated values for standard entropies with the latter values confirmed to be within the entropic range predicted by Latimer's method.[64, 205] Standard formation enthalpies were optimized to the phase equilibria data discussed in Section 7.4.1.

The $CsAlTiO_4$ and $Cs_2AlGaTi_2O_8$ line compounds were observed to form as secondary phases in Ba-Cs-Fe and Bs-Cs-Ga hollandites fabricated by Amoroso et al.[37] and Aubin-Chevaldonnet et al.,[36] respectively, and thus, included in the database. Gibbs energy functions for the $CsAlTiO_4$ and $Cs_2AlGaTi_2O_8$ phases were determined from heat capacities and standard entropies derived in the same manner as those for the cesium titanate compounds. Standard enthalpies of formation were then optimized to allow experimentally observed phase assemblages to be computed to form.

7.5.3. Hollandite solid solution

The hollandite sublattice model was developed to coincide with the hollandite general formula:[36, 37] $\left(Ba_xCs_y\right)(M,Ti)^{+2,+3,+4}_{2x+y}(Ti)^{+4}_{8-2x-y}O_{16}$, $x + y < 2$

where M represents a divalent, trivalent, or tetravalent cation, which resulted in the CEF four sublattice formalism:

$$(Ba^{+2},Cs^{+1},Va)^{\alpha}_2\left[Ti^{+4},Cr^{+3},Al^{+3},Fe^{+3},Fe^{+2},Ga^{+3}\right]^{\beta}_4\left\{Ti^{+4}\right\}_4\langle O^{-2}\rangle_{16}$$

As x + y < 2, the first and second sublattice stoichiometric coefficients of 2 and 4, respectively, bound all potential stoichiometric values of the first and second general formula terms (Ba_xCs_y) and $(M,Ti)_{2x+y}^{+2,+3,+4}$, respectively. The second and third sublattice stoichiometric coefficients sum to 8 to be consistent with the hollandite crystallographic tunnel sites composed of octahedrally-coordinated M-site cations.[30, 36] Thus, with the variation of sublattice species site fractions, the hollandite CEF model encompasses the range of possible hollandite compositions.

7.5.3.1. Optimization of hollandite CEF model

The Neumann-Kopp rule[204] was applied to derive endmember heat capacities and estimated values for standard entropies with the latter values also approximated by the entropic range predicted by Latimer's method.[64, 205] Endmember standard formation enthalpies (Table 7.3) were then optimized to the hollandite targeted compositions of the studies discussed in Section 7.4.2 for the respective waste compositions listed in Table 7.1. An example of the Gibbs energy relation for a neutral endmember such as $Ba_2Fe_4Ti_4O_{16}$ as generated by this approach is seen in eq. (7.7).

$$^{o}G_{Ba_2Fe_4Ti_4O_{16}} = 2\,^{o}G_{BaO(s)} + 2\,^{o}G_{Fe_2O_3(s)} + 4\,^{o}G_{TiO_2(s)} + \Delta H_{opt,298.15\,K} \quad (7.7)$$

where ^{o}G represents the standard Gibbs energy function of a specified oxide and $\Delta H_{opt,298.15K}$ is the enthalpy of formation at 298.15 K obtained from optimization to experimental data.

Gibbs energies of charged endmembers were defined as per the example of eq. (7.8) for $Cs_2Al_4Ti_4O_{16}^{-2}$.

$$^{o}G_{Cs_2Al_4Ti_4O_{16}^{-2}} = {}^{o}G_{Cs_2O(s)} + 2\,{}^{o}G_{Al_2O_3(s)} + 4\,{}^{o}G_{TiO_2(s)} + 2\,{}^{o}G_{Ti_3O_5(s)} - 3\,{}^{o}G_{Ti_2O_3(s)} + \Delta H_{opt,298.15\,K} \quad (7.8)$$

where ${}^{o}G_{Ti_3O_5(s)}$ and ${}^{o}G_{Ti_2O_3(s)}$ were included to obtain the correct oxygen stoichiometry and oxidation state.

Six RK parameters in the hollandite CEF were used to obtain representative Gibbs energy functions for the targeted compositions. Equation (7.9) defines the 298 K molar Gibbs energy function of the optimized hollandite solid solution with endmember and RK parameter values listed in Table 7.3.

$$
\begin{aligned}
G_m^{\text{hollandite}} = {} & y_{Ba^{+2}}^{\alpha} y_{Ti^{+4}}^{\beta}\ {}^{o}G_{Ba_2Ti_8O_{16}^{+4}} + y_{Cs^{+1}}^{\alpha} y_{Ti^{+4}}^{\beta}\ {}^{o}G_{Cs_2Ti_8O_{16}^{+2}} + y_{Va}^{\alpha} y_{Ti^{+4}}^{\beta}\ {}^{o}G_{Ti_8O_{16}} \\
& + y_{Ba^{+2}}^{\alpha} y_{Cr^{+3}}^{\beta}\ {}^{o}G_{Ba_2Cr_4Ti_4O_{16}} + y_{Cs^{+1}}^{\alpha} y_{Cr^{+3}}^{\beta}\ {}^{o}G_{Cs_2Cr_4Ti_4O_{16}^{-2}} \\
& + y_{Va}^{\alpha} y_{Cr^{+3}}^{\beta}\ {}^{o}G_{Cr_4Ti_4O_{16}^{-4}} + y_{Ba^{+2}}^{\alpha} y_{Al^{+3}}^{\beta}\ {}^{o}G_{Ba_2Al_4Ti_4O_{16}} \\
& + y_{Cs^{+1}}^{\alpha} y_{Al^{+3}}^{\beta}\ {}^{o}G_{Cs_2Al_4Ti_4O_{16}^{-2}} + y_{Va}^{\alpha} y_{Al^{+3}}^{\beta} G_{Al_4Ti_4O_{16}^{-4}} \\
& + y_{Ba^{+2}}^{\alpha} y_{Fe^{+3}}^{\beta}\ {}^{o}G_{Ba_2Fe_4Ti_4O_{16}} + y_{Cs^{+1}}^{\alpha} y_{Fe^{+3}}^{\beta}\ {}^{o}G_{Cs_2Fe_4Ti_4O_{16}^{-2}} \\
& + y_{Va}^{\alpha} y_{Fe^{+3}}^{\beta}\ {}^{o}G_{Fe_4Ti_4O_{16}^{-4}} + y_{Ba^{+2}}^{\alpha} y_{Fe^{+2}}^{\beta}\ {}^{o}G_{Ba_2Fe_4Ti_4O_{16}^{-4}} \\
& + y_{Cs^{+1}}^{\alpha} y_{Fe^{+2}}^{\beta}\ {}^{o}G_{Cs_2Fe_4Ti_4O_{16}^{-6}} + y_{Va}^{\alpha} y_{Fe^{+2}}^{\beta}\ {}^{o}G_{Fe_4Ti_4O_{16}^{-8}} \\
& + y_{Ba^{+2}}^{\alpha} y_{Ga^{+3}}^{\beta}\ {}^{o}G_{Ba_2Ga_4Ti_4O_{16}} + y_{Cs^{+1}}^{\alpha} y_{Ga^{+3}}^{\beta}\ {}^{o}G_{Cs_2Ga_4Ti_4O_{16}^{-2}} \\
& + y_{Va}^{\alpha} y_{Ga^{+3}}^{\beta}\ {}^{o}G_{Ga_4Ti_4O_{16}^{-4}} \\
& + RT\Big(y_{Ba^{+2}}^{\alpha} \ln y_{Ba^{+2}}^{\alpha} + 2y_{Cs^{+1}}^{\alpha} \ln y_{Cs^{+1}}^{\alpha} + 2y_{Va}^{\alpha} \ln y_{Va}^{\alpha} + 4y_{Ti^{+4}}^{\beta} \ln y_{Ti^{+4}}^{\beta} \\
& + 4y_{Cr^{+3}}^{\beta} \ln y_{Cr^{+3}}^{\beta} + 4y_{Al^{+3}}^{\beta} \ln y_{Al^{+3}}^{\beta} + 4y_{Fe^{+3}}^{\beta} \ln y_{Fe^{+3}}^{\beta} + 4y_{Fe^{+2}}^{\beta} \ln y_{Fe^{+2}}^{\beta} \\
& + 4y_{Ga^{+3}}^{\beta} \ln y_{Ga^{+3}}^{\beta}\Big) + y_{Cs^{+1}}^{\alpha} y_{Va}^{\alpha} y_{Cr^{+3}}^{\beta}\ {}^{0}L_{Cs^{+1},Va:Cr^{+3}:Ti^{+4}:O^{-2}} \\
& + y_{Cs^{+1}}^{\alpha} y_{Va}^{\alpha} y_{Al^{+3}}^{\beta}\ {}^{0}L_{Cs^{+1},Va:Al^{+3}:Ti^{+4}:O^{-2}} \\
& + y_{Cs^{+1}}^{\alpha} y_{Va}^{\alpha} y_{Fe^{+3}}^{\beta}\ {}^{0}L_{Cs^{+1},Va:Fe^{+3}:Ti^{+4}:O^{-2}}
\end{aligned}
\tag{7.9}
$$

$$+ y^{\alpha}_{Cs^{+1}} y^{\beta}_{Cr^{+3}} y^{\beta}_{Fe^{+3}} \; {}^{0}L_{Cs^{+1}:Cr^{+3},Fe^{+3}:Ti^{+4}:O^{-2}}$$

$$+ y^{\alpha}_{Cs^{+1}} y^{\beta}_{Al^{+3}} y^{\beta}_{Fe^{+3}} \; {}^{0}L_{Cs^{+1}:Al^{+3},Fe^{+3}:Ti^{+4}:O^{-2}}$$

$$+ y^{\alpha}_{Ba^{+2}} y^{\beta}_{Cr^{+3}} y^{\beta}_{Fe^{+2}} \; {}^{0}L_{Ba^{+2}:Cr^{+3},Fe^{+2}:Ti^{+4}:O^{-2}}$$

7.5.4. Liquid phase of hollandite-forming system

As discussed in Section 7.4.2, the hollandite sample fabrication methods of solid-state reaction, sol-gel, and combustion synthesis with final sintering at temperatures of 1473 to 1523 K for 3 to 30 hours did not provide liquid phase data.[30, 35, 36, 361] Hence, the liquid phase was not addressed. Additionally, while Amoroso et al.[37] noted that Fe-containing samples exhibited signs of melting when melt processing was attempted, inspection of CAF samples indicated only near or partial melting occurred, and Cr-containing samples showed minimal signs of melting, formed largely from solid-state reactions. Thus, only solid-state behavior of the CAF and Cr samples was considered.

As the Fe samples were not rapidly quenched but instead allowed to naturally cool in the powered off furnace,[37] the phases observed were deemed to be the equilibrium state assemblage.

7.5.4.1. Liquid phase of Cs_2O-TiO_2 system

While it was largely unnecessary to assess the melts for the constituent systems, the exception was Cs_2O-TiO_2. A TSPIL model was required to allow consideration of the liquid phase as the solidus/liquidus values were useful in generating the molar Gibbs energies of the intermediate stoichiometric phases. The liquid phase was modeled such that Cs^{+1} and Ti^{+4} cations appear on the first sublattice and the O^{-2} anion resides on the second sublattice:

$(Cs^{+1},Ti^{+4})_P(O^{-2})_Q$

Grey et al.[367] were unable to measure liquidus data due to high Cs volatility, and the liquidus data reported by Schmitz-Dumont & Reckhard[366] was neglected as the measurements indicated the formation of $Cs_2Ti_4O_9$, which did not agree with other experimental studies of the C_2O-TiO_2 system.[367-372] As such, estimation of the Cs_2O-TiO_2 liquidus curve was required, which was based on the analogous K_2O-TiO_2 phase diagram reported by Eriksson & Pelton.[379] As K_2O and Cs_2O are alkali metal oxides with no polymorphs, it is reasonable to assume that the phase equilibrium behavior of the Cs_2O-TiO_2 system can be generally approximated by the K_2O-TiO_2 system. Inspection of the K_2O-TiO_2 phase diagram computed by Eriksson & Pelton[379] indicates that the liquidus curve continuously decreases from 100 to 36 mol% TiO_2. Intermediate line compounds at TiO_2 mol fractions > 50% are seen to melt incongruently, and a eutectic point forms at 20 mol% TiO_2. The TSPIL model for the Cs_2O-TiO_2 system was optimized to agree with the trends exhibited by the K_2O-TiO_2 phase diagram, which required a single RK parameter (eq. (7.10), values listed in Table 7.3).

$$G_m^{liquid} = y_{Cs^{+1}} y_{O^{-2}} \, {}^{o}G_{Cs^{+1}:O^{-2}} + y_{Ti^{+4}} y_{O^{-2}} \, {}^{o}G_{Ti^{+4}:O^{-2}} + RT\left(2y_{O^{-2}}\left(y_{Cs^{+1}} \ln y_{Cs^{+1}} + y_{Ti^{+4}} \ln y_{Ti^{+4}}\right) + \left(y_{Cs^{+1}} + 4y_{Ti^{+4}}\right)\left(y_{O^{-2}} \ln y_{O^{-2}}\right)\right) + y_{Cs^{+1}} y_{Ti^{+4}} y_{O^{-2}} \, {}^{0}L_{Cs^{+1},Ti^{+4}:O^{-2}} \quad (7.10)$$

7.6. Results and discussion

7.6.1. Cs_2O-TiO_2 pseudo-binary system

The available Cs_2O-TiO_2 crystalline phase data consists of $Cs_2Ti_2O_5$, $C_2Ti_5O_{11}$, and $Cs_2Ti_6O_{13}$ incongruent melting temperatures as well as the Cs_2O and TiO_2 congruent melting temperatures. The phase diagram resulting from the combined optimizations of the liquid, $Cs_2Ti_2O_5$, $C_2Ti_5O_{11}$, and $Cs_2Ti_6O_{13}$ Gibbs energy functions (Fig. 7.1) indicates that

all melting temperatures were well reproduced. Altogether with the analogous features of the K_2O-TiO_2 phase diagram.

7.6.2. Thermodynamic database of hollandite-forming oxide system

Results of the hollandite CEF optimizations are displayed in Table 7.4 & Table 7.5, which contain targeted, measured, and calculated hollandite compositions (Table 7.4) as well as calculated mass fractions of secondary phases (Table 7.5). Experimentally observed secondary phases for each composition are also listed in Table 7.5. Database calculations to determine non-melt processed hollandite compositions were conducted at the temperatures listed in Table 7.4, which are sintering temperatures for hollandite pellets fabricated in the studies discussed in Section 7.4.2. Again, the reported 1473 K temperature at which the cooling rate of melt processed samples started slowing was adopted as the equilibrium temperature. Equilibrium calculations using assessed thermochemical models and values predict the hollandite phase is stable for the experimental compositions of Amoroso et al.,[37] Xu et al.,[35, 40] Aubin-Chevaldonnet et al.,[36] and Costa et al.[361] (Table 7.4).

Analysis of the optimization results for the hollandite phases fabricated by Amoroso et al.[37] indicates that calculated stoichiometries overall agree well with measured compositions with minor deviations for melt processed samples. As discussed by Amoroso et al.,[37] melt processed hollandite samples prepared with Fe_2O_3 contained FeO and Al_2O_3 either from the crucible used to prepare the sample or added to the batch in the case of CAF samples, which caused $FeAl_2O_4$ to precipitate. Regardless, the computed phase equilibria confirm the observation of secondary phase $FeAl_2O_4$ in all Fe-containing waste types (Table 7.5). Amoroso et al.[37] concluded that the Fe and CAF hollandite samples would be

deficient in Fe and thus drive the hollandite compositions off stoichiometry, which was observed in all Fe- and CAF-SPH computed compositions (Table 7.4).

It was experimentally observed that the addition of Cr and a Ti/TiO_2 buffer stabilized the hollandite structure and increased Cs incorporation.[37] The enhancement of Cs content can be ascribed to the suppression of the formation of the parasitic Cs secondary phase $CsAlTiO_4$.[37] Equilibrium calculations confirmed these experimental results as $CsAlTiO_4$ was not stable for any Cr-SPH formulations, and the Cr-SPH-Ti and CAF-SPH-Ti hollandites tolerated more Cs than the other respective melt processed waste compositions. Secondary phase formation was suppressed in hollandite compositions containing solely Cr as an additional element with only excess TiO_2 observed in samples.[37] Computations generally agreed with TiO_2 forming along with minor amounts of Cr_2O_3 (Table 7.5). In contrast, melt processed Fe and CAF waste types were observed to precipitate titanate and aluminate phases as well as possibly $CsAlTiO_4$.[37] Equilibrium calculations generally agreed as Fe waste type compositions yielded titanate and aluminate phases as well as TiO_2 and $CsAlTiO_4$ while the CAF waste types were computed to predominantly form TiO_2 and $FeAl_2O_4$ as secondary phases (Table 7.5). XRD measurements conducted by Amoroso et al.[37] detected a precipitated $CsAlTiO_4$ phase in only one of the four CAF samples, and thus a computed result indicating $CsAlTiO_4$ is not stable in these systems is reasonable. Similarly, as $BaFe_{12}O_{19}$ was not detected by SEM analysis, the lack of the computed $BaFe_{12}O_{19}$ phase in Fe-SPHR and CAF-SPHR compositions was deemed reasonable.

Computed hollandite phase stoichiometries agreed well with targeted and/or measured hollandite phase compositions fabricated by Xu et al.,[35, 40] Aubin-Chevaldonnet

et al.,[36] and Costa et al.[361] (Table 7.4). Aubin-Chevaldonnet et al.[36] reported that Ba and Cs containing hollandite samples with only the Al^{+3} or Cr^{+3} substitutional elements contained only a fraction of the Cs targeted. A possible cause of this result noted by Aubin-Chevaldonnet et al.[36] was that a high fraction of Cs vaporized during the solid-state reaction synthesis process and caused formation of low density samples. Comparatively, the Al-SPH-1 hollandites fabricated by Xu et al.[35] via a sol-gel method had the expected Cs content. Thus, the equivalency of the calculated and targeted Al-SPH-3 Cs fraction is acceptable (Table 7.4).[36, 37] Also, good agreement of computed results with the Cr-SPH measured compositions by Amoroso et al.[37] indicates that the hollandite model accurately reflects the less than expected Cs content observed by Amoroso et al.[37] and Aubin-Chevaldonnet et al.[36]

Secondary phases computed to form were generally consistent with experimental observations for non-melt processed waste types (Table 7.5). The $CsGaSi_{0.4}Ti_{0.6}O_4$ phase that was observed by Aubin-Chevaldonnet et al.[36] to precipitate in the Ga-SPH-6 hollandite was omitted in equilibrium calculations as it was likely due to SiO_2 contamination from the silicate glass-ceramic balls used in an attrition mill as noted by the authors. The $CsAl_{0.5}Ga_{0.5}TiO_4$ phase, however, was included in the assessment of the AG-SPH-2 hollandite with the calculated result indicating that the parasitic compound reduced the fraction of Cs expected in the hollandite phase, which agreed with the experimental result (Table 7.4). Al-SPH-1 was experimentally observed to have no secondary phases while Al-SPH-3 with a similar composition was reported to form $Ba_2Ti_9O_{20}$ and TiO_2 alongside hollandite.[35, 36] A barium titanate phase, $BaTiO_3(\beta)$, was calculated to be stable for this general composition. While Fe_2TiO_5 and $BaTi_4O_9$ were identified as minor phases in Fe-

SPH-3 prepared with zirconia/silicate glass-ceramic attritor balls. Aubin-Chevaldonnet et al.[36] reported that $BaTi_4O_9$ was not detected and the amount of Fe_2TiO_5 decreased in samples milled with yttrium-stabilized zirconia attritor balls, which indicates that the formation of these secondary phases was affected by sample preparation. Given these issues, it is reasonable that Fe-SPH-3 is computed to be single phase. The three minor phases containing Y, Zr, O; Cs, Si, O; and Al, O in AF-SPH-2 were likely a result of contamination from the attritor mill glass-ceramic balls as discussed by Aubin-Chevaldonnet et al.[36] However, as the AF-SPH-2 composition is similar to the melt processed Fe and CAF compositions but without Cr to suppress $CsAlTiO_4$ formation (Table 7.1), a relatively minor amount of $CsAlTiO_4$ is calculated to be stable (Table 7.5). Computations determined Cs was incorporated in the AF-SPH-2 hollandite composition and thus are consistent with experimental observations.

Table 7.1 lists the component compositions assumed in computing standard enthalpies of formation for comparison with experimental measurements and DFT results (Table 7.3). Waste types for this purpose are identified with the label inclusion of DS (drop solution) or DFT. Measured/DFT derived hollandite oxide formation enthalpies were converted to molar or 'elemental' enthalpies by adding the sum of the standard formation enthalpies of the constituent oxides listed in Table 7.3 to the Table 7.6 hollandite oxide formation enthalpies. Results are displayed in Table 7.6 as well as Fig. 7.2.

Fe-SPH computed enthalpies were extrapolated to the $Cs_{1.35}Fe_{1.35}Ti_{6.65}O_{16}$ endmember. Computed values agree well with experimental measurements and DFT calculations for Al-SPH-DS/DFT and Fe-SPH-DS. Discrepancies exist between database calculations and Ga-SPH-DFT values near the Ba endmember with both data sets

converging at a Cs stoichiometry of 1 before diverging at 1.33 (Table 7.6 & Fig. 7.2). Hollandite CEF optimized parameters were generated to accurately represent measured compositions, thus Ga-SPH-DFT_calc enthalpy values are a result of targeting the Ga-SPH-1–5 and AG-SPH-1/2 compositions. Further adjustment of CEF Ga-containing endmembers would cause disagreement in Ga-SPH compositions; hence a compromise was required to obtain reasonable values of calculated compositions and experimental and DFT derived formation enthalpies. The Cr-SPH-BASE Cs endmember extends to a stoichiometric Cs value of 1.38, which is also a result of a compromise requiring adjustment of the ${}^{o}G_{Cs_2Cr_4Ti_4O_{16}^{-2}}$ endmember optimized standard formation enthalpy to approximate the $Cs_{1.33}Ga_{1.33}Ti_{6.67}O_{16}$ composition for the Cr-SPH-BASE-5 waste type while suppressing $CsAlTiO_4$ formation in the melt processed Cr-SPH waste types.

As discussed in Section 7.4.2, Wu et al.[377] measured the heat capacity at a constant pressure of 1.2 mPa for the hollandite phase $Ba_{1.18}Cs_{0.21}Al_{2.44}Ti_{5.53}O_{16}$. Fig. 7.3 displays the computed hollandite heat capacity for the Al-SPH-C_p composition (Table 7.1), which consists of the oxides BaO, Cs_2O, TiO_2, and Al_2O_3 in amounts representative of the hollandite stoichiometry $Ba_{1.18}Cs_{0.21}Al_{2.44}Ti_{5.53}O_{16}$. Although a minor amount of Al_2O_3(corundum) and $BaTiO_3$(β) is computed to form with hollandite at this composition, the minimal stoichiometric difference from that measured phase was negligible, providing good agreement between measured and computed heat capacity values. The low temperature is due to extrapolating heat capacity functions of component oxides below 298 K which is outside of the reported range for the values (Section 7.5.3.1).

7.6.3. Extrapolation of hollandite compositions

A main benefit of thermochemical models of phases is the ability to extrapolate system behavior to compositional regions that have not been experimentally evaluated.[26] The developed database was so used to generate a 1473 K isothermal BaO-Cs_2O-TiO_2 pseudo-ternary diagram (Fig. 7.4) containing Cr_2O_3, Al_2O_3, Fe_2O_3, and FeO in amounts equivalent to CAF-SPH-1 (Table 7.1). The diagram phase regions have been defined in Table 7.7. Due to the complexity of Fig. 7.4, the smaller regions were not separately identified. Fig. 7.5 displays an expanded section of Fig. 7.4 in the high TiO_2, low BaO and Cs_2O region.

The database development approach described in Section 7.3 was designed to yield detailed equilibrium calculations in the high TiO_2 and low to moderate BaO and Cs_2O mole fraction region of a BaO-Cs_2O-TiO_2 pseudo-ternary diagram. Fig. 7.4 is thus truncated at 40 mol% TiO_2 and 60 mol% BaO and Cs_2O, which is a reasonable range to display as phase stabilities calculated beyond these mole fractions would be unreliable due to neglected secondary phases consisting exclusively of BaO, Cs_2O, and/or additive oxides.

The accurate computed phase equilibria and the relations that they embody can assist in development of hollandite-based waste sequestration phases, and most notably those that can effectively accommodate Cs. For example, Fig. 7.4 indicates secondary phases that are likely to form within a region, yet they can be seen to not necessarily impact the effectiveness of a waste form composition. This can, however, alert the developer to compositional regions containing a parasitic Cs secondary phase(s), and thus allow design of systems that avoid their formation, thereby maximizing effective hollandite waste loading. Additionally, waste compositions likely to yield a high fraction of hollandite can

be projected by targeting locations on a BaO-Cs_2O-TiO_2 isothermal diagram near a phase boundary of two regions that share hollandite as a stable phase or in a region with minimal secondary phases. Approaching a boundary results in amounts of secondary phases not stable in both regions reducing to zero close to the boundary thereby increasing the ratio of hollandite to total phases formed. The waste compositions and stable phase amounts of the Fig. 7.4 composition points near the shared boundary of regions 11 & 17 and in region 25, which contains only the secondary phases $FeTiO_3$ and Cr_2O_3, are shown in Table 7.1 & 3, respectively. According to the results in Table 7.8, phases within region 11 and adjacent regions are predicted to yield 96.6 and 92.5% hollandite, respectively. While region 25 has a lower predicted hollandite yield than region 17, the hollandite phase of region 25 is calculated to contain more Cs (Table 7.8), of which none is lost to a Cs parasitic phase. This is thus a good example of how equilibrium calculations can be used to optimize waste loading.

7.7. Conclusion

An assessed thermodynamic database has been developed that allows successful calculation of observed equilibrium behavior of hollandite-forming BaO-Cs_2O-TiO_2-Cr_2O_3-Al_2O_3-Fe_2O_3-FeO-Ga_2O_3 systems. The variable composition hollandite and related phases were modeled using the CEF with the TSPIL model used to represent the Cs_2O-TiO_2 system oxide melt. The assessment included titanate and aluminate compounds Gibbs energies generated in this work as well as the Cs parasitic phases $CsAlTiO_4$ and $Cs_2AlGaTi_2O_8$. The constructed database was then used to generate a partial 1473 K BaO-Cs_2O-TiO_2 pseudo-ternary diagram that included fixed fractions of additional expected waste stream elements in prospective waste-form hollandite phases. These calculations

extrapolate the phase equilibrium behavior of the hollandite-forming system to regions that have not been experimentally addressed, with such capability expected to be of substantial value to the development and evaluation of waste form compositions.

Future work will involve expanding the database to include oxides of additional waste elements and related titanate phases as well as non-titanate phases. These should include the oxides ZrO_2, CaO, Eu_2O_3, Y_2O_3, among others, and complex phases such as zirconolite and/or +2/+3 titanates to ultimately develop a database that supports the efforts on multiphase ceramic waste forms.

7.8. Acknowledgements

Research was conducted by the Center for Hierarchical Waste Form Materials (CHWM), an Energy Frontier Research Center (EFRC). Research was supported by the U.S. Department of Energy, Office of Basic Energy Sciences, Division of Materials Sciences and Engineering under Award DE-SC0016574.

7.9. Tables

Table 7.1. Oxide compositions of specified waste types

Waste type[a]	Oxide amount (mol·10^2)							
	BaO	Cs_2O	TiO_2	Cr_2O_3	Al_2O_3	Fe_2O_3	FeO	Ga_2O_3
Fe-SPH-1[28, 37]	8.17	0.601	61.4	0	7.20	6.66	5.20	0
Fe-SPHR[28, 37]	7.42	0.511	54.8	0	9.50	0	18.3	0
Fe-SPH-Ti[28, 37]	6.57	0.712	60.6	0	14.2	5.89	3.07	0
Cr-SPH-1[28, 37]	9.00	0.662	67.6	10.4	0.296	0.041	0.030	0
Cr-SPHR[28, 37]	9.13	0.629	67.5	10.6	0.365	0	0.122	0
Cr-SPH-Ti[28, 37]	7.74	0.838	71.3	8.99	0.364	0.073	0.059	0
Cr-SPHR-Ti[28, 37]	7.74	0.678	71.1	9.05	0.443	0	0.102	0
CAF-SPH-1[28, 37]	8.84	0.686	65.4	4.68	3.83	3.35	2.10	0
CAF-SPHR[28, 37]	8.37	0.533	61.1	5.02	7.36	0	7.54	0
CAF-SPH-Ti[28, 37]	7.46	0.941	70.5	4.13	2.44	3.27	0.899	0
CAF-SPHR-Ti[28, 37]	7.13	0.604	63.3	3.59	10.5	0	6.75	0
Ga-SPH-1[30]	16.6	0	66.8	0	0	0	0	16.6
Ga-SPH-2[30]	13.0	1.50	71.0	0	0	0	0	14.5
Ga-SPH-3[30]	8.34	4.17	75.0	0	0	0	0	12.5
Ga-SPH-4[30]	0	8.31	83.4	0	0	0	0	8.31
Al-SPH-1[35]	14.7	1.31	68.8	0	15.2	0	0	0
Al-SPH-2[36]	14.5	0	71.0	0	14.5	0	0	0
Cr-SPH-2[36]	14.5	0	71.0	14.5	0	0	0	0
Ga-SPH-5[36]	14.5	0	71.0	0	0	0	0	14.5
Fe-SPH-2[36]	14.5	0	71.0	0	0	14.5	0	0
AF-SPH-1[36]	16.0	0	68.0	0	10.3	5.75	0	0
AG-SPH-1[36]	16.0	0	68.0	0	10.3	0	0	5.75
Al-SPH-3[36]	13.9	0.625	71.0	0	14.5	0	0	0
Cr-SPH-3[36]	13.0	1.50	71.0	14.5	0	0	0	0
Ga-SPH-6[36]	13.0	1.50	71.0	0	0	0	0	14.5
AG-SPH-2[36]	12.5	1.75	71.5	0	9.13	0	0	5.13
Fe-SPH-3[36]	13.0	1.50	71.0	0	0	14.5	0	0
AF-SPH-2[36]	12.5	1.75	71.5	0	9.13	5.13	0	0
Al-SPH-4[361]	15.5	0	69.0	0	15.5	0	0	0
Fe-SPH-4[361]	15.5	0	69.0	0	0	15.5	0	0
Al-SPH-DS-1[361]	15.5	0	69.0	0	15.5	0	0	0
Fe-SPH-DS-1[361]	15.5	0	69.0	0	0	15.5	0	0
Al-SPH-DS-2[35]	14.7	1.31	68.8	0	15.2	0	0	0
Al-SPH-DFT-1[39]	16.6	0	66.7	0	16.7	0	0	0
Al-SPH-DFT-2[39]	12.5	2.06	70.9	0	14.6	0	0	0
Al-SPH-DFT-3[39]	8.37	4.18	75.0	0	12.5	0	0	0
Al-SPH-DFT-4[39]	4.13	6.25	79.2	0	10.4	0	0	0
Al-SPH-DFT-5[39]	0	8.31	83.4	0	8.31	0	0	0
Ga-SPH-DFT-1[39]	16.6	0	66.7	0	0	0	0	16.7
Ga-SPH-DFT-2[39]	12.5	2.06	70.9	0	0	0	0	14.6
Ga-SPH-DFT-3[39]	8.37	4.18	75.0	0	0	0	0	12.5
Ga-SPH-DFT-4[39]	4.13	6.25	79.2	0	0	0	0	10.4
Ga-SPH-DFT-5[39]	0	8.31	83.4	0	0	0	0	8.31
Fe-SPH-BASE-1	16.6	0	66.7	0	0	16.7	0	0
Fe-SPH-BASE-2	12.5	2.06	70.9	0	0	14.6	0	0
Fe-SPH-BASE-3	8.37	4.18	75.0	0	0	12.5	0	0
Fe-SPH-BASE-4	4.13	6.25	79.2	0	0	10.4	0	0
Fe-SPH-BASE-5	0	8.31	83.4	0	0	8.31	0	0
Al-SPH-C_p	14.7	1.31	68.8	0	15.2	0	0	0
✳ point (Fig. 7.4)	1.50	6.68	77.9	4.68	3.83	3.35	2.10	0
◓ point (Fig. 7.4)	12.7	0.735	72.7	4.68	3.83	3.35	2.10	0

[a] For waste types with abbreviated elements: C = Cr, A = Al, F = Fe, G = Ga

Table 7.2. Enthalpy, entropy, and heat capacity constant values of specified compounds

Compound	T range (K)	$\Delta H_{298.15\ K}$ (J/mol)	$S_{298.15\ K}$ (J/mol·K)	C_p[a] constants							Reference
				a	*b*	*c*	*d*	*e*	*f*	*g h*	
Al_2O_3(corundum)	298 < T < 2327.01 2327 < T < 3000	-1675700	50.81999	155.018882 192.464		-38.61363015		-828.38698	4.09083646192		Bale et al.[b,43]
TiO_2(s)	298.15 < T < 2185 2185 < T < 5000	-944000	50.62	63.19571 100	11.82047	-10.34714	-0.1951847				Bale et al.[c,43]
TiO_2(ℓ)	298.15 < T < 2185	-876000	81.74128	63.19571	11.82047	-10.34714	-0.1951847				"
Ti_2O_3(s)	298.15 < T < 470 470 < T < 2115 2115 < T < 2500	-1520884	77.25297	100 730.23381288 169.96110912	1.8808385408E+10	16.0964894072		14604.8657928 -750.21868888	-15.65521004		Bale et al.[b,43]
Ti_3O_5(s)	298.15 < T < 450 450 < T < 1991	-2465422	129.369	156.9 278.899892		71.360165976		-2149.47088008	-21.1960050912		"
Cr_2O_3(s)	298.15 < T < 306 306 < T < 335 335 < T < 2705 2705 < T < 4500	-1140600	81.1	-2205.58 -10335.4 134.438 170	5442.26 21480.4 -12.6174	624.9626 3642.033 -28.3957	8437.26				Bale et al.[c,43]
FeO(s)	298.15 < T < 1650 1650 < T< 3000	-265700	57.58	57.49 68.2	-9.7619	-6.4624 0.0003	9120.26				"
Fe_2O_3(s)	298.15 < T < 700 700 < T < 955 955 < T < 970 970 < T < 1050 1050 < T < 1812 1812 < T < 4000	-825000	87.4	143.718 638.059 -5041690 -34422.16 80.37801 165	-36.8323 -964.0469 6908191 43508.09 55.8247	-31.4702 -447.4924 7957924 64561.86 166.8551	72252.2 561229.3 -2.662215E+09 -15398440 -12364.54				"
$FeAl_2O_4$(s)	298.15 < T < 2053	-1980873	106.274	155.3938	26.15	-31.33816					"
$FeTiO_3$(s)	298.15 < T < 1650	-1233142.16	108.6275	149.999500344		-33.2369399512		-441.62199496	3.4815103748		Bale et al.[b,43]
Fe_2TiO_5(s)	298.15 < T < 2000	-1738786.72	171.9624	192.58952	22.00784	-31.00344					Bale et al.[d,43]
$FeTi_2O_5$(s)	298.15 < T < 1728	-2152814.44	176.5694	247.154001216		-45.02760132		-1026.15001616	4.5551601296		Bale et al.[b,43]
Fe_2TiO_4(s)	298.15 < T < 2000	-1515609.69	168.87	249.630000368				-1817.39997968	-0.54530000872		"
Ga_2O_3(s)	298.15 < T < 2080 2080 < T < 4000	-1091000	84.94	114.3972 160	14.96308 -2.694611E-13	-23.7587 -3.693633E-12	-0.3472236 3.667516E-11				Bale et al.[c,43]
Cs_2O(s)	298.15 < T < 768 768 < T < 2500	-346400	146.9	66.00865 100	33.50166	0.004812183	-28.2838				"
Cs_2O(ℓ)	298.15 < T < 768 768 < T < 2500	-326400	172.9417	66.00865 100	33.50166	0.004812183	-28.2838				"
$Cs_2Ti_2O_5$(s)	298.15 < T < 768 768 < T < 2500	-2256315	246.73	213.21851 247.20986	35.668554 2.166894	-32.817827817 -32.82264	-31.049508 -2.765708				This work

Table 7.2 cont'd. Enthalpy, entropy, and heat capacity constant values of specified compounds

Compound	T range (K)	$\Delta H_{298.15\,K}$ (J/mol)	$S_{298.15\,K}$ (J/mol·K)	C_p[a] constants							Reference
				a	b	c	d	e	f	g	h	
$Cs_2Ti_5O_{11}$(s)	298.15 < T < 768	-5086020	396.475	434.0333	38.918895	-82.051787817	-35.19807					This work
	768 < T < 2500			468.02465	0.00541724	-8205660	-6.91E-09					
$Cs_2Ti_6O_{13}$(s)	298.15 < T < 768	-6020900	446.39	507.63823	40.002342	-98.463107817	-36.580924					"
	768 < T < 2500			541.62958	6.500682	-98.46792	-8.297124					
BaO(s)	298.15 < T < 900	-548104	72.0694	45.367112	17.6602456	-2.52747072	-5722.875198					Lu & Jin[373]
	900 < T < 2286			51.308392	6.671388	-7.809436	-45.43824					
	2286 < T < 3000			66.944								
BaO(ℓ)	298.15 < T < 900	-489528	97.6932	45.367112	17.6602456	-2.52747072	-5722.875198					"
	900 < T < 2286			51.308392	6.671388	-7.809436	-45.43824					
	2286 < T < 3000			66.944								
$BaTiO_3$(α)	298.15 < T < 3000	-1664124.46	103.1662	121.462	8.535	-19.16						"
$BaTiO_3$(β)	298.15 < T < 3000	-1660674.46	105.1662	121.462	8.535	-19.16						"
$BaTi_4O_9$(s)	298.15 < T < 900	-4518418	-259.6794	298.149952	64.9421256	-43.91603072	-5723.6559368					"
	900 < T < 2185			304.091232	53.953268	-49.197996	-46.2189788					
	2185 < T < 2286			451.308392	6.671388	-7.809436	-45.43824					
	2286 < T < 3000			466.944								
	3000 < T < 5000			466.944								
Ba_2TiO_4(s)	298.15 < T < 3000	-2198892.82	207.41	179.912	6.694	-29.12						"
$Ba_2Ti_9O_{20}$(s)	298.15 < T < 900	-9999010	559.1888	659.495614	141.7047212	-98.17920144	-11447.5070583					"
	900 < T < 2185			671.378174	119.727006	-108.743132	-92.6331423					
	2185 < T < 2286			1002.616784	13.342776	-15.618872	-90.87648					
	2286 < T < 3000			1033.888								
	3000 < T < 5000			1033.888								
$Ba_4Ti_{13}O_{30}$(s)	298.15 < T < 900	-15207662	897.2676	1003.012678	224.3070924	-144.62270288	-22894.0381931					"
	900 < T < 2185			1026.777798	180.351662	-165.750564	-184.2903611					
	2185 < T < 2286			1505.233568	26.685552	-31.237744	-181.75296					
	2286 < T < 3000			1567.776								
	3000 < T < 5000			1567.776								
$Ba_6Ti_{17}O_{40}$(s)	298.15 < T < 900	-20423235	1225.366	1346.529742	306.9094636	-191.06620432	-34340.5693279					"
	900 < T < 2185			1382.177422	240.976318	-222.757996	-275.9475799					
	2185 < T < 2286			2007.850352	40.028328	-46.856616	-272.62944					
	2286 < T < 3000			2101.664								
	3000 < T < 5000			2101.664								

Table 7.2 cont'd. Enthalpy, entropy, and heat capacity constant values of specified compounds

Compound	T range (K)	$\Delta H_{298.15\,K}$ (J/mol)	$S_{298.15\,K}$ (J/mol·K)	C_p[a] constants								Reference
				a	b	c	d	e	f	g	h	
$BaFe_2O_4$(s)	298.15 < T < 6000	-1453142.3	166.2	149.786	66.5006	-22.7682						Bale et al.[e,43]
	6000 < T < 6001			548.72636								
$BaFe_{12}O_{19}$(s)	298.15 < T < 6000	-5578071.9	637.5529	1030.2544	-174.75556	-294.11018	72082.92					"
	6000 < T < 6001			2575.8892								
$Ba_2Fe_2O_5$(s)	298.15 < T < 6000	-2062197.5	222.7464	302.01658	-100.57268	-75.20816	48151.68					"
	6000 < T < 6001			1431.8321								
$Ba_2Fe_6O_{11}$(s)	298.15 < T < 6000	-3749875	413.0252	612.71755	-135.61578	-162.08784	62697.12					"
	6000 < T < 6001			2055.6689								
$Ba_7Fe_4O_{13}$(s)	298.15 < T < 6000	-5896630.8	597.5824	817.03455	-317.03746	-191.8279	154889.46					"
	6000 < T < 6001			4490.2975								
$CsAlTiO_4$(s)	298.15 < T < 500	-2072500	190	40.437623132	142.1381254	-104.3200452	-44295.7297773	2566.4436429	7.99935874227	4317.06172	-771.917578	This work
	500 < T < 1166			42.801228326	138.3531592	-85.14951962	-44295.7297773	2566.4436429	7.99935874227	-2850.41894	-771.917578	
	1166 < T < 1200			210.408714902	-6.0495792	-67.35682022	15697.2870444		7.99935874227	-2850.41894	-771.917578	
	1200 < T < 1939			196.234896884	-6.0495792	-67.35682022			8.05881344576			
	1939 < T < 2130			184.426242784		-67.35682022			8.05881344576			
	2130 < T < 3000			229.583								
$Cs_2AlGaTi_2O_8$(s)	298.15 < T < 500	-3889000	379.729	21.692077477	322.3278203	-230.57227864	-104288.7465989	5132.8872858	16.05817218803	27175.1138217	-771.91757787	"
	500 < T < 1166			68.053340206	276.7063184	-170.29903924	-104288.7465989	5132.8872858	16.05817218803	-2850.4189384	-771.91757787	
	1166 < T < 1200			403.268313358	-12.0991584	-134.71364044	15697.28704439		16.05817218803	-2850.4189384	-771.91757787	
	1200 < T < 1939			389.09449534	-12.0991584	-134.71364044			16.11762689152			
	1939 < T < 2130			365.47718714		-134.71364044			16.11762689152			
	2130 < T < 3000			455.790701572								

[a] $C_p\ (\mathrm{J \cdot mol^{-1} \cdot K^{-1}}) = a + b \cdot 10^{-3} T + c \cdot 10^{5} T^{-2} + d \cdot 10^{-9} T^{2} + e \cdot T^{-0.5} + f \cdot 10^{8} T^{-3} + g \cdot T^{3} + h \cdot 10^{-3} T^{0.5}$

[b] Obtained from FTOxid FactSage 7.2[43] database

[c] Obtained from SGPS FactSage 7.2[43] database

[d] Obtained from FactPS FactSage 7.2[43] database

[e] Obtained from TDnucl FactSage 7.2[43] database

Table 7.3. Model parameters for solid solutions and oxide melt (all ^oG and L parameter units are J/mol)

Hollandite $(Ba^{+2},Cs^{+1},Va)_2[Ti^{+4},Cr^{+3},Al^{+3},Fe^{+3},Fe^{+2},Ga^{+3}]_4\{Ti^{+4}\}\langle O^{-2}\rangle_{16}$

$^oG_{Ba_2Ti_8O_{16}^{+4}} = 2^oG_{BaO(s)} + 8^oG_{TiO_2(s)} + 6^oG_{Ti_2O_3(s)} - 4^oG_{Ti_3O_5(s)} - 320000$

$^oG_{Cs_2Ti_8O_{16}^{+2}} = {}^oG_{Cs_2O(s)} + 8^oG_{TiO_2(s)} + 3^oG_{Ti_2O_3(s)} - 2^oG_{Ti_3O_5(s)} - 250000$

$^oG_{Ti_8O_{16}} = 8^oG_{TiO_2(s)} + 170000$

$^oG_{Ba_2Cr_4Ti_4O_{16}} = 2^oG_{BaO(s)} + 2^oG_{Cr_2O_3(s)} + 4^oG_{TiO_2(s)} - 390000 - 80T$

$^oG_{Cs_2Cr_4Ti_4O_{16}^{-2}} = {}^oG_{Cs_2O(s)} + 2\,{}^oG_{Cr_2O_3(s)} + 4\,{}^oG_{TiO_2(s)} + 2\,{}^oG_{Ti_3O_5(s)} - 3\,{}^oG_{Ti_2O_3(s)} - 120000 - 60T$

$^oG_{Cr_4Ti_4O_{16}^{-4}} = 2^oG_{Cr_2O_3(s)} + 4^oG_{TiO_2(s)} + 4^oG_{Ti_3O_5(s)} - 6^oG_{Ti_2O_3(s)} - 340000 + 30T$

$^oG_{Ba_2Al_4Ti_4O_{16}} = 2^oG_{BaO(s)} + 2^oG_{Al_2O_3(s)} + 4^oG_{TiO_2(s)} - 250000$

$^oG_{Cs_2Al_4Ti_4O_{16}^{-2}} = {}^oG_{Cs_2O(s)} + 2\,{}^oG_{Al_2O_3(s)} + 4\,{}^oG_{TiO_2(s)} + 2\,{}^oG_{Ti_3O_5(s)} - 3\,{}^oG_{Ti_2O_3(s)} - 250000 - 100T$

$^oG_{Al_4Ti_4O_{16}^{-4}} = 2^oG_{Al_2O_3(s)} + 4^oG_{TiO_2(s)} + 4^oG_{Ti_3O_5(s)} - 6^oG_{Ti_2O_3(s)} - 450000$

$^oG_{Ba_2Fe_4Ti_4O_{16}} = 2^oG_{BaO(s)} + 2^oG_{Fe_2O_3(s)} + 4^oG_{TiO_2(s)} - 520000 - 100T$

$^oG_{Cs_2Fe_4Ti_4O_{16}^{-2}} = {}^oG_{Cs_2O(s)} + 2^oG_{Fe_2O_3(s)} + 4^oG_{TiO_2(s)} + 2^oG_{Ti_3O_5(s)} - 3^oG_{Ti_2O_3(s)} - 290000$

$^oG_{Fe_4Ti_4O_{16}^{-4}} = 2^oG_{Fe_2O_3(s)} + 4^oG_{TiO_2(s)} + 4^oG_{Ti_3O_5(s)} - 6^oG_{Ti_2O_3(s)} - 550000 + 30T$

$^oG_{Ba_2Fe_4Ti_4O_{16}^{-4}} = 2\,{}^oG_{BaO(s)} + 4\,{}^oG_{FeO(s)} + 4\,{}^oG_{TiO_2(s)} + 4\,{}^oG_{Ti_3O_5(s)} - 6\,{}^oG_{Ti_2O_3(s)} - 620000 - 100T$

$^oG_{Cs_2Fe_4Ti_4O_{16}^{-6}} = {}^oG_{Cs_2O(s)} + 4\,{}^oG_{FeO(s)} + 4\,{}^oG_{TiO_2(s)} + 6\,{}^oG_{Ti_3O_5(s)} - 9\,{}^oG_{Ti_2O_3(s)} - 300000 + 100T$

$^oG_{Fe_4Ti_4O_{16}^{-8}} = 4^oG_{FeO(s)} + 4^oG_{TiO_2(s)} + 8^oG_{Ti_3O_5(s)} - 12^oG_{Ti_2O_3(s)} - 550000$

$^oG_{Ba_2Ga_4Ti_4O_{16}} = 2^oG_{BaO(s)} + 2^oG_{Ga_2O_3(s)} + 4^oG_{TiO_2(s)} - 290000$

$^oG_{Cs_2Ga_4Ti_4O_{16}^{-2}} = {}^oG_{Cs_2O(s)} + 2^oG_{Ga_2O_3(s)} + 4^oG_{TiO_2(s)} + 2^oG_{Ti_3O_5(s)} - 3^oG_{Ti_2O_3(s)} - 250000$

$^oG_{Ga_4Ti_4O_{16}^{-4}} = 2^oG_{Ga_2O_3(s)} + 4^oG_{TiO_2(s)} + 4^oG_{Ti_3O_5(s)} - 6^oG_{Ti_2O_3(s)} - 550000$

$^0L_{Cs^{+1},Va:Cr^{+3}:Ti^{+4}:O_2^{-2}} = -155000$

$^0L_{Cs^{+1},Va:Al^{+3}:Ti^{+4}:O_2^{-2}} = -350000$

$^0L_{Cs^{+1},Va:Fe^{+3}:Ti^{+4}:O_2^{-2}} = -100000$

$^0L_{Cs^{+1}:Cr^{+3},Fe^{+3}:Ti^{+4}:O_2^{-2}} = -150000$

$^0L_{Cs^{+1}:Al^{+3},Fe^{+3}:Ti^{+4}:O_2^{-2}} = 70000$

$^0L_{Ba^{+2}:Cr^{+3},Fe^{+2}:Ti^{+4}:O_2^{-2}} = -250000$

$BaTiO_3(\alpha)$ $(Ba^{+2},Va)_1[Ti^{+4}]_1\{O^{-2},Va\}_3$ (obtained from Lu & Jin[373])

$^oG_{BaTiO_3} = {}^oG_{BaTiO_3(\alpha)}$

$^oG_{BaTi^{+6}} = {}^oG_{BaTiO_3(\alpha)} + 3^oG_{TiO_2(s)} + 259032 + 47.6278T$

$^oG_{TiO_3^{-2}} = 0$

$^oG_{Ti^{+4}} = 3^oG_{TiO_2(s)} + 259032 + 47.6278T$

$BaTiO_3(\beta)$ $(Ba^{+2},Va)_1[Ti^{+4}]_1\{O^{-2},Va\}_3$ (obtained from Lu & Jin[373])

$^oG_{BaTiO_3} = {}^oG_{BaTiO_3(\beta)}$

$^oG_{BaTi^{+6}} = {}^oG_{BaTiO_3(\beta)} + 3^oG_{TiO_2(s)} + 259032 + 47.6278T$

$^oG_{TiO_3^{-2}} = 0$

$^oG_{Ti^{+4}} = 3^oG_{TiO_2(s)} + 434652 - 86.2622T$

Oxide liquid $(Cs^{+1},Ti^{+4})_P(O^{-2})_Q$

$^oG_{Cs^{+1}:O^{-2}} = {}^oG_{Cs_2O(\ell)}$

$^oG_{Ti^{+4}:O_2^{-2}} = 2^oG_{TiO_2(\ell)}$

$^0L_{Cs^{+1},Ti^{+4}:O_2^{-2}} = -30483.9 - 51.22T$

Table 7.4. Targeted, measured, and calculated hollandite phase compositions for specified waste types

Waste type	*T* (K)Targeted composition	Measured composition	Calculated composition[a]
Fe-SPH-1[37]	1473 $Ba_{1.0}Cs_{0.3}Fe_{2.3}Ti_{5.7}O_{16}$	$Ba_{1.0}Cs_{0.16}Fe_{2.4}Ti_{5.8}O_{15.9}$	$Ba_{1.04}Cs_{0.047}Fe_{1.74}Al_{0.357}Ti_{5.90}O_{16}$
Fe-SPHR[37]	1473 "	$Ba_{1.0}Cs_{0.14}Fe_{2.4}Ti_{5.7}O_{15.0}$	$Ba_{1.14}Cs_{0.105}Fe_{0.80}Al_{0.781}Ti_{6.42}O_{16}$
Fe-SPH-Ti[37]	1473 "	$Ba_{1.0}Cs_{0.24}Fe_{2.4}Ti_{5.6}O_{15.8}$	$Ba_{1.08}Cs_{0.027}Fe_{1.97}Al_{0.210}Ti_{5.83}O_{16}$
Cr-SPH-1[37]	1473 $Ba_{1.0}Cs_{0.3}Cr_{2.3}Ti_{5.7}O_{16}$	$Ba_{1.0}Cs_{0.14}Cr_{2.3}Ti_{5.8}O_{16.2}$	$Ba_{1.04}Cs_{0.153}Cr_{2.15}Al_{0.069}Fe_{0.013}Ti_{5.77}O_{16}$
Cr-SPHR[37]	1473 "	$Ba_{1.0}Cs_{0.19}Cr_{2.3}Ti_{5.8}O_{15.0}$	$Ba_{1.05}Cs_{0.145}Cr_{2.14}Al_{0.084}Fe_{0.014}Ti_{5.77}O_{16}$
Cr-SPH-Ti[37]	1473 "	$Ba_{1.0}Cs_{0.15}Cr_{2.4}Ti_{5.6}O_{16.1}$	$Ba_{0.981}Cs_{0.213}Cr_{2.05}Al_{0.092}Fe_{0.026}Ti_{5.83}O_{16}$
Cr-SPHR-Ti[37]	1473 "	$Ba_{1.0}Cs_{0.19}Cr_{2.4}Ti_{5.7}O_{14.9}$	$Ba_{1.01}Cs_{0.178}Cr_{2.06}Al_{0.116}Fe_{0.013}Ti_{5.81}O_{16}$
CAF-SPH-1[37]	1473 $Ba_{1.0}Cs_{0.3}Cr_{1.0}Al_{0.3}Fe_{1.0}Ti_{5.7}O_{16}$	$Ba_{1.0}Cs_{0.16}Cr_{1.0}Al_{0.3}Fe_{1.0}Ti_{5.8}O_{16.1}$	$Ba_{0.968}Cs_{0.150}Cr_{0.900}Al_{0.397}Fe_{0.761}Ti_{5.94}O_{16}$
CAF-SPHR[37]	1473 "	$Ba_{1.0}Cs_{0.15}Cr_{1.0}Al_{0.4}Fe_{1.0}Ti_{5.7}O_{15.6}$	$Ba_{1.06}Cs_{0.135}Cr_{1.27}Al_{0.471}Fe_{0.258}Ti_{6.00}O_{16}$
CAF-SPH-Ti[37]	1473 "	$Ba_{1.0}Cs_{0.16}Cr_{1.1}Al_{0.4}Fe_{1.0}Ti_{5.7}O_{16.1}$	$Ba_{0.893}Cs_{0.226}Cr_{0.775}Al_{0.411}Fe_{0.805}Ti_{6.01}O_{16}$
CAF-SPHR-Ti[37]	1473 "	$Ba_{1.0}Cs_{0.17}Cr_{0.9}Al_{0.6}Fe_{1.0}Ti_{5.7}O_{15.2}$	$Ba_{0.901}Cs_{0.153}Cr_{0.907}Al_{0.93}Fe_{0.059}Ti_{6.10}O_{16}$
Ga-SPH-1[30]	1523 $Ba_{1.33}Ga_{2.66}Ti_{5.34}O_{16}$	$Ba_{1.39}Ga_{2.6}Ti_{5.4}O_{16}$ $Ba_{1.3}Ga_{2.7}Ti_{5.3}O_{16.0}$	$Ba_{1.33}Ga_{2.66}Ti_{5.34}O_{16}$
Ga-SPH-2[30]	1523 $Ba_{1.04}Cs_{0.24}Ga_{2.32}Ti_{5.68}O_{16}$	$Ba_{1.09}Cs_{0.229}Ga_{2.6}Ti_{5.68}O_{16}$ $Ba_{1.1}Cs_{0.2}Ga_{2.4}Ti_{5.7}O_{16.0}$	$Ba_{1.04}Cs_{0.240}Ga_{2.32}Ti_{5.68}O_{16}$
Ga-SPH-3[30]	1523 $Ba_{0.667}Cs_{0.667}Ga_2Ti_6O_{16}$	$Ba_{0.77}Cs_{0.529}Ga_{2.06}Ti_6O_{16}$ $Ba_{0.7}Cs_{0.5}Ga_{2.1}Ti_{6.0}O_{16.1}$	$Ba_{0.667}Cs_{0.667}Ga_{2.00}Ti_{6.00}O_{16}$
Ga-SPH-4[30]	1523 $Cs_{1.33}Ga_{1.33}Ti_{6.67}O_{16}$	$Cs_{1.22}Ga_{1.44}Ti_{6.67}O_{16}$ $Cs_{1.2}Ga_{1.4}Ti_{6.6}O_{16.0}$	$Cs_{1.33}Ga_{1.33}Ti_{6.67}O_{16}$
Al-SPH-1[35]	1473 $Ba_{1.18}Cs_{0.21}Al_{2.44}Ti_{5.53}O_{16}$	$Ba_{1.18}Cs_{0.21}Al_{2.44}Ti_{5.53}O_{16}$	$Ba_{1.13}Cs_{0.213}Al_{2.47}Ti_{5.53}O_{16}$
Al-SPH-2[36]	1473 $Ba_{1.16}Al_{2.32}Ti_{5.68}O_{16}$	$Ba_{1.18}Al_{2.32}Ti_{5.67}O_{16}$	$Ba_{1.16}Al_{2.32}Ti_{5.68}O_{16}$
Cr-SPH-2[36]	1473 $Ba_{1.16}Cr_{2.32}Ti_{5.68}O_{16}$	$Ba_{1.16}Cr_{2.29}Ti_{5.70}O_{16}$	$Ba_{1.21}Cr_{2.42}Ti_{5.58}O_{16}$
Ga-SPH-5[36]	1473 $Ba_{1.16}Ga_{2.32}Ti_{5.68}O_{16}$	$Ba_{1.18}Ga_{2.30}Ti_{5.68}O_{16}$	$Ba_{1.16}Ga_{2.32}Ti_{5.68}O_{16}$
Fe-SPH-2[36]	1473 $Ba_{1.16}Fe_{2.32}Ti_{5.68}O_{16}$	$Ba_{1.13}Fe_{2.32}Ti_{5.70}O_{16}$	$Ba_{1.16}Fe_{2.32}Ti_{5.68}O_{16}$
AF-SPH-1[36]	1473 $Ba_{1.28}Al_{1.64}Fe_{0.92}Ti_{5.44}O_{16}$	$Ba_{1.29}Al_{1.71}Fe_{0.93}Ti_{5.38}O_{16}$	$Ba_{1.28}Al_{1.64}Fe_{0.920}Ti_{5.44}O_{16}$
AG-SPH-1[36]	1473 $Ba_{1.28}Al_{1.64}Ga_{0.92}Ti_{5.44}O_{16}$	$Ba_{1.29}Al_{1.65}Ga_{0.85}Ti_{5.48}O_{16}$	$Ba_{1.28}Al_{1.64}Ga_{0.920}Ti_{5.44}O_{16}$
Al-SPH-3[36]	1473 $Ba_{1.11}Cs_{0.10}Al_{2.32}Ti_{5.68}O_{16}$	$Ba_{1.17}Cs_{0.05}Al_{2.30}Ti_{5.67}O_{16}$ $Ba_{1.22}Cs_{0.01}Al_{2.49}Ti_{5.52}O_{16}$	$Ba_{1.11}Cs_{0.10}Al_{2.32}Ti_{5.68}O_{16}$
Cr-SPH-3[36]	1473 $Ba_{1.04}Cs_{0.24}Cr_{2.32}Ti_{5.68}O_{16}$	$Ba_{1.08}Cs_{0.11}Cr_{2.10}Ti_{5.86}O_{16}$ $Ba_{1.11}Cs_{0.06}Cr_{2.09}Ti_{5.86}O_{16}$	$Ba_{1.04}Cs_{0.240}Cr_{2.32}Ti_{5.68}O_{16}$
Ga-SPH-6[36]	1473 $Ba_{1.04}Cs_{0.24}Ga_{2.32}Ti_{5.68}O_{16}$	$Ba_{1.15}Cs_{0.15}Ga_{2.45}Ti_{5.55}O_{16}$	$Ba_{1.04}Cs_{0.240}Ga_{2.32}Ti_{5.68}O_{16}$
AG-SPH-2[36]	1473 $Ba_{1.00}Cs_{0.28}Al_{1.46}Ga_{0.82}Ti_{5.72}O_{16}$	$Ba_{1.05}Cs_{0.24}Al_{1.41}Ga_{0.76}Ti_{5.78}O_{16}$	$Ba_{1.03}Cs_{0.165}Al_{1.44}Ga_{0.784}Ti_{5.77}O_{16}$
Fe-SPH-3[36]	1473 $Ba_{1.04}Cs_{0.24}Fe_{2.32}Ti_{5.68}O_{16}$	$Ba_{1.06}Cs_{0.26}Fe_{2.28}Ti_{5.70}O_{16}$ $Ba_{1.10}Cs_{0.24}Fe_{2.35}Ti_{5.65}O_{16}$ $Ba_{0.97}Cs_{0.21}Fe_{2.23}Ti_{5.79}O_{16}$	$Ba_{1.04}Cs_{0.240}Fe_{2.32}Ti_{5.68}O_{16}$
AF-SPH-2[36]	1473 $Ba_{1.00}Cs_{0.28}Al_{1.46}Fe_{0.82}Ti_{5.72}O_{16}$	$Ba_{1.05}Cs_{0.25}Al_{1.43}Fe_{0.98}Ti_{5.74}O_{16}$ $Ba_{1.08}Cs_{0.21}Al_{1.45}Fe_{0.84}Ti_{5.69}O_{16}$ $Ba_{1.00}Cs_{0.28}Al_{1.44}Fe_{0.79}Ti_{5.76}O_{16}$	$Ba_{1.03}Cs_{0.153}Al_{1.37}Fe_{0.848}Ti_{5.78}O_{16}$
Al-SPH-4[361]	1523 $Ba_{1.24}Al_{2.48}Ti_{5.52}O_{16}$	$Ba_{1.3\pm0.07}Al_{2.4\pm0.1}Ti_{5.6\pm0.3}O_{16.0\pm0.3}$ $Ba_{1.259\pm0.004}Al_{2.24\pm0.04}Ti_{5.69\pm0.01}O_{16.01\pm0.04}$	$Ba_{1.24}Al_{2.48}Ti_{5.52}O_{16}$
Fe-SPH-4[361]	1523 $Ba_{1.24}Fe_{2.48}Ti_{5.52}O_{16}$	$Ba_{1.27\pm0.06}Fe_{2.4\pm0.1}Ti_{5.6\pm0.3}O_{16.0\pm0.3}$ $Ba_{1.236\pm0.003}Fe_{2.42\pm0.01}Ti_{5.57\pm0.02}O_{16.00\pm0.02}$	$Ba_{1.24}Fe_{2.48}Ti_{5.52}O_{16}$

[a] Compositions computed at 1 atm

Table 7.5. Calculated secondary phase amounts as well as experimentally observed secondary phases that were stable for each waste type

Waste Type[a]	Phase mass fraction[b] (%)								Experimentally observed secondary phases
	TiO_2(s)	$FeAl_2O_4$(s)	$CsAlTiO_4$(s)	$Cs_2AlGaTi_2O_8$(s)	$FeTi_2O_5$(s)	$BaTiO_3$(β)	Al_2O_3(corundum)	Cr_2O_3(s)	
Fe-SPH-1[37]	13.5	10.1	2.66	0	0	0	0.559	0	$Fe_2Ti_3O_9$, $Fe_3Ti_3O_{10}$, $CsAlTiO_4$
Fe-SPHR[37]	0	14.8	1.16	0	18.4	0	0	0	$BaFe_{12}O_{19}$, $Fe_3Ti_3O_{10}$, $CsAlTiO_4$, $FeAl_2O_4$
Fe-SPH-Ti[37]	22.2	5.90	3.96	0	0	0	11.8	0	$Fe_3Ti_3O_{10}$, $CsAlTiO_4$
Cr-SPH-1[37]	16.6	0	0	0	0	0	0	2.00	TiO_2(s)
Cr-SPHR[37]	16.2	0	0	0	0	0	0	2.42	"
Cr-SPH-Ti[37]	23.7	0	0	0	0	0	0	1.62	"
Cr-SPHR-Ti[37]	25.2	0	0	0	0	0	0	2.11	"
CAF-SPH-1[37]	10.4	3.74	0	0	0	0	0.202	1.02	Fe_2TiO_4
CAF-SPHR[37]	13.2	11.4	0	0	0	0	0	0	Fe_2TiO_4, $FeAl_2O_4$, $BaFe_{12}O_{19}$, $CsAlTiO_4$
CAF-SPH-Ti[37]	19.1	1.48	0	0	0	0	0	1.60	TiO_2, $CsAlTiO_4$
CAF-SPHR-Ti[37]	14.2	13.0	0	0	0	0	0.674	0	Fe_2TiO_4, $CsAlTiO_4$
Ga-SPH-1[30]	0	0	0	0	0	0	0	0	None detected
Ga-SPH-2[30]	0	0	0	0	0	0	0	0	"
Ga-SPH-3[30]	0	0	0	0	0	0.014	0	0	"
Ga-SPH-4[30]	0	0	0	0	0	0	0	0	Ti-rich phase
Al-SPH-1[35]	0	0	0	0	0	1.96	0	0	None detected
Al-SPH-2[36]	0	0	0	0	0	0	0	0	"
Cr-SPH-2[36]	3.27	0	0	0	0	0	0	0	"
Ga-SPH-5[36]	0	0	0	0	0	0	0	0	"
Fe-SPH-2[36]	0	0	0	0	0	0	0	0	"
AF-SPH-1[36]	0	0	0	0	0	0	0	0	"
AG-SPH-1[36]	0	0	0	0	0	0	0	0	"
Al-SPH-3[36]	0	0	0	0	0	0	0	0	TiO_2, $Ba_2Ti_9O_{20}$
Cr-SPH-3[36]	0	0	0	0	0	0	0	0	None detected
Ga-SPH-6[36]	0	0	0	0	0	0	0	0	$CsGaSi_{0.4}Ti_{0.6}O_4$
AG-SPH-2[36]	0	0	0	4.37	0	0	0	0	$CsAl_{0.5}Ga_{0.5}TiO_4$
Fe-SPH-3[36]	0	0	0	0	0	0	0	0	Fe_2TiO_5, $BaTi_4O_9$
AF-SPH-2[36]	0	0	4.56	0	0	0	0	0	Phases containing Y, Zr, Cs, Si, Al, O
Al-SPH-4[361]	0	0	0	0	0	0	0	0	None detected
Fe-SPH-4[361]	0	0	0	0	0	0	0	0	None detected

[a] Waste types correspond with compositions listed in Table S1

[b] Remaining mass fraction for each waste type consists of the hollandite phase such that the total mass fraction sums to 100%.

Table 7.6. Hollandite phase standard enthalpies of formation from constituent elements

Waste type	Measured/determined using DFT			Calculated from database	
	Phase	$\Delta H_{298.15\ K,ox}$[a] (J/mol)	$\Delta H_{298.15\ K,el}$[b] (J/mol)	Phase	$\Delta H_{298.15\ K,el}$ (J/mol)
Al-SPH-DS-1[361c]	$Ba_{1.24}Al_{2.48}Ti_{5.52}O_{16}$	$-207800 \pm 5.7 \cdot 10^3$	–8176197	$Ba_{1.23}Al_{2.46}Ti_{5.54}O_{16}$	–8217750
Fe-SPH-DS-1[361]	$Ba_{1.24}Fe_{2.48}Ti_{5.52}O_{16}$	$-223500 \pm 9.1 \cdot 10^3$	–7298310	$Ba_{1.24}Fe_{2.48}Ti_{5.52}O_{16}$	–7293915
Al-SPH-DS-2[35]	$Ba_{1.18}Cs_{0.21}Al_{2.44}Ti_{5.53}O_{16}$	$-212000 \pm 12.6 \cdot 10^3$	–8159809	$Ba_{1.07}Cs_{0.220}Al_{2.37}Ti_{5.63}O_{16}$	–8182266
Al-SPH-DFT-1[39d]	$Ba_{1.33}Al_{2.67}Ti_{5.33}O_{16}$	–228796	–8226354	$Ba_{1.23}Al_{2.46}Ti_{5.54}O_{16}$	–8217750
Al-SPH-DFT-2[39]	$Ba_1Cs_{0.33}Al_{2.33}Ti_{5.67}O_{16}$	–235183	–8145114	$Ba_{0.995}Cs_{0.331}Al_{2.32}Ti_{5.68}O_{16}$	–8164211
Al-SPH-DFT-3[39]	$Ba_{0.670}Cs_{0.67}Al_2Ti_6O_{16}$	–236754	–8059728	$Ba_{0.665}Cs_{0.670}Al_{2.0}Ti_{6.0}O_{16}$	–8065136
Al-SPH-DFT-4[39]	$Ba_{0.33}Cs_1Al_{1.67}Ti_{6.33}O_{16}$	–242513	–7971317	$Ba_{0.330}Cs_{1.0}Al_{1.66}Ti_{6.34}O_{16}$	–7956986
Al-SPH-DFT-5[39]	$Cs_{1.33}Al_{1.33}Ti_{6.67}O_{16}$	–255602	–7896779	$Cs_{1.34}Al_{1.34}Ti_{6.66}O_{16}$	–7848655
Ga-SPH-DFT-1[39]	$Ba_{1.33}Ga_{2.67}Ti_{5.33}O_{16}$	–208377	–7425360	$Ba_{1.33}Ga_{2.66}Ti_{5.34}O_{16}$	–7523784
Ga-SPH-DFT-2[39]	$Ba_1Cs_{0.33}Ga_{2.33}Ti_{5.67}O_{16}$	–216126	–7444881	$Ba_{1.0}Cs_{0.330}Ga_{2.33}Ti_{5.67}O_{16}$	–7504888
Ga-SPH-DFT-3[39]	$Ba_{0.67}Cs_{0.67}Ga_2Ti_6O_{16}$	–227225	–7465499	$Ba_{0.665}Cs_{0.670}Ga_{2.0}Ti_{6.0}O_{16}$	–7483853
Ga-SPH-DFT-4[39]	$Ba_{0.33}Cs_1Ga_{1.67}Ti_{6.33}O_{16}$	–238743	–7479323	$Ba_{0.330}Cs_{1.0}Ga_{1.66}Ti_{6.34}O_{16}$	–7463380
Ga-SPH-DFT-5[39]	$Cs_{1.33}Ga_{1.33}Ti_{6.67}O_{16}$	–247330	–7499681	$Cs_{1.34}Ga_{1.34}Ti_{6.66}O_{16}$	–7441511
Cr-SPH-BASE-1[e]	-	-	-	$Ba_{1.33}Cr_{2.66}Ti_{5.34}O_{16}$	–7587448
Cr-SPH-BASE-2	-	-	-	$Ba_{1.0}Cs_{0.330}Cr_{2.33}Ti_{5.67}O_{16}$	–7543319
Cr-SPH-BASE-3	-	-	-	$Ba_{0.667}Cs_{0.672}Cr_{2.01}Ti_{5.99}O_{16}$	–7501921
Cr-SPH-BASE-4	-	-	-	$Ba_{0.330}Cs_{1.0}Cr_{1.66}Ti_{6.34}O_{16}$	–7466041
Cr-SPH-BASE-5	-	-	-	$Cs_{1.38}Cr_{1.38}Ti_{6.62}O_{16}$	–7430217
Fe-SPH-BASE-1[e]	-	-	-	$Ba_{1.33}Fe_{2.66}Ti_{5.34}O_{16}$	–7271530
Fe-SPH-BASE-2	-	-	-	$Ba_{1.0}Cs_{0.330}Fe_{2.33}Ti_{5.67}O_{16}$	–7269052
Fe-SPH-BASE-3	-	-	-	$Ba_{0.667}Cs_{0.672}Fe_{2.01}Ti_{5.99}O_{16}$	–7267548
Fe-SPH-BASE-4	-	-	-	$Ba_{0.330}Cs_{1.0}Fe_{1.66}Ti_{6.34}O_{16}$	–7273386
Fe-SPH-BASE-5	-	-	-	$Cs_{1.35}Fe_{1.35}Ti_{6.65}O_{16}$	–7277723

[a] Formation of hollandite from constituent oxides
[b] Formation of hollandite from constituent elements
[c] Determined from drop solution (DS) calorimetry
[d] Determined from DFT
[e] Determined from thermodynamic database

Table 7.7. Stable phases displayed in the isothermal BaO-Cs_2O-TiO_2 diagram with Cr, Al, and Fe additives (Fig. 7.4)

Region	Stable phases[a]	Region	Stable phases
1	H + AF + A + BT2 + C2 + BT1	22	H + AF + A + C1 + FT4 + T
2	H + AF + A + C2 + BT1	23	H + AF + C1 + FT3 + FT4 + T
3	H + A + C2 + BT1	24	H + C1 + FT3 + FT4 + T
4	H + C2 + BT1	25	H + FT1 + C1
5	H + BT5 + C2 + BT1	26	H + FT1 + C1 + C2
6	H + BT5 + C2	27	H + FT1 + C2
7	H + BT4 + BT5 + C2	28	H + FT2 + C1 + C2
8	H + BT4 + C2	29	H + FT2 + C2
9	H + BT3 + BT4 + C2	30	H + C2 + F1
10	H + AF + C2	31	H + C2 + L + F1
11	H + AF + FT3	32	H + C2 + L
12	H + BT3 + C2 + T	33	H + C1 + C2 + F2 + L + F1
13	H + AF + A + T	34	H + C1 + C2 + L + F1
14	H + AF + C2 + FT3	35	H + C1 + C2 + L
15	H + C2 + FT3	36	H + C2 + BT1 + L
16	H + AF + C1 + FT3	37	H + C2 + BT1 + L + F1
17	H + AF + FT3 + T	38	H + BT2 + C2 + BT1 + L + F1
18	H + C1 + FT3	39	H + BT2 + C2 + L + F1
19	H + C1 + FT3 + T	40	H + BT2 + C1 + C2 + L + F1
20	H + AF + C1 + FT3 + T	41	H + BF + BT2 + C1 + C2 + L + F1
21	H + AF + A + C1 + T		

[a] Stable phases: H = Hollandite, A = Al_2O_3(corundum), AF = $FeAl_2O_4$, BF = $Ba_2Fe_2O_5$, BT1 = $BaTiO_3(\alpha)$, BT2 = Ba_2TiO_4, BT3 = $Ba_2Ti_9O_{20}$, BT4 = $Ba_4Ti_{13}O_{30}$, BT5 = $Ba_6Ti_{17}O_{40}$, C1 = Cr_2O_3, C2 = $CsAlTiO_4$, F1 = FeO, F2 = Fe_2O_3, FT1 = $FeTiO_3$, FT2 = Fe_2TiO_4, FT3 = $FeTi_2O_5$, FT4 = Fe_2TiO_5, T = TiO_2, L = Liquid

Table 7.8. Stable phases and amounts of ✳ and ◓ symbols located in Fig. 7.4

Symbol	Stable phase	Amount (g)
✳	Hollandite ($Ba_{0.892}Cs_{0.230}Cr_{0.786}Al_{0.573}Fe_{0.608}Ti_{6.03}O_{16}$)	93.8
	$FeTi_2O_5$	2.62
	$FeAl_2O_4$	0.723
◓	Hollandite ($Ba_{0.143}Cs_{1.25}Cr_{0.295}Al_{0.659}Fe_{0.577}Ti_{6.47}O_{16}$)	94.7
	Cr_2O_3	4.52
	$FeTi_2O_5$	3.17

7.10. Figures

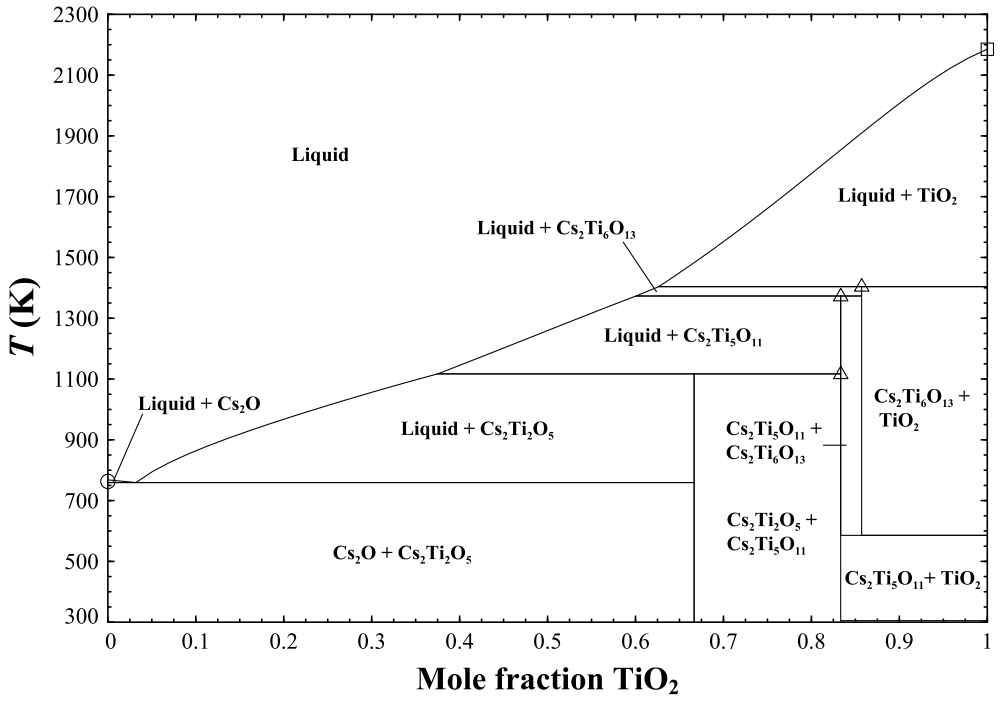

Fig. 7.1. Computed Cs_2O-TiO_2 pseudo-binary phase diagram with experimental measurements shown as points. Data: ◯[375] □[373] △[367]

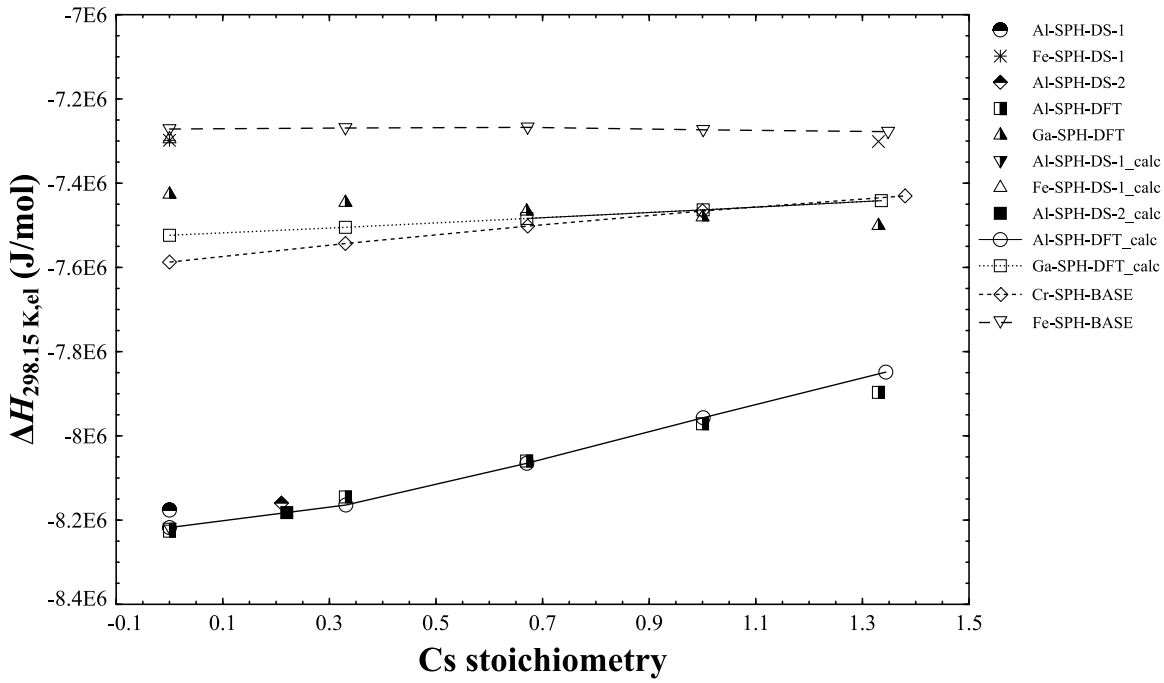

Fig. 7.2. Computed hollandite standard enthalpies of formation from constituent elements compared with experimental and DFT derived values. Legend corresponds to Table 7.3 in which labels with '_calc' indicate values computed from the thermodynamic database.

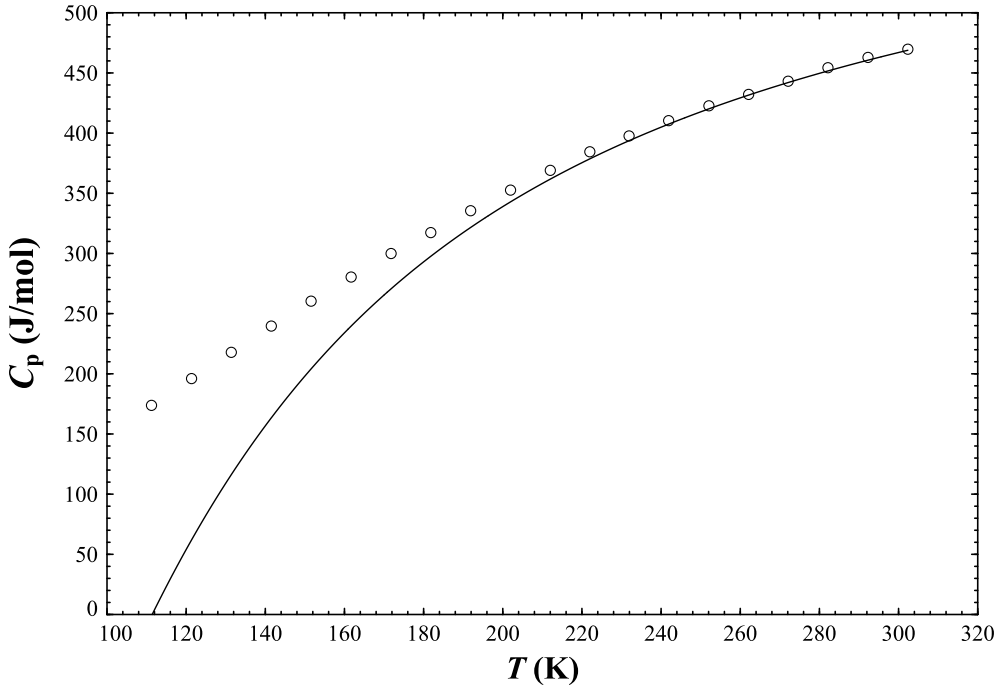

Fig. 7.3. Computed heat capacity of $Ba_{1.07}Cs_{0.221}Al_{2.36}Ti_{5.64}O_{16}$ hollandite at 1.2 mPa with experimental measurements for the $Ba_{1.18}Cs_{0.21}Al_{2.44}Ti_{5.53}O_{16}$ hollandite shown as points. Data: ◯[377]

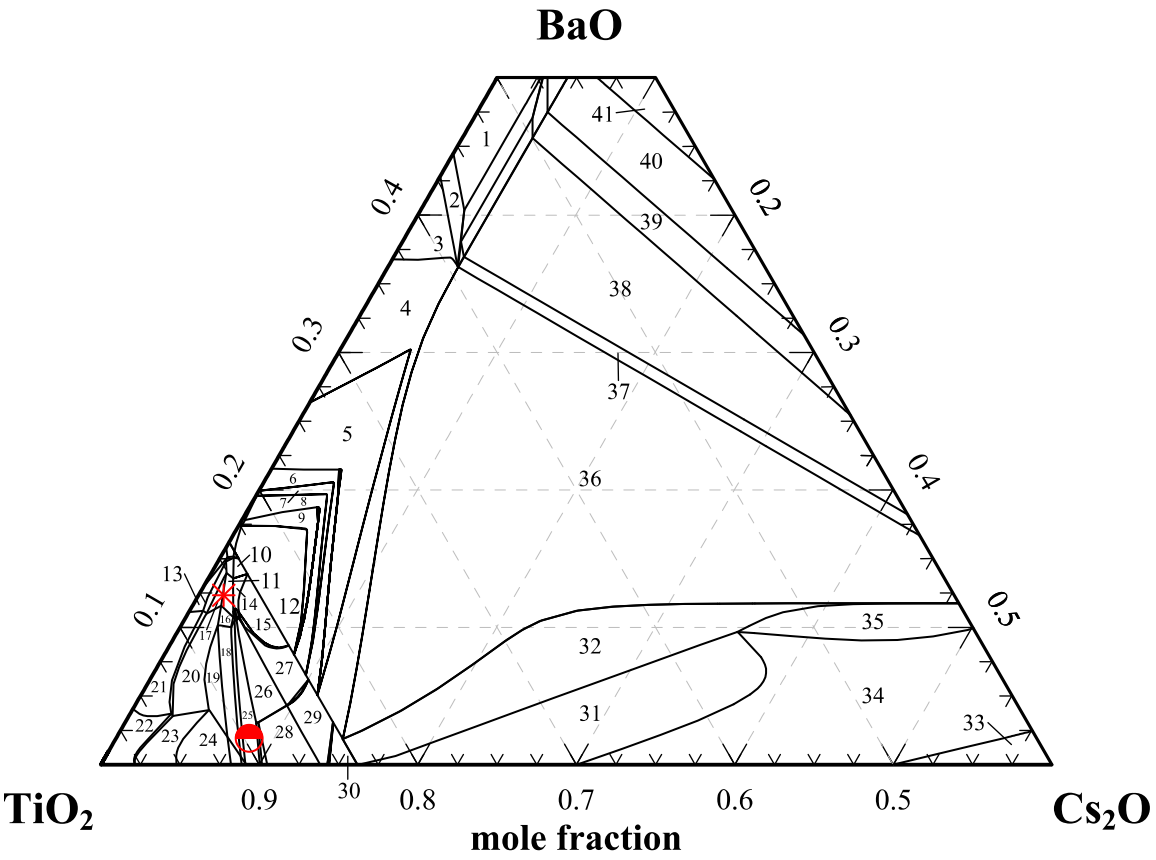

Fig. 7.4. Computed 1473 K isothermal diagram of pseudo-ternary BaO-Cs_2O-TiO_2 system with oxides of Cr, Al, and Fe additives in CAF-SPH-1 quantities. Numbered phase regions are defined in Table 7.7.

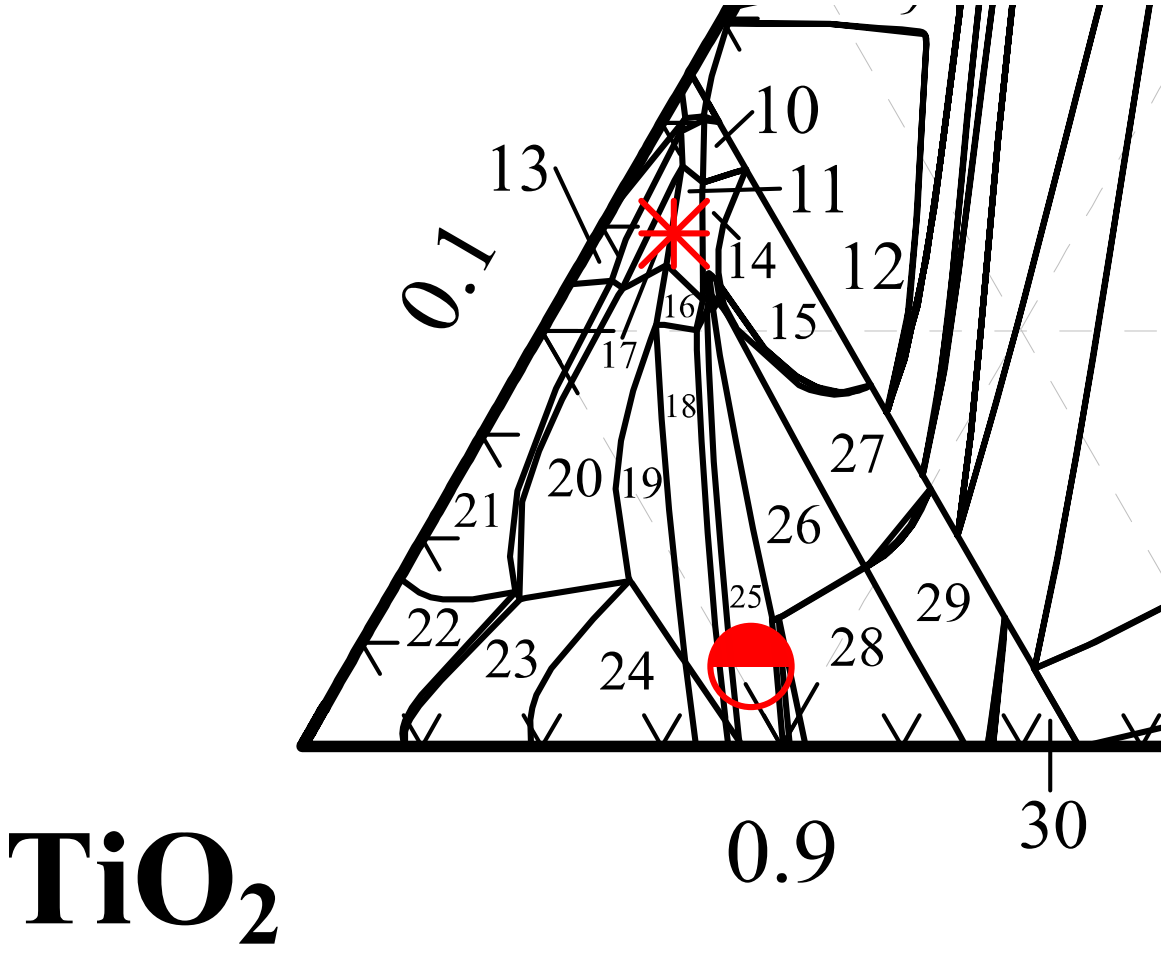

Fig. 7.5. Expanded section of 1473 K of pseudo-ternary BaO-Cs_2O-TiO_2 isothermal diagram of Fig. 7.4

7.11. Copyright permission

JOHN WILEY AND SONS LICENSE TERMS AND CONDITIONS

Apr 13, 2019

This Agreement between University of South Carolina -- Stephen Utlak ("You") and John Wiley and Sons ("John Wiley and Sons") consists of your license details and the terms and conditions provided by John Wiley and Sons and Copyright Clearance Center.

License Number	4567140391627
License date	Apr 13, 2019
Licensed Content Publisher	John Wiley and Sons
Licensed Content Publication	Journal of the American Ceramic Society
Licensed Content Title	Thermodynamic assessment of the hollandite high-level radioactive waste form
Licensed Content Date	Apr 12, 2019
Licensed Content Pages	14
Type of use	Dissertation/Thesis
Requestor type	Author of this Wiley article
Format	Print and electronic
Portion	Full article
Will you be translating?	No
Title of your thesis / dissertation	Modeling complex oxides: Thermochemical behavior of nepheline-forming Na-Al-Si-B-K-Li-Ca-Mg-Fe-O and hollandite-forming Ba-Cs-Ti-Cr-Al-Fe-Ga-O systems
Expected completion date	Apr 2019
Expected size (number of pages)	275
Requestor Location	University of South Carolina
	Attn: University of South Carolina
Publisher Tax ID	EU826007151
Total	0.00 USD
Terms and Conditions	

TERMS AND CONDITIONS

This copyrighted material is owned by or exclusively licensed to John Wiley & Sons, Inc. or one of its group companies (each a"Wiley Company") or handled on behalf of a society with which a Wiley Company has exclusive publishing rights in relation to a particular work (collectively "WILEY"). By clicking "accept" in connection with completing this licensing transaction, you agree that the following terms and conditions apply to this transaction (along with the billing and payment terms and conditions established by the Copyright Clearance Center Inc., ("CCC's Billing and Payment terms and conditions"), at the time that you opened your RightsLink account (these are available at any time at http://myaccount.copyright.com).

Terms and Conditions

- The materials you have requested permission to reproduce or reuse (the "Wiley Materials") are protected by copyright.

- You are hereby granted a personal, non-exclusive, non-sub licensable (on a stand-alone basis), non-transferable, worldwide, limited license to reproduce the Wiley Materials for the purpose specified in the licensing process. This license, **and any CONTENT (PDF or image file) purchased as part of your order,** is for a one-time use only and limited to any maximum distribution number specified in the license. The first instance of republication or reuse granted by this license must be completed within two years of the date of the grant of this license (although copies prepared before the end date may be distributed thereafter). The Wiley Materials shall not be used in any other manner or for any other purpose, beyond what is granted in the license. Permission is granted subject to an appropriate acknowledgement given to the author, title of the material/book/journal and the publisher. You shall also duplicate the copyright notice that appears in the Wiley publication in your use of the Wiley Material. Permission is also granted on the understanding that nowhere in the text is a previously published source acknowledged for all or part of this Wiley Material. Any third party content is expressly excluded from this permission.

- With respect to the Wiley Materials, all rights are reserved. Except as expressly granted by the terms of the license, no part of the Wiley Materials may be copied, modified, adapted (except for minor reformatting required by the new Publication), translated, reproduced, transferred or distributed, in any form or by any means, and no derivative works may be made based on the Wiley Materials without the prior permission of the respective copyright owner.**For STM Signatory Publishers clearing permission under the terms of the STM Permissions Guidelines only, the terms of the license are extended to include subsequent editions and for editions in other languages, provided such editions are for the work as a whole in situ and does not involve the separate exploitation of the permitted figures or extracts,** You may not alter, remove or suppress in any manner any copyright, trademark or other notices displayed by the Wiley Materials. You may not license, rent, sell, loan, lease, pledge, offer as security, transfer or assign the Wiley Materials on a stand-alone basis, or any of the rights granted to you hereunder to any other person.

- The Wiley Materials and all of the intellectual property rights therein shall at all times remain the exclusive property of John Wiley & Sons Inc, the Wiley Companies, or their respective licensors, and your interest therein is only that of having possession of and the right to reproduce the Wiley Materials pursuant to Section 2 herein during the continuance of this Agreement. You agree that you own no right, title or interest in or to the Wiley Materials or any of the intellectual property rights therein. You shall have no rights hereunder other than the license as provided for above in Section 2. No right, license or interest to any trademark, trade name, service mark or other branding ("Marks") of WILEY or its licensors is granted hereunder, and you agree that you shall not assert any such right, license or interest with respect thereto

- NEITHER WILEY NOR ITS LICENSORS MAKES ANY WARRANTY OR REPRESENTATION OF ANY KIND TO YOU OR ANY THIRD PARTY, EXPRESS, IMPLIED OR STATUTORY, WITH RESPECT TO THE MATERIALS OR THE ACCURACY OF ANY INFORMATION CONTAINED IN THE MATERIALS, INCLUDING, WITHOUT LIMITATION, ANY IMPLIED WARRANTY OF MERCHANTABILITY, ACCURACY, SATISFACTORY

QUALITY, FITNESS FOR A PARTICULAR PURPOSE, USABILITY, INTEGRATION OR NON-INFRINGEMENT AND ALL SUCH WARRANTIES ARE HEREBY EXCLUDED BY WILEY AND ITS LICENSORS AND WAIVED BY YOU.

- WILEY shall have the right to terminate this Agreement immediately upon breach of this Agreement by you.

- You shall indemnify, defend and hold harmless WILEY, its Licensors and their respective directors, officers, agents and employees, from and against any actual or threatened claims, demands, causes of action or proceedings arising from any breach of this Agreement by you.

- IN NO EVENT SHALL WILEY OR ITS LICENSORS BE LIABLE TO YOU OR ANY OTHER PARTY OR ANY OTHER PERSON OR ENTITY FOR ANY SPECIAL, CONSEQUENTIAL, INCIDENTAL, INDIRECT, EXEMPLARY OR PUNITIVE DAMAGES, HOWEVER CAUSED, ARISING OUT OF OR IN CONNECTION WITH THE DOWNLOADING, PROVISIONING, VIEWING OR USE OF THE MATERIALS REGARDLESS OF THE FORM OF ACTION, WHETHER FOR BREACH OF CONTRACT, BREACH OF WARRANTY, TORT, NEGLIGENCE, INFRINGEMENT OR OTHERWISE (INCLUDING, WITHOUT LIMITATION, DAMAGES BASED ON LOSS OF PROFITS, DATA, FILES, USE, BUSINESS OPPORTUNITY OR CLAIMS OF THIRD PARTIES), AND WHETHER OR NOT THE PARTY HAS BEEN ADVISED OF THE POSSIBILITY OF SUCH DAMAGES. THIS LIMITATION SHALL APPLY NOTWITHSTANDING ANY FAILURE OF ESSENTIAL PURPOSE OF ANY LIMITED REMEDY PROVIDED HEREIN.

- Should any provision of this Agreement be held by a court of competent jurisdiction to be illegal, invalid, or unenforceable, that provision shall be deemed amended to achieve as nearly as possible the same economic effect as the original provision, and the legality, validity and enforceability of the remaining provisions of this Agreement shall not be affected or impaired thereby.

- The failure of either party to enforce any term or condition of this Agreement shall not constitute a waiver of either party's right to enforce each and every term and condition of this Agreement. No breach under this agreement shall be deemed waived or excused by either party unless such waiver or consent is in writing signed by the party granting such waiver or consent. The waiver by or consent of a party to a breach of any provision of this Agreement shall not operate or be construed as a waiver of or consent to any other or subsequent breach by such other party.

- This Agreement may not be assigned (including by operation of law or otherwise) by you without WILEY's prior written consent.

- Any fee required for this permission shall be non-refundable after thirty (30) days from receipt by the CCC.

- These terms and conditions together with CCC's Billing and Payment terms and conditions (which are incorporated herein) form the entire agreement between you and WILEY concerning this licensing transaction and (in the absence of fraud) supersedes all prior agreements and representations of the parties, oral or written. This Agreement may not be amended except in writing signed by both parties. This Agreement shall be binding upon and inure to the benefit of the parties' successors, legal representatives,

and authorized assigns.

- In the event of any conflict between your obligations established by these terms and conditions and those established by CCC's Billing and Payment terms and conditions, these terms and conditions shall prevail.

- WILEY expressly reserves all rights not specifically granted in the combination of (i) the license details provided by you and accepted in the course of this licensing transaction, (ii) these terms and conditions and (iii) CCC's Billing and Payment terms and conditions.

- This Agreement will be void if the Type of Use, Format, Circulation, or Requestor Type was misrepresented during the licensing process.

- This Agreement shall be governed by and construed in accordance with the laws of the State of New York, USA, without regards to such state's conflict of law rules. Any legal action, suit or proceeding arising out of or relating to these Terms and Conditions or the breach thereof shall be instituted in a court of competent jurisdiction in New York County in the State of New York in the United States of America and each party hereby consents and submits to the personal jurisdiction of such court, waives any objection to venue in such court and consents to service of process by registered or certified mail, return receipt requested, at the last known address of such party.

WILEY OPEN ACCESS TERMS AND CONDITIONS

Wiley Publishes Open Access Articles in fully Open Access Journals and in Subscription journals offering Online Open. Although most of the fully Open Access journals publish open access articles under the terms of the Creative Commons Attribution (CC BY) License only, the subscription journals and a few of the Open Access Journals offer a choice of Creative Commons Licenses. The license type is clearly identified on the article.

The Creative Commons Attribution License

The Creative Commons Attribution License (CC-BY) allows users to copy, distribute and transmit an article, adapt the article and make commercial use of the article. The CC-BY license permits commercial and non-

Creative Commons Attribution Non-Commercial License

The Creative Commons Attribution Non-Commercial (CC-BY-NC)License permits use, distribution and reproduction in any medium, provided the original work is properly cited and is not used for commercial purposes.(see below)

Creative Commons Attribution-Non-Commercial-NoDerivs License

The Creative Commons Attribution Non-Commercial-NoDerivs License (CC-BY-NC-ND) permits use, distribution and reproduction in any medium, provided the original work is properly cited, is not used for commercial purposes and no modifications or adaptations are made. (see below)

Use by commercial "for-profit" organizations

Use of Wiley Open Access articles for commercial, promotional, or marketing purposes requires further explicit permission from Wiley and will be subject to a fee.

Further details can be found on Wiley Online Library

http://olabout.wiley.com/WileyCDA/Section/id-410895.html

Other Terms and Conditions:

References

1. Li H., Hrma P., Vienna J. D., et al., Effects of Al_2O_3, B_2O_3, Na_2O, and SiO_2 on nepheline formation in borosilicate glasses: chemical and physical correlations. *J. Non-Cryst. Solids.* 2003*;*331:202-216.

2. Hrma P., Crystallization during processing of nuclear waste glass. *J. Non-Cryst. Solids.* 2010*;*356:3019-3025.

3. Pierce E. M., Reed L. R., Shaw W. J., et al., Experimental determination of the effect of the ratio of B/Al on glass dissolution along the nepheline ($NaAlSiO_4$)-malinkoite ($NaBSiO_4$) join. *Geochim. Cosmochim. Ac.* 2010*;*74:2634-2654.

4. Fox K. M., Edwards T. B., Peeler D. K., Control of nepheline crystallization in nuclear waste glass. *Int. J. Appl. Ceram. Tec.* 2008*;*5:666-673.

5. McCloy J., Washton N., Gassman P., et al., Nepheline crystallization in boron-rich alumino-silicate glasses as investigated by multi-nuclear NMR, Raman, & Mossbauer spectroscopies. *J. Non-Cryst. Solids.* 2015*;*409:149-165.

6. Marcial J., Crum J., Neill O., et al., Nepheline structural and chemical dependence on melt composition. *Am. Mineral.* 2016*;*101:266-276.

7. Goel A., McCloy J. S., Fox K. M., et al., Structural analysis of some sodium and alumina rich high-level nuclear waste glasses. *J. Non-Cryst. Solids.* 2012*;*358:674-679.

8. Li H., Vienna J. D., Hrma P., et al., Nepheline precipitation in high-level waste glasses: Compositional effects and impact on the waste form acceptability. *Mater. Res. Soc. Symp. Proc.* 1997*;*465:261-268.

9. Panda S. K., Jung I. H., Critical evaluation and thermodynamic modeling of the Mg–Mn–O (MgO–MnO–MnO_2) system. *J. Am. Ceram. Soc.* 2014*;*97:3328-3340.

10. Boulay E., Nakano J., Turner S., et al., Critical assessments and thermodynamic modeling of BaO-SiO_2 and SiO_2-TiO_2 systems and their extensions into liquid immiscibility in the BaO-SiO_2-TiO_2 system. *Calphad-Comput. Coupling Ph. Diagrams Thermochem.* 2014*;*47:68-82.

11. Fabrichnaya O., Lakiza S., Wang C., et al., Assessment of thermodynamic functions in the ZrO_2-La_2O_3-Al_2O_3 system. *J. Alloy Compd.* 2008;453:271-281.

12. Hillert M., Some properties of the compound energy model. *Calphad-Comput. Coupling Ph. Diagrams Thermochem.* 1996;20:333-341.

13. Hillert M., Agren J., A comparison between the associate model and the two-sublattice model for melts. *Z. Metallkd.* 1986;77:794-797.

14. Duke D. A., Macdowell J. F., Karstetter B. R., Crystallization and chemical strengthening of nepheline glass-ceramics. *J. Am. Ceram. Soc.* 1967;50:67-74.

15. Palmer D. C., Stuffed derivatives of the silica polymorphs. *Rev. Mineral.* 1994;29:83-122.

16. Tait K. T., Sokolova E., Hawthorne F. C., et al., The crystal chemistry of nepheline. *Can. Mineral.* 2003;41:61-70.

17. Amoroso J. W., Nepheline nucleation and crystal growth in waste glasses: Interim report. SRNL-STI-2011-00549, Savannah River National Laboratory, Aiken, SC, 2011. 1-20.

18. Fox K. M., Edwards T. B., Refinement of the nepheline discriminator: Results of a phase II study. SRNS-STI-2008-00099, Savannah River National Laboratory, Aiken, SC, 2008. 1-110.

19. Fox K. M., Edwards T. B., Experimental results of the nepheline phase III study. SRNL-STI-2009-00608, Savannah River National Laboratory, Aiken, SC, 2009. 1-177.

20. Fox K. M., Edwards T. B., McClane D. L., Chemical composition analysis and product consistency tests supporting refinement of the nepheline model for the high aluminum Hanford glass composition region. SRNL-STI-2016-00028, Savannah River National Laboratory, Aiken, SC, 2016. 1-246.

21. Fox K. M., Edwards T. B., Peeler D. K., Nepheline formation potential in Sludge Batch 4 (SB4) and its impact on durability: Selecting glasses for a phase 3 study. WSRC-TR-2006-00053, Savannah River National Laboratory, Aiken, SC, 2006. 1-24.

22. Fox K. M., Edwards T. B., Peeler D. K., et al., Nepheline formation study for Sludge Batch 4 (SB4): Phase 3 experimental results. WSRC-TR-2006-00093, Savannah River National Laboratory, Aiken, SC, 2006. 1-182.

23. Fox K. M., Newell J. D., Edwards T. B., et al., Refinement of the nepheline discriminator: Results of a phase I study. WSRC-STI-2007-00659, Savannah River National Laboratory, Aiken, SC, 2007. 1-206.

24. Li H., Jones B., Hrma P., et al., Compositional effects on liquidus temperature of Hanford simulated high-level waste glasses precipitating nepheline ($NaAlSiO_4$). *Ceram. Trans.* 1998;87:279-288.

25. McCloy J. S., Schweiger M. J., Rodriguez C. P., et al., Nepheline crystallization in nuclear waste glasses: Progress toward acceptance of high-alumina formulations. *Int. J. Appl. Glass Sci.* 2011;2:201-214.

26. Lukas H., Fries S. G., Sundman B., Computational thermodynamics: The calphad method, 1sted. New York, NY: Cambridge University Press; 2007.

27. Crum J. V., Turo L. A., Riley B. J., et al., Multi-phase glass-ceramics as a waste form for combined fission products: Alkalis, alkaline earths, lanthanides, and transition metals. *J. Am. Ceram. Soc.* 2012;95:1297-1303.

28. Amoroso J., Marra J. C., Tang M., et al., Melt processed multiphase ceramic waste forms for nuclear waste immobilization. *J. Nucl. Mater.* 2014;454:12-21.

29. Ewing R. C., Long-term storage of spent nuclear fuel. *Nat. Mater.* 2015;14:252-257.

30. Xu Y., Wen Y., Grote R., et al., A-site compositional effects in Ga-doped hollandite materials of the form $Ba_xCs_yGa_{2x+y}Ti_{8-2x-y}O_{16}$: implications for Cs immobilization in crystalline ceramic waste forms. *Sci. Rep.-UK.* 2016;6:1-8.

31. Vance E. R., Chavara D. T., Gregg D. J., et al., Synroc development-Past and present applications. *MRS Energy & Sustainability.* 2017;4:8.

32. Ringwood A. E., Kesson S. E., Ware N. G., et al., Immobilization of high level nuclear reactor wastes in SYNROC. *Nature.* 1979;278:219-223.

33. Ringwood A. E., Kesson S. E., Ware N. G., et al., The SYNROC process: A geochemical approach to nuclear waste immobilization. *Geochem. J.* 1979;13:141-165.

34. Brinkman K. S., Amoroso J. W., Tang M., Crystalline ceramic waste forms: Comparison of reference process for ceramic waste form fabrication. SRNL-STI-2013-000229, Savannah River National Laboratory, Aiken, SC, 2013. 1-40.

35. Xu H., Wu L., Zhu J., et al., Synthesis, characterization and thermochemistry of Cs-, Rb- and Sr-substituted barium aluminium titanate hollandites. *J. Nucl. Mater.* 2015;459:70-76.

36. Aubin-Chevaldonnet V., Caurant D., Dannoux A., et al., Preparation and characterization of $(Ba,Cs)(M,Ti)_8O_{16}$ ($M = Al^{3+}$, Fe^{3+}, Ga^{3+}, Cr^{3+}, Sc^{3+}, Mg^{2+}) hollandite ceramics developed for radioactive cesium immobilization. *J. Nucl. Mater.* 2007;366:137-160.

37. Amoroso J., Marra J., Conradson S. D., et al., Melt processed single phase hollandite waste forms for nuclear waste immobilization: $Ba_{1.0}Cs_{0.3}A_{2.3}Ti_{5.7}O_{16}$; A = Cr, Fe, Al. *J. Alloy Compd.* 2014;584:590-599.

38. Dandeneau C. S., Hong T., Brinkman K. S., et al., Comparison of structure, morphology, and leach characteristics of multi-phase ceramics produced via melt processing and hot isostatic pressing. *J. Nucl. Mater.* 2018;502:113-122.

39. Wen Y., Xu Y., Brinkman K. S., et al., Atomistic scale investigation of cation ordering and phase stability in Cs-substituted $Ba_{1.33}Zn_{1.33}Ti_{6.67}O_{16}$, $Ba_{1.33}Ga_{2.66}Ti_{5.67}O_{16}$ and $Ba_{1.33}Al_{2.66}Ti_{5.33}O_{16}$ hollandite. *Sci. Rep.-UK.* 2018;8:1-11.

40. Xu Y., Feygenson M., Page K., et al., Structural Evolution in Hollandite Solid Solutions Across the A-Site Compositional Range from Ba1.33Ga2.66Ti5.34O16 to Cs1.33Ga1.33Ti6.67O16. *J. Am. Ceram. Soc.* 2016;99:4100-4106.

41. Hillert M., The compound energy formalism. *J. Alloy Compd.* 2001;320:161-176.

42. Hillert M., Jansson B., Sundman B., et al., A two-sublattice model for molten solutions with different tendency for ionization. *Metall. Trans. A.* 1985;16A:261-266.

43. Bale C. W., Bélisle E., Chartrand P., et al., FactSage thermochemical software and databases, 2010–2016. *CALPHAD.* 2016;54:35-53.

44. Menkhaus T. J., Hrma P., Li H., Kinetics of nepheline crystallization from high-level waste glass. *Ceram. Trans.* 2000;107:461-468.

45. Edwards T. B., Peeler D. K., Fox K. M., The nepheline discriminator: Justification and DWPF PCCS implementation details. WSRC-STI-2006-00014, Savannah River National Laboratory, Aiken, SC, 2006.

46. Vienna J. D., Fluegel A., Kim D. S., Glass property data and models for estimating high-level waste glass volume. PNNL-18501, Pacific Northwest National Laboratory, Richland, WA, 2009. 1-561.

47. Vienna J. D., Kroll J. O., Hrma P. R., et al., Submixture model to predict nepheline precipitation in waste glasses. *Int. J. Appl. Glass Sci.* 2017;8:143-157.

48. McHale A. E., Roth R. S., Phase equilibria diagrams, Vol. XII, oxides, Westerville, OH: American Ceramic Society; 1996.

49. Dollase W. A., Thomas W. M., The crystal chemistry of silica-rich, alkali-deficient nepheline. *Contrib. Mineral. Petr.* 1978;66:311-318.

50. Stebbins J. F., Murdoch J. B., Carmichael I. S. E., et al., Defects and short-range order in nepheline group minerals: A silicon-29 nuclear magnetic resonance study. *Phys. Chem. Miner.* 1986;13:371-381.

51. Vulic P., Balic-Zunic T., Belmonte L. J., et al., Crystal chemistry of nephelines from ijolites and nepheline-rich pegmatites: influence of composition and genesis on the crystal structure investigated by X-ray diffraction. *Miner. Petrol.* 2011;101:185-194.

52. Rossi G., Oberti R., Smith D. C., The crystal structure of a K-poor Ca-rich silicate with the nepheline framework, and crystal-chemical relationships in the compositional space $(K,Na,Ca,Va)_8(Al,Si)_{16}O_{32}$. *Eur. J. Mineral.* 1989;1:59-70.

53. Lambert S. L., Stegen G. E., Vienna J. D., Tank waste remediation system phase I high-level waste feed processability assessment report. WHC-SD-WM-TI-768, Richland, WA, 1996. 203.

54. Hrma P., Piepel G. F., Schweiger M. J., et al., Property/composition relationships for Hanford high-level waste glasses melting at 1150°C, 1. PNL-10359, Pacific Northwest National Laboratory, Richland, WA, 1994. 1-347.

55. Vienna J. D., Hrma P. R., Schweiger M. J., et al., Effect of composition and temperature on the properties of high-level waste (HLW) glass melting above 1200ºC. PNNL-10987, Pacific Northwest National Laboratory, Richland, WA, 1996. 1-55.

56. Hrma P., Piepel G. F., Vienna J. D., et al., Database and interim glass property models for hanford HLW glasses. PNNL-13573, Pacific Northwest National Laboratory, Richland, WA, 2001. 1-90.

57. Matlack K. S., Gan H., Gong W., et al., High level waste vitrification system improvements. VSL-07R1010-1, Vitreous State Laboratory, the Catholic University of America, Washington, DC, 2007. 1-275.

58. Schreiber H. D., Kozak S. J., Merkel R. C., et al., Redox equilibria and kinetics of iron in a borosilicate glass-forming melt. *J. Non-Cryst. Solids.* 1986;84:186-195.

59. Donald S. B., Swink A. M., Schreiber H. D., High-iron ferric glass. *J. Non-Cryst. Solids.* 2006;352:539-543.

60. Cacciamani G., An introduction to the calphad method and the compound energy formalism (CEF). *Tecnol. Metal. Mater. Min.* 2016;13:16-24.

61. Andersson J. O., Helander T., Hoglund L. H., et al., THERMO-CALC & DICTRA, computational tools for materials science. *Calphad-Comput. Coupling Ph. Diagrams Thermochem.* 2002;26:273-312.

62. Kumar K. C. H., Wollants P., Some guidelines for thermodynamic optimisation of phase diagrams. *J. Alloy Compd.* 2001;320:189-198.

63. Saunders N., Miodownik A. P., CALPHAD (calculation of phase diagrams): A comprehensive guide, 1ed. UK, USA, Japan: Elsevier Science Ltd.; 1998.

64. Spencer P. J., Estimation of thermodynamic data for metallurgical applications. *Thermochim. Acta.* 1997;314:1-21.

65. Parr R. G., Yang W. T., Density-functional theory of the electronic structure of molecules. *Annu. Rev. Phys. Chem.* 1995;46:701-728.

66. Konigsberger E., Eriksson G., A new optimization routine for ChemSage. *Calphad-Comput. Coupling Ph. Diagrams Thermochem.* 1995;19:207-214.

67. Walton W. B., Parameter estimation for nonlinear models - convergence, data and parameter uncertainty, and constraints on parameter changes. *Math. Comput. Model.* 1989;12:181-192.

68. Konigsberger E., Gamsjager H., Analysis of phase diagrams employing Bayesian excess parameter estimation. *Monatsh. Chem.* 1990;121:119-127.

69. Konigsberger E., Improvement of excess parameters from thermodynamic and phase diagram data by a sequential Bayes algorithm. *Calphad-Comput. Coupling Ph. Diagrams Thermochem.* 1991;15:69-78.

70. Hillert M., Some viewpoints on the use of a computer for calculating phase diagrams. *Physica B & C.* 1981;103:31-40.

71. Berman R. G., Brown T. H., Heat capacity of minerals in the system Na_2O-K_2O-CaO-MgO-FeO-Fe_2O_3-Al_2O_3-SiO_2-TiO_2-H_2O-CO_2: representation, estimation, and high temperature extrapolation. *Contrib. Mineral. Petr.* 1985;89:168-183.

72. DeHoff R., Thermodynamics in materials science, 2nded. Boca Raton, FL: CRC Press; 2006.

73. Inden G., The role of magnetism in the calculation of phase diagrams. *Physica B & C.* 1981;103:82-100.

74. Schairer J. F., Bowen N. L., The system: $Na_2O.Al_2O_3.SiO_2$. *Am. J. Sci.* 1956;254:129-195.

75. Koukkari P., Introduction to constrained gibbs energy methods in process and materials research, VTT Technology, 160. VTT Technical Research Centre of Finland, Espoo, Finland, 2014. 1-100.

76. Lambotte G., Chartrand P., Thermodynamic modeling of the (Al_2O_3 + Na_2O), (Al_2O_3 + Na_2O + SiO_2), and (Al_2O_3 + Na_2O + AlF_3 + NaF) systems. *J. Chem. Thermodyn.* 2013*;*57:306-334.

77. Jak E., Hayes P. C., Pelton A. D., et al., Thermodynamic modeling of the Al_2O_3–CaO–FeO–Fe_2O_3–PbO–SiO_2–ZnO system with addition of K and Na with metallurgical applications, VIII International Conference on Molten Slags, Fluxes and Salts – MOLTEN 2009. Santiago, Chile, 2009. 473-490.

78. Besmann T. M., Spear K. E., Thermochemical modeling of oxide glasses. *J. Am. Ceram. Soc.* 2002*;*85:2887-2894.

79. Spear K. E., Besmann T. M., Beahm E. C., Thermochemical modeling of glass: Application to high-level nuclear waste glass. *MRS Bull.* 1999*;*24:37-44.

80. Eriksson G., Wu P., Pelton A. D., Critical evaluation and optimization of the thermodynamic properties and phase diagrams of the MgO-Al_2O_3, MnO-Al_2O_3, FeO-Al_2O_3, Na_2O-Al_2O_3 and K_2O-Al_2O_3 systems. *Calphad-Comput. Coupling Ph. Diagrams Thermochem.* 1993*;*17:189-205.

81. Lambotte G., Chartrand P., Thermodynamic optimization of the (Na_2O + SiO_2 + NaF + SiF_4) reciprocal system using the modified quasichemical model in the quadruplet approximation. *J. Chem. Thermodyn.* 2011*;*43:1678-1699.

82. Zhang L. G., Schmetterer C., Masset P. J., Thermodynamic description of the M_2O-SiO_2 (M = K, Na) systems. *Comp. Mater. Sci.* 2013*;*66:20-27.

83. Chartrand P., Pelton A. D., Modeling the charge compensation effect in silica-rich Na_2O-K_2O-Al_2O_3-SiO_2 melts. *Calphad-Comput. Coupling Ph. Diagrams Thermochem.* 1999*;*23:219-230.

84. Wu P., Eriksson G., Pelton A. D., Optimization of the thermodynamic properties and phase diagrams of the Na_2O-SiO_2 and K_2O-SiO_2 systems. *J. Am. Ceram. Soc.* 1993*;*76:2059-2064.

85. Romero-Serrano A., Gomez-Yanez C., Hallen-Lopez M., et al., Thermodynamic modeling of alkali metal oxide-silica binary melts. *J. Am. Ceram. Soc.* 2005*;*88:141-145.

86. RomeroSerrano A., Pelton A. D., Extensions of a structural model for binary silicate systems. *Metall. Mater. Trans. B.* 1995*;*26:305-315.

87. Zhang Z., Li G. Q., Yang Y. X., et al., Thermodynamics of the vitrified bottom ash slag from municipal solid waste incinerators-Phase relations of CaO-SiO_2-Na_2O oxide system. *Adv. Mat. Res.* 2014*;*881-883:574-578.

88. Swamy V., Jung I. H., Decterov S. A., Thermodynamic modeling of the Al_2O_3-B_2O_3-SiO_2 system. *J. Non-Cryst. Solids.* 2009;355:1679-1686.

89. Mao H. H., Selleby M., Sundman B., Phase equilibria and thermodynamics in the Al_2O_3-SiO_2 system - Modeling of mullite and liquid. *J. Am. Ceram. Soc.* 2005;88:2544-2551.

90. Lambotte G., Chartrand P., Thermodynamic evaluation and optimization of the Al_2O_3-SiO_2-AlF_3-SiF_4 reciprocal system using the modified quasichemical model. *J. Am. Ceram. Soc.* 2011;94:4000-4008.

91. Howald R. A., Eliezer I., Thermodynamic properties of mullite. *J. Phys. Chem.-US.* 1978;82:2199-2204.

92. Kaufman L., Calculation of quasibinary and quasiternary oxide systems - II. *Calphad-Comput. Coupling Ph. Diagrams Thermochem.* 1979;3:27-44.

93. Dorner P., Gauckler L. J., Krieg H., et al., On the calculation and representation of multicomponent systems. *Calphad-Comput. Coupling Ph. Diagrams Thermochem.* 1979;3:241-257.

94. Hillert M., Sundman B., Wang X., A thermodynamic evaluation of the Al_2O_3–SiO_2 system, 1sted. Stockholm, Sweden: KTH; 1989.

95. Dumitrescu L., Sundman B., A thermodynamic reassessment of the Si-Al-O-N System. *J. Eur. Ceram. Soc.* 1995;15:239-247.

96. Schneider H., Fischer R. X., Schreuer J., Mullite: Crystal structure and related properties. *J. Am. Ceram. Soc.* 2015;98:2948-2967.

97. Bragg W. L., Gottfried C., West J., The structure of β alumina. *Z. Kristallogr.* 1931;77:255-274.

98. Beevers C. A., Ross M. A. S., The crystal structure of "beta alumina" $Na_2O{\cdot}11Al_2O_3$. *Z. Kristallogr.* 1937;97:59-66.

99. Hovis G. L., Spearing D. R., Stebbins J. F., et al., X-ray powder diffraction and ^{23}Na, ^{27}Al, and ^{29}Si MAS-NMR investigation of nepheline-kalsilite crystalline solutions. *Am. Mineral.* 1992;77:19-29.

100. Mao H. H., Hillert M., Selleby M., et al., Thermodynamic assessment of the CaO-Al_2O_3-SiO_2 system. *J. Am. Ceram. Soc.* 2006;89:298-308.

101. Benoit M., Ispas S., Tuckerman M. E., Structural properties of molten silicates from ab initio molecular-dynamics simulations: Comparison between CaO-Al_2O_3-SiO_2 and SiO_2. *Phys. Rev. B.* 2001;64:10.

102. Rolin M., Thanh P. H., The phase diagrams of the mixtures which do not react with molybdenum. *Rev. Int. Hautes. Temp. 2.* 1965*;*175-185.

103. Weber N., Venero A. F., Revision of the phase diagram $NaAlO_2$–Al_2O_3. In: 72nd Annual Meeting of the American Ceramic Society. Philadelphia, PA, USA: 1970:

104. Saxena S. K., Chatterjee N., Fei Y., et al., Thermodynamic data on oxides and silicates, 1sted. Springer-Verlag, NY: 1993.

105. Klug F. J., Prochazka S., Doremus R. H., Alumina-silica phase diagram in the mollite region. *J. Am. Ceram. Soc.* 1987*;*70:750-759.

106. Rys M., Investigation of thermodynamic properties of alkali metals in oxide systems relevant to coal slags, Fakultät für Maschinenwesen*,* Ph.D., The Rheinisch-Westfälische Technische Hochschule, Aachen, Germany, 2008. 132.

107. Kracek F. C., The system sodium oxide-silica. *J. Phys. Chem.-US.* 1930*;*34:1583-1598.

108. D'Ans J., Lottler J., Analysis of the system Na_2O-SiO_2-ZrO_2. *Z. Anorg. Allg. Chem.* 1930*;*191:1-35.

109. Meshalkin A. B., Kaplun A. B., Phase equilibria in the Na_2O-SiO_2 system. *Zhurnal Neorg. Khimii.* 2003*;*48:1712-1714.

110. Willgallis A., Contribution to the system SiO_2-Na_2O-NaF. *Glastech. Ber.-Glass.* 1969*;*42:506-509.

111. Williams J., Glasser F. P., Phase relations in the system $Na_2Si_2O_5$-SiO_2. *Science.* 1965*;*148:1589-1591.

112. Schairer J. F., Yoder Jr. H. S., The compound $3Na_2O{\cdot}8SiO_2$ in the system Na_2O-SiO_2. *Carnegie I Wash.* 1971*;*69:160-163.

113. Tilley C. E., The ternary system, Na_2SiO_3-$Na_2Si_2O_5$-$NaAlSiO_4$. *Z. Kristallogr. Abt. B.* 1933*;*43:406-421.

114. Greig J. W., Barth T. F. W., The system, $Na_2O.Al_2O_3.2SiO_2$ (nephelite, carnegieite)-$Na_2O.Al_2O_3.6SiO_2$ (albite). *Am. J. Sci.* 1938*;*35:93-112.

115. Spivak J., The system $NaAlSiO_4$-$CaSiO_3$-Na_2SiO_3. *J. Geol.* 1944*;*52:24-52.

116. Davis R. F., Pask J. A., Diffusion and reaction studies in the system Al_2O_3-SiO_2. *J. Am. Ceram. Soc.* 1972*;*55:525-531.

117. Bowen N. L., Greig J. W., The system: Al_2O_3.SiO_2. *J. Am. Ceram. Soc.* 1924;7:238-254.

118. Aksay I. A., Pask J. A., Stable and metastable equilibria in the system SiO_2-Al_2O_3. *J. Am. Ceram. Soc.* 1975;58:507-512.

119. Aramaki S., Roy R., Revised phase diagram for the system Al_2O_3-SiO_2. *J. Am. Ceram. Soc.* 1962;45:229-242.

120. Konopicky K., Equilibrium diagram of the system SiO_2–Al2O_3. *Bull. Soc. Chim. Fr.* 1956;33:3-6.

121. Toropov N. A., Galakhov F. Y., New data on the system Al_2O_3–SiO_2. *Dokl. Akad. Nauk*+. 1951;78:299-302.

122. Eriksson G., Pelton A. D., Critical evaluation and optimization of the thermodynamic properties and phase diagrams of the CaO-Al_2O_3, Al_2O_3-SiO_2, and CaO-Al_2O_3-SiO_2 systems. *Metall. Mater. Trans. B.* 1993;24:807-816.

123. Hamano K., Sato T., Nakagawa Z., Properties of mullite powder prepared by coprecipitation and microstructure of fired bodies. *Nippon Seram. Kyo. Gak.* 1986;94:818-822.

124. Okada K., Otsuka N., Change in chemical composition of mullite formed from $2SiO_2 \cdot 3Al_2O_3$ xerogel during the formation process. *J. Am. Ceram. Soc.* 1987;70:C-245-C-247.

125. Prochazka S., Klug F. J., Infrared-transparent mullite ceramic. *J. Am. Ceram. Soc.* 1983;66:874-880.

126. Bouaziz R., Papin G., Rollet A. P., Contribution to the study of sodium oxide and the binary oxide-sodium hydroxide system. *Cr. Acad. Sci. C Chim.* 1966;262:1051-1054.

127. Christensen A. U., Conway K. C., Kelley K. K., High-temperature heat contents and entropies of aluminates and ferrites of lithium and sodium, and of lithium titanate. *Bureau of Mines Report of Investigations No. 5565.* 1960;7.

128. Rolin M., Thanh P. H., The phase diagrams of the mixtures not reacting with the molybdenum. 1. Equipment and procedure for the application up to 2100°C the method of the cooling curves. *Bull. Soc. Chim. Fr.* 1963;5:1030-1035.

129. Liebertz J., Formation and existence of the two Na-β-Al_2O_3 phases. *Ber. Deut. Ker. Ges.* 1972;49:288-290.

130. Le Cars Y., Thery J., Collongues R., On the non-stoichiometry and stability of aluminas β and β". *Cr. Acad. Sci. C Chim.* 1972;274:4-7.

131. Jacob K. T., Swaminathan K., Sreedharan O. M., Potentiometric determination of activities in the two-phase fields of the system Na_2O-(α)Al_2O_3. *Electrochim. Acta.* 1991;36:791-798.

132. Hammel J. J., Experimental evidence for spinodal decomposition in glasses of the Na_2O-SiO_2 system. In: VIIth International Congress on Glass, International Commission on Glass. Brussels: 1965:

133. Morey G. W., Bowen N. L., The binary system sodium metasilicate-silica. *J. Phys. Chem.-US.* 1924;28:1167-1179.

134. Kracek F. C., Phase equilibrium relations in the system, Na_2SiO_3-Li_2SiO_3-SiO_2. *J. Am. Chem. Soc.* 1939;61:2863-2877.

135. Zaitsev A. I., Shelkova N. E., Lyakishev N. P., et al., Thermodynamic properties and phase equilibria in the Na_2O-SiO_2 system. *Phys. Chem. Chem. Phys.* 1999;1:1899-1907.

136. Zaitsev A. I., Shelkova N. E., Mogutnov B. M., Thermodynamics of Na_2O-SiO_2 melts. *Inorg. Mater+.* 2000;36:529-543.

137. Fan M., Thermochemical study of the melts Na_2O-SiO_2, Na_2O–GeO_2, Na_2O–B_2O_3 and Li_2O-B_2O_3, Fakultät für Bergbau, Hüttenwesen und Geowissenschaften. 1991. 1-98.

138. Hovis G. L., Toplis M. J., Richet P., Thermodynamic mixing properties of sodium silicate liquids and implications for liquid-liquid immiscibility. *Chem. Geol.* 2004;213:173-186.

139. Takahashi K., Yoshio T., Energy relations in alkali silicates by solution calorimetry. *Nippon Seram. Kyo. Gak.* 1970;78:35-44.

140. Tischer R. E., Heat of annealing in simple alkali silicate glasses. *J. Am. Ceram. Soc.* 1969;52:499-503.

141. Yamaguchi S., Imai A., Goto K. S., Activity measurement of Na_2O in Na_2O-SiO_2 melts using the beta-alumina as the solid electrolyte. *Scand. J. Metall.* 1982;11:263-264.

142. Yamaguchi S., Imai A., Goto K. S., Measurement of activity of Na_2O in Na_2O-SiO_2 binary melt using beta-alumina as a solid electrolyte. *J. Jpn. I Met.* 1983;47:736-742.

143. Tsukihashi F., Sano N., Measurement of the activity of Na_2O in Na_2O-SiO_2 melts by chemical equilibration method. *Tetsu to Hagane.* 1985;71:815-822.

144. Rego D. N., Sigworth G. K., Philbrook W. O., Thermodynamic study of Na_2O-SiO_2 melts at 1300º and 1400 ºC. *Metall. Trans. B.* 1985;16:313-323.

145. Itoh H., Yokokawa T., Thermodynamic activity of Na_2O in Na_2O-SiO_2-Al_2O_3 melt. *T. Jpn. I Met.* 1984;25:879-884.

146. de Pablo-Galan L., Foster W. R., Investigation of role of beta alumina in the system Na_2O-Al_2O_3-SiO_2. *J. Am. Ceram. Soc.* 1959;42:491-498.

147. Thompson J. G., Melnitchenko A., Palethorpe S. R., et al., An XRD and electron diffraction study of cristobalite-related phases in the $NaAlO_2$-$NaAlSiO_4$ system. *J. Solid State Chem.* 1997;131:24-37.

148. Utlak S. A., Besmann T. M., Thermodynamic assessment of the pseudoternary Na_2O-Al_2O_3-SiO_2 system. *J. Am. Ceram. Soc.* 2018;101:928-948.

149. Deer W. A., Howie R. A., Wise W. S., et al., Rock-forming minerals volume 4B: Framework silicates: silica minerals, feldspathoids and the zeolites, London: The Geological Society; 2004.

150. Buerger M. J., The stuffed derivatives of the silica structures. *Am. Mineral.* 1954;39:600-614.

151. Buerger M. J., Klein G. E., Donnay G., Determination of the crystal structure of nepheline. *Am. Mineral.* 1954;39:805-818.

152. Sundman B., Modification of the two-sublattice model for liquids. *Calphad-Comput. Coupling Ph. Diagrams Thermochem.* 1991;15:109-119.

153. Andersson J. O., Guillermet A. F., Hillert M., et al., A compound-energy model of ordering in a phase with sites of different coordination numbers. *Acta Metall. Mater.* 1986;34:437-445.

154. Havrig H., An extended version of the regular solution model for stoichiometric phases and ionic melts. *Acta Chem. Scand.* 1971;25:3199-3204.

155. Hillert M., Staffansson L. I., Regular solution model for stoichiometric phases and ionic melts. *Acta Chem. Scand.* 1970;24:3618-3626.

156. Sundman B., Agren J., A regular solution model for phases with several components and sublattices, suitable for computer applications. *J. Phys. Chem. Solids.* 1981;42:297-301.

157. Wang C., Yu H., Liu H. S., et al., Thermodynamic optimization of the Na_2O-B_2O_3 pseudo-binary system. *J. Phase Equilib.* 2003;24:12-20.

158. Yu H., Chen Q., Jin Z. P., Thermodynamic assessment of the CaO-B_2O_3 system. *Calphad-Comput. Coupling Ph. Diagrams Thermochem.* 1999;23:101-111.

159. Yu H., Chen Q., Jin Z., Thermodynamic reassessment of the $BaO-B_2O_3$ system. *J. Phase Equilib.* 1999;20:479-484.

160. Yu H., Jin Z. P., Chen Q., et al., Thermodynamic assessment of the lithium-borate system. *J. Am. Ceram. Soc.* 2000;83:3082-3088.

161. Chen H. M., Chen J. M., Wang S., et al., Thermodynamic Assessment of B_2O_3-SiO_2 Binary System, 68-72. in Materials Science, Mechanical Engineering and Applied Research, Vol. 628**.** *Applied Mechanics and Materials.* Edited by F. Zhang. Trans Tech Publications Ltd, Durnten-Zurich, 2014.

162. Chen S. H., Su J., Wang Y., et al., Thermodynamic assessment of B_2O_3-MgO binary system. *Calphad-Comput. Coupling Ph. Diagrams Thermochem.* 2015;51:67-74.

163. Morey G. W., Merwin H. E., Phase equilibrium relationships in the binary system, sodium oxide-boric oxide, with some measurements of the optical properties of the glasses. *J. Am. Chem. Soc.* 1936;58:2248-2254.

164. Milman T., Bouaziz R., Contribution to the study of sodium borates. *Ann. Chim. France.* 1968;3:311-321.

165. Liang J. K., Fang C. M., Huang Q. Z., Formation and crystallization mechanism of glasses in $NaBO_2$-B_2O_3 system. *Chinese Phys.* 1990;10:689-697.

166. Shartsis L., Capps W., Energy relations in binary alkali borates. *J. Am. Ceram. Soc.* 1954;37:27-32.

167. Navrotsky A., Hervig R. L., Roy B. N., et al., Thermochemical studies of silicate, aluminosilicate, and borosilicate glasses. *High Temp. Sci.* 1985;19:133-150.

168. Itoh M., Sato S., Yokokawa T., E.m.f. measurements of molten mixtures of lithium oxide +, sodium oxide +, and potassium oxide + boron oxide. *J. Chem. Thermodyn.* 1976;8:339-352.

169. Itoh H., Sasahira A., Maekawa T., et al., Electromotive-force measurements of molten oxide mixtures. Part 8. Thermodynamic properties of $Na_2O-B_2O_3$ melts. *J. Chem. Soc. Farad. T 1.* 1984;80:473-487.

170. Park J. H., Min D. J., Thermodynamic behavior of $Na_2O-B_2O_3$ melt. *Metall. Mater. Trans. B.* 2001;32:297-303.

171. Stegmaier V. W., Dietzel A., The importance of the basicity of glass melts and attempts to measure them. *Glastech. Ber.-Glass.* 1940;18:353-362.

172. Sato S., Yokokawa T., Kita H., et al., Thermodynamic activity of Na_2O-B_2O_3 melt - Use of stabilized zirconia as an electrode constituent. *J. Electrochem. Soc.* 1972;119:1524-1526.

173. Decterov S. A., Swamy V., Jung I. H., Thermodynamic modeling of the B_2O_3-SiO_2 and B_2O_3-Al_2O_3 systems. *Int. J. Mater. Res.* 2007;98:987-994.

174. Pelton A. D., Blander M., Thermodynamic analysis of ordered liquid solutions by a modified quasichemical approach - Application to silicate slags. *Metall. Trans. B.* 1986;17:805-815.

175. Pelton A. D., Degterov S. A., Eriksson G., et al., The modified quasichemical model I - Binary solutions. *Metall. Mater. Trans. B.* 2000;31:651-659.

176. Baumann H. N., Moore C. H., Electric furnace boroaluminate. *J. Am. Ceram. Soc.* 1942;25:391-394.

177. Scholze H., About aluminum borates. *Z. Anorg. Allg. Chem.* 1956;284:272-277.

178. Kim K. H., Hummel F. A., Studies in lithium oxide systems: XII, Li_2O-B_2O_3-Al_2O_3. *J. Am. Ceram. Soc.* 1962;45:487-489.

179. Gielisse P. J., Investigation of phase equilibria in the system alumina-boron oxide-silica, Mineralogy, Doctor of Philosophy. The Ohio State University, Columbus, OH, 1961. 1-96.

180. Gielisse P. J., Foster W. R., The system Al_2O_3-B_2O_3. *Nature.* 1962;195:69-70.

181. Rymon-Lipinski T., Hennicke H., Lingenberg W., Decomposition of $9Al_2O_3 \cdot 2B_2O_3$ at high temperatures. *Keram. Z.* 1985;37:450-453.

182. Mazza D., Vallino M., Busca G., Mullite-type structures in the systems Al_2O_3-Me_2O (Me = Na,A) and Al_2O_3-B_2O_3. *J. Am. Ceram. Soc.* 1992;75:1929-1934.

183. Rockett T. J., Foster W. R., Phase relations in the system boron oxide-silica. *J. Am. Ceram. Soc.* 1965;48:75-80.

184. Pichavant M., Study of the SiO_{-2}-B_2O_3 system at one kb. Phase diagram and thermodynamic interpretation. *B Mineral.* 1978;101:498-502.

185. Charles R. J., Wagstaff F. E., Metastable immiscibility in the B_2O_3-SiO_2 system. *J. Am. Ceram. Soc.* 1968;51:16-20.

186. Morey G. W., The ternary system Na_2O-B_2O_3-SiO_2. *J. Soc. Glass Tech.* 1951;35:270-283.

187. Ghanbari-Ahari K., Cameron A. M., Phase diagram of Na_2O-B_2O_3-SiO_2 system. *J. Am. Ceram. Soc.* 1993;76:2017-2022.

188. Rockett T. J., Foster W. R., The system silica-sodium tetraborate. *J. Am. Ceram. Soc.* 1966;49:30-33.

189. Asai K., Yokokawa T., Thermodynamic activity of Na_2O in Na_2O-B_2O_3-SiO_2 melt. *T. Jpn. I Met.* 1982;23:571-577.

190. Konakov V. G., Kozhina E. L., Shultz M. M., A study of the acid-base properties of melts in the Na_2O-B_2O_3-SiO_2 system: I. Composition joins with a Na_2O content of less than 20 mol %. *Glass Phys. Chem.* 2001;27:182-187.

191. Kozhina E. L., Shultz M. M., Thermodynamic properties of sodium-containing glassforming oxide melts. *Ceram.-Silikaty.* 2000;44:91-97.

192. Binev D., Nikolov V., Peshev P., Regions of phase crystallization in the ternary system Na_2O-Al_2O_3-B_2O_3. *J. Alloy Compd.* 2005;391:256-261.

193. Abdullaev G. K., Rzazade P. F., Mamedov K. S., The Na_2O-Al_2O_3-B_2O_3 system. *Zhurnal Neorg. Khimii.* 1983;28:208-211.

194. Peshev P., Pechev S., Nikolov V., et al., Studies on some ternary oxyborates of the Na_2O-Me_2O_3-B_2O_3 (Me = rare earth or aluminum) systems: Synthesis, structure and crystal growth. *J. Solid State Chem.* 2006;179:2834-2849.

195. He M., Chen X. L., Zhou T., et al., Crystal structure and infrared spectra of $Na_2Al_2B_2O_7$. *J. Alloy Compd.* 2001;327:210-214.

196. He M., Kienle L., Simon A., et al., Re-examination of the crystal structure of $Na_2Al_2B_2O_7$: Stacking faults and twinning. *J. Solid State Chem.* 2004;177:3212-3218.

197. He M., Chen X. L., Okudera H., et al., $(K_{1-x}Na_x)_2Al_2B_2O_7$ with $0 \leq x \leq 0.6$: A promising nonlinear optical crystal. *Chem. Mat.* 2005;17:2193-2196.

198. Perras F. A., Bryce D. L., Multinuclear magnetic resonance crystallographic structure refinement and cross-validation using experimental and computed electric field gradients: Application to $Na_2Al_2B_2O_7$. *J. Phys. Chem. C.* 2012;116:19472-19482.

199. Meng X. Y., Gao J. H., Wang Z. Z., et al., Structure instability of $A_2Al_2B_2O_7$ (A=K, Na) crystals. *J. Phys. Chem. Solids.* 2005;66:1655-1659.

200. Salman S. M., Salama S. N., Abo-Mosallam H. A., Crystallization features and physico-chemical properties of alkali and alkaline aluminoborate glass-ceramics. *J. Aust. Ceram. Soc.* 2017;53:953-961.

201. Wakasugi T., Ota R., Fukunaga J., Glass-forming ability and crystallization tendency evaluated by the DTA method in the Na_2O-B_2O_3-Al_2O_3 system. *J. Am. Ceram. Soc.* 1992*;*75:3129-3132.

202. Wakasugi T., Ota R., Nozawa Y., et al., Amorphous regions and crystallization behavior of rf-sputtered films in the B_2O_3-Na_2O-Al_2O_3 system. *J. Non-Cryst. Solids.* 1995*;*191:238-247.

203. Dietzel A., Scholze H., Investigations in the system B_2O_3-Al_2O_3-SiO_2. *Glastech. Ber.-Glass.* 1955*;*28:47-51.

204. Kopp H., III. Investigations of the specific heat of solid bodies. *Phil. Trans.* 1865*;*155:71-202.

205. Latimer W. M., Methods of estimating the entropies of solid compounds. *J. Am. Chem. Soc.* 1951*;*73:1480-1482.

206. Schneider H., Florke O. W., Stoeck R., The $NaAlSiO_4$ nepheline-carnegieite solid-state transformation. *Z. Kristallogr.* 1994*;*209:113-117.

207. Yu H., Liu H. S., Jin Z. P., Thermodynamic calculation of the Li_2O-BaO-B_2O_3 pseudo-ternary phase diagram. *Z. Metallkd.* 1999*;*90:499-504.

208. Barin I., Thermochemical data of pure substances, Weinheim, Federal Republic of Germany; New York, NY, USA: VCH; 1989.

209. Chase M. W., NIST-JANAF Thermochemical Tables, 4th Edition, American Institute of Physics; 1998.

210. Taylor J. R., Dinsdale A. T., Hillert M., et al., A critical assessment of thermodynamic and phase diagram data for the Al-O system. *Calphad-Comput. Coupling Ph. Diagrams Thermochem.* 1992*;*16:173-179.

211. Swamy V., Decterov S. A., Pelton A. D., Thermodynamic assessment of the Ge-Si-O-Cl-H system. *Glass Sci. Technol.* 2003*;*76:62-70.

212. Burgess C. H., Junr A. H., Some physical characters of the sodium borates, with a new and rapid method for the determination of melting points. *P. R. Soc. London.* 1904*;*74:285-295.

213. van Klooster H. S., About the behavior of metaboric and metaphosphoric acids in the melts of their alkali salts. *Z. Anorg. Chem.* 1911*;*69:122-134.

214. Cole S. S., Taylor N. W., Scholes S. R., The system Na_2O-B_2O_3, III. The optical properties, x-ray patterns, and melting points of the anhydrous sodium borates. *J. Am. Ceram. Soc.* 1935*;*18:79-81.

215. Day A. L., Allen E. T., The isomorphism and thermal properties of the feldspars. *Am. J. Sci.* 1905;19:93-142.

216. Ponomareff J. E., Investigation of the glassy state by the method of enforced crystallisation. *J. Soc. Glass Tech.* 1927;11:39-52.

217. Menzel H., Information on boric acids and boric acid alkali salts. IX. The system $Na_2B_4O_7$-H_2O. *Z. Anorg. Allg. Chem.* 1935;224:1-22.

218. Weber N., Venero A. F., Revision of Phase Diagram $NaAlO_2$-Al_2O_3. *Am. Ceram. Soc. Bull.* 1970;49:491-492.

219. Hoch M., Thermodynamic properties and phase diagrams of the binary systems B2O3-Ga2O3, B2O3-Al2O3 and B2O3-In2O3. *J. Alloy Compd.* 2001;320:267-275.

220. Selleby M., An assessment of the Fe-O-Si system. *Metall. Mater. Trans. B.* 1997;28:563-576.

221. Fabrichnaya O. B., Sundman B., The assessment of thermodynamic parameters in the Fe-O and Fe-Si-O systems. *Geochim. Cosmochim. Ac.* 1997;61:4539-4555.

222. Dreval L., Zienert T., Fabrichnaya O., Calculated phase diagrams and thermodynamic properties of the Al_2O_3-Fe_2O_3-FeO system. *J. Alloy Compd.* 2016;657:192-214.

223. Moosavi-Khoonsari E., Jung I. H., Critical evaluation and thermodynamic optimization of the Na_2O-FeO-Fe_2O_3 system. *Metall. Mater. Trans. B.* 2016;47:576-594.

224. Zienert T., Fabrichnaya O., Thermodynamic assessment and experiments in the system MgO-Al_2O_3. *Calphad-Comput. Coupling Ph. Diagrams Thermochem.* 2013;40:1-9.

225. Leitner J., Voňka P., Sedmidubský D., et al., Application of Neumann–Kopp rule for the estimation of heat capacity of mixed oxides. *Thermochim. Acta.* 2010;497:7-13.

226. Rankin G. A., Merwin H. E., The ternary system CaO-Al_2O_3-MgO. *J. Am. Chem. Soc.* 1916;38:568-588.

227. Tsutsumi K., Ohtake J., Nagasaka T., et al., Crystallization behavior of Li_2O-SiO_2, Na_2O-SiO_2 and Na_2O-CaO-SiO_2 glasses. *Tetsu to Hagane.* 1998;84:464-469.

228. Vedishcheva N. M., Shakhmatkin B. A., Wright A. C., Thermodynamic modelling of the structure and properties of glasses in the sytems Na_2O-B_2O_3-SiO_2 and Na_2O-CaO-SiO_2. *Phys. Chem. Glasses.* 2005;46:99-107.

229. Zhang Z., Xiao Y. P., Voncken J., et al., Phase Equilibria in the Na_2O-CaO-SiO_2 system. *J. Am. Ceram. Soc.* 2011;94:3088-3093.

230. Hodge J. D., Phase Relations in the System Na_2O-Li_2O-Al_2O_3. *J. Am. Ceram. Soc.* 1984;67:183-185.

231. Weber N., Venero A. F., Subsolidus Relations in System $NaAlO_2$-$MgAl_2O_4$-Al_2O_3. *Am. Ceram. Soc. Bull.* 1970;49:498.

232. Imai A., Harata M., Ionic conduction of impurity-doped β-alumina ceramics. *Jpn. J. Appl. Phys.* 1972;11:180-185.

233. Duncan G. K., West A. R., Formation of Beta Aluminas in the System Li_2O-Na_2O-Al_2O_3. *Solid State Ionics.* 1983;9-10:259-264.

234. Huang W. M., Hillert M., Wang X. Z., Thermodynamic assessment of the CaO-MgO-SiO_2 system. *Metall. Mater. Trans. A.* 1995;26:2293-2310.

235. Chastel R., Bergman C., Rogez J., et al., Excess thermodynamic functions in ternary Na_2O-K_2O-SiO_2 melts by Knudsen cell mass spectrometry. *Chem. Geol.* 1987;62:19-29.

236. Moya J. S., Criado E., DeAza S., The $K_2O \cdot Al_2O_3$-Al_2O_3 system. *J. Mater. Sci.* 1982;17:2213-2217.

237. Eliezer I., Howald R. A., High-temperature thermodynamics and phase equilibria in potassium oxide-aluminum oxide system. *High Temp. Sci.* 1978;10:1-16.

238. Roth R. S., Phase equilibria research in portions of the system K_2O-MgO-Fe_2O_3-Al_2O_3-SiO_2. *Adv. Chem. Ser.* 1980;186:391-408.

239. Rollet A. P., Borate and potassium. Study of the B_2O_3-K_2O system. *C. R. Hebd. Seances Acad. Sci.* 1935;200:1763-1765.

240. Rollet A. P., The polymorphism of potassium pentaborate $5B_2O_3.K_2O$. *C. R. Hebd. Seances Acad. Sci.* 1936;202:1863-1865.

241. Polyakova I. G., Tokareva E. V., A study of phase equilibria in the potassium borate system: Glass crystallization and solid state reaction. *Glass Phys. Chem+.* 1997;23:354-367.

242. Kaplun A. B., Meshalkin A. B., Phase equilibria of the K_2O-B_2O_3 system. *Russ. J. Inorg. Chem+.* 2002;47:1058-1062.

243. Stahleisen V., Eisenhüttenleute V. D., Slag atlas, 2ed. Dusseldorf: Verlag Stahleisen GmbH; 1995.

244. Fujiwara H., Moriya H., Iwase M., Thermochemical activities in Fe_xO+ B_2O_3 slags and phase relation in the system Fe + B + O. *Ironmak. Steelmak.* 1991;18:43-49.

245. Jakobsson L. K., Tranell G., Jung I. H., Experimental investigation and thermodynamic modeling of the B_2O_3-FeO-Fe_2O_3-Nd_2O_3 system for recycling of NdFeB magnet scrap. *Metall. Mater. Trans. B.* 2017;48:60-72.

246. Zhang C. T., Ji C. L., Activities of components in MgO–B_2O_3 melt. *Acta Metall. Sin.* 1989;25:240-243.

247. Wang Z. C., Tong S. X., Liu X., et al., Activity of MgO in {(1-*x*)MgO+*x*B_2O_3}, determined by (slag+metal) equilibrium at the temperature 1723 K, using germanium as metal solvent. *J. Chem. Thermodyn.* 1995;27:873-878.

248. Ahmadzadeh M., Marcial J., McCloy J., Crystallization of iron-containing sodium aluminosilicate glasses in the NaAlSiO4-NaFeSiO4 join. *J. Geophys. Res.-Sol. Ea.* 2017;122:2504-2524.

249. Onuma K., Yoshikawa K., Nepheline solid solutions in the system Na_2O-Fe_2O_3-Al_2O_3-SiO_2. *Jpn. Assoc. Min. Sci.*. 1972;67:395-401.

250. Onuma K., Iwai T., Yagi K., Nepheline-"iron nepheline" solid solutions. *J. Fac. Sci. Hokkaido U. Ser. 4.* 1972;15:179-190.

251. Yagi A., A reconnaissance of the systems acmite-diopside and acmite-nepheline. *Carnegie I Wash.* 1961;61:98-99.

252. Bailey D. K., Schairer J. F., The system Na_2O-Al_2O_3-Fe_2O_3-SiO_2 at 1 atmosphere and petrogenesis of alkaline rocks. *J. Petrol.* 1966;7:114-170.

253. Ahmadzadeh M., Scrimshire A., Bingham P. A., et al., Structural role of iron in nepheline-based aluminosilicates for nuclear waste applications, Waste Management Symposia. Phoenix, Az, 2018. 1-13.

254. Haccuria E., Crivits T., Hayes P. C., et al., Selected Phase Equilibria Studies in the Al_2O_3-CaO-SiO_2 System. *J. Am. Ceram. Soc.* 2016;99:691-704.

255. Bale C., Chartrand P., Degterov S. A., et al., FactSage thermochemical software and databases. *Calphad-Comput. Coupling Ph. Diagrams Thermochem.* 2002;26:189-228.

256. Mao H. H., Fabrichnaya A., Selleby M., et al., Thermodynamic assessment of the MgO-Al_2O_3-SiO_2 system. *J. Mater. Res.* 2005;20:975-986.

257. Badger W. B., Hummel F. A., Phase equilibrium in the system $LiAlSiO_4$-$NaAlSiO_4$-SiO_2. *J. Am. Ceram. Soc.* 1985;68:C46-C47.

258. Ota T., Yamai I., Hayashi T., Nepheline gradient solid solutions. *J. Mater. Sci.* 1995;30:2701-2705.

259. Marcial J., Kabel J., Saleh M., et al., Structural dependence of crystallization in glasses along the nepheline ($NaAlSiO_4$) - eucryptite ($LiAlSiO_4$) join. *J. Am. Ceram. Soc.* 2018;101:2840-2855.

260. Rodriguez C. P., McCloy J. S., Schweiger M. J., et al., Optical basicity and nepheline crystallization in high alumina glasses. PNNL-20184, Pacific Northwest National Laboratory, Richland, WA, 2011. 1-92.

261. El-Damrawi G., Muller-Warmuth W., Doweidar H., et al., ^{11}B, ^{29}Si and ^{27}Al nuclear magnetic resonance studies of Na_2O-Al_2O_3-B_2O_3-SiO_2 glasses. *Phys. Chem. Glasses.* 1993;34:52-57.

262. Yamashita H., Inoue K., Nakajin T., et al., Nuclear magnetic resonance studies of $0.139MO$ (or M'_2O)$\cdot 0.673SiO_2 \cdot (0.188 - x)Al_2O_3 \cdot xB_2O_3$ (M = Mg, Ca, Sr and Ba, M' = Na and K) glasses. *J. Non-Cryst. Solids.* 2003;331:128-136.

263. Du L.-S., Stebbins J. F., Network connectivity in aluminoborosilicate glasses: A high-resolution ^{11}B, ^{27}Al and ^{17}O NMR study. *J. Non-Cryst. Solids.* 2005;351:3508-3520.

264. Hallstedt B., Assessment of the CaO-Al_2O_3 system. *J. Am. Ceram. Soc.* 1990;73:15-23.

265. Eriksson G., Wu P., Blander M., et al., Critical evaluation and optimization of the thermodynamic properties and phase diagrams of the MnO-SiO_2 and CaO-SiO_2 systems. *Can. Metall. Q.* 1994;33:13-21.

266. Kulkarni N. S., Besmann T. M., Spear K. E., Thermodynamic optimization of lithia-alumina. *J. Am. Ceram. Soc.* 2008;91:4074-4083.

267. Konar B., Van Ende M. A., Jung I. H., Critical evaluation and thermodynamic optimization of the Li-O, and Li_2O-SiO_2 systems. *J. Eur. Ceram. Soc.* 2017;37:2189-2207.

268. Fabrichnaya O. B., Thermodynamic modelling of melting in the system FeO-MgO-SiO_2-O_2 at pressure of 1 bar. *CALPHAD.* 2000;24:113-131.

269. Kracek F. C., Bowen N. L., Morey G. W., Equilibrium relations and factors influencing their determination in the system K_2SiO_3-SiO_2. *J. Phys. Chem.-US.* 1937;41:1183-1193.

270. Zaitsev A. I., Shelkova N. E., Lyakishev N. P., et al., The thermodynamic properties of K_2O-SiO_2 melts. *Russ. J. Phys. Ch.* 2000;74:907-913.

271. Steiler J. M., Thermochemical data for the steel industry, Commission of the European Community, Report EUR 7820. 1982.

272. Cook L. P., Plante E. R., Phase diagram of the system Li_2O–Al_2O_3. *Ceram. Trans.* 1992;27:193-222.

273. Skokan A., Wedemeyer H., Vollath D., et al., Thermal properties and application of potential lithium silicate breeder materials, 1255-1259. in Fusion Technology 1986**.** Pergamon, 1986.

274. Claus S., Kleykamp H., SmykatzKloss W., Phase equilibria in the Li_4SiO_4-Li_2SiO_3 region of the pseudobinary Li_2O-SiO_2 system. *J. Nucl. Mater.* 1996;230:8-11.

275. Meshalkin A. B., Kaplun A. B., Phase equilibria in the range 33.33-58 mol % SiO_2 of the Li_2O-SiO_2 system. *Russ. J. Inorg. Chem.* 2004;49:772-774.

276. Kracek F. C., The binary system Li_2O-SiO_2. *J. Phys. Chem.-US.* 1930;34:2641-2650.

277. Murthy M. K., Hummel F. A., Phase equilibria in the system lithium metasilicate-forsterite-silica. *J. Am. Ceram. Soc.* 1955;38:55-63.

278. Charles R. J., Activities in Li_2O-, Na_2O-, and K_2O-SiO_2 solutions. *J. Am. Ceram. Soc.* 1967;50:631-641.

279. Shul'ts M. M., Kozhina E. L., Shakhmatkin B. A., Thermodynamic properties of Li_2O-SiO_2 melts. *Vestn. Lenin. U Fiz. Kh.* 1986;1:55-60.

280. Morishita M., Navrotsky A., Wilding M. C., Direct measurement of relative partial molar enthalpy of SiO_2 in SiO_2-M_2O (M=Li, Na, K, Cs) binary and SiO_2-CaO-Al_2O_3 ternary melts. *J. Am. Ceram. Soc.* 2004;87:1550-1555.

281. Rollet A. P., Bouaziz R., The binary lithium oxide-boric anhydride system. *Cr. Hebd. Acad. Sci.* 1955;240:2417-2419.

282. Sastry B. S. R., Hummel F. A., Studies in lithium oxide systems: I, $Li_2O{\cdot}B_2O_3$-B_2O_3. *J. Am. Ceram. Soc.* 1958;41:7-17.

283. Sastry B. S. R., Hummel F. A., Studies in lithium oxide systems: V, Li2O-Li2O·B_2O_3. *J. Am. Ceram. Soc.* 1959;42:216-218.

284. Ostvold T., Kleppa O. J., Thermochemistry of liquid borates. II. Partial enthalpies of solution of boric oxide in its liquid mixtures with lithium, sodium, and potassium oxides. *Inorg. Chem.* 1970;9:1395-1400.

285. Nurse R. W., Welch J. H., Majumdar A. J., The CaO-Al_2O_3 system in a moisture-free atmosphere. *Brit. Ceram. Trans. J.* 1965;64:409-418.

286. Rolin M., T. P. H., The phase diagrams of the mixtures not reacting with molybdenum. *Rev. Int. Hautes. Temp.* 1965;2:175-185.

287. Rankin G. A., Wright F. E., The ternary system $CaO-Al_2O_3-SiO_2$, with optical study by F. E. Wright. *Am. J. Sci.* 1915;39:1-79.

288. Shepherd E. S., Rankin G. A., The binary systems of alumina with silica, lime, and magnesia; with optical study by Fred. Eugene Wright. *Am. J. Sci.* 1909;28:293-333.

289. Nityanand N., Fine H. A., The effect of TiO_2 additions and oxygen potential on liquidus temperatures of some $CaO-Al_2O_3$ melts. *Metall. Trans. B.* 1983;14:685-692.

290. Allibert M., Chatillon C., Jacob K. T., et al., Mass-spectrometric and electrochemical studies of thermodynamic properties of liquid and solid phases in the system $CaO-Al_2O_3$. *J. Am. Ceram. Soc.* 1981;64:307-314.

291. Zou Y., Zhou J., Xu Y., et al., Some aspects of the thermodynamics of melts. *Acta Metall. Sin.* 1982;18:133-140.

292. Cameron J., Gibbons T. B., Taylor J., Calcium sulphide solubilities and lime activities in lime-alumina-silica system. *J. Iron. Steel I.* 1966;204:1223-1228.

293. Sharma R. A., Richardson F. D., Activities in lime-alumina melts. *J. Iron. Steel I.* 1961;198:386-390.

294. Edmunds D. M., Taylor J., Reaction $CaO+3C=CaC_2+CO$ and activity of lime in $CaO-Al_2O_3-CaF_2$ system. *J. Iron. Steel I.* 1972;210:280-283.

295. Greig J. W., Immiscibility in silicate melts. *Am. J. Sci.* 1927;13:1-44.

296. Hageman V. B. M., Vandenberg G. J. K., Janssen H. J., et al., A reinvestigation of liquid immiscibility in the SiO_2-CaO system. *Phys. Chem. Glasses.* 1986;27:100-106.

297. Tewhey J. D., Hess P. C., The two phase region in the $CaO-SiO_2$ system: Experimental data and thermodynamic analysis. *Phys. Chem. Glasses.* 1979;20:41-53.

298. Osborn E. F., Muan A., Phase Equilibrium Diagrams of Oxide Systems, S. $Na_2O-Al_2O_3-SiO_2$. American Ceramic Society and the Edward Orton, Jr., Ceramic Foundation, 1960.

299. Rein R. H., Chipman J., Activities in liquid solution $SiO_2-CaO-MgO-Al_2O_3$ at 1600°C. *T. Metall. Soc. AIME.* 1965;233:415-425.

300. Carter P. T., Macfarlane T. G., Part II - The thermodynamic properties of $CaO-SiO_2$ slags. *J. Iron. Steel I.* 1957;185:62-66.

301. Kay D. A. R., Taylor J., Activities of silica in the lime+alumina+silica system. *T. Faraday Soc.* 1960;56:1372-1386.

302. Sharma R. A., Richardson F. D., Solubility of calcium sulphide and activities in lime-silica melts. *J. Iron. Steel I.* 1962;200:373-379.

303. Carlson E. T., The system: $CaO-B_2O_3$. *Bur. Stand. J. Res.* 1932;9:825-832.

304. Hageman V. B. M., Oonk H. A. J., Liquid immiscibility in the B_2O_3-MgO, B_2O_3-CaO, B_2O_3-SrO, and B_2O_3-BaO systems. *Phys. Chem. Glasses.* 1987;28:183-187.

305. Ohta Y., Morinaga K., Yanagase T., Liquid-liquid immiscibility in several binary borate systems. *J. Ceram. Soc. Jpn.* 1982;90:511-516.

306. Klein J., Müller F., Measurement of the enthalpy of mixing of the liquid system $CaO-B_2O_3$ by drop calorimetry. *High Temp.-High Press.* 1987;19:201-209.

307. Muller F., Demirok S., Thermochemical study of the liquid systems $BaO-B_2O_3$ and $CaO-B_2O_3$. *Glastech. Ber.-Glass.* 1989;62:142-149.

308. Knick R., Kohlmeyer E. J., On the molten properties of soda-iron oxide mixtures. *Z. Anorg. Allg. Chem.* 1940;244:67-84.

309. Atlas L. M., Sumida W. K., Solidus, subsolidus, and subdissociation phase equilibria in the system Fe-Al-O. *J. Am. Ceram. Soc.* 1958;41:150-160.

310. Hansson R., Hayes P. C., Jak E., Experimental study of phase equilibria in the Al-Fe-Zn-O system in air. *Metall. Mater. Trans. B.* 2004;35:633-642.

311. Ladavos A. K., Bakas T. V., The Al_2O_3-Fe_2O_3 mixed oxidic system, I. Preparation and characterization. *React. Kinet. Catal. L.* 2001;73:223-228.

312. Muan A., Gee C. L., Phase equilibrium studies in the system iron oxide-Al_2O_3 in air and at 1 atm. O_2 pressure. *J. Am. Ceram. Soc.* 1956;39:207-214.

313. Rhamdhani M. A., Hidayat T., Hayes P. C., et al., Subsolidus phase equilibria of Fe-Ni-X-O (X = Mg, Al) systems in air. *Metall. Mater. Trans. B.* 2009;40:25-38.

314. Richards R. G., White J., Phase relationships of iron-oxide-containing spinels. Part I. Relationships in the system Fe-Al-O. *Brit. Ceram. Trans. J.* 1954;53:233-270.

315. Turnock A. C., Eugster H. P., Fe-Al oxides: Phase relationships below 1,000°C. *J. Petrol.* 1962;3:533-565.

316. Joubert J. C., Shirk T., White W. B., et al., Stability infrared spectrum and magnetic properties of $FeBO_3$. *Mater. Res. Bull.* 1968;3:671-676.

317. Makram H., Touron L., Loriers J., Phase relations in the system $Fe_2O_3 \cdot B_2O_3$ and its application in single crystal growth of $FeBO_3$. *J. Cryst. Growth.* 1972;13-14:585-587.

318. Dai W., Seetharaman S., Staffansson L. I., Phase relationships in the system Fe-Na-O. *Metall. Trans. B.* 1984;15:319-327.

319. Galakhov F. Y., Alumina regions of ternary aluminosilicate systems. Communication 1. The systems FeO-Al_2O_3-SiO_2 and MnO-Al_2O_3-SiO_2. *Izv. An. SSSR.* 1957;539-545.

320. Novokhatsky I. A., Belov B. F., Phase equilibria and distribution of elements in the Fe-O-Al system. *Izv. An. SSSR.* 1966;1:38-48.

321. Oelsen W., Heynert G., The reactions between iron-manganese melts and the melts of their aluminates. *Arch. Eisenhuttenwes.* 1955;26:567-575.

322. Fischer W. A., Hoffmann A., The phase diagram ferrous oxide-aluminium oxide. *Arch. Eisenhuttenwes.* 1956;27:343-346.

323. Rosenbach K., Schmitz J. A., Investigations in the ternary-system iron(II)-oxide-chromium(III)-oxide-alumina. *Arch. Eisenhuttenwes.* 1974;45:843-847.

324. Greig J. W., On liquid immiscibility in the system FeO-Fe_2O_3,-Al_2O_3-SiO_2. *Am. J. Sci.* 1927;14:473-484.

325. Muan A., Phase equilibria in the system FeO-Fe_2O_3-SiO_2. *T. Am. I Min. Met. Eng.* 1955;203:965-976.

326. Allen W. C., Snow R. B., The orthosilicate-iron oxide portion of the system CaO-"FeO"-SiO_2. *J. Am. Ceram. Soc.* 1955;38:264-280.

327. Bowen N. L., Schairer J. F., The system, FeO-SiO_2. *Am. J. Sci.* 1932;24:177-213.

328. Michal E. J., Schuhmann R., Thermodynamics of iron-silicate slags: Slags saturated with solid silica. *T. Am. I Min. Met. Eng.* 1952;194:723-728.

329. Schuhmann R., Ensio P. J., Thermodynamics of iron-silicate slags: Slags saturated with gamma iron. *T. Metall. Soc. AIME.* 1951;194:401-412.

330. Bodsworth C., The activity of ferrous oxide in silicate melts. *J. Iron. Steel I.* 1959;193:13-24.

331. Distin P. A., Whiteway S. G., Masson C. R., Solubility of oxygen in liquid iron from 1785º to 1960ºC. A new technique for the study of slag-metal equilibria. *Can. Metall. Q.* 1971;10:13-18.

332. Alper A. M., McNally R. N., Ribbe P. H., et al., The system MgO-$MgAl_2O_4$. *J. Am. Ceram. Soc.* 1962;45:263-268.

333. Fujii K., Nagasaka T., Hino M., Activities of the constituents in spinel solid solution and free energies of formation of MgO, MgO · Al_2O_3. *ISIJ Int.* 2000;40:1059-1066.

334. Mori T., Solubility of Al_2O_3 in MgO. *J. Cer. Assoc. Jpn.* 1982;90:551-552.

335. Viechnicki D., Schmid F., McCauley J. W., Liquidus-solidus determinations in the system $MgAl_2O_4$-Al_2O_3. *J. Am. Ceram. Soc.* 1974;57:47-48.

336. Wartenberg H. V., Reusch H. J., Melt diagrams of ultrafine oxyde. IV. (Aluminum oxide). *Z. Anorg. Allg. Chem.* 1932;207:1-20.

337. Viertel H., Seifert F., Thermal stability of defect spinels in the system $MgAl_2O_4$-Al_2O_4. *Neues. Jb. Miner. Abh.* 1980;140:89-101.

338. Shirasuka K., Yamaguchi G., Precise measurement of the crystal data and the solid solution range of the defective spinel, MgO·*n*Al_2O_3. *J. Cer. Assoc. Jpn.* 1974;82:650-653.

339. Hageman V. B. M., Oonk H. A. J., Liquid immiscibility in the SiO_2 + MgO, SiO_2 + SrO, SiO_2 + Al_2O_3, and SiO_2 + Y_2O_3 systems. *Phys. Chem. Glasses.* 1986;27:194-198.

340. Davis H. M., Knight M. A., The system magnesium oxide-boric oxide. *J. Am. Ceram. Soc.* 1945;28:97-102.

341. Mutluer T., Timucin M., Phase quilibria in the system MgO-B_2O_3. *J. Am. Ceram. Soc.* 1975;58:196-197.

342. Kim D., Schweiger M. J., Rodriguez C. P., et al., Formulation and characterization of waste glasses with varying processing temperature. PNNL-20774, Pacific Northwest National Laboratory, Richland, WA, 2011. 1-178.

343. Kim D., Vienna J. D., Peeler D. K., et al., Improved alumina loading in high-level waste glasses, Waste Management. Phoenix, AZ, 2008. 1-12.

344. Schweiger M. J., Riley B. J., Crum J. V., et al., Expanded high-level waste glass property data development: Phase I. PNNL-17950, Pacific Northwest National Laboratory, Richland, WA, 2011. 1-227.

345. Matlack K. S., Gan H., Chaudhuri M., et al., Melt rate enhancement for high aluminum HLW glass formulations. VSL-08R1360-1, Vitreous State Laboratory, the Catholic University of America, Washington, DC, 2008. 1-310.

346. Matlack K. S., Kot W. K., Pegg I. L., et al., DM100 and DM1200 melter testing with high waste loading glass formulations for Hanford high aluminum HLW streams. VSL-09T1690-1, Vitreous State Laboratory, the Catholic University of America, Washington, DC, 2009. 1-64.

347. Matlack K. S., Kot W. K., Gan H., et al., Glass formulation development and testing for DWPF high-Al_2O_3 HLW sludges. VSL-10R1670-1, Vitreous State Laboratory, the Catholic University of America, Washington, DC, 2010. 1-122.

348. Johnson F. C., Edwards T. B., Results of the FY09 enhanced DOE high-level waste melter throughput studies at SRNL. SRNL-STI-2009-00778, Savannah River National Laboratory, Aiken, SC, 2010. 1-386.

349. Fox K. M., Peeler D. K., Edwards T. B., et al., International study of aluminum impacts on crystallization in U.S. high level waste glass. SRNS-STI-2008-00057, Savannah River National Laboratory, Aiken, SC, 2008. 1-172.

350. Peeler D. K., Edwards T. B., Herman C. C., et al., Development of high waste loading glasses for advanced melter technologies. WSRC-TR-2002-00426, Savannah River National Laboratory, Aiken, SC, 2002. 1-78.

351. Peeler D. K., Edwards T. B., Reamer I. A., et al., Nepheline formation study for sludge batch 4 (SB4): Phase 1 experimental results. WSRC-TR-2005-00371, Savannah River National Laboratory, Aiken, SC, 2005. 1-174.

352. Peeler D. K., Edwards T. B., Best D. R., et al., Nepheline formation study for sludge batch 4 (SB4): Phase 2 experimental results. WSRC-TR-2006-00006, Savannah River National Laboratory, Aiken, SC, 2006. 1-205.

353. Billings A. L., Edwards T. B., Time-temperature-transformation (TTT) diagrams for the sludge batch 3 - frit 418 glass system. SRNL-STI-2009-00025, Savannah River National Laboratory, Aiken, SC, 2009. 1-36.

354. Billings A. L., Edwards T. B., Time-temperature-transformation (TTT) diagrams for future waste compositions. SRNL-STI-2010-00373, Savannah River National Laboratory, Aiken, SC, 2010. 1-49.

355. Smith E. C., Butler T. A., Ciorneiu B., et al., Advanced Joule Heated Melter Design to Reduce Hanford Waste Treatment Plant Operating Costs - 11131, Waste Management 2011. Phoenix, AZ, 2011. 1-9.

356. Guerrero H. N., Bickford D. F., DWPF melter air-lift bubbler: Development and testing for increasing glass melt rates and waste dissolution. WSRC-TR-2002-0196, Savannah River National Laboratory, Aiken, SC, 2002. 1-23.

357. Vance E. R., Begg B. D., Gregg D. J., 10 - Immobilization of high-level radioactive waste and used nuclear fuel for safe disposal in geological repository systems, 269-295. in Geological Repository Systems for Safe Disposal of Spent Nuclear Fuels and Radioactive Waste (Second Edition)**.** Edited by M. J. Apted and J. Ahn. Woodhead Publishing, 2017.

358. Taylor P., A review of phase separation in borosilicate glasses, with reference to nuclear fuel waste immobilization. AECL-10173, Atomic Energy of Canada Ltd., Pinawa, MB, Canada, 1990. 1-54.

359. Peeler D. K., Hrma P. R., Predicting liquid immiscibility in multicomponent nuclear waste glasses. PNL-SA--23488, Pacific Northwest National Laboratory, United States, 1994. 1-12.

360. Marra S. L., Jantzen C. M., Characterization of projected DWPF glasses heat treated to simulate canister centerline cooling (U). WSRC-TR-92-142, Rev. 1, Savannah River National Laboratory, Aiken, SC, 1993. 1-40.

361. Costa G. C. C., Xu H. W., Navrotsky A., Thermochemistry of barium hollandites. *J. Am. Ceram. Soc.* 2013;96:1554-1561.

362. Jung I. H., Eriksson G., Wu P., et al., Thermodynamic modeling of the Al_2O_3-Ti_2O_3-TiO_2 system and its applications to the Fe-Al-Ti-O inclusion diagram. *ISIJ Int.* 2009;49:1290-1297.

363. Lejus A. M., Goldberg D., Revcolev.A, On some new compounds formed by the TiO_2 rutile with trivalent and tetravalent metal oxides. *Cr. Acad. Sci. C Chim.* 1966;263:1223-1226.

364. Kamiya S., Tilley R. J. D., Phase relations in pseudobinary system TiO_2-Ga_2O_3. *J. Solid State Chem.* 1977;22:205-216.

365. Bursill L. A., Stone G. G., Tunnel and intergrowth structures in the gallia-rich gallium titanate system. *J. Solid State Chem.* 1981;38:149-157.

366. Schmitz-Dumont O., Reckhard H., Characterization of the Alkali Titanates. *Monatsh. Chem.* 1959;90:134-142.

367. Grey I. E., Madsen I. C., Watts J. A., et al., New cesium titanate layer structures. *J. Solid State Chem.* 1985;58:350-356.

368. Grey I. E., Li C., Madsen I. C., et al., The stability and structure of $Cs_x[Ti_{2-x/4}\square_{x/4}]O_4$, $0.61 < x < 0.65$. *J. Solid State Chem.* 1987;66:7-19.

369. Kwiatkowska J., Grey I. E., Madsen I. C., et al., An x-ray and neutron-diffraction study of $Cs_2Ti_5O_{11}$ and $Cs_2Ti_5O_{11}.X_2O$, X = H,D. *Acta Crystallogr. Sect. B-Struct. Commun.* 1987;43:258-265.

370. Bursill L. A., Smith D. J., Kwiatkowska J., Identifying characteristics of the fibrous cesium titanate $Cs_2Ti_5O_{11}$. *J. Solid State Chem.* 1987;69:360-368.

371. Peres V., Fabry P., Genet F., et al., Preparations and characterizations of ceramics based on cesium titanate. *J. Eur. Ceram. Soc.* 1994;13:403-410.

372. Kobyakov V. P., Barinova T. V., Sichinava M. A., Phase relations in the TiO_2-$CsNO_3$ system between 550 and 1140 K. *Inorg. Mater+.* 2011*;*47:290-295.

373. Lu X. G., Jin Z. P., Thermodynamic assessment of the BaO-TiO_2 quasibinary system. *Calphad-Comput. Coupling Ph. Diagrams Thermochem.* 2000*;*24:319-338.

374. Sanderson R. T., Chemical Periodicity, New York: Reinhold Publishing Corporation; 1960.

375. Whaley T. P., 8 - Sodium, potassium, rubidium, cesium and francium, 369-529. in The Chemistry of Lithium, Sodium, Potassium, Rubidium, Cesium and Francium**.** Edited by W. A. Hart, O. F. Beumel, and T. P. Whaley. Pergamon, 1973.

376. Parr R. G., Density functional theory. *Annu. Rev. Phys. Chem.* 1983*;*34:631-656.

377. Wu L. L., Schliesser J., Woodfield B. F., et al., Heat capacities, standard entropies and Gibbs energies of Sr-, Rb- and Cs-substituted barium aluminotitanate hollandites. *J. Chem. Thermodyn.* 2016*;*93:1-7.

378. Hanaor D. A. H., Sorrell C. C., Review of the anatase to rutile phase transformation. *J. Mater. Sci.* 2011*;*46:855-874.

379. Eriksson G., Pelton A. D., Critical evaluation and optimization of the thermodynamic properties and phase diagrams of the MnO-TiO_2, MgO-TiO_2, FeO-TiO_2, Ti_2O_3-TiO_2, Na_2O-TiO_2, and K_2O-TiO_2 systems. *Metall. Trans. B.* 1993*;*24:795-805.

380. Karkhanavala M. D., Momin A. C., Subsolidus reactions in the system Fe_2O_3-TiO_2. *J. Am. Ceram. Soc.* 1959*;*42:399-402.

381. Cheynet B., Chaud P., Chevalier P. Y., et al., NUCLEA - Thermodynamic properties and phase equilibria in nuclear systems. *J. Phys. IV.* 2004*;*113:61-64.

382. Fischer W. A., Hoffmann A., The state diagram iron oxide-aluminum oxide. *Arch. Eisenhuttenwes.* 1956*;*27:343-346.

383. Vidacak B., Sichen D., Seetharaman S., The existence of a ternary phase in the Al_2O_3-CaO-FeO system. *ISIJ Int.* 2002*;*42:561-563.